

# Neuroscience Bulletin

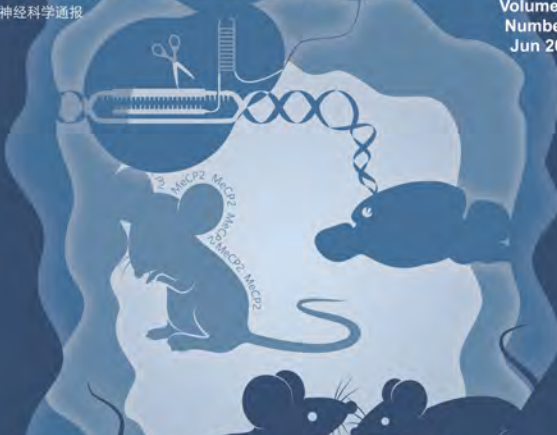
The Official Journal of The Chinese Neuroscience Society

神经科学通报

Volume 36

Number 6

Jun 2020



Medial Prefrontal Cortex is Critical for  
Autistic Phenotype

  Springer

[www.neurosci.cn](http://www.neurosci.cn)

## About the Cover

*MECP2* transgenic mice recapitulate some of the core symptoms of *MECP2* duplication syndrome, including social deficits. The cover illustrates that normalization of MeCP2 expression in the medial prefrontal cortex of the *MECP2* duplication mouse model *via* CRISPR-Cas9 gene-editing reverses the social recognition deficit and mice perform social interactions normally. See pages 570–584. (Cover image provided by Dr. Yefei Li)



Volume 36 Number 6  
June 2020

## Editorial

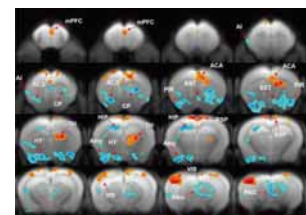
### 567 Gene Editing to the Rescue: Reversal of Social Deficits Associated with *MECP2* Duplication

Zi-Xian Yu · Dan-Yang Wang · Xiao-Hong Xu

## Original Articles

### 570 Reversal of Social Recognition Deficit in Adult Mice with *MECP2* Duplication *via* Normalization of MeCP2 in the Medial Prefrontal Cortex

Bin Yu · Bo Yuan · Jian-Kun Dai · Tian-lin Cheng · Sheng-Nan Xia · Ling-Jie He · Yi-Ting Yuan · Yue-Fang Zhang · Hua-Tai Xu · Fu-Qiang Xu · Zhi-Feng Liang · Zi-Long Qiu



p 578

### 585 Whole-Brain Monosynaptic Inputs to Hypoglossal Motor Neurons in Mice

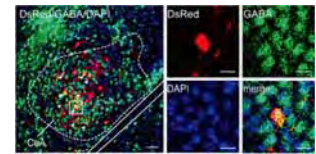
Han Guo · Xiang-Shan Yuan · Ji-Chuan Zhou · Hui Chen · Shan-Qun Li · Wei-Min Qu · Zhi-Li Huang

**598 Plasticity of Sniffing Pattern and Neural Activity in the Olfactory Bulb of Behaving Mice During Odor Sampling, Anticipation, and Reward**

Penglai Liu · Tiantian Cao · Jinshan Xu · Xingfeng Mao · Dejuan Wang · Anan Li

**611 Social Isolation in Male Rats During Adolescence Inhibits the Wnt/ $\beta$ -Catenin Pathway in the Prefrontal Cortex and Enhances Anxiety and Cocaine-Induced Plasticity in Adulthood**

Santiago Cuesta · Alejandrina Funes · Alejandra M. Pacchioni



p 592

**625 Aloin Protects Against Blood–Brain Barrier Damage After Traumatic Brain Injury in Mice**

Yao Jing · Dian-Xu Yang · Wei Wang · Fang Yuan · Hao Chen · Jun Ding · Zhi Geng · Heng-Li Tian

**639 EPAC Negatively Regulates Myelination *via* Controlling Proliferation of Oligodendrocyte Precursor Cells**

Zhen-Zhen Gao · Ying-Cong Li · Chong-Yu Shao · Jian Xiao · Ying Shen · Liang Zhou

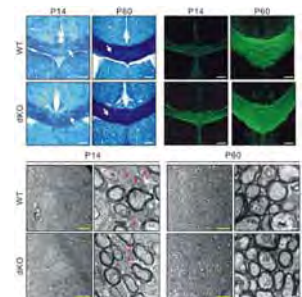
## Letters to the Editor

**649 Empathic Contagious Pain and Consolation in Laboratory Rodents: Species and Sex Comparisons**

Rui Du · Wen-Jun Luo · Kai-Wen Geng · Chun-Li Li · Yang Yu · Na Wei · Jun Chen

**654 Low-frequency Stimulation at the Subiculum is Anti-convulsant and Anti-drug-resistant in a Mouse Model of Lamotrigine-resistant Temporal Lobe Epilepsy**

Yeping Ruan · Cenglin Xu · Jile Lan · Jiazhen Nao · Shuo Zhang · Fei Fan · Yi Wang · Zhong Chen

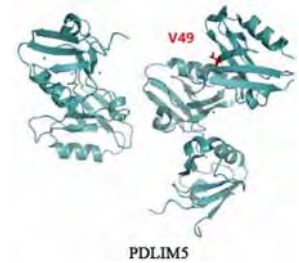


p 642

**659 The Role of Frontal and Occipital Cortices in Processing Sustained Visual Attention in Young Adults with Attention-Deficit/Hyperactivity Disorder: A Functional Near-Infrared Spectroscopy Study**

Ziyan Wu · Yuyang Luo · Yu Gao · Ying Han · Kai Wu · Xiaobo Li

- 664 **Somatic Mutations Confer Severe Peripheral Neuropathy in POEMS Syndrome-Associated Multicentric Castleman Disease**  
Qingqing Lin · Juying Wei · Jiejing Qian · Liangshun You · Wenbin Qian



p 665

## Review

- 667 **Pathophysiology and Individualized Management of Vasovagal Syncope and Postural Tachycardia Syndrome in Children and Adolescents: An Update**  
Ying Liao · Junbao Du

## Correction

- 682 **Correction to: EPAC Negatively Regulates Myelination via Controlling Proliferation of Oligodendrocyte Precursor Cells**  
Zheng-Zheng Gao · Ying-Cong Li · Chong-Yu Shao · Jian Xiao · Ying Shen · Liang Zhou



## Gene Editing to the Rescue: Reversal of Social Deficits Associated with *MECP2* Duplication

Zi-Xian Yu<sup>1,2,3</sup> · Dan-Yang Wang<sup>1,2,3</sup> · Xiao-Hong Xu<sup>1,3</sup> 

Received: 16 April 2020 / Accepted: 9 May 2020 / Published online: 29 May 2020  
© Shanghai Institutes for Biological Sciences, CAS 2020

Methyl-CpG-binding protein 2 (MeCP2) is broadly recognized as the genetic cause of Rett Syndrome (RTT), a devastating neurodevelopmental disorder with the progressive loss in motor skills and speech that is found almost exclusively in young girls [1, 2]. Over 95% of RTT patients carry loss-of-function mutations in the X-linked *MECP2* gene, while the same mutations in males largely lead to infantile death. Still, micro-duplications of the X chromosome segment that encompasses the *MECP2* gene give rise to another neurological disorder known as MeCP2 duplication syndrome (MDS) that predominantly affects males, with symptoms including autistic features, seizures, profound intellectual disabilities, recurrent infections, hypotonia, and impaired social interactions. MeCP2 is expressed throughout the body with high levels in neurons, where it functions as a transcriptional repressor, a microRNA processor, and a regulator of RNA splicing within the nucleus to modulate gene expression, thereby regulating diverse aspects of neuronal function including fate determination, morphology, synaptogenesis, and synaptic plasticity. Indeed, neurons derived from the

induced pluripotent stem cells of RTT or MDS patients exhibit altered dendritic morphology and spine density [3, 4].

Over the past two decades, transgenic animal models have been established to recapitulate the genetic defects of the *MECP2* gene seen in RTT and MDS (null mutations or duplications), and have successfully reproduced many of the core behavioral symptoms found in patients. Remarkably, researchers have been able to demonstrate with the aid of genetic ‘tricks’ that systematically correcting *MECP2* genetic abnormalities at the organism level in adult mice, either by re-expressing the *MECP2* gene in an otherwise null background or by normalizing the expression level in duplication models, reverses the behavioral deficits after symptom onset [2]. These findings spark the hope that similar genetic correction procedures may also be beneficial in patients. Yet, as different cells likely contribute to distinct aspects of the behavioral deficits, the key question becomes which brain area/cell population to target in patients. In an exciting study published recently in *Neuroscience Bulletin*, Bin Yu and colleagues demonstrated that normalizing MeCP2 expression in the medial prefrontal cortex (mPFC) reverses the social deficits associated with *MeCP2* duplication (Fig. 1) [5].

Using a transgenic mouse model of MDS, in which insertion of genomic sequences of the human version of the *MECP2* (*hMECP2*) gene results in overexpression of MECP2, the authors first extensively characterized the behaviors of transgenic animals (males). Consistent with previous reports, they found that *MECP2*-transgenic (*MECP2*-Tg) males displayed heightened anxiety as well as potentiated fear learning and generalization. Moreover, *MECP2*-Tg males showed deficits in social recognition in that they had difficulty discriminating novel from familiar conspecifics (Fig. 1). Nevertheless, *MECP2*-Tg males were

---

Zi-Xian Yu and Dan-Yang Wang have contributed equally to this article.

---

✉ Xiao-Hong Xu  
xiaohong.xu@ion.ac.cn

<sup>1</sup> Institute of Neuroscience, State Key Laboratory of Neuroscience, Chinese Academy of Sciences Center for Excellence in Brain Science and Intelligence Technology, Chinese Academy of Sciences, Shanghai 200031, China

<sup>2</sup> University of the Chinese Academy of Sciences, Beijing 100049, China

<sup>3</sup> Shanghai Center for Brain Science and Brain-Inspired Intelligence Technology, Shanghai 200031, China

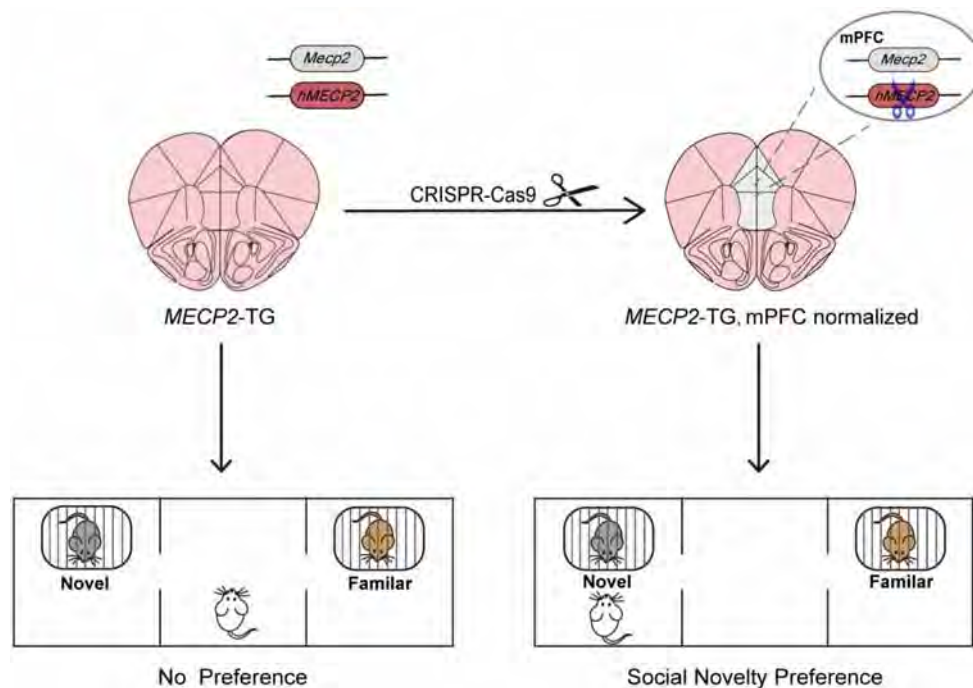


**Fig. 1** Normalizing MeCP2 expression in the mPFC through a virus-based CRISPR-Cas9 system rescues the social deficits associated with MeCP2 duplication. *MECP2-TG* animals positive for transgenes of the human *MECP2* gene (*hMECP2*) overexpress the MECP2 protein throughout the brain and show deficits in a social recognition test, in which they cannot discriminate between novel and familiar conspecifics and do not show a preference for novel conspecifics. Yu

*et al.* used a virus-based CRISPR-Cas9 system to normalize MeCP2 expression in the mPFC by delivering single guide RNAs that specifically target, and thereby cause loss-of-function mutations, in the *hMECP2* gene. *MECP2-TG* males with normalized mPFC MeCP2 expression now show preference for novel conspecifics, indicating rescue of the social recognition deficit.

normal in terms of sucrose consumption, cocaine-induced place preference, recognition of novel objects, and learning and remembering the location of a hidden escape box in a maze, demonstrating unimpaired reward processing and learning/memory capacity.

Next, to search for the neural substrates that correlate with the behavioral deficits, the authors performed resting-state fMRI analysis using a 9.4T scanner. Specifically, they measured the Regional Homogeneity (ReHo) value, which evaluates the similarity or synchronization of fMRI signals at a given voxel to those of its nearest neighbors by calculating Kendall's coefficient of concordance. *MECP2-Tg* males had higher ReHo values in the mPFC, anterior cingulate cortex, thalamus, and the retrosplenial and visual areas of cortex than control males, indicating higher neural activity/synchrony in these regions. Meanwhile, the ReHo values were lower in the nucleus accumbens, piriform cortex, bed nuclei of the stria terminalis (BST), hypothalamus, hippocampus, amygdala, and periaqueductal gray in *MECP2-Tg* males. Interestingly, these ReHo value differences were concentrated in areas implicated in the regulation of aversive and social behaviors, in line with the anxiety and social recognition deficits in *MECP2-Tg* males.

Following these discoveries, the authors chose the mPFC as the target, since this region shows increased ReHo signals in *MECP2-Tg* males, and convergent evidence suggests that it plays a key role in social cognition. For example, lower gamma oscillation synchrony in the mPFC during social interactions but higher synchrony in a quiet state have been found in a transgenic mouse model of autism spectrum disorder (ASD) [6], which also shows social recognition deficits similar to *MECP2-Tg* males. To normalize MeCP2 expression, the authors cleverly used a virus-based CRISPR-Cas9 system that destroys the transgenic *hMECP2* gene by delivering single guide RNA designed to specifically target the human but not the mouse *MECP2* gene (Fig. 1). After virus injection, MECP2 expression in the mPFC was indeed decreased to the wild-type level in *MECP2-Tg* males. Even more excitingly, the social recognition deficits were also corrected in these males as they now showed a clear preference for novel conspecifics just like the wild-type controls (Fig. 1). By comparison, normalizing the mPFC MECP2 expression failed to rectify other behavioral abnormalities such as the increased anxiety and enhanced fear learning/memory. In addition, using the same viral strategy, the authors also normalized MeCP2 expression in the BST, a region that

shows decreased ReHo signals in *MECP2*-Tg males and is known to regulate anxiety-related behaviors. Unfortunately, this manipulation did not result in any behavioral improvements, again highlighting the importance of the target site. Taken together, these results clearly demonstrate that normalizing mPFC MeCP2 expression reverses social recognition deficits in a mouse model of MDS (Fig. 1).

Thus, Yu *et al.* have made an important step forward beyond the previous finding that showed whole-organism level correction of *MECP2* gene can reverse behavioral deficits, by showing that region-specific correction of MeCP2 expression in the mPFC improves social cognition, at least in mice. It would be both interesting and informative in the future to test the relevance and effectiveness of the strategy used by Yu *et al.* in other animal models of MeCP2 disorders such as primate MeCP2-null or overexpression models. Thus, fMRI, as in Yu *et al.* could be first used to compare the whole-brain activity of MeCP2 transgenic animals with controls in different models to reveal candidate target sites [6–9]. Following this, a customized virus-based CRISPR-Cas9 system could be used to normalize MeCP2 levels in each site to determine whether different aspects of behavioral deficits could be rescued. Along this line, it would be imperative to subject animals to fMRI analysis again after MeCP2 expression is corrected. Such analysis will reveal whether the resting-state activity and the associated neural networks are also normalized in the targeted areas and whether these measurements predict or correlate with behavioral improvements. With such systematic efforts, normalizing MeCP2 expression *via* the CRISPR-Cas9 system may become a viable treatment option for RTT patients.

Furthermore, as social deficits are a core symptom in many other heritable psychiatric diseases such as ASD, for which there is also no treatment available, it will be interesting to determine whether gene-editing strategies coupled with neuroimaging studies such as that championed here by Yu *et al.* would provide an option to alleviate symptoms in these disorders. On this front, the rapidly evolving CRISPR-Cas9 field is providing ever-increasing

possibilities to both turn up and turn down gene expression *in vivo* in a targeted manner [10]. In addition, newly developed CRISPR-Cas9 systems could edit the genome with single-nucleotide precision in both the coding and regulatory regions of any gene, thereby correcting any *de novo* single-nucleotide mutations that might have caused a disease state. It is exciting to think that personalized treatments for psychiatric disorders using neuroimaging and gene-editing strategies may be a reality not too far ahead. In any case, Yu *et al.* have shown us a way forward.

## References

1. Lombardi LM, Baker SA, Zoghbi HY. MECP2 disorders: from the clinic to mice and back. *J Clin Invest* 2015, 125: 2914–2923.
2. Qiu Z. Deciphering MECP2-associated disorders: disrupted circuits and the hope for repair. *Curr Opin Neurobiol* 2018, 48: 30–36.
3. Djuric U, Cheung AYL, Zhang W, Mok RS, Lai W, Piekna A, *et al.* MECP2e1 isoform mutation affects the form and function of neurons derived from Rett syndrome patient iPS cells. *Neurobiol Dis* 2015, 76: 37–45.
4. Nageshappa S, Carromeu C, Trujillo CA, Mesci P, Espuny-Camacho I, Pasciuto E, *et al.* Altered neuronal network and rescue in a human MECP2 duplication model. *Mol Psychiatry* 2016, 21: 178–188.
5. Yu B, Yuan B, Dai JK, Cheng TL, Xia SN, He LJ, *et al.* Reversal of social recognition deficit in adult mice with MECP2 duplication *via* Normalization of MeCP2 in the medial prefrontal cortex. *Neurosci Bull* 2020. <https://doi.org/10.1007/s12264-020-00467-w>
6. Cao W, Lin S, Xia QQ, Du YL, Yang Q, Zhang MY, *et al.* Gamma oscillation dysfunction in mPFC leads to social deficits in neuroligin 3 R451C knockin mice. *Neuron* 2018, 97: 1253–1260 e1257.
7. Qian A, Wang X, Liu H, Tao J, Zhou J, Ye Q, *et al.* Dopamine D4 receptor gene associated with the frontal-striatal-cerebellar loop in children with ADHD: A resting-state fMRI study. *Neurosci Bull* 2018, 34: 497–506.
8. Reddan MC, Wager TD. Modeling Pain Using fMRI: From regions to biomarkers. *Neurosci Bull* 2018, 34: 208–215.
9. Wang XH, Yu A, Zhu X, Yin H, Cui LB. Cardiopulmonary comorbidity, radiomics and machine learning, and therapeutic regimens for a cerebral fMRI predictor study in psychotic disorders. *Neurosci Bull* 2019, 35: 955–957.
10. Wang D, Zhang F, Gao G. CRISPR-Based therapeutic genome editing: Strategies and *in vivo* delivery by AAV vectors. *Cell* 2020, 181: 136–150.



# Reversal of Social Recognition Deficit in Adult Mice with *MECP2* Duplication *via* Normalization of MeCP2 in the Medial Prefrontal Cortex

Bin Yu<sup>1,2</sup> · Bo Yuan<sup>1</sup> · Jian-Kun Dai<sup>1</sup> · Tian-lin Cheng<sup>1</sup> · Sheng-Nan Xia<sup>1,2</sup> ·  
Ling-Jie He<sup>3</sup> · Yi-Ting Yuan<sup>1</sup> · Yue-Fang Zhang<sup>1</sup> · Hua-Tai Xu<sup>1</sup> · Fu-Qiang Xu<sup>4</sup> ·  
Zhi-Feng Liang<sup>1</sup> · Zi-Long Qiu<sup>1</sup>

Received: 19 August 2019 / Accepted: 16 November 2019 / Published online: 7 March 2020  
© Shanghai Institutes for Biological Sciences, CAS 2020

**Abstract** Methyl-CpG binding protein 2 (MeCP2) is a basic nuclear protein involved in the regulation of gene expression and microRNA processing. Duplication of *MECP2*-containing genomic segments causes *MECP2* duplication syndrome, a severe neurodevelopmental disorder characterized by intellectual disability, motor dysfunction, heightened anxiety, epilepsy, autistic phenotypes, and early death. Reversal of the abnormal phenotypes in adult mice with *MECP2* duplication (*MECP2*-TG) by normalizing the MeCP2 levels across the whole brain has been demonstrated. However, whether different brain areas or neural circuits contribute to different aspects of the behavioral deficits is still unknown. Here, we found that *MECP2*-TG mice showed a significant social recognition deficit, and were prone to display aversive-like behaviors, including heightened anxiety-like behaviors and a fear generalization phenotype. In addition, reduced locomotor activity was observed in *MECP2*-TG mice. However,

appetitive behaviors and learning and memory were comparable in *MECP2*-TG and wild-type mice. Functional magnetic resonance imaging illustrated that the differences between *MECP2*-TG and wild-type mice were mainly concentrated in brain areas regulating emotion and social behaviors. We used the CRISPR-Cas9 method to restore normal MeCP2 levels in the medial prefrontal cortex (mPFC) and bed nuclei of the stria terminalis (BST) of adult *MECP2*-TG mice, and found that normalization of MeCP2 levels in the mPFC but not in the BST reversed the social recognition deficit. These data indicate that the mPFC is responsible for the social recognition deficit in the transgenic mice, and provide new insight into potential therapies for *MECP2* duplication syndrome.

**Keywords** *MECP2* duplication · Medial prefrontal cortex · Social recognition deficit · CRISPR-Cas9

**Electronic supplementary material** The online version of this article (<https://doi.org/10.1007/s12264-020-00467-w>) contains supplementary material, which is available to authorized users.

✉ Zi-Long Qiu  
zqiu@ion.ac.cn

- <sup>1</sup> Institute of Neuroscience, State Key Laboratory of Neuroscience, Chinese Academy of Sciences Center for Excellence in Brain Science and Intelligence Technology, Chinese Academy of Sciences, Shanghai 200031, China
- <sup>2</sup> University of Chinese Academy of Sciences, Beijing 100049, China
- <sup>3</sup> Department of Molecular and Human Genetics, Howard Hughes Medical Institute, Baylor College of Medicine, Houston, TX 77030, USA
- <sup>4</sup> Wuhan Institute of Physics and Mathematics, Chinese Academy of Sciences, Wuhan 430071, China

## Introduction

Methyl-CpG binding protein 2 (MeCP2) is a critical nuclear protein involved in transcriptional and post-transcriptional regulation [1–5]. Loss-of-function mutations in the *MECP2* gene have been found in 95% of patients with Rett syndrome, a devastating neurodevelopmental disorder with autistic phenotypes [6, 7]. Conversely, gain-of-function has also been identified in humans, typically through duplication or triplication of Xq28, which contains *MECP2* and defines another progressive neurological disorder, *MECP2* duplication syndrome, which shares core symptoms with autism spectrum disorder [8, 9].

*MECP2* duplication syndrome is a severe childhood neurodevelopmental disease that mainly affects males; it is characterized by profound mental retardation, poor speech

development, recurrent infections, epilepsy, motor dysfunction, anxiety, and autism [9, 10]. Transgenic mice that express a double or triple level of MeCP2 *via* insertion of the human *MECP2* gene (*MECP2*-TG) have been established, and recapitulate some of the symptoms in patients, including decreased motor activity, increased anxiety-like behaviors, seizures, and social deficits [11, 12]. Consistent with the clinical observations in humans, the phenotypes in mice that express a threefold dose of MeCP2 are much more severe [11, 13]. Interestingly, mice that overexpress the version of MeCP2 with mutations in either the methyl-CpG binding domain (MBD) or the transcriptional repression domain (TRD) are indistinguishable from wild-type littermates, indicating that both the MBD and TRD are indispensable for double MeCP2 to be toxic [14]. The neuropathological mechanism underlying *MECP2* duplication syndrome is still elusive. Recent studies have demonstrated that the relative cell density and number across cortical layers are essentially identical in *MECP2*-TG mice and controls; however, the spine turnover rate of layer V pyramidal neurons and dendritic arborization are dramatically changed during development in the transgenic mice [15]. Moreover, synaptogenesis, dendritic complexity, and the excitatory synaptic response are enhanced in neurons with *MECP2* duplication [16, 17], and the synaptic plasticity and synchrony of hippocampal neurons are abnormally elevated in *MECP2*-TG mice [11, 18]. These lines of evidence strongly imply that overexpression of MeCP2 does not affect the survival of neurons, and synaptic defects and circuit malfunction are the main manifestations of *MECP2* duplication syndrome.

Understanding the neuropathological mechanism of *MECP2* duplication syndrome has just begun, and no good intervention is available in the clinic. It is noteworthy that reversal of phenotypes in adult symptomatic *MECP2*-TG mice by correction of MeCP2 levels across the whole brain has been demonstrated [19], indicating that the neuroanatomy may remain intact in this disorder, so that correction of the molecular dysfunction can restore healthy physiology. However, whether different brain areas or neural circuits contribute to diverse aspects of the behavioral deficits is still unknown. Here, we report that using CRISPR-Cas9 technology to normalize MeCP2 levels in the medial prefrontal cortex (mPFC), but not the bed nuclei of the stria terminalis (BST) can reverse the social recognition deficit in adult *MECP2*-TG mice.

## Materials and Methods

### Mice

Mice with *MECP2* duplication (Stock No: 008679) on a pure FVB/N background were obtained from The Jackson Laboratory [11]. To bypass the issue of probable behavioral defects due to the premature retinal degeneration that develops in the pure FVB/N background [20], we used F1 hybrid *MECP2*-TG mice (FVB/N × C57Bl/6) as previously reported [12] for all experiments.

Mice were maintained in a temperature-controlled, SPF-level facility on a 12-h light–dark cycle and with *ad libitum* access to food and water. Only male mice were used. All animal breeding and experimental procedures were approved by and complied with the guidelines of the Animal Advisory Committee at the Shanghai Institutes for Biological Sciences, Chinese Academy of Sciences.

### Behavioral Phenotyping

*MECP2*-TG mice and littermate controls (2–4 months old) were familiarized with an experimenter blinded to the genotype for 4 to 5 days before behavioral phenotyping. All behavioral tests were performed during the dark period. Mice were habituated in the test room for 1 h before each test and at least one day of recovery was allowed between assays.

#### Open Field Test

After habituation, each mouse was placed in the center of an open arena ( $40 \times 40 \times 40 \text{ cm}^3$ ), and its behavior was tracked for 30 min by a camera above the arena. General locomotor activity was automatically analyzed by Ethovision XT 11.5 software (Noldus Information Technology, Wageningen, Netherlands).

#### Light/Dark Box Test

After habituation, each mouse was placed on the dark side ( $15 \times 27 \times 30 \text{ cm}^3$ ) of the light/dark box; this was connected to the light side ( $30 \times 27 \times 30 \text{ cm}^3$ ) by a small hole. Recording was performed by the overhead camera for 10 min. The time and frequency of mouse entries to the light side were recorded and analyzed by Ethovision XT 11.5 software.

#### Elevated Plus Maze

After habituation, each mouse was placed in the center of a plus maze consisting of two open arms ( $6 \times 30 \text{ cm}^2$ ) and two closed arms ( $6 \times 30 \times 20 \text{ cm}^3$ ) 50 cm above ground. The time spent in the open arms was recorded for 10 min. Data analysis was performed by Ethovision XT 11.5 software.

### *Three-Chamber Test*

This test was performed as previously described [21] with a few modifications. Age-matched C57BL/6 males were used as partner mice. Two days before the test, partner mice were placed randomly in either the left or right wire cage of the three chambers ( $60 \times 40 \times 30 \text{ cm}^3$ ) to habituate for 1 h per day. After habituation on the day of testing, the test mouse was first placed in the center of the three-chamber apparatus for the side-preference test. The time spent in exploring each wire cage was measured for 10 min. Next, during the social approach test, the partner mouse and a toy mouse was assigned to either the left or right cage in a counterbalanced manner. The amount of time the test animal spent in investigating the partner mouse or the toy mouse was measured for 10 min. Lastly, during the social novelty test, the toy mouse was replaced by a novel partner mouse and the partner mouse during the social approach test became the familiar partner mouse. The amount of time test animals spent investigating the familiar or novel partner mouse was measured for 10 min. All data were analyzed by Ethovision XT 11.5 software.

### *Fear Conditioning Test*

Test animals were submitted to an auditory fear conditioning paradigm. Two different contexts, for conditioning (context A) and cued memory testing (context B), were used and the experiment lasted for three days. Freezing behavior was quantified by video-based software (FreezeFrame, Actimetrics Software, Wilmette, IL). In brief, each mouse was placed in context A to habituate for 10 min on the first day. Twenty-four hours after habituation, the mouse was subjected to fear conditioning sessions. The 4 min prior to the first conditioned stimulus (CS) (5 kHz, 90 dB, 20 s) were used to measure baseline freezing. The CS was paired to the unconditioned stimulus (US) (2 s, 0.5 mA footshock back to back with the last CS) and 5 CS/US pairings were presented in each conditioning session with an 80-s inter-trial interval. Twenty-four hours after conditioning, the mouse was tested for contextual fear memory in context A for 5 min. For the cued fear memory test, each mouse was placed in context B to habituate for 3 min, then the CS was presented and lasted for 3 min. The interval between the two tests in the same mouse was not less than 30 min. The percentage freezing in the first 3 min (in a new context) represented the extent of fear generalization, and the percentage freezing in the last 3 min reflected the cued fear memory.

### *Novel Object Recognition Test*

This test lasted for three days. On the first day, each mouse was put into the apparatus ( $40 \text{ cm} \times 40 \text{ cm} \times 40 \text{ cm}$ ) to acclimate to the environment for 10 min after habituation in the test room. On day 2, two identical objects (blue cones) were placed on the same side of the apparatus, and the mouse

was put into the apparatus to explore for 10 min. On day 3, all the processes were the same as on day 2, except that one of the old objects was randomly replaced with a new different object (a yellow cylinder). The exploration time was counted as the period for which mouse's nose entered the designated area 2 cm around the object. All data were analyzed by Ethovision XT 11.5 software.

### *Sucrose Preference Test*

The tested mice, one per cage, were presented with two drinking bottles. Prior to the test, each mouse was habituated in their home cage for at least 3 days. After the acclimatization, the water in one bottle was replaced by 0.5% sucrose solution. Water and sucrose solution intake were measured daily for 4 days by weighing the bottles. The positions of the bottles were switched daily to reduce side bias. Mice were again presented with two bottles of water after the 0.5% sucrose preference test for 1 week. Then, the 2% sucrose preference test was performed using the same cohorts. All the procedures were the same as for the 0.5% sucrose preference test, except that the concentration of sucrose was 2%. Sucrose preference was calculated as the percentage of the volume of sucrose intake over the total volume of fluid intake and averaged over the 4 days of testing.

### *Cocaine Conditioned Place Preference (CPP) Test*

The CPP boxes consisted of three compartments ( $16.8 \text{ cm} \times 12.7 \text{ cm} \times 12.7 \text{ cm}$  for the left and right compartments and  $7.2 \text{ cm} \times 12.7 \text{ cm} \times 12 \text{ cm}$  for the central compartment). The right compartment was painted white and had a steel mesh floor, the left was painted black and had a steel rod floor, and the central compartment had gray walls and a smooth floor as a neutral zone. The test lasted for 11 days. On day 1, each mouse was put into the central compartment to freely explore the three compartments for 20 min for habituation. On day 2, the times each mouse spent in the black and the white compartments were recorded for 20 min with Anilab software. The less preferred compartment was used as the conditioned compartment, and the other was regarded as the unconditioned compartment. On day 3, the mouse received a cocaine injection (20 mg/kg) and was confined for 30 min in the conditioned compartment determined by the test on day 2. On day 4, the mouse received a saline injection paired with the unconditioned compartment for 30 min. Four drug sessions and four saline sessions were administered, and the last day of treatment was with saline. On the day of testing, day 11, the mouse received a saline injection, and the time spent in the black and white compartments was recorded for 20 min with Anilab software. The cocaine CPP score was calculated as the time spent in the conditioned compartment minus the time spent in the unconditioned compartment.

### Barnes Maze Test

This test lasted for 13 days. Each day, experiments began after habituation for 1 h in the test room (strong light was applied to increase the motivation of mice to escape from the circular platform). Day 1 was for adaptation; each mouse was placed in a cylindrical black start chamber in the middle of the maze. Ten seconds later, the chamber was lifted and the mouse guided to the escape box. The mouse was allowed to stay in the box after covering with a lid for a dark reward for 2 min. On day 2, the mouse was placed in the middle of the maze as on day 1 and allowed to explore the maze for 3 min. The trial ended when the mouse entered the escape box or after 3 min had elapsed. The box was covered with a lid immediately after the mouse entered, and it was allowed to stay there for 1 min. If the mouse did not reach the goal within 3 min, the experimenter guided the mouse gently to the escape box and left it inside for 1 min. Mice received 4 trials per day with an inter-trial interval of 15 min for 4 days. During the training (days 2–5), the time to find and enter the escape box was measured manually. On day 6, 24 h after the last training day, the target hole was closed and short-term memory was tested. Mice were placed in the middle of the maze and allowed to explore for 90 s. The time to find the right target hole was measured manually. Long-term memory was assessed on day 13, using the same process as on day 6.

### MRI Data Acquisition and Data Processing

All imaging was performed on a 9.4 T/30 cm Bruker BioSpec scanner (Bruker, Ettlingen, Germany) with a 20 mm-diameter volume coil for radiofrequency pulse transmission and a mouse cryoprobe surface coil for signal detection. To overcome significant echo-planar imaging (EPI) signal dropout deep in the brain caused by the aural cavity magnetic susceptibility artifact, we introduced a liquid-phase fluorocarbon into the middle ear before imaging [22]. During an imaging session, the body temperature was maintained at  $37^{\circ}\text{C} \pm 0.5^{\circ}\text{C}$  by combining a warm water pad and a hot-air blower with temperature feedback (SAIL, Stony Brook, NY), and respiratory rate was monitored (Model 1025, SAIL, Stony Brook, NY). A rapid acquisition relaxation enhancement (RARE)  $T_2$ -weighted sequence was selected to acquire 22 coronal slices of 0.4 mm thickness, which covered the whole mouse brain volume. The anatomical images were obtained with an in-plane resolution of  $0.063 \text{ mm} \times 0.063 \text{ mm}$  (matrix size  $256 \times 256$  and field of view (FOV)  $16 \text{ mm} \times 16 \text{ mm}$ ), repetition time (TR) 3200 ms, echo time (TE) 33 ms, RARE factor 8, and three averages. During imaging, the mice were anesthetized with 3% isoflurane (0.5 bar). Resting-state fMRI data were scanned using a gradient echo EPI sequence with the following parameters:

TR 2500 ms; TE 12 ms; flip angle  $75^{\circ}$ ; matrix size  $100 \times 100$ ; FOV  $16 \text{ mm} \times 16 \text{ mm}$ ; in-plane resolution  $0.16 \text{ mm} \times 0.16 \text{ mm}$ ; slice thickness, 0.4 mm; 22 coronal slices. One hundred twenty EPI volumes were acquired in each run, and 6 runs were obtained for each session. During imaging, the mice were anesthetized with a combination of 0.5% isoflurane (0.5 bar) and dexmedetomidine (0.015 mg/kg per hour), and the respiratory rate was maintained at  $\sim 90$  breaths/min.

All the functional images of each mouse were first time-sliced and then realigned for motion correction using SPM8 (Wellcome Trust Centre for Neuroimaging, London, UK). For each mouse, the average of aligned functional volumes was rigidly co-registered to its anatomical image. The anatomical image from each mouse was subsequently non-linearly warped to the space of a high-resolution three-dimensional mouse brain atlas [23]. Then, all the functional images from each mouse were directly warped to the space of the atlas by concatenating the transformation from each registration step. All the registration processes were carried out using Advanced Neuroimaging Tools [24]. After registration, all functional images were pre-processed with steps for motion, white matter, and cerebrospinal fluid signal regression, de-trending, and 0.01–0.1 Hz band-pass filtering. After preprocessing, a regional homogeneity (ReHo) map was generated by calculating Kendall's coefficient of concordance of the time series of a given voxel with those of its nearest neighbors (26 voxels). The pre-processed data without band-pass filtering were used to generate fractional amplitude of low-frequency fluctuation (fALFF) maps by dividing the sum of the amplitude across 0.01 Hz–0.08 Hz with that across the entire frequency range, 0 Hz–0.25 Hz [25]. Both ReHo and fALFF calculations were carried out using the free software REST (Resting-State fMRI Data Analysis Toolkit V1.8, [http://restfmri.net/forum/REST\\_V1.8](http://restfmri.net/forum/REST_V1.8)). All the ReHo and fALFF maps were smoothed with a 0.4-mm full width at half maximum Gaussian kernel.

### AAV Preparation

To construct the pAAV-Guide vector, sgRNAs that specifically target exon 3 of the human *MECP2* gene were designed using CRISPR design tools (<http://crispr.mit.edu/> and <http://crispr.dfci.harvard.edu/SSC/>). The sgRNAs were introduced into the vector PX458 (Addgene, Watertown, MA, no. 48138) and U6-sgRNA cassettes were amplified by PCR. Then, the U6-sgRNA cassettes were ligated with the vector pAAV-GFP (Addgene, no. 50465). The pAAV-spCas9 plasmid was obtained from Addgene (no. PX551). High titer AAV-Guide ( $3.9 \times 10^{12}$  viral genomes (vg)/mL), AAV-spCas9 ( $1.7 \times 10^{13}$  vg/mL), and AAV-GFP ( $5 \times 10^{12}$  vg/mL) particles were produced by the Gene

Editing Core Facility in the Institute of Neuroscience, Chinese Academy of Sciences.

### Analysis of On-Target Gene Editing *In Vitro*

For *in vitro* assays, primary cortical neuron cultures were prepared from transgenic mice on embryonic day 15. Cells were plated on poly-D-lysine-coated 6-well plates (ThermoFisher Scientific, Waltham, MA). About  $1 \times 10^{11}$  viruses (1:1 mixture of AAV-spCas9 and AAV-Guide) were incubated with  $\sim 1 \times 10^6$  cells per well at 2 days *in vitro* (DIV). The cells were digested at DIV 6 and GFP-positive cells were collected by a flow cytometer (MoFlo XDP, Beckman Coulter, Brea, CA). DNA extracted from sorted cells was used as the PCR template with forward primer 5'-GCCTGCCTCTGCTCACTTGTTTC-3' and reverse primer 5'-CCCTGCCCTGTAGAGATAGGAG-3'. The PCR product was purified and ligated with T easy vector (Promega, Madison, WI). Ligated plasmids were transfected into competent *Escherichia coli* and single clones were picked for further sequencing analysis.

### Stereotactic Injection

Mice were anesthetized by intraperitoneal injection of pentobarbital sodium (100 mg/kg) and mounted in a stereotaxic apparatus (RWD, Shenzhen, China). Body temperature was maintained by a heating pad and ophthalmic ointment was applied to maintain eye lubrication. A craniotomy was performed according to approved procedures by the Animal Advisory Committee at the Shanghai Institutes for Biological Sciences, Chinese Academy of Sciences. The craniotomy window was made using a hand-held drill, and a glass micropipette filled with viruses suspended in mineral oil was used to reach the target brain areas. Injections of viruses were carried out via a stereotaxic injector (Stoelting, Wood Dale, IL). After each injection, the micropipette was held in place for 10 min before retraction to allow for diffusion of viruses. The incision was sutured and mice were allowed to recover on a heating blanket before returning to their home cage.

To normalize MeCP2 levels in the mPFC (anterior/posterior: 2.3 mm; mediolateral:  $\pm 0.3$  mm; dorsal/ventral:  $-2.0$  mm), a 1:1 AAV mixture of AAV-spCas9 and AAV-Guide was injected bilaterally into the mPFC of *MECP2-TG* mice at a volume of 500 nL for each site. To normalize MeCP2 levels in the BST (anterior/posterior: 0.15 mm; mediolateral:  $\pm 0.9$  mm; dorsal/ventral:  $-4.9$  mm/ $-4.25$  mm), a 1:1 AAV mixture of AAV-spCas9 and AAV-Guide was injected bilaterally into the BST of *MECP2-TG* mice at a volume of 300 nL for each site. A 1:1 AAV mixture of

AAV-spCas9 and AAV-GFP at the same volume was used as control. After 6 weeks of expression, behavioral phenotyping was performed.

### Immunofluorescent Staining

Mice were anesthetized with pentobarbital sodium and perfused transcardially with saline followed by 4% paraformaldehyde (PFA, Sigma-Aldrich, St. Louis, MO). The brain was extracted and post-fixed in 4% PFA overnight at 4°C, followed by cryoprotection in 30% sucrose in phosphate-buffered saline (PBS) at 4°C. Coronal sections were cut at 50  $\mu$ m on a vibratome (CM1950, Leica, Wetzlar, Germany). The sections were blocked for 1 h at room temperature in PBST (0.3% Triton X-100) with 5% bovine serum albumin, fraction V, followed by incubation with primary antibodies at 4°C overnight and secondary antibodies at room temperature for 2 h. The primary antibodies used were rabbit anti-MeCP2 (1:1000, CST, Danvers, MA) which recognizes both human and mouse MeCP2, and goat anti-GFP (1:500, Abcam, Cambridge, MA). The secondary antibodies used were donkey anti-rabbit IgG-CF 555 (1:1000, Biotium, Fremont, CA) and donkey anti-goat IgG-CF 488 (1:1000, Biotium). DAPI (1:10000, Roche, Basel, Switzerland) was used to stain nuclei. Images were acquired on a Nikon TiE-A1 plus confocal microscope (Nikon, Tokyo, Japan) and an Olympus VS120 fluorescence microscope (Olympus, Tokyo, Japan). Fluorescence intensity was measured using ImageJ (Open Source Software from NIH, Bethesda, MD). In Fig. 4D, the fluorescence intensity was compared between the mPFC (gene editing area) and an adjacent cortical area.

### Western Blot Analysis

Individual mice were rapidly decapitated, and the brain was immediately extracted and placed in ice-cold PBS. The transduced mPFC was microdissected under a dissecting microscope, and transferred to a 1.5-mL centrifuge tube containing ice-cold RIPA buffer and protease inhibitors (Roche). The tissue was homogenized with an electric homogenizer, then the tube was left on an orbital shaker for 2 h at 4°C. The cell lysate was centrifuged for 20 min at 12,000 rpm at 4°C in a microcentrifuge. Supernatants were dissolved in SDS-PAGE sample buffer, and proteins were separated on 8% SDS-PAGE gels. The primary antibodies used were rabbit anti-MeCP2 (1:1000, CST) and mouse anti-GAPDH (1:5000, Sigma-Aldrich, St. Louis, MO). The secondary antibodies used were anti-rabbit and anti-mouse HRP antibodies (1:2000, Sigma-Aldrich). Blots were imaged with a GE Amersham Imager600 system (GE Healthcare, Chicago, IL), and quantified using ImageJ.

## Statistical Analysis

GraphPad Prism software was used for statistical significance tests. The number of animals used and the specific statistical tests used are described in the figure legends. SPSS Software (SPSS Inc., Chicago, IL) test showed that all data values appeared to be normally distributed.

## Results

### Behavioral Phenotyping of Adult *MECP2*-TG Mice

The *MECP2*-TG mice were on a pure FVB/N background at first [11], but mice on this background develop premature retinal degeneration, which can confuse the interpretation of some behavioral phenotypes [20]. To overcome this issue, previous studies have characterized F1 hybrid *MECP2*-TG mice (FVB/N × C57BL/6 or FVB/N × 129S6/SvEv), which have several phenotypes reminiscent of patients with *MECP2* duplication syndrome, including increased anxiety, reduced locomotor activity, and abnormal social behaviors [12]. Therefore, we used F1 hybrid *MECP2*-TG mice. First, we performed more extensive behavioral phenotyping of F1 hybrid *MECP2*-TG mice (FVB/N × C57BL/6), and found that they displayed decreased locomotor activity in the open field test, as previously described (Fig. 1D). In addition, transgenic mice were prone to manifest aversive-like behaviors, including a heightened anxiety and fear generalization phenotype. Compared to their wild-type littermates, *MECP2*-TG mice spent less time in the light compartment of the light–dark box and in the open arms of the elevated plus maze (Fig. 1E, F), which represented a robust anxiety phenotype in the *MECP2*-TG mice. In the fear conditioning test, *MECP2*-TG mice exhibited a remarkable increase of percentage freezing, whether in the training phase (Fig. 1G), the contextual and cued fear memory test phase (Fig. 1H, I), or when test mice were placed in a new context after training (Fig. 1J). It is worth noting that the baseline percentage freezing before the first trial was very low in both genotypes, and transgenic mice displayed an extremely high percentage freezing in the first trial. These data indicated that *MECP2*-TG mice have an excessive startle response and fear generalization phenotype. To investigate social behavior, we tested *MECP2*-TG mice in the three-chamber test for social approach and social novelty (Fig. 1A–C), and discovered that they had a deficit in social novelty behavior as revealed by an inability to distinguish a novel partner mouse from familiar partner mouse, but social approach behavior was basically normal, demonstrating that social recognition is impaired in *MECP2*-TG mice.

Because *MECP2*-TG mice presented elevated aversive-like behaviors, we hypothesized that their appetitive behaviors may be disturbed as well. Next, we sought to examine reward-related behaviors using the sucrose preference test and the cocaine CPP test. Surprisingly, *MECP2*-TG mice exhibited normal preference for 0.5% and 2% sugar water (Fig. 2A), and spent more time in the cocaine-conditioned chamber, consistent with wild-type littermates (Fig. 2B). There was no statistically significant difference in the performance between transgenic mice and littermate controls, indicating that reward-related behaviors are basically intact in *MECP2*-TG mice. Moreover, freezing behavior was dramatically enhanced in *MECP2*-TG mice, which may be due to increased learning and memory in the transgenic mice. We thus used a less stressful behavioral paradigm to explore learning and memory in *MECP2*-TG mice. In the novel object recognition test, both transgenic mice and their wild-type littermates showed normal preference for the novel object (Fig. 2C). And no difference was observed in the Barnes maze test between *MECP2*-TG mice and controls (Fig. 2D–F). These data suggested that learning and memory functions are not damaged in *MECP2*-TG mice, and the increased freezing behaviors in the fear conditioning test probably result from fear generalization.

### Resting-State fMRI Analysis of Adult *MECP2*-TG Mice

Although MeCP2 is ubiquitously expressed across the whole brain, another question to be addressed is whether all cell types are equally affected by doubling the MeCP2 levels or whether certain cell types or regions are more sensitive. Previous studies of conditional knockout of *Mecp2* in mouse brain have provided strong evidence that MeCP2 plays different roles and is not equally important in different cell types and areas [26–28]. In addition, our behavioral phenotyping results showed that appetitive behaviors and learning and memory were basically normal in *MECP2*-TG mice, implying that the regions or neural circuits associated with these behaviors are intact in *MECP2*-TG mice. To identify which areas or circuits are responsible for the abnormal behaviors, we used resting-state fMRI to scan the whole brain of *MECP2*-TG mice and wild-type controls. Because significant EPI signal is lost in deep brain areas due to the aural cavity magnetic susceptibility artifact, we introduced a liquid-phase fluorocarbon into the middle ear by needle puncture as previously reported. This method allowed us to acquire whole brain fMRI data without signal dropout [22]. Our imaging data manifested significant ReHo value differences in multiple areas between *MECP2*-TG and wild-type control mice (Fig. 3A, B). Importantly, differences were concentrated in

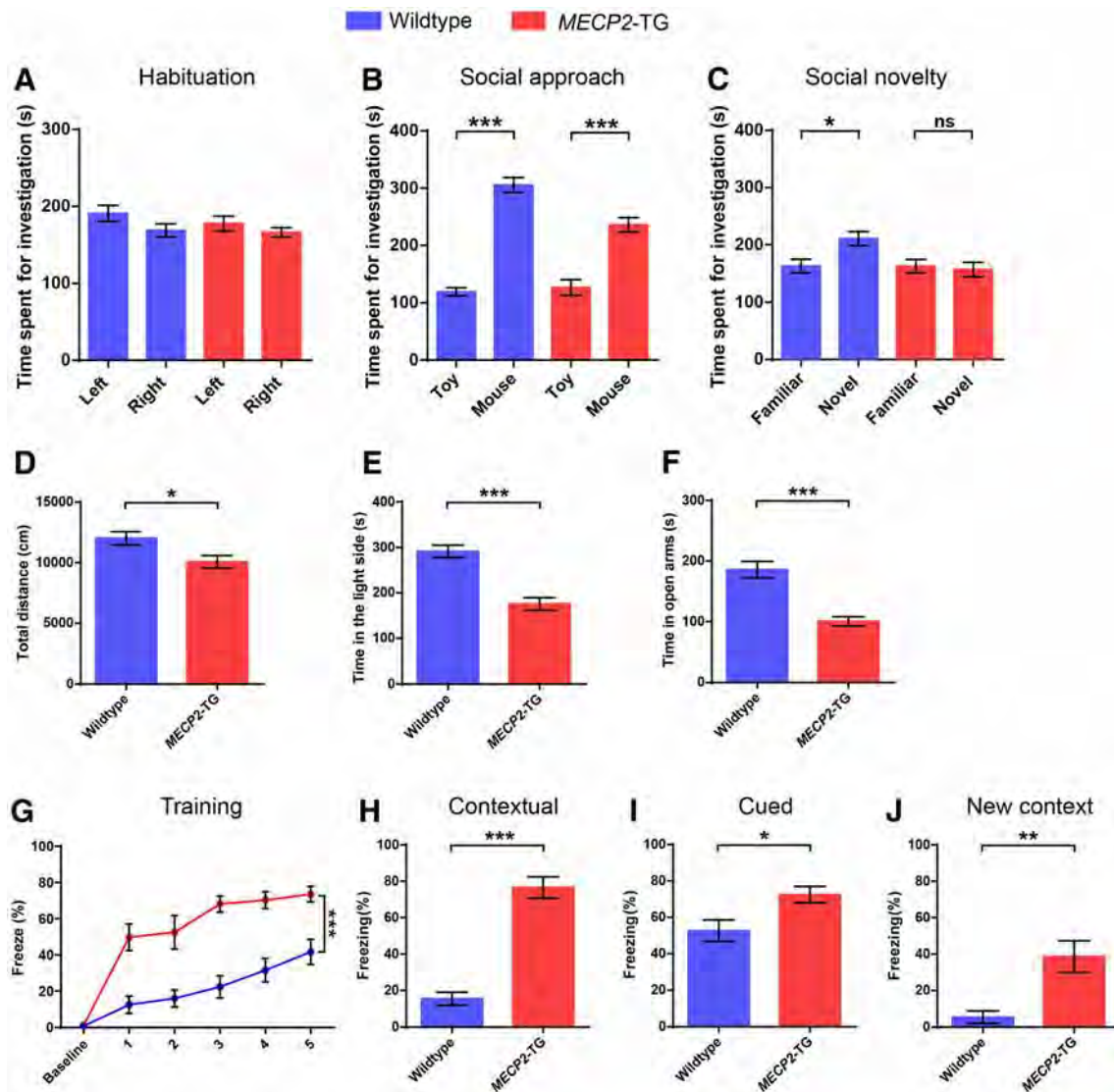


**Fig. 1** *MECP2-TG* mice display reduced locomotor activity, enhanced aversive behaviors, and a social recognition deficit. **A–C** *MECP2-TG* mice and wild-type littermates manifested no side preference (**A**) and normal social approach behavior (**B**), but *MECP2-TG* mice did not distinguish familiar partners from novel partners (**C**) as wild-type littermates did in the three-chamber test. **D** *MECP2-TG* mice travelled less in the open field than their wild-type littermates. **E, F** Compared to their wild-type littermates, *MECP2-TG* mice spent less time on the light side of the light/dark exploration box, and less time in the open arms of an elevated plus maze. **G–**

**J** Percentage freezing was significantly higher in the *MECP2-TG* mice than in wild-type littermates during the training phase (**G**), the contextual fear memory testing phase (**H**), the cued fear memory testing phase (**I**), or when presented with a mouse in a new context after training (**J**).  $n = 10–14$  for wild-type,  $n = 10–14$  for *MECP2-TG*. Data are the mean  $\pm$  SEM. ns, not significant.  $*P < 0.05$ ,  $**P < 0.01$ ,  $***P < 0.001$  (two-tailed paired *t*-test in **A–C**, two-tailed *t*-test in **D–F** and **H–J**, and two-way repeated-measures ANOVA in **G**).

areas modulating aversive behaviors, including the mPFC, BST, amygdala, hypothalamus (HY), thalamus, piriform area, anterior cingulate, and periaqueductal gray. Furthermore, we generated fALFF maps and found that the fALFF values showed differences consistent with the ReHo results in most areas (Fig. S1). These data were consistent with our behavioral results.

### Normalization of MeCP2 Levels in the mPFC Reverses the Social Recognition Deficit in Adult *MECP2-TG* Mice

Reversal of abnormal phenotypes in adult *MECP2-TG* mice by normalizing the MeCP2 levels across the whole brain has been demonstrated [19]. However, which brain areas or neural circuits have defects that contribute to disease phenotypes was not known. Accumulating

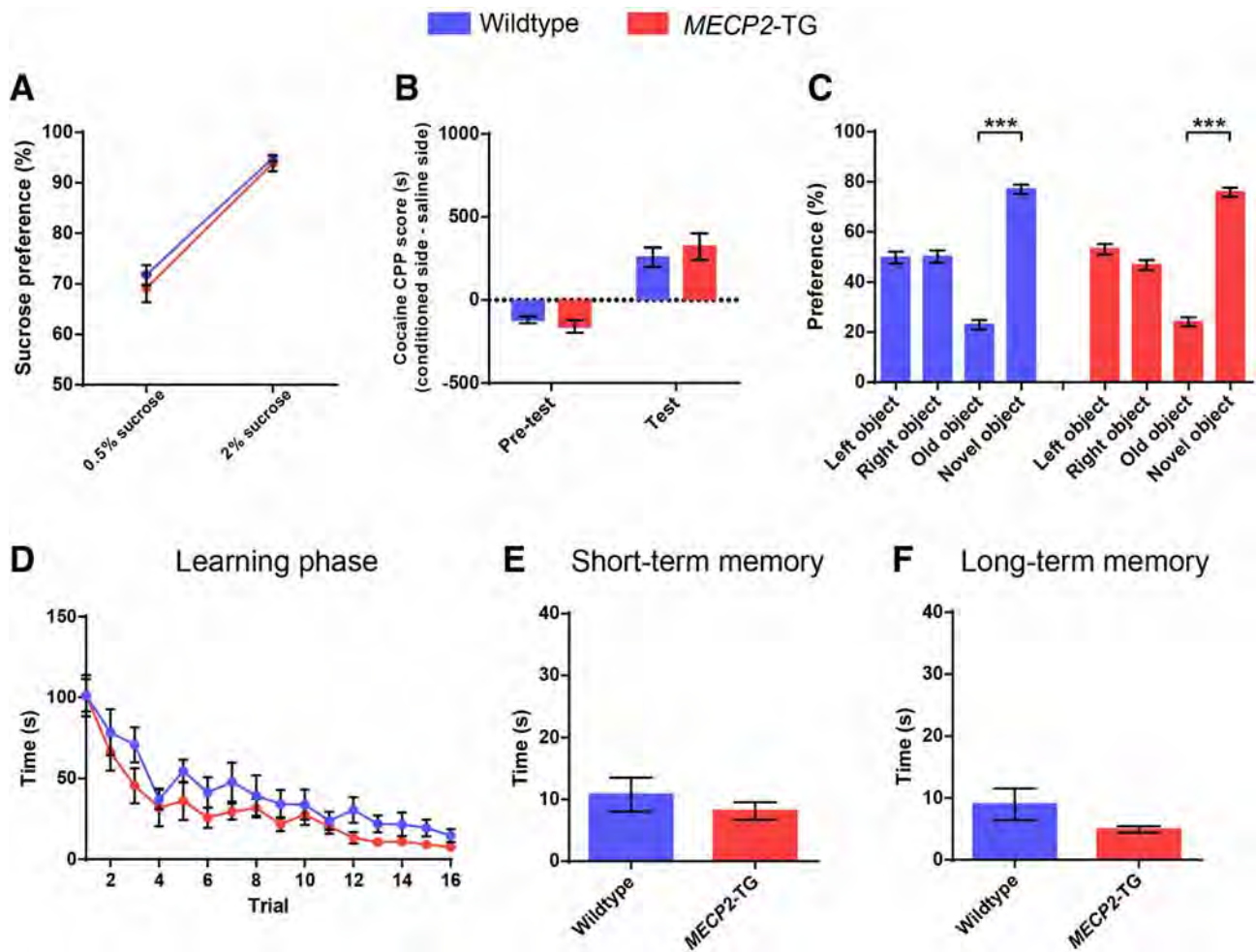


**Fig. 2** *MECP2*-TG mice display normal appetitive behaviors, novel object recognition, and spatial learning and memory. **A**, **B** *MECP2*-TG mice and wild-type littermates showed comparable sucrose preference (**A**), and cocaine conditioned place preference (**B**). **C** In the novel object recognition test, *MECP2*-TG mice and wild-type littermates showed no side preference during habituation, and normal preference for the novel object in the test phase. **D–F** No significant

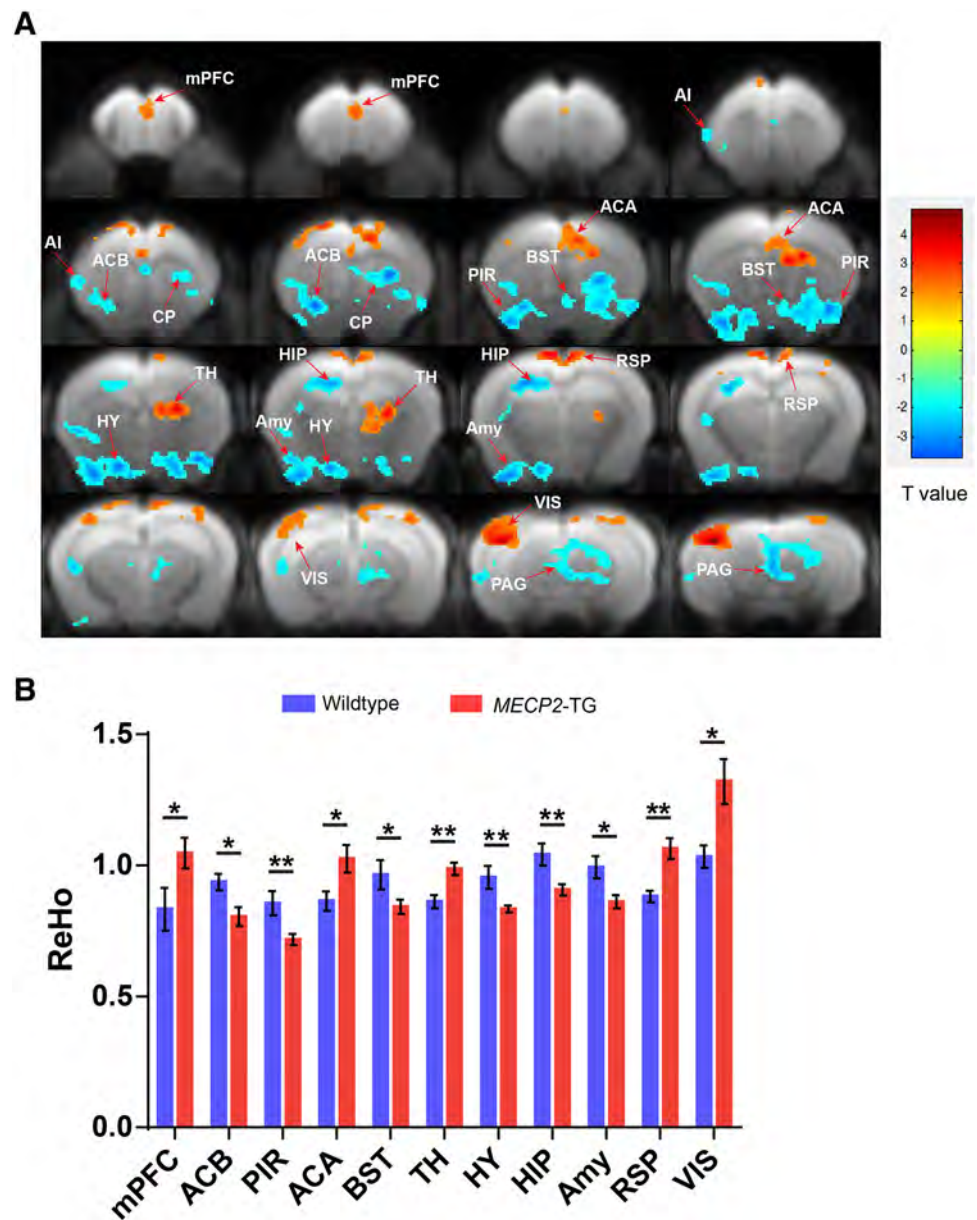
difference was found between *MECP2*-TG mice and wild-type littermates during the learning phase (**D**), the short-term memory test (**E**), and the long-term memory test (**F**) in the Barnes maze test.  $n = 10–14$  for wild-type,  $n = 10–14$  for *MECP2*-TG. Data represent the mean  $\pm$  SEM.  $***P < 0.001$  (two-tailed *t*-test in **A**, **B**, **E**, and **F**, two-tailed paired *t*-test in **C**, and two-way repeated-measures ANOVA in **D**).

evidence has shown that the mPFC mediates social recognition behaviors, and its dysfunction leads to social recognition deficits [21, 29–32]. The mPFC was also one of the areas showing the most significant difference in ReHo value in our fMRI data (Fig. 3), so we reasoned that mPFC dysfunction is likely to underlie the social recognition deficit in *MECP2*-TG mice. To test the hypothesis, we used the CRISPR-Cas9 gene editing system similar to that previously reported to restore normal MeCP2 expression in the mPFC *in vivo* [33] (Fig. 4A). To this end, we designed several sgRNAs specifically targeting exon 3 of the human *MECP2* (Fig. 4B) gene and selected the most efficient sgRNA for follow-up experiments. We discovered that a large number of mutations occurred within the human *MECP2* locus, but none were detected within the

counterpart locus of mouse *Mecp2* in an efficiency test of on-target gene editing *in vitro* (Fig. 4C). Moreover, we injected two viruses that packaged SpCas9 (AAV-SpCas9) and sgRNA expression cassettes (AAV-Guide) into the mPFC of transgenic mice, and evaluated the MeCP2 protein levels after 4–6 weeks of viral infection. Our immunofluorescence staining and western blot results showed that the MeCP2 protein levels were decreased by nearly half in the mPFC (Fig. 4D, E). These data demonstrated that our system normalized the MeCP2 levels in specific brain areas *in vivo*.

Next, we explored the hypothesis that normalization of MeCP2 levels in the mPFC is sufficient to reverse the impairment of social recognition. Three groups were used for phenotyping: wild-type mice bilaterally injected with

**Fig. 3** Significant ReHo value differences between *MECP2*-TG and wild-type mice in the whole brain resting-state fMRI. **A** Regions manifesting significant ReHo value differences between *MECP2*-TG and wild-type mice (red, *MECP2*-TG > wild-type; blue, wild-type > *MECP2*-TG; color bar represents significance of difference). **B** Quantification of ReHo values in specific brain areas [ $n = 10$  for wild-type,  $n = 14$  for *MECP2*-TG; data represent the mean  $\pm$  SEM; \* $P < 0.05$ , \*\* $P < 0.01$  (two-tailed  $t$ -test)]. mPFC, medial prefrontal cortex; AI, agranular insular area; ACB, nucleus accumbens; CP, caudoputamen; PIR, piriform area; BST, bed nuclei of the stria terminalis; ACA, anterior cingulate area; TH, thalamus; HY, hypothalamus; HIP, hippocampal region; Amy, amygdala; RSP, retrosplenial area; VIS, visual areas; PAG, periaqueductal gray.



viruses expressing SpCas9 and GFP (Wildtype-CTL), *MECP2*-TG mice bilaterally injected with viruses expressing SpCas9 and GFP (*MECP2*-TG-CTL), and *MECP2*-TG mice bilaterally injected with viruses expressing SpCas9 and sgRNA (*MECP2*-TG-normalized) (Fig. 5A). In our results, the *MECP2*-TG-normalized group indeed spent more time with novel mice than with familiar mice in the three-chamber test, indicating a complete reversal of the social recognition deficit in *MECP2*-TG mice (Fig. 5D). Besides, all three groups showed no side preference and normal social approach behavior, illustrating that viral

infection and gene editing manipulation in the mPFC did not impact habituation and social approach behaviors (Fig. 5B, C). Moreover, the reduced locomotor activity, the heightened anxiety-like behaviors, and the fear generalization phenotype were not reversed in the *MECP2*-TG-normalized group (Fig. 5E–J). Together, our results suggested that dysfunction of the mPFC specifically affects social recognition behaviors in *MECP2*-TG mice, and normalization of MeCP2 levels in the mPFC is sufficient to restore the function of the mPFC or mPFC-related circuits, thus completely reversing the social recognition deficit.

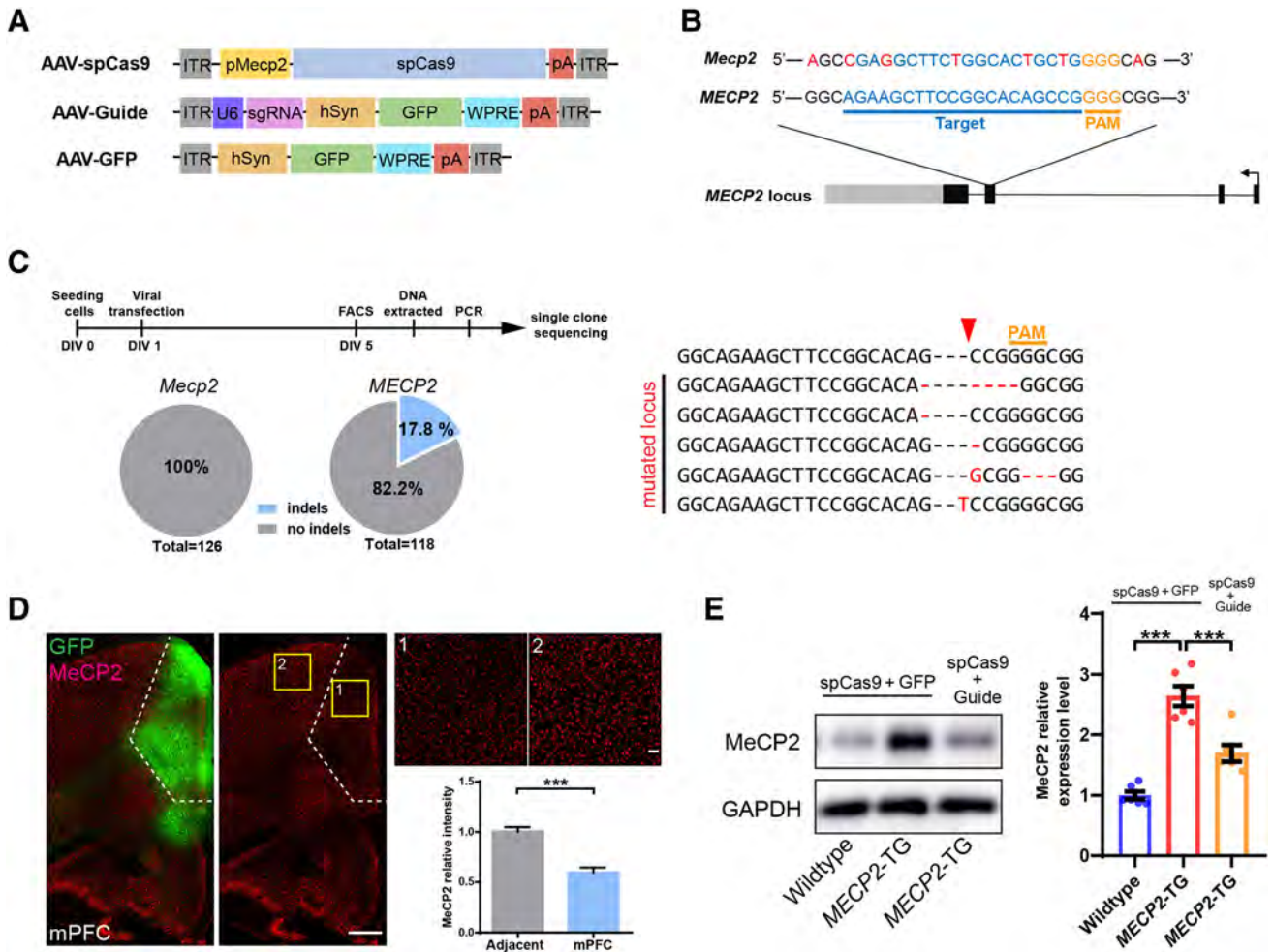


**Fig. 4** Strategy for specific knockout of the human *MECP2* copy in *MECP2* duplication neurons and brain areas of interest in *MECP2* duplication mice. **A** AAV-SpCas9, AAV-Guide, and AAV-GFP expression vectors. **B** SpCas9 target location of the human *MECP2* locus (blue, targeted genomic locus; yellow, PAM (protospacer adjacent motif) sequence; red, mismatched bases between mouse *Mecp2* and the human *MECP2* gene in the targeted locus). **C** Left, protocol for and analysis of on-target gene editing *in vitro*. The efficiency of indel mutations in the *MECP2* locus was ~17.8%, but no indel mutations were detected in the *Mecp2* locus in infected

cultured neurons. Right, representative mutation patterns detected by sequencing of the *MECP2* locus (red arrowhead, Cas9 cutting site). **D** Representative images and analysis of MeCP2 expression after CRISPR-Cas9-mediated human *MECP2* knockout in the mPFC *in vivo* (scale bars, 500  $\mu$ m;  $n = 9$  brain slices from 3 mice for each genotype). **E** Western blots and analysis of MeCP2 protein expression 1.5 months after AAV injection [ $n = 6$ /group; data represent the mean  $\pm$  SEM; \*\*\* $P < 0.001$  (two-tailed *t*-test in **D**, and one-way ANOVA followed by Tukey's honest significant difference *post-hoc* correction for multiple comparisons in **E**)].

**Normalization of MeCP2 Levels in the BST Has no Effect on the Behavioral Defects of *MECP2*-TG Mice**

In addition to social defects, heightened anxiety is the most prominent behavioral deficit in *MECP2*-TG mice, and a common comorbid condition in patients with *MECP2* duplication syndrome. Many studies have shown that the BST plays a central role in modulating anxiety-related behaviors [34, 35]. Our fMRI data also revealed a significant difference in ReHo values in the BST region between *MECP2*-TG and wild-type mice. We hypothesized that BST dysfunction caused by MeCP2 overexpression

leads to a heightened anxiety phenotype in *MECP2*-TG mice. We tested this hypothesis by reducing MeCP2 to normal levels in the BST as we did in the mPFC (Fig. 6A, B). However, neither anxiety-like behaviors in the light-dark box test, nor in the elevated plus maze test were reversed in the *MECP2*-TG-normalized group (Fig. 6G, H). Furthermore, the *MECP2*-TG-normalized group showed no improvement in the reduced locomotor activity in the open field test (Fig. 6F), the impaired social recognition in the three-chamber test (Fig. 6C-E), and the increased freezing behavior in the fear conditioning paradigm (Fig. 6I-K). Given these results, we speculated that the BST is intact in *MECP2*-TG mice, or multiple

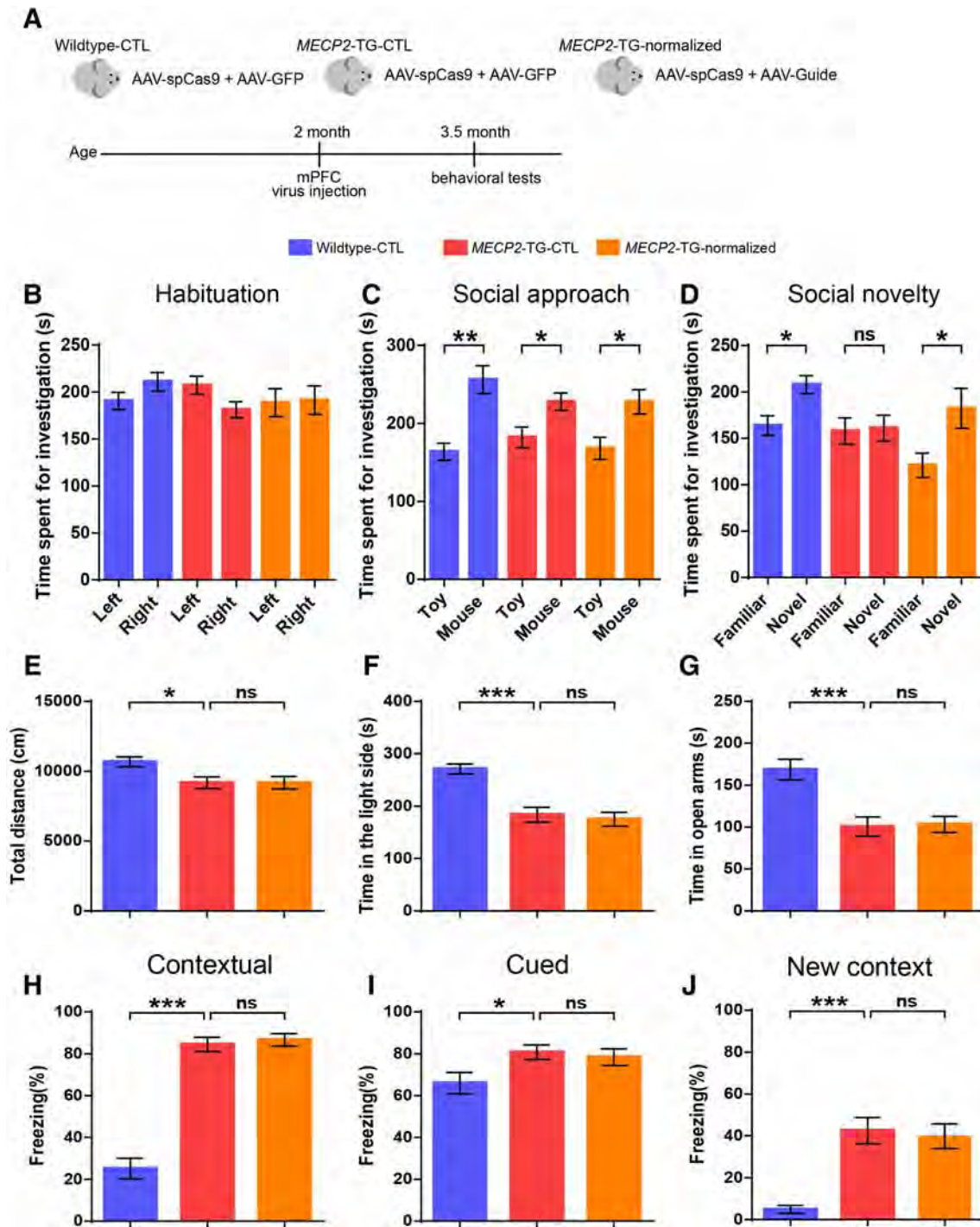


**Fig. 5** Restoration of normal MeCP2 levels in the mPFC reverses the social recognition deficit in adult *MECP2*-TG mice. **A** Schematic of the experimental design. **B–D** Normalizing MeCP2 levels in the mPFC reverses impaired social recognition behavior (**D**) in the three-chamber test. No side preference (**B**) and normal social approach (**C**) were found in the test. **E–J** Normalizing MeCP2 levels in the mPFC of *MECP2*-TG mice did not reverse the decreased locomotor activity in the open field test (**E**), the heightened anxiety-like behaviors in light/dark exploration (**F**) and elevated plus maze

(**G**) tests, the percentage freezing when tested on contextual fear memory (**H**) and cued fear memory (**I**), and when presented with a mouse in a new context (**J**).  $n = 15$  each for Wildtype-CTL, *MECP2*-TG-CTL, and *MECP2*-TG-normalized; data represent the mean  $\pm$  SEM; ns, not significant; \* $P < 0.05$ , \*\* $P < 0.01$ , \*\*\* $P < 0.001$  (two-tailed paired  $t$ -test in **B–D**, and one-way ANOVA followed by Tukey's honest significant difference *post-hoc* correction for multiple comparisons in **E–J**).

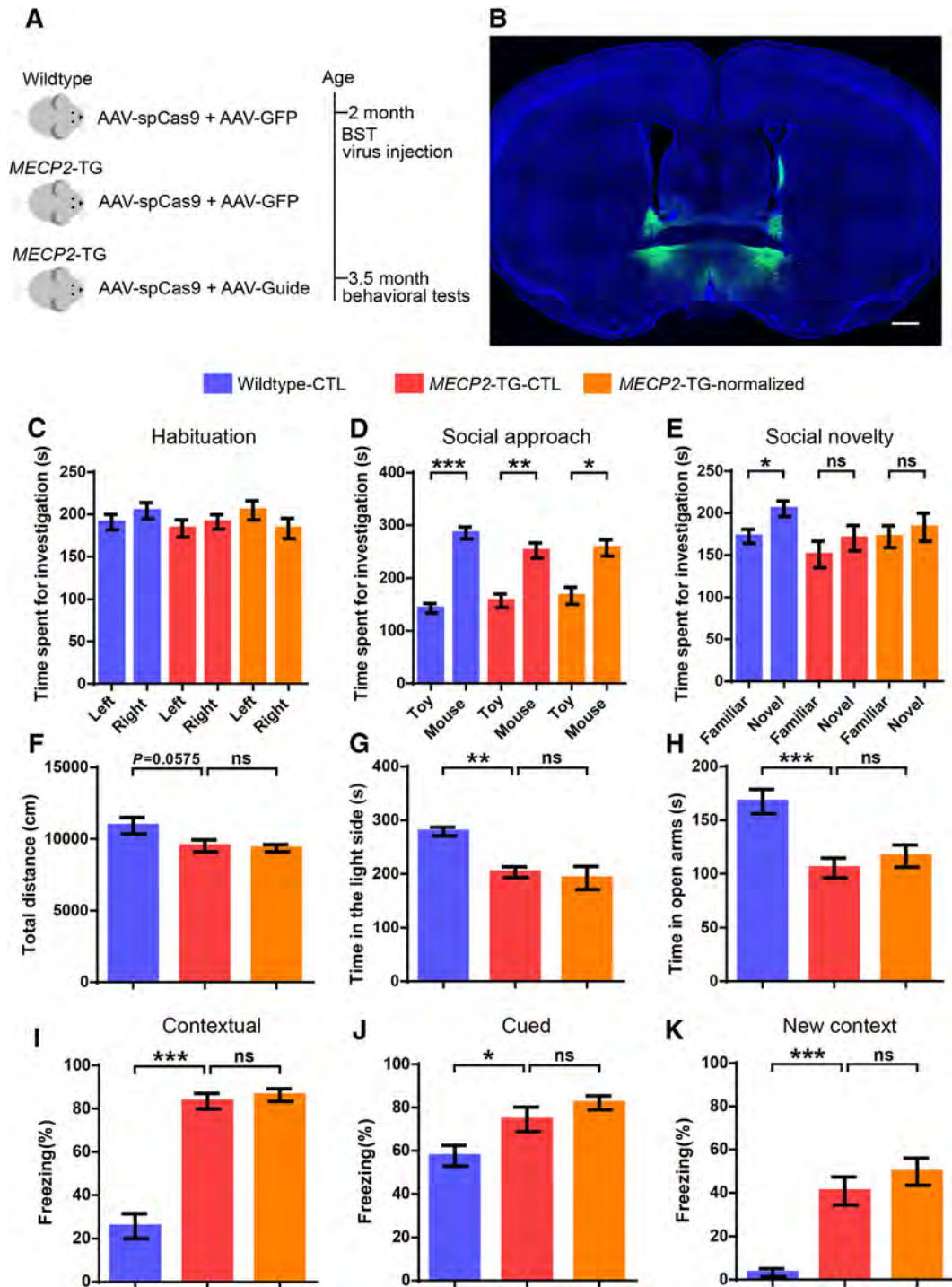


**Fig. 6** Normalization of MeCP2 levels in the BST does not reverse the behavioral defects in *MECP2-TG* mice. **A** Schematic of the experimental design. **B** Representative image of the injection site in the BST (scale bar, 500  $\mu$ m). **C–K** Normalizing MeCP2 levels in the BST of *MECP2-TG* mice did not reverse the social recognition deficit in the three-chamber test (**C–E**), the decreased locomotor activity in the open field test (**F**), the heightened anxiety-like behaviors in the light/dark exploration (**G**) and elevated plus maze tests (**H**), and the

fear generalization phenotype in the fear conditioning test (**I–K**).  $n = 14$  for wild-type-CTL,  $n = 14$  for *MECP2-TG*-CTL,  $n = 13$  for *MECP2-TG*-normalized. Data represent the mean  $\pm$  SEM; ns, not significant; \* $P < 0.05$ , \*\* $P < 0.01$ , \*\*\* $P < 0.001$  (two-tailed paired *t*-test in **C–E**, one-way ANOVA followed by Tukey's honest significant difference *post-hoc* correction for multiple comparisons in **G–K**, and one-way ANOVA followed by Fisher's least significant difference *post-hoc* test in **F**).

brain areas implicated in anxiety are damaged in *MECP2-TG* mice and restoration of MeCP2 levels in the BST is not sufficient to reverse the anxiety-like behaviors.

## Discussion

Our results showed that restoration of normal MeCP2 levels in the mPFC completely reverses the social recognition deficit in adult *MECP2-TG* mice. However, the neural circuit mechanism underlying this deficit in these mice still needs to be investigated. A recent study reported that local gamma oscillation dysfunction in the mPFC is a causative factor for social recognition deficits in a mouse model of autism [21], so local microcircuit dysregulation is probably the main cause of the social defect in *MECP2-TG* mice. Another possibility is that the ability of the mPFC to process social information from upstream brain areas is impaired in *MECP2-TG* mice. Indeed, the ventral tegmental area (VTA), ventral hippocampus (vHIP), HY, and nucleus accumbens are widely reported to project to the mPFC and regulate social behaviors in rodents [34]. Especially, mPFC-projecting neurons in the VTA are mainly dopaminergic, and axons from the VTA innervate broad areas of the mPFC. The latest research shows that dopamine activation in the VTA controls mPFC ensemble activity and oscillations, and oscillation dysfunction in the mPFC is responsible for social recognition impairment in an autistic mouse model [21, 36]. Besides, the vHIP–mPFC projection is hyperactive in the *Mecp2* knockout mouse model of Rett syndrome, which is another widely-reported autism spectrum disorder mouse model and displays obvious defects in social novelty behavior. And long-term inhibition of mPFC-projecting vHIP neurons in Rett mice rescues the social novelty deficits [37]. These results imply that the VTA–mPFC or vHIP–mPFC projection participates in the regulation of social recognition in rodents. Furthermore, mPFC-mediated top-down control is also implicated in social behaviors. Dysregulation of the input from the mPFC to the basolateral amygdala (BLA) results in impairment of the excitation/inhibition balance in the BLA, which may be the cause of social behavioral defects in autistic model mice [38, 39]. However, whether these neural circuits are damaged and responsible for the behavioral defects in *MECP2-TG* mice remains to be investigated.

We restored normal MeCP2 expression in the BST of adult *MECP2-TG* mice in an attempt to reverse their anxiety-like behaviors, but these behaviors did not improve. Anxiety is an extremely complicated state, and its underlying neural circuit mechanism remains mysterious. A variety of evidence has revealed that

neuromodulation systems, the amygdala, vHIP, HY, BST, lateral septal nucleus, and related neural circuits are involved in the regulation of anxiety-like behaviors [35]. It is possible that multiple brain areas or neural circuits involved in anxiety behaviors are damaged in *MECP2-TG* mice, and normalizing the MeCP2 expression only in the BST is not enough to reverse these behaviors. The alternative is that other brain regions contribute more to anxiety than the BST in *MECP2-TG* mice. Our fMRI data showed significant differences in ReHo values between transgenic and wild-type mice in the HY and periaqueductal gray in the midbrain which participate in the regulation of anxiety in rodents. Together, further investigation is needed on the neural mechanisms underlying anxiety in *MECP2-TG* mice.

Another finding that *MECP2-TG* mice showed significant fear generalization deserves further exploration. Many studies indicate that the BLA is the center for regulating fear, and a previous study has demonstrated that BLA-specific deletion of *Mecp2* decreases the freezing level in the cue-dependent fear conditioning test [40]; whether overexpression of MeCP2 in the BLA leads to increased freezing behavior in the fear conditioning test requires further investigation.

## Conclusions

In sum, our study demonstrated that overexpression of MeCP2 in the mPFC is responsible for social deficits. Further studies are still needed to elucidate the neural mechanism underlying the heightened anxiety behaviors and fear generalization phenotype in the transgenic mice. Furthermore, whether specific neural circuit dysfunctions in the transgenic mice are responsible for the behavioral deficits is still to be investigated.

**Acknowledgements** We thank Wen-jing Chen and Kai-Wei Zhang, Institute of Neuroscience, Chinese Academy of Sciences, for assistance with fMRI data collection and advice on the manuscript. And we thank Zhi-Jiang Zhang and Sen Jin, Wuhan Institute of Physics and Mathematics, Chinese Academy of Sciences, for help with the rabies virus tracing experiments. This work was supported by National Natural Science Foundation of China grants (31625013 and 91732302); a Shanghai Brain-Intelligence Project of the Science and Technology Commission of Shanghai Municipality (16JC1420501); and the Strategic Priority Research Program of the Chinese Academy of Sciences (XDBS01060200); Program of Shanghai Academic Research Leader, the Open Large Infrastructure Research of Chinese Academy of Sciences, and the Shanghai Municipal Science and Technology Major Project (2018SHZDZX05); and National Natural Science Foundation of China (81801354).

**Conflict of interest** The authors declare that they have no competing interests.

## References

- Nan XS, Campoy FJ, Bird A. MeCP2 is a transcriptional repressor with abundant binding sites in genomic chromatin. *Cell* 1997, 88: 471–481.
- Chahrouh M, Jung SY, Shaw C, Zhou XB, Wong STC, Qin J, *et al.* MeCP2, a key contributor to neurological disease, activates and represses transcription. *Science* 2008, 320: 1224–1229.
- Young JI, Hong EP, Castle JC, Crespo-Barreto J, Bowman AB, Rose MF, *et al.* Regulation of RNA splicing by the methylation-dependent transcriptional repressor methyl-CpG binding protein 2. *Proc Natl Acad Sci U S A* 2005, 102: 17551–17558.
- Cheng TL, Wang ZZ, Liao QM, Zhu Y, Zhou WH, Xu WQ, *et al.* MeCP2 suppresses nuclear microRNA processing and dendritic growth by regulating the DGCR8/Drosha complex. *Devel Cell* 2014, 28: 547–560.
- Cheng TL, Qiu ZL. MeCP2: multifaceted roles in gene regulation and neural development. *Neurosci Bull* 2014, 30: 601–609.
- Amir RE, Van den Veyver IB, Wan M, Tran CQ, Francke U, Zoghbi HY. Rett syndrome is caused by mutations in X-linked MECP2, encoding methyl-CpG-binding protein 2. *Nat Genet* 1999, 23: 185–188.
- Chahrouh M, Zoghbi HY. The story of Rett syndrome: From clinic to neurobiology. *Neuron* 2007, 56: 422–437.
- Van Esch H, Bauters M, Ignatius J, Jansen M, Raynaud M, Hollanders K, *et al.* Duplication of the MECP2 region is a frequent cause of severe mental retardation and progressive neurological symptoms in males. *Am J Hum Genet* 2005, 77: 442–453.
- Ramocki MB, Peters SU, Tavyev YJ, Zhang F, Carvalho CMB, Schaaf CP, *et al.* Autism and other neuropsychiatric symptoms are prevalent in individuals with MECP2 duplication syndrome. *Ann Neurol* 2009, 66: 771–782.
- Ramocki MB, Tavyev YJ, Peters SU. The MECP2 duplication syndrome. *Am J Med Genet Part A* 2010, 152A: 1079–1088.
- Collins AL, Levenson JM, Vilaythong AP, Richman R, Armstrong DL, Noebels JL, *et al.* Mild overexpression of MeCP2 causes a progressive neurological disorder in mice. *Hum Mol Genet* 2004, 13: 2679–2689.
- Samaco RC, Mandel-Brehm C, McGraw CM, Shaw CA, McGill BE, Zoghbi HY. Crh and Oprm1 mediate anxiety-related behavior and social approach in a mouse model of MECP2 duplication syndrome. *Nat Genet* 2012, 44: 206–211.
- del Gaudio D, Fang P, Scaglia F, Ward PA, Craigen WJ, Glaze DG, *et al.* Increased MECP2 gene copy number as the result of genomic duplication in neurodevelopmentally delayed males. *Genet Med* 2006, 8: 784–792.
- Heckman LD, Chahrouh MH, Zoghbi HY. Rett-causing mutations reveal two domains critical for MeCP2 function and for toxicity in MECP2 duplication syndrome mice. *Elife* 2014, 3.
- Jiang MH, Ash RT, Baker SA, Suter B, Ferguson A, Park J, *et al.* Dendritic arborization and spine dynamics are abnormal in the mouse model of MECP2 duplication syndrome. *J Neurosci* 2013, 33: 19518–19533.
- Nageshappa S, Carroumeu C, Trujillo CA, Mesci P, Espuny-Camacho I, Pasciuto E, *et al.* Altered neuronal network and rescue in a human MECP2 duplication model. *Molecular Psychiatry* 2016, 21: 178–188.
- Chao HT, Zoghbi HY, Rosenmund C. MeCP2 controls excitatory synaptic strength by regulating glutamatergic synapse number. *Neuron* 2007, 56: 58–65.
- Lu H, Ash RT, He LJ, Kee SE, Wang W, Yu DH, *et al.* Loss and gain of MeCP2 cause similar hippocampal circuit dysfunction that is rescued by deep brain stimulation in a Rett syndrome mouse model. *Neuron* 2016, 91: 739–747.
- Sztainberg Y, Chen HM, Swann JW, Hao S, Tang B, Wu ZY, *et al.* Reversal of phenotypes in MECP2 duplication mice using genetic rescue or antisense oligos. *Nature* 2015, 528: 123–126.
- Cook MN, Williams RW, Flaherty L. Anxiety-related behaviors in the elevated zero-maze are affected by genetic factors and retinal degeneration. *Behav Neurosci* 2001, 115: 468–476.
- Cao W, Lin S, Xia QQ, Du YL, Yang Q, Zhang MY, *et al.* Gamma oscillation dysfunction in mPFC leads to social deficits in Neuroigin 3 R451C knockin mice. *Neuron* 2018, 97: 1253–1260.
- Li RP, Liu XP, Sidabras JW, Paulson ES, Jesmanowicz A, Nencka AS, *et al.* Restoring susceptibility induced MRI signal loss in rat brain at 9.4 T: a step towards whole brain functional connectivity imaging. *PLoS One* 2015, 10.
- Dorr AE, Lerch JP, Spring S, Kabani N, Henkelman RM. High resolution three-dimensional brain atlas using an average magnetic resonance image of 40 adult C57Bl/6 J mice. *Neuroimage* 2008, 42: 60–69.
- Avants BB, Tustison NJ, Song G, Cook PA, Klein A, Gee JC. A reproducible evaluation of ANTs similarity metric performance in brain image registration. *Neuroimage* 2011, 54: 2033–2044.
- Zou QH, Zhu CZ, Yang YH, Zuo XN, Long XY, Cao QJ, *et al.* An improved approach to detection of amplitude of low-frequency fluctuation (ALFF) for resting-state fMRI: Fractional ALFF. *J Neurosci Methods* 2008, 172: 137–141.
- Fyffe SL, Neul JL, Samaco RC, Chao HT, Ben-Shachar S, Moretti P, *et al.* Deletion of MeCP2 in Sim1-expressing neurons reveals a critical role for MeCP2 in feeding behavior, aggression, and the response to stress. *Neuron* 2008, 59: 947–958.
- Ito-Ishida A, Ure K, Chen H, Swann JW, Zoghbi HY. Loss of MeCP2 in parvalbumin- and somatostatin-expressing neurons in mice leads to distinct rett syndrome-like phenotypes. *Neuron* 2015, 88: 651–658.
- Samaco RC, Mandel-Brehm C, Chao HT, Ward CS, Fyffe-Maricich SL, Ren J, *et al.* Loss of MeCP2 in aminergic neurons causes cell-autonomous defects in neurotransmitter synthesis and specific behavioral abnormalities. *Proc Natl Acad Sci U S A* 2009, 106: 21966–21971.
- Finlay JM, Dunham GA, Isherwood AM, Newton CJ, Nguyen TV, Reppar PC, *et al.* Effects of prefrontal cortex and hippocampal NMDA NR1-subunit deletion on complex cognitive and social behaviors. *Brain Res* 2015, 1600: 70–83.
- Liang B, Zhang LF, Barbera G, Fang WT, Zhang J, Chen XC, *et al.* Distinct and dynamic ON and OFF neural ensembles in the prefrontal cortex code social exploration. *Neuron* 2018, 100: 700–714.e9.
- Niu B, Liu PP, Shen MJ, Liu C, Wang L, Wang FF, *et al.* GRK5 regulates social behavior via suppression of mTORC1 signaling in medial prefrontal cortex. *Cereb Cortex* 2018, 28: 421–432.
- Tan Y, Singhal SM, Harden SW, Cahill KM, Nguyen DTM, Colon-Perez LM, *et al.* Oxytocin receptors are expressed by glutamatergic prefrontal cortical neurons that selectively modulate social recognition. *J Neurosci* 2019, 39: 3249–3263.
- Swiech L, Heidenreich M, Banerjee A, Habib N, Li YQ, Trombetta J, *et al.* *In vivo* interrogation of gene function in the mammalian brain using CRISPR-Cas9. *Nat Biotechnol* 2015, 33: U102–U286.
- Allsop SA, Vander Weele CM, Wichmann R, Tye KM. Optogenetic insights on the relationship between anxiety-related behaviors and social deficits. *Front Behav Neurosci* 2014, 8.
- Tovote P, Fadok JP, Luthi A. Neuronal circuits for fear and anxiety. *Nat Rev Neurosci* 2015, 16: 317–331.
- Lohani S, Martig AK, Deisseroth K, Witten IB, Moghaddam B. Dopamine modulation of prefrontal cortex activity is manifold and operates at multiple temporal and spatial scales. *Cell Rep* 2019, 27: 99–114.e6.

37. Phillips ML, Robinson HA, Pozzo-Miller L. Ventral hippocampal projections to the medial prefrontal cortex regulate social memory. *Elife* 2019, 8.
38. Li Y, Missig G, Finger BC, Landino SM, Alexander AJ, Mokler EL, *et al.* Maternal and early postnatal immune activation produce dissociable effects on neurotransmission in mPFC-amygdala circuits. *J Neurosci* 2018, 38: 3358–3372.
39. Huang WC, Chen YJ, Page DT. Hyperconnectivity of prefrontal cortex to amygdala projections in a mouse model of macrocephaly/autism syndrome. *Nat Commun* 2016, 7.
40. Adachi M, Autry AE, Covington HE, Monteggia LM. MeCP2-mediated transcription repression in the basolateral amygdala may underlie heightened anxiety in a mouse model of rett syndrome. *J Neurosci* 2009, 29: 4218–4227.



# Whole-Brain Monosynaptic Inputs to Hypoglossal Motor Neurons in Mice

Han Guo<sup>1,3</sup> · Xiang-Shan Yuan<sup>1,2</sup> · Ji-Chuan Zhou<sup>1</sup> · Hui Chen<sup>1</sup> · Shan-Qun Li<sup>3</sup> · Wei-Min Qu<sup>1</sup> · Zhi-Li Huang<sup>1</sup>

Received: 30 July 2019 / Accepted: 25 November 2019 / Published online: 24 February 2020  
© The Author(s) 2020

**Abstract** Hypoglossal motor neurons (HMNs) innervate tongue muscles and play key roles in a variety of physiological functions, including swallowing, mastication, suckling, vocalization, and respiration. Dysfunction of HMNs is associated with several diseases, such as obstructive sleep apnea (OSA) and sudden infant death syndrome. OSA is a serious breathing disorder associated with the activity of HMNs during different sleep–wake states. Identifying the neural mechanisms by which the state-dependent activities of HMNs are controlled may be helpful in providing a theoretical basis for effective therapy for OSA. However, the presynaptic partners governing the activity of HMNs remain to be elucidated. In the present study, we used a cell-type-specific retrograde tracing system based on a modified rabies virus along with a Cre/loxP gene-expression strategy to map the whole-brain

monosynaptic inputs to HMNs in mice. We identified 53 nuclei targeting HMNs from six brain regions: the amygdala, hypothalamus, midbrain, pons, medulla, and cerebellum. We discovered that GABAergic neurons in the central amygdaloid nucleus, as well as calretinin neurons in the parabrachial nucleus, sent monosynaptic projections to HMNs. In addition, HMNs received direct inputs from several regions associated with respiration, such as the pre-Botzinger complex, parabrachial nucleus, nucleus of the solitary tract, and hypothalamus. Some regions engaged in sleep–wake regulation (the parafacial zone, parabrachial nucleus, ventral medulla, sublateral dorsal tegmental nucleus, dorsal raphe nucleus, periaqueductal gray, and hypothalamus) also provided primary inputs to HMNs. These results contribute to further elucidating the neural circuits underlying disorders caused by the dysfunction of HMNs.

Han Guo and Xiang-Shan Yuan contributed equally to this work.

**Electronic supplementary material** The online version of this article (<https://doi.org/10.1007/s12264-020-00468-9>) contains supplementary material, which is available to authorized users.

✉ Wei-Min Qu  
quweimin@fudan.edu.cn

✉ Zhi-Li Huang  
huangzl@fudan.edu.cn

<sup>1</sup> Department of Pharmacology, School of Basic Medical Sciences; State Key Laboratory of Medical Neurobiology and Ministry of Education Frontiers Center for Brain Science, Institutes of Brain Science, Fudan University, Shanghai 200032, China

<sup>2</sup> Department of Anatomy, School of Basic Medical Sciences, Fudan University, Shanghai 200032, China

<sup>3</sup> Department of Pulmonary Medicine, Zhongshan Hospital, Fudan University, Shanghai 200032, China

**Keywords** Hypoglossal motor neuron · Monosynaptic input · Rabies virus · Respiration · Sleep and wake

## Introduction

The hypoglossal nucleus (12N) is located in the dorsomedial medulla oblongata and consists of cholinergic hypoglossal motor neurons (HMNs). HMNs innervate several extrinsic and intrinsic tongue muscles that participate in basic and important motor functions, including swallowing, mastication, suckling, vocalization, and respiration [1–5]. Dysfunction of HMNs leads to physiological behavioral disorders and is associated with several diseases, such as obstructive sleep apnea (OSA) and sudden infant death syndrome [6]. OSA is a serious breathing disorder caused by sleep-dependent changes in

neuromodulators acting on critical pharyngeal motor pools. Among these pools, HMNs innervating the genioglossus (GG) have been explored most extensively, as the GG is the largest and most accessible upper airway dilator [7]. Aberrant changes in the activity of HMNs have been demonstrated to induce low muscular tone of the GG and represent the key pathogenesis of OSA. A recent study in rodents demonstrated that chemogenetic activation of HMNs causes significant and sustained increases in GG activity during sleep but without effects on sleep–wake states [8], indicating that modulation of HMNs may be a potential means of improving ventilation during sleep in OSA. The activity of HMNs is modulated by excitatory and inhibitory signals in the brain during physiological behaviors [9–11]. However, it is not clear which specific excitatory or inhibitory signals directly control HMNs. Therefore, identifying the whole-brain inputs to HMNs is critical for a better understanding of the modulation of HMN activity during different behaviors.

Conventional approaches with non-specific tracers have been used to classify the major inputs from the brainstem to the 12N [12–14], while little attention has been paid to whole-brain inputs. Using horseradish peroxidase, a non-specific tracer, a previous study showed that the 12N mainly receives inputs from brainstem reticular regions, the nucleus of the solitary tract (Sol), and the sensory trigeminal complex [14]. Due to their poor cell-type specificity, non-specific tracers easily exceed the range of the 12N and spread to other nuclei, which has led to inaccurate results [14]. Pseudorabies virus has been injected into tongue muscles to explore the multisynaptic afferents to 12N; although this method improves efficiency, it cannot accurately identify monosynaptic transmission [12, 15]. Therefore, it is essential to adopt a cutting-edge viral tracing system with high specificity to identify monosynaptic inputs that target the 12N to yield a comprehensive anatomical-functional understanding of HMNs.

To avoid the limitations of traditional technology, we combined a genetically modified rabies virus for trans-synaptic retrograde tracing [16] with the Cre/loxP gene expression system [17] to comprehensively identify the monosynaptic inputs onto HMNs from the entire brain.

## Materials and Methods

### Animals

Adult choline acetyltransferase (ChAT)-IRES-Cre mice [18] of the C57BL/6J strain and non-Cre-expressing littermates (2–4 months old) were used for retrograde tracing experiments. Adult GAD2-IRES-Cre mice [19] and

calretinin (CR)-IRES-Cre mice were used for anterograde tracing experiments. Mice were bred and housed under a 12/12 light/dark cycle (lights on at 07:00) at  $22\text{ }^{\circ}\text{C} \pm 1\text{ }^{\circ}\text{C}$  with  $55\% \pm 5\%$  humidity, and were provided with unlimited food and water [20]. All experiments were approved by the Committee on the Ethics of Animal Experiments of the Basic Medical Sciences School at Fudan University (permit number 20140226-024).

### Viruses and Surgery

AAV2/9-CAG-DIO-TVA-GFP ( $1.7 \times 10^{13}$  genome copies/mL), AAV2/9-CAG-DIO-RG ( $6.8 \times 10^{12}$  genome copies/mL), and an EnvA-pseudotyped glycoprotein (RG)-deleted and DsRed-expressing rabies virus (RV-EnvA- $\Delta$ G-DsRed,  $5.0 \times 10^8$  fluorescence-forming units/mL) were purchased from BrainVTA (Wuhan, China) [21, 22]. The two Cre-dependent AAVs were mixed at a 1:1 ratio in 100 nL as helper viruses for retrograde monosynaptic-tracing experiments. AAV-EF1 $\alpha$ -DIO-ChR2-mCherry ( $3 \times 10^{12}$  genome copies/mL) was used for anterograde tracing experiments and was provided by Taitool Bioscience Co., Ltd (Shanghai, China).

Surgical procedures were performed as described in previous studies [22, 23]. Briefly, mice were anesthetized with chloral hydrate (350 mg/kg, intraperitoneal) and placed in a stereotaxic apparatus. A glass micropipette was used to deliver a viral vector to the 12N (anteroposterior [AP],  $-7.5$  mm; medio-lateral [ML],  $-0.3$  mm; dorso-ventral [DV], 4.5 mm) after exposing the skull. The viral vector was microinjected with a compressed-air delivery system, as described previously [24]. For retrograde tracing, helper viruses (100 nL) were injected into the 12N and left in place for 10 min to allow their diffusion away from the injection site. Fourteen days later, 200 nL of RV-EnvA- $\Delta$ G-DsRed was injected into the same location. After one week, these mice were perfused for immunostaining ( $n = 4$ ). For anterograde tracing, AAV-EF1 $\alpha$ -DIO-ChR2-mCherry was injected into the central amygdaloid nucleus (CeA; AP,  $-1.22$  mm; ML  $-2.4$  mm; DV, 4.8 mm) of GAD2-Cre mice and into the paraventricular nucleus (PVN; AP,  $-2.0$  mm; ML,  $-1.1$  mm; DV, 5.0 mm) of CR-Cre mice, using the procedures described above. After three weeks, all of these mice were perfused.

### Histology and Immunostaining

Mice were perfused with 50 mL PBS, followed by 100 mL 4% paraformaldehyde in PBS. Brains were removed, post-fixed for 24 h at  $4\text{ }^{\circ}\text{C}$ , and then cryoprotected in 30% sucrose until they sank. Sections were cut at  $30\text{ }\mu\text{m}$  on a freezing cryostat (CM1950; Leica, Wetzlar, Germany).

To confirm that the neurons initially infected were cholinergic neurons in the 12N, we immunostained sections containing the 12N with primary antibodies to ChAT. To characterize the inputs and initially-infected neurons of the CeA and PSTN, we immunostained sections containing these areas with primary antibodies against  $\gamma$ -aminobutyric acid (GABA) for the CeA and CR for the PSTN [21, 22]. The sections were incubated overnight at 4 °C in PBST (PBS with 0.3% Triton X-100 [*v/v*]) and with the following primary antibodies: goat anti-ChAT (1:500, cat. #AB144P, Millipore, Billerica, MA), rabbit anti-GABA (1:1000, cat. #PA5-32241, Life Technologies, Carlsbad, CA), and rabbit anti-CR (1:2000, cat. #7697, Swant, Bellinzona, Ticino, Switzerland). After three washes in PBS, the sections were incubated with an Alexa Fluor-conjugated IgG antibody (1:1000, Invitrogen, Carlsbad, CA) at room temperature (RT, 20 °C–22 °C) for 2 h. Then, the sections were counterstained with 4', 6-diamidino-2-phenylindole (DAPI, 1:3000, cat. # D9542, Sigma-Aldrich, St. Louis, MO) and coverslipped with Fluoromount G<sup>TM</sup> (Southern Biotech, Birmingham, AL). Finally, we captured fluorescence images using an Olympus confocal system.

To investigate the axons projecting from GABAergic CeA neurons and PSTN CR neurons to the HMNs, sections containing the 12N were washed in PBST and incubated with a rabbit polyclonal anti-mCherry primary antibody (1:5000, cat. #632496, Clontech, San Diego, CA) for 24 h at 4 °C. For chromogenic detection of mCherry, sections were then washed three times in PBS (5 min each) and incubated in donkey anti-rabbit biotinylated IgG (1:1000, cat. #711-065-152, Jackson ImmunoResearch, West Grove, PA) in PBST for 2 h at RT. The sections were then washed in PBS and incubated with an avidin–biotin–peroxidase complex (1:1000, cat. #PK-6100, Vector Laboratories, Burlingame, CA) in PBST for 2 h at RT. Then, the sections were washed and incubated in a solution of 3, 3' -diaminobenzidine (0.2 mg/mL) and 0.005% H<sub>2</sub>O<sub>2</sub> in PBS until mCherry-immunoreactive axons could be identified. Finally, we placed the immunostained sections on the glass slides, dehydrated them, and cover-slipped them as described previously [25].

### Imaging and Data Analysis

For the whole-brain mapping of monosynaptic inputs, images of sections were captured with a 10 × objective on an Olympus microscope (VS-120, Tokyo, Japan) and further imaging analyses were done using Olympus analysis software and ImageJ. The numbers of DsRed-labeled cells (excluding the injection site) were counted automatically by ImageJ. By adjusting the threshold of the image, we set a minimum size of cells in the section as the threshold, and the algorithm automatically counted cells

larger than this value. The boundaries of brain nuclei were defined according to the atlas of Paxinos and Franklin [26]. The proportion of inputs from each of the 53 brain regions was calculated as the ratio of the number of afferent cells in each nucleus to the total number of DsRed-labeled cells. In addition, we used a 100 × oil objective on the Olympus microscope to determine whether there were axons in the 12N from the CeA and PSTN. We also used an Olympus confocal system to calculate the co-labeling rates of GABAergic and CR neurons occupying the total DsRed-labeled populations in the CeA and PSTN, respectively. Lastly, we analyzed the proportion of inputs from each of the 53 brain regions [26] and the co-labeling rates of GABAergic and CR neurons in the total DsRed-labeled populations (*n* = 4). We used GraphPad prism 7.0 and the paired *t* test for statistical analysis. All data are presented as the mean ± SEM (standard error of the mean).

## Results

### Identification of Monosynaptic Inputs to HMNs Using a Rabies-Based System

To identify the monosynaptic inputs to HMNs, we applied a trans-synaptic viral system based on a modified rabies virus [16] using a transgenic mouse line expressing Cre recombinase in cholinergic neurons (ChAT-Cre mice) [17, 24]. We first injected two Cre-dependent helper viruses (AAV-CAG-DIO-TVA-GFP and AAV-CAG-DIO-RG) to express the avian receptor (TVA protein) and the rabies glycoprotein G (RG) in the unilateral 12N (Fig. 1A, B, Fig. S1). Two weeks later, the modified rabies virus (RV-EnvA-ΔG-DsRed) was injected into the same site (Fig. 1A, B). This rabies virus only infected neurons with TVA expression and spread retrogradely with the RG expression in the brain (Fig. 1C). After seven days, the starter neurons were defined and characterized by the co-expression of DsRed and GFP; they were restricted to the 12N ipsilateral to the injection site (Fig. 1E). Moreover, we observed DsRed-labeled neurons in other regions around the 12N, which represented the monosynaptic afferents to cholinergic HMNs (Fig. 1C–E). The same strategy was used in wild-type mice, and we did not detect any DsRed-positive neuron anywhere in the brains of these control mice (Fig. 1D). Therefore, this technique is reliable for visualizing monosynaptic afferent inputs to HMNs from the whole brain.

### Whole-Brain Inputs to HMNs

To investigate the inputs to HMNs from the whole brain, we cut serial coronal sections (Fig. 2) after enough

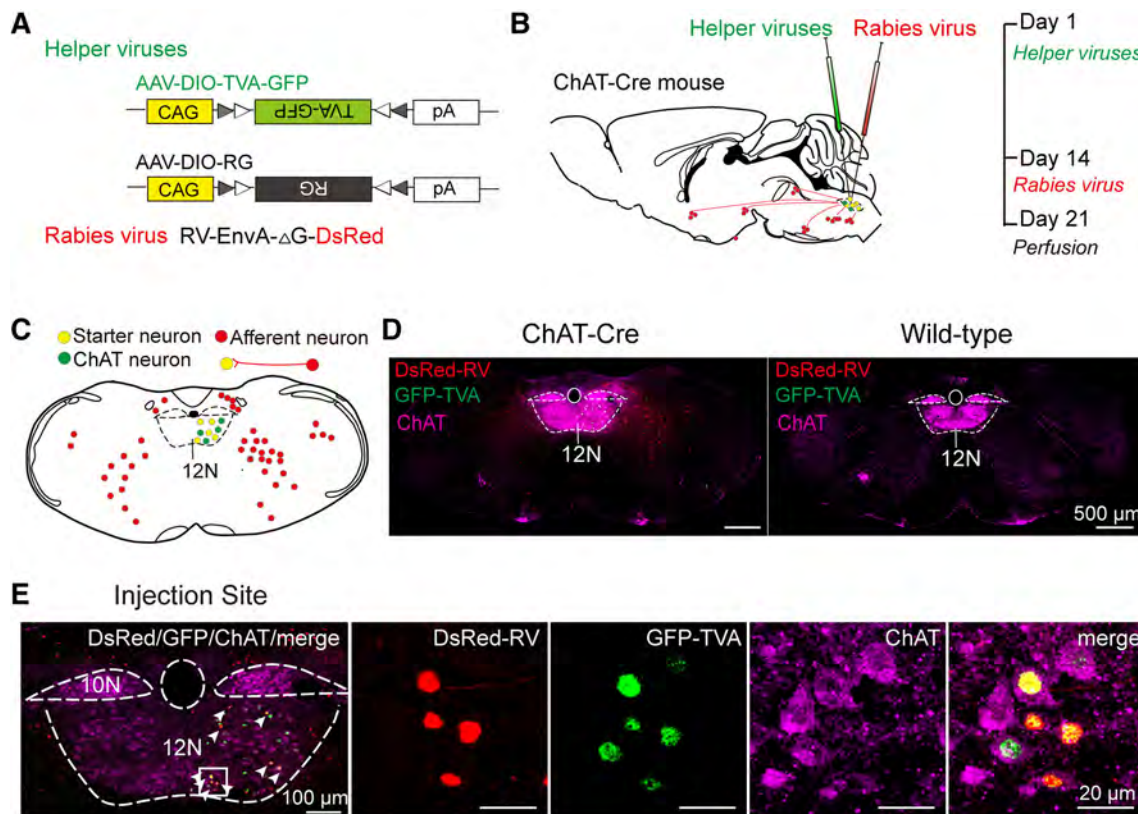


**Fig. 1** Experimental system based on trans-synaptic rabies virus tracing to identify monosynaptic inputs to HMNs. **A** Design of viral vectors for rabies virus-based trans-synaptic retrograde tracing, including helper viruses with Cre-dependent expression of TVA receptor (AAV-CAG-DIO-TVA-GFP) and RG (AAV-CAG-DIO-RG). The rabies virus was genetically modified by pseudotyping with EnvA (RV-EnvA-DsRed). **B** Schematic of the 12N injection procedure and experimental timeline for helper viruses and rabies virus in the ChAT-Cre mouse. **C** Schematic coronal section to

illustrate viral infection in 12N (yellow, starter neurons; green, AAV helper virus-infected neurons; red, rabies virus-infected neurons). **D** Representative images showing rabies virus-labeled neurons in a ChAT-Cre mouse (left) but not in a wild-type mouse (right) (scale bars, 500  $\mu$ m). **E** A representative section stained with ChAT (purple, left). The section was infected with helper virus (green) and rabies virus (red); starter neurons are restricted to the unilateral 12N (right four panels; scale bar, 20  $\mu$ m). 10N, vagus nerve nucleus; 12N, hypoglossal nucleus.

infection time for the three injected viruses. Sections from a typical ChAT-Cre brain (Fig. 2) revealed that DsRed-labeled afferent neurons were largely located in the medulla oblongata, while some were found in the pons and midbrain. Furthermore, a few input neurons were found in the hypothalamus, amygdala, and cerebellum (Fig. 2). To display the whole-brain distribution of neurons presynaptic to HMNs in detail (Fig. 3), we enlarged and selected representative coronal images from the following major afferent nuclei: the paraventricular hypothalamus (PVH), CeA, lateral hypothalamus (LH), PSTN, parabrachial nucleus (PB), dorsal raphe nucleus (DR), periaqueductal gray (PAG), pontine reticular nucleus, oral part (PnO), sublateralodorsal tegmental nucleus (SLD), dorsal paragigantocellular nucleus, parafacial zone (PZ), prepositus nucleus, parvocellular reticular nucleus (PCRt), gigantocellular reticular nucleus (Gi), gigantocellular reticular nucleus, alpha part (GiA), lateral paragigantocellular nucleus (LPGi), gigantocellular reticular nucleus, ventral

part (GiV), pre-Botzinger complex (PrBo), intermediate reticular nucleus (IRT), and Sol.

Next, we conducted a statistical analysis of the distribution of input nuclei from the whole brain based on the ratio of the number of DsRed-labeled neurons in each nucleus to the total number of labeled neurons in each brain (Fig. 4,  $n = 4$ ). We identified 53 nuclei that each had a ratio of  $> 0.1\%$  of the total number of labeled neurons (Fig. 4,  $n = 4$ ). The inputs to HMNs originated in six brain structures: the amygdala, hypothalamus, midbrain, pons, medulla, and cerebellum. Large numbers of neurons providing direct projections to HMNs were found in the IRT ( $23.02\% \pm 2.55\%$ ), Sol ( $10.07\% \pm 2.71\%$ ), and Gi ( $7.74\% \pm 1.21\%$ ) of the medulla. The ventral medullary reticular region, including the LPGi ( $3.25\% \pm 0.40\%$ ), GiA ( $2.82\% \pm 0.44\%$ ), and GiV ( $0.57\% \pm 0.26\%$ ), also had strong projections to HMNs. The PnO ( $1.96\% \pm 0.58\%$ ) in the pons, and the CeA

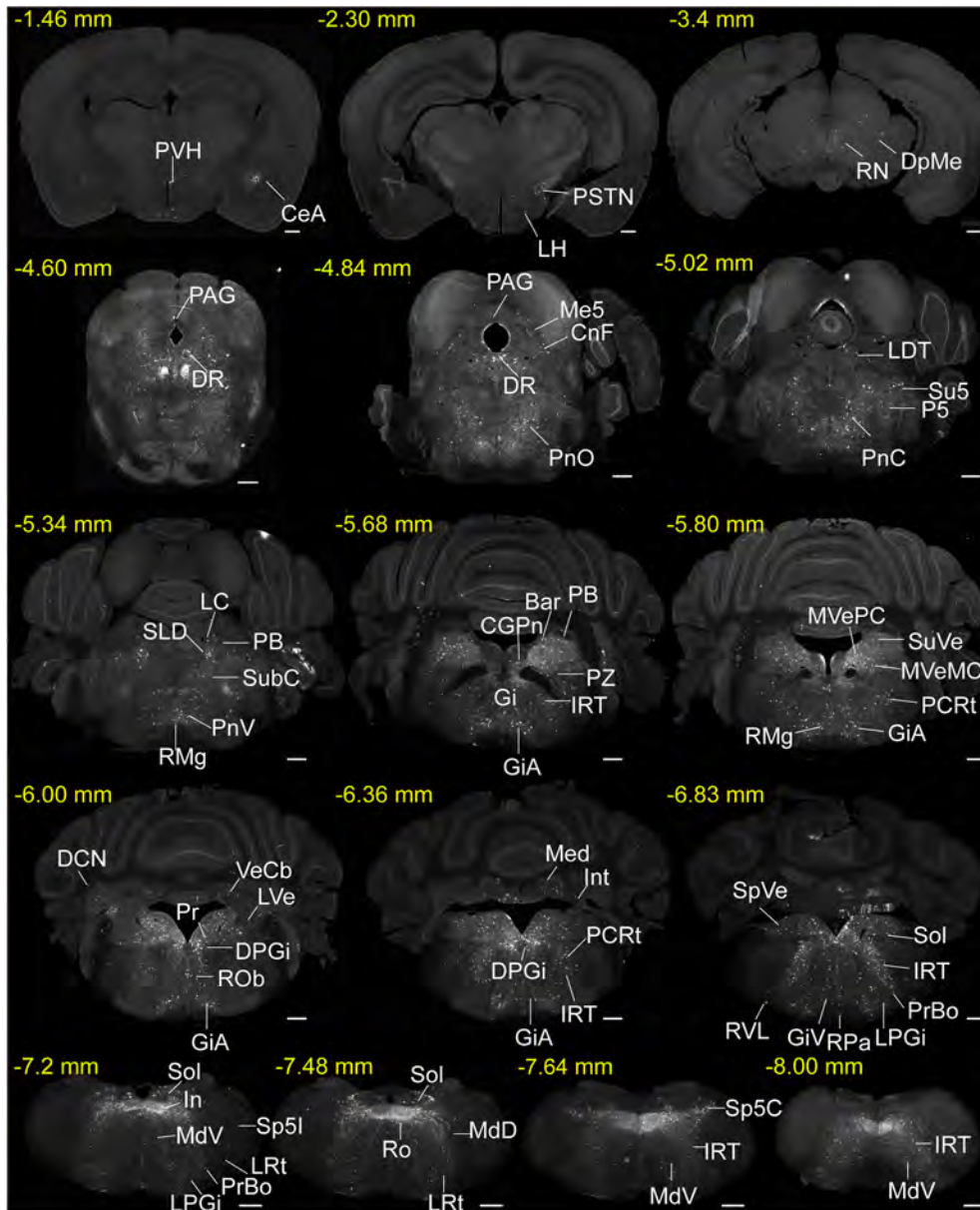


**Fig. 2** Representative images of monosynaptic inputs to HMNs from the whole brain. Regions are labeled according to the mouse brain atlas [26] (scale bars, 500  $\mu$ m). Abbreviations: CeA, central amygdaloid nucleus; PVH, paraventricular hypothalamus; LH, lateral hypothalamic area; PSTN, paraventricular nucleus; DpMe, deep mesencephalic nucleus; RN, red nucleus; PAG, periaqueductal gray; DR, dorsal raphe nucleus; Me5, mesencephalic trigeminal nucleus; CnF, cuneiform nucleus; PnO, pontine reticular nucleus, oral part; PnC, pontine reticular nucleus, caudal part; LDT, laterodorsal tegmental nucleus; P5, peritrigeminal zone; Su5, supratrigeminal nucleus; LC, locus coeruleus; SLD, sublateral dorsal nucleus; PB, parabrachial nucleus; PnV, pontine reticular nucleus, ventral part; SubC, subcoeruleus nucleus; RMg, raphe magnus nucleus; Gi, gigantocellular reticular nucleus; GiA, gigantocellular reticular nucleus, alpha part; CGPn, central gray of the pons; Bar, Barrington's nucleus; PZ, parafacial zone; IRT, intermediate reticular nucleus;

PCRt, parvocellular reticular nucleus; MVeMC, medial vestibular nucleus, magnocellular part; MVePC, medial vestibular nucleus, parvocellular part; SuVe, superior vestibular nucleus; LVe, lateral vestibular nucleus; DCN, deep cerebellar nucleus; VeCb, vestibulo-cerebellar nucleus; Pr, prepositus nucleus; DPGi, dorsal paragigantocellular nucleus; ROb, raphe obscurus nucleus; Med, medial (fastigial) cerebellar nucleus; Int, interposed cerebellar nucleus; SpVe, spinal vestibular nucleus; RVL, rostroventrolateral reticular nucleus; RPa, raphe pallidus nucleus; LPGi, lateral paragigantocellular nucleus; GiV, gigantocellular reticular nucleus, ventral part; Sol, nucleus of the solitary tract; PrBo, pre-Botzinger complex; In, intercalated nucleus of the medulla; LRt, lateral reticular nucleus; Sp5I, spinal trigeminal nucleus, interpolar part; Sp5C, spinal trigeminal nucleus, caudal part; Ro, nucleus of Roller; MdD, medullary reticular nucleus, dorsal part; MdV, medullary reticular nucleus, ventral part.

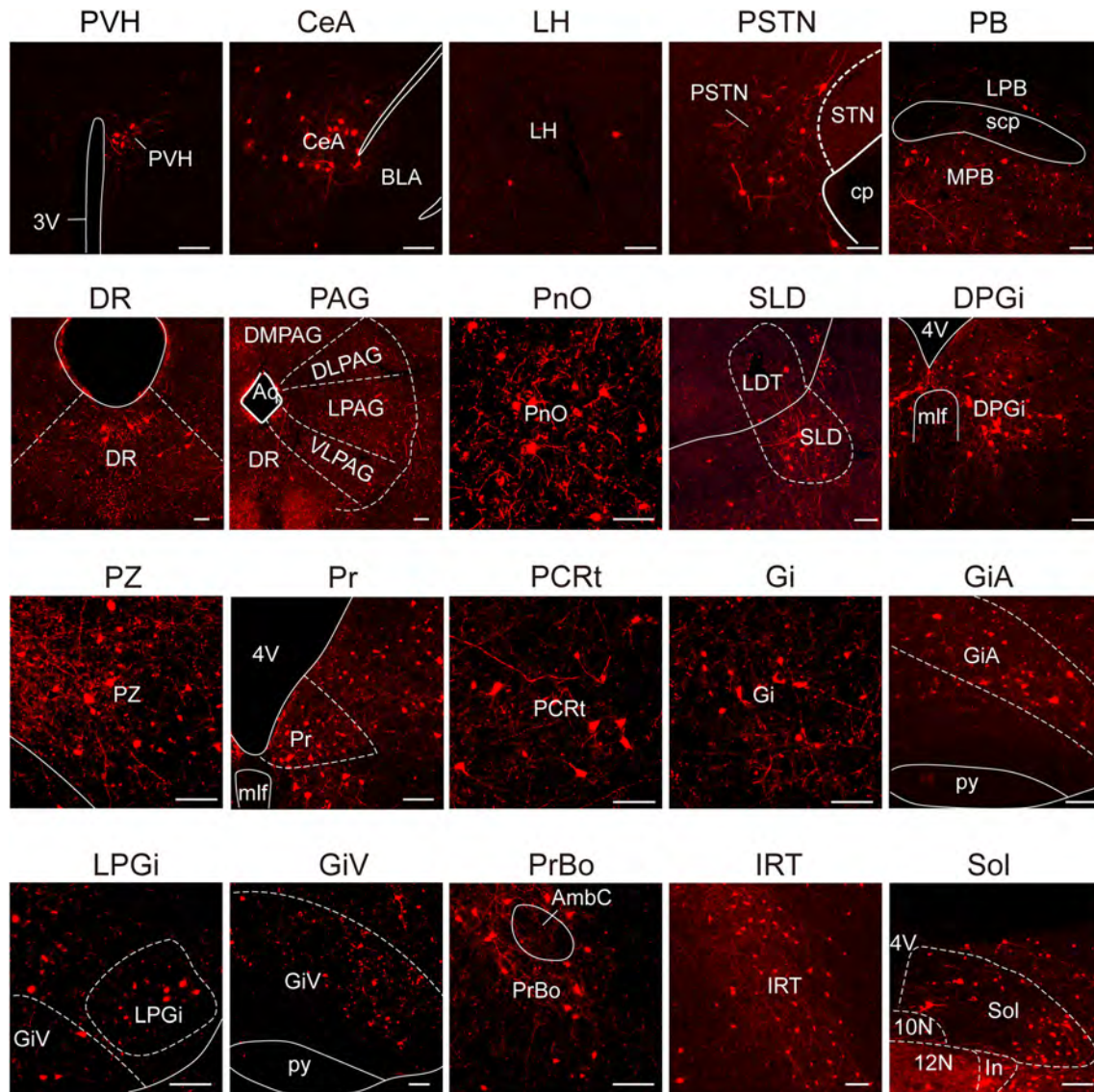


**Fig. 3** Representative nuclei with monosynaptic inputs to HMNs. Primary inputs to HMNs include multiple nuclei associated with respiration (e.g., Sol, PrBo, PB, ventral medulla, and hypothalamus) and sleep–wake regulation (e.g., PZ, PB, hypothalamus, SLD, and ventral medulla) (scale bars, 100  $\mu$ m). Abbreviations: PVH, paraventricular hypothalamus; 3V, third ventricle; CeA, central amygdaloid nucleus; BLA, basolateral amygdaloid nucleus, anterior part; LH, lateral hypothalamic area; PSTN, paraventricular nucleus; STN, subthalamic nucleus; cp, cerebral peduncle; PB, parabrachial nucleus; LPB, lateral parabrachial nucleus; MPB, medial parabrachial nucleus; scp, superior cerebellar peduncle; DR, dorsal raphe nucleus; PAG, periaqueductal gray; DMPAG, dorsomedial periaqueductal gray; DLPAG, dorsolateral periaqueductal gray; LPAG, lateral

periaqueductal gray; VLPAG, ventrolateral periaqueductal gray; Aq, aqueduct; PnO, pontine reticular nucleus, oral part; SLD, sublateral dorsal nucleus; LDT, laterodorsal tegmental nucleus; DPGi, dorsal paragigantocellular nucleus; 4V, fourth ventricle; mlf, medial longitudinal fasciculus; PZ, parafacial zone; Pr, prepositus nucleus; PCRt, parvocellular reticular nucleus; Gi, gigantocellular reticular nucleus; ROb, raphe obscurus nucleus; GiA, gigantocellular reticular nucleus, alpha part; py, pyramidal tract; LPGi, lateral paragigantocellular nucleus; GiV, gigantocellular reticular nucleus, ventral part; PrBo, pre-Botzinger complex; AmbC, ambiguus nucleus, compact part; IRT, intermediate reticular nucleus; 10N, vagus nerve nucleus; 12N, hypoglossal nucleus; In, intercalated nucleus; Sol, nucleus of the solitary tract.

(2.38%  $\pm$  1.15%), were the other major nuclei providing inputs to HMNs.

Our results showed that HMNs received mass monosynaptic inputs from regions associated with respiration, such as the Sol, PrBo (0.58%  $\pm$  0.28%), ventral medulla (VM), PB (0.32%  $\pm$  0.09%), and hypothalamus. Some nuclei

controlling sleep and wakefulness, including the PZ (1.99%  $\pm$  0.25%), SLD (0.91%  $\pm$  0.25%), PB (0.32%  $\pm$  0.09%), DR (0.94%  $\pm$  0.20%), PAG (0.46%  $\pm$  0.22%), PSTN (0.82%  $\pm$  0.32%), and LH (0.51%  $\pm$  0.30%), also projected direct inputs to HMNs (Fig. 4,  $n = 4$ ). In summary, our results provide a concrete

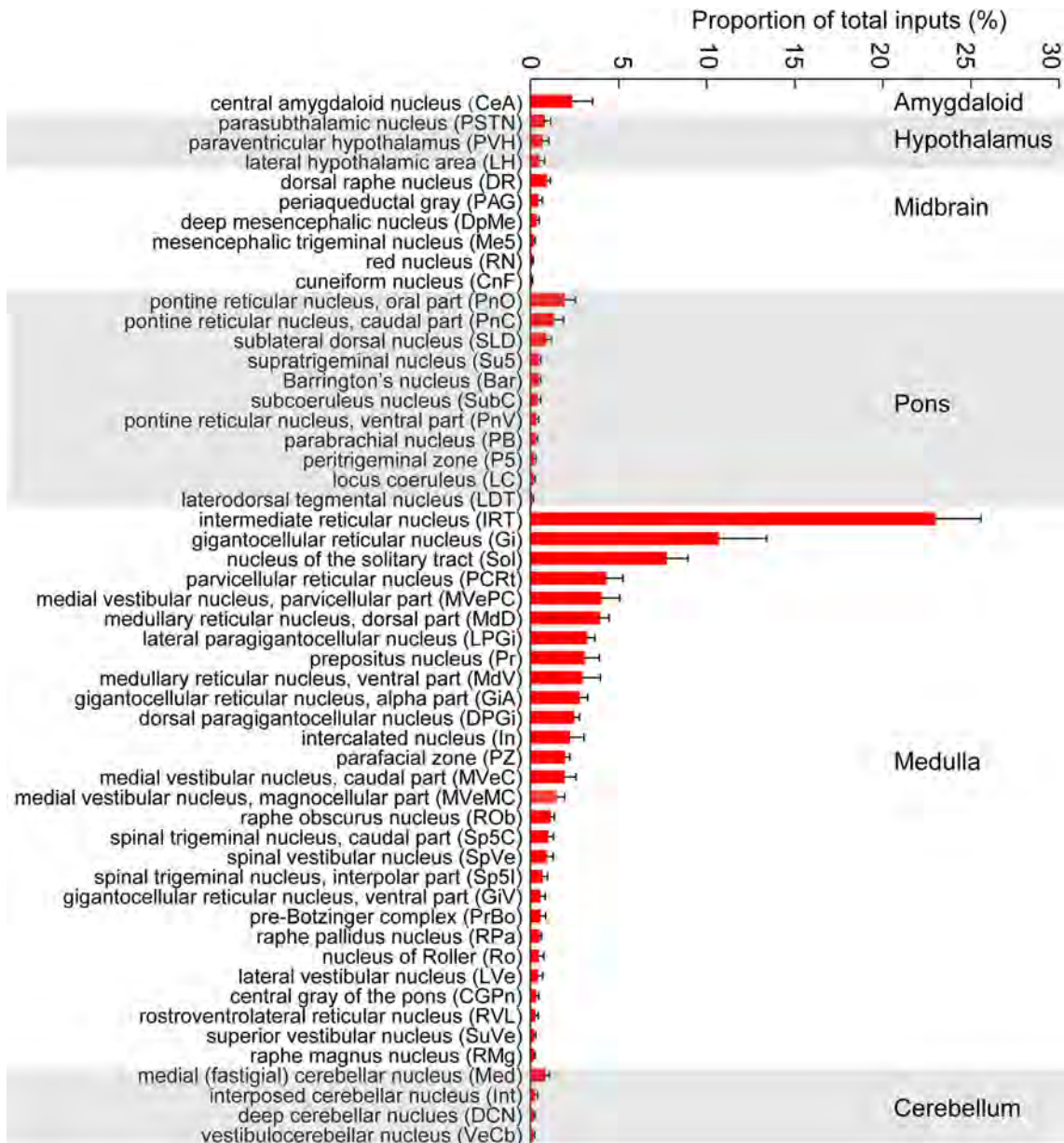


**Fig. 4** Statistical analysis of the whole-brain distribution of monosynaptic inputs to HMNs. Average proportion of DsRed-labeled neurons in 53 brain regions with > 0.1% of the total input to HMNs in ChAT-

Cre mice ( $n = 4$ ). Brain areas are grouped into six general structures: the amygdala, hypothalamus, midbrain, pons, medulla, and cerebellum.

input distribution in the whole brain and identify specific regions that are known to be involved in the regulation of different physiological functions.

**HMNs Receive Inputs from GABAergic CeA Neurons**

The CeA is a structure critical for learning, memory, consolidation of fear conditioning, predatory hunting, cataplexy, and emotion [27–31]. A previous study has shown that the CeA has connections with tongue premotor

neurons, as demonstrated by retrograde trans-synaptic transport of pseudorabies virus inoculated into the GG [32]. Unexpectedly, we found that HMNs received inputs from the bilateral CeA, as shown by our retrograde rabies-based system. Moreover, the ipsilateral CeA tended to have more DsRed-labeled neurons than that on the contralateral side ( $1.66\% \pm 0.76\%$  versus  $0.88\% \pm 0.33\%$ ,  $n = 4$ , Fig. S3). The DsRed-labeled neurons in the CeA were mainly co-localized with GABA ( $63.87\% \pm 4.83\%$ ; Fig. 5A, B). To further confirm that GABAergic CeA neurons send direct projections to 12N, we injected an

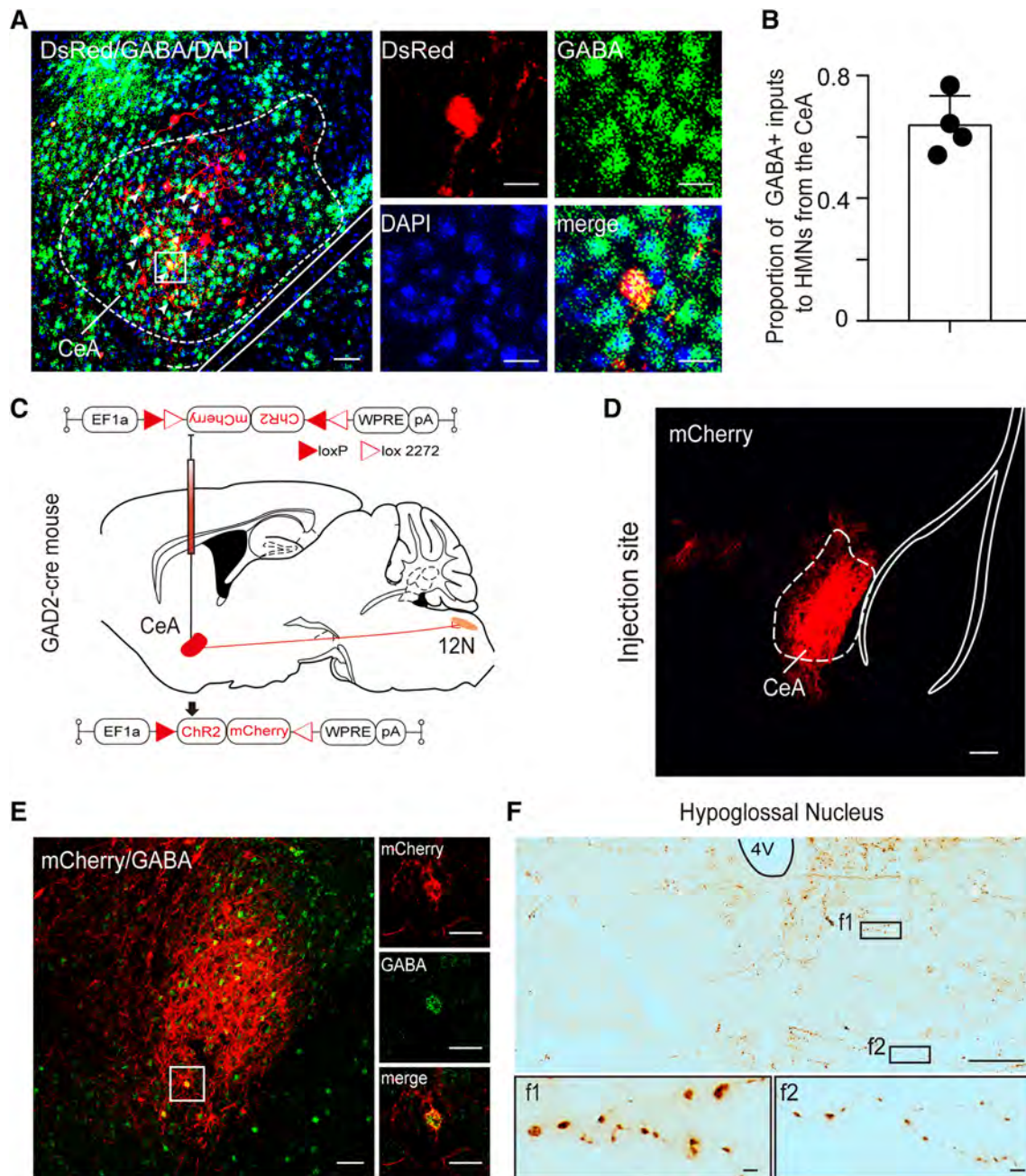


**Fig. 5** Cholinergic HMNs receive monosynaptic inputs from GABAergic CeA neurons. **A** Left, a large portion of DsRed neurons co-localize with GABA in the CeA (scale bar, 50  $\mu$ m). Right, higher magnification images of the area outlined by the white box (scale bars, 10  $\mu$ m). **B** The co-labeling rate of GABAergic neurons was  $63.87\% \pm 4.83\%$  of the total number of DsRed-labeled neurons in the CeA. **C** Schematic of the CeA injection site and viral vectors for AAV-EF1a-DIO-ChR2-mCherry in GAD2-Cre mice. **D** Representative image of the location of viral AAV-EF1a-DIO-ChR2-mCherry

(red) infection covering most of the CeA (scale bar, 100  $\mu$ m). **E** Left, fluorescence image showing that the neurons infected with ChR2-mCherry are mostly co-localized with GABA in the CeA (scale bar, 50  $\mu$ m). Right, higher magnification images of the area outlined by the white box (scale bars, 20  $\mu$ m). **F** Upper, representative image showing mCherry-labeled axons of GABAergic CeA neurons in 12N (scale bar, 100  $\mu$ m). Lower, higher magnification images of the areas enclosed by the black boxes f1 and f2 (scale bars, 100  $\mu$ m). CeA, central amygdaloid nucleus.

AAV expressing Cre-dependent ChR2-mCherry into the CeA of GAD2-Cre mice (Fig. 5C, D). After AAV injection, the mCherry-expressing neurons in the CeA mainly overlapped with GABA (Fig. 5E, Fig. S2). In addition to

finding funicular mCherry-labeled axons from the CeA in the bilateral 12N, we also observed mCherry axons with varicosities and boutons in 12N (Fig. 5F), indicating that the GABAergic CeA neurons project directly to 12N. Thus,

our results from retrograde and anterograde tracing demonstrated that the HMNs receive direct innervation from GABAergic CeA neurons.

### HMNs Receive Inputs from Calretinin Neurons in the PSTN

The hypothalamus is a heterogeneous structure that participates in the regulation of various functions, including sleep–wake behavior, feeding, energy balance, and reproductive behaviors [33–35]. The PSTN has recently been identified as a small subregion in the hypothalamus that is crucial in sleep–wake and feeding behavior [36, 37]. Here, we found that HMNs received small afferent inputs from the bilateral PSTN (Fig. 2), and the ipsilateral PSTN tended to have more projections than the contralateral PSTN ( $0.61\% \pm 0.23\%$  vs  $0.29\% \pm 0.07\%$ ,  $n = 4$ , Fig. S3). As demonstrated by immunofluorescent staining, DsRed-labeled neurons in the PSTN were co-labeled with CR-immunoreactive labeling ( $49.72\% \pm 8.00\%$ ; Fig. 6A, B). Furthermore, we injected an anterograde-tracing virus expressing Cre-dependent ChR2-mCherry into the PSTN in CR-Cre mice to confirm that PSTN CR neurons sent direct projections to the 12N (Fig. 6C–E, Fig. S2). After three weeks, we observed funicular mCherry-labeled axon terminals in the bilateral 12N, as well as many varicosities and boutons expressing mCherry in the 12N (Fig. 6F). These results indicated that PSTN CR neurons directly project to the 12N and that PSTN CR neurons form connections with ChAT neurons within the 12N.

### Discussion

To better understand the pathogenesis of diseases caused by HMN dysfunction, it is necessary to elucidate the neuromodulatory mechanisms that influence them. Some studies have reported afferent inputs to 12N using traditional retrograde-tracing techniques, including horseradish peroxidase and pseudorabies virus [12, 14]. Due to the non-specificity and inefficiency of these tracers, the data likely do not represent the comprehensive monosynaptic inputs to the cholinergic neurons of the 12N [14]. In the present study, we used a rabies-based system to comprehensively and accurately label monosynaptic inputs to HMNs at the whole-brain scale and found that HMNs received extensive direct inputs from the brainstem. Moreover, we found monosynaptic inputs from the CeA, PSTN, LH, and PVH. Taken together, our results provide a comprehensive and precise map of the spatial pattern of presynaptic inputs that modulate the activity of cholinergic HMNs for different behaviors.

### Comparison with Previous Retrograde Tracing Studies

The afferent inputs to HMNs have been extensively investigated for their critical roles in the modulation of tongue movements. Previous studies using classical non-specific tracers have shown that projections to the 12N originate from the brainstem reticular formation, the sensory trigeminal complex, and the Sol [14]. Injection of multi-synaptic pseudorabies virus into tongue muscles has revealed many multi-synaptic connections with HMNs in the brainstem [12, 15]. However, the non-specificity and multi-synaptic delivery characteristics of pseudorabies viruses make these results inaccurate. Therefore, a recent study used the ChAT-Cre: Rabies-G-crossed mouse line to specifically express glycoprotein G in cholinergic neurons and injected a glycoprotein G-defective rabies virus into the GG to label the premotor neurons of the HMNs innervating that muscle [38]. Although this approach achieved monosynaptic retrograde tracing with improved transfer efficiency, this tracing system was still defective for its spurious two-step labeling if any premotor neurons expressed ChAT, which may have induced possible deviations in the tracing results [38]. It is unclear whether the premotor neurons of HMNs express ChAT, although a previous study reported that some cholinergic neurons in the IRT of the brainstem project to HMNs [39], and there may be other hypoglossal premotor neurons that express ChAT. Meanwhile, that study used the ChAT-Cre: Rabies-G-crossed mouse line [38] and focused on whether the premotor circuitry of jaw and tongue motoneurons contains elements for coordination, rather than investigating the primary input circuitry of HMNs from the whole brain [38]. In addition, no previous studies have quantified the number of nuclei that input to HMNs, and most studies did not focus on HMN inputs from forebrain regions. Here, we used a rabies virus-mediated retrograde tracing system in ChAT-Cre mice, which allowed for specific labeling of whole-brain monosynaptic inputs to HMNs. We built a detailed and quantitative map of these inputs by counting the proportion of inputs from each region and found that the majority of these inputs originated in the IRT, Gi, and Sol of the medulla, which is consistent with previous results [12, 14, 40]. In addition, the PCRt, MVePC, Mdd, and LPGi in the medulla each contained a large number of labeled cells that innervated HMNs. Moreover, relatively dense inputs to HMNs also originated from the PnO, PnC, and SLD in the pons, as well as the DR and PAG in the midbrain.

Our results not only confirmed previous studies that used conventional retrograde tracing but also yielded the novel finding that HMNs receive direct inputs from the CeA and hypothalamus. The CeA is involved in the

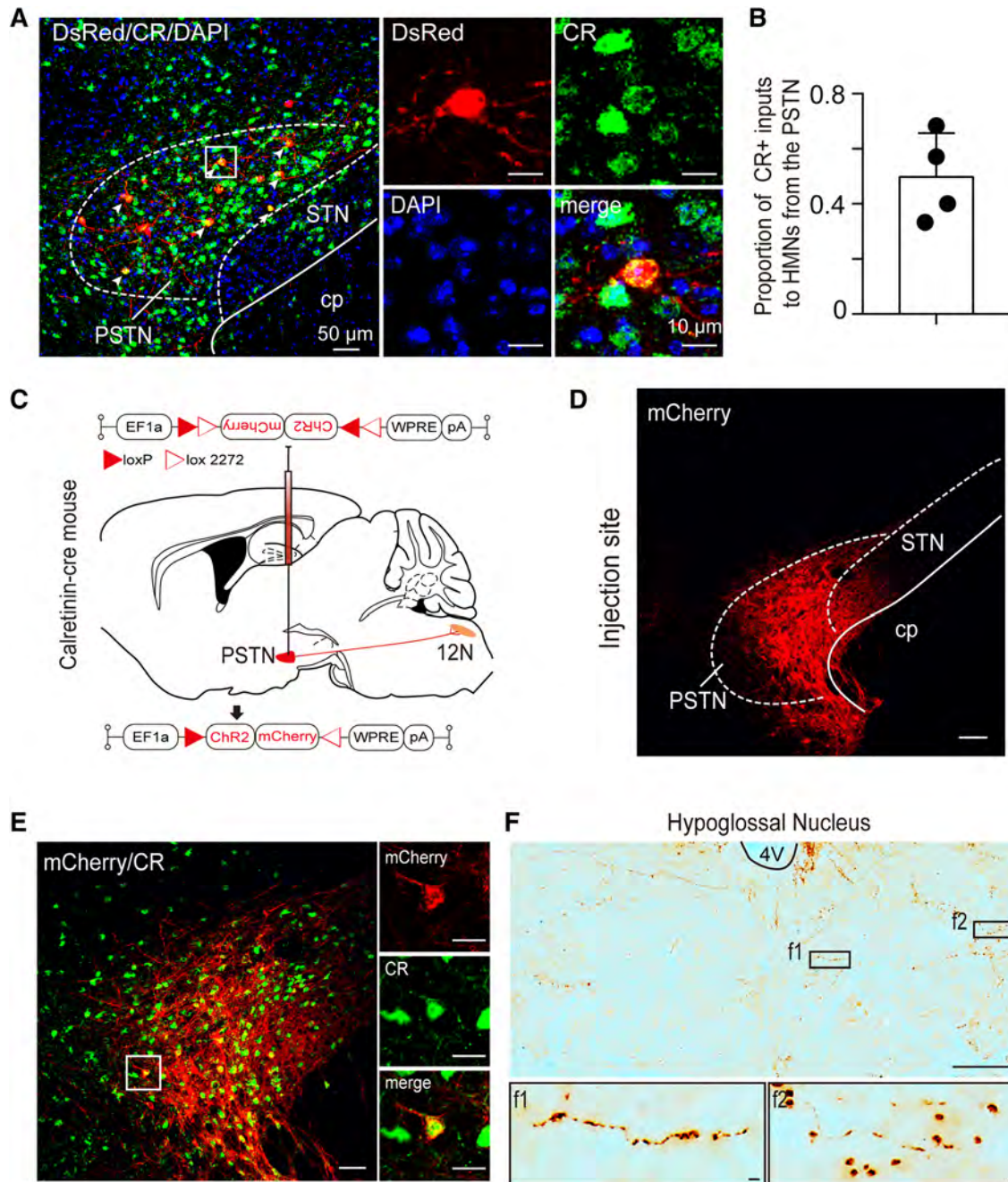


**Fig. 6** Cholinergic HMNs receive monosynaptic inputs from PSTN calretinin neurons. **A** Left, image showing that DsRed-labeled neurons are highly co-localized with CR neurons in the PSTN (scale bar, 50  $\mu\text{m}$ ). Right, higher magnification images of the white boxed area (scale bars, 10  $\mu\text{m}$ ). **B** The co-labeling rate of CR neurons was  $49.72\% \pm 8.00\%$  of the total number of DsRed-labeled neurons in the PSTN. **C** Schematic of the PSTN injection site and viral vectors for AAV-EF1a-DIO-ChR2-mCherry in CR-Cre mice. **D** Representative image showing that the location of viral AAV-EF1a-DIO-ChR2-mCherry (red) infection covered most of the PSTN (scale bar,

100  $\mu\text{m}$ ). **E** Left, representative fluorescence image showing that almost all the neurons infected with ChR2-mCherry co-localized with CR in the PSTN (scale bar, 50  $\mu\text{m}$ ). Right, higher magnification images of the area outlined by the white box (scale bars, 20  $\mu\text{m}$ ). **F** Upper, representative image showing mCherry-labeled axons of PSTN CR neurons in the 12N (scale bar, 100  $\mu\text{m}$ ). Lower, higher magnification images of the areas outlined by the black boxes f1 and f2 (scale bars, 100  $\mu\text{m}$ ). CR, calretinin; cp, cerebral peduncle; STN, subthalamic nucleus; PSTN, paraventricular nucleus.

expression of conditioned responses to aversive oral stimuli, including the gaping and tongue protrusion that are driven by central pattern generators and other premotor

neurons in the ponto-medullary reticular formation [41]. A previous study showed that the CeA is the only amygdalar nucleus to send axons to the pons and medulla and that it

has serial connections with premotor neurons of the tongue musculature [32]. Here, we found that GABAergic CeA neurons directly innervated HMNs, which may explain the changes of tongue muscle activity in response to aversive oral stimuli. The hypothalamus is a higher-order center of the autonomic nervous system and maintains essential homeostatic processes including respiration, sleep–wake behavior, and feeding. Here, we found primary inputs to HMNs from the hypothalamic PVH, PSTN, and LH, which morphologically corroborates the roles of the hypothalamus in the regulation of tongue activity. The proportion of inputs from the PSTN projecting to HMNs among hypothalamic inputs was relatively dense; ~ 50% colocalized with CR neurons. PSTN CR neurons might engage in the regulation of feeding [37] and modulate the activity of HMNs during eating.

### Neural Circuitry Underlying Modulation of HMN Activity During Respiration

HMNs innervate the GG muscle of the tongue, which plays a significant role in maintaining an open airspace for effective breathing [42]. The Sol, an important medullary area, integrates and relays afferent signals from the hypoglossal nerves to the respiratory center. Previous tracing studies have suggested that the Sol contains neurons that project densely to 12N [14, 40]. Our results support these findings, as we revealed that numerous Sol neurons provided monosynaptic inputs onto HMNs. These inputs could play an important role in the well-established respiratory reactivity of the GG. The PrBo, a compact medullary region, is essential for generating normal breathing rhythms and patterns [43]. Here, we found that the PrBo had sparse axonal terminals on HMNs, indicating that the PrBo–HMN pathway could play a role in maintaining the activity of HMNs in order to maintain an open upper airway.

The hypercapnia, hypoxia, and negative intrapharyngeal-airway pressure created by inspiratory effort against a blocked airway induce progressive activation of the GG. The Sol, PB, and ventrolateral medulla receive projections from chemosensory neurons in the retrotrapezoid nucleus, so they sense the hypercapnia, hypoxia, and other chemosensory information caused by apnea [44]. Our results indicated that all of these regions affect GG activity by innervating HMNs directly. The PVH and LH are critically involved in respiratory control. The most prominent role of the PVH is its involvement in mediation of the respiratory response to hypoxia [45]. Meanwhile, the activity of LH neurons increases in response to hypercapnia [46]. Here, we found that HMNs received direct inputs from the PVH and LH, which helps to explain why GG

activity increases quickly in response to hypercapnia and hypoxia.

### Neural Circuitry Underlying the Modulation of HMN Activity During Sleep–Wake Behavior

OSA increases the incidence of cardiovascular diseases such as angina, myocardial infarction, and hypertension and reduces sleep quality to induce excessive daytime sleepiness that can impair work performance [47]. OSA is a state-dependent process ultimately caused by the influence of sleep–wake circuits on pharyngeal muscle tone in individuals with an already narrow upper airway, especially in terms of the influence of neuromodulators acting upon the HMNs that innervate the GG, which is critical to OSA in humans [47]. Exploring the neural mechanisms that regulate HMNs may be critical for the identification and development of new pharmacological strategies to augment GG activity in sleep, especially during REM sleep, as potential treatments for OSA. In the present study, we found that many nuclei involved in sleep–wake regulation sent inputs to HMNs, such as the VM, SLD, PZ, and DR, which might affect HMN activity during sleep–wake transitions.

The VM (including the GiA, GiV, and LPGi) is involved in the regulation of the sleep–wake cycle [48]. It has been reported that GABAergic VM neurons powerfully promote REM sleep and that glutamatergic neurons participate in the regulation of wakefulness [48]. Glutamatergic SLD neurons trigger REM sleep and muscle hypotonia [49] by activating glycinergic/GABAergic premotor neurons that are localized in the VM [50]. Our results revealed that HMNs are one of the major targets of both the VM and SLD, indicating that the activity of HMNs is affected by these nuclei across sleep–wake states. This finding contributes to clarifying the mechanism for lingual muscle tone being at its lowest during REM sleep in OSA patients.

The PZ is located in the medulla oblongata and is lateral and dorsal to the facial nerve. The GABAergic PZ has been identified as a medullary slow-wave sleep-promoting center [51–53], and here we found that the PZ projected directly to HMNs. This may be related to the decreased activity of HMNs during NREM sleep. In addition, we found that other regions known to be involved in sleep–wake regulation such as the PB, PAG, DR, and hypothalamus sent few afferents to HMNs. Hence, these regions may participate in the regulation of HMN activity, along with modulating sleep–wake states.

In summary, we have comprehensively mapped the monosynaptic afferents to HMNs and provide a new perspective for exploring the circuit mechanisms underlying the modulation of HMNs. Unexpectedly, we revealed for the first time that the CeA and the hypothalamus

innervate HMNs directly and also provided evidence for other neural pathways that may be involved in the regulation of HMN activity during respiration and different sleep–wake states. Therefore, our data provide an anatomical basis for the treatment of diseases caused by HMN dysfunction.

**Acknowledgements** This work was supported by the National Natural Science Foundation of China (31530035, 81420108015, 31671099, 31871072, 81570081, 81770083 and 31971110); the National Basic Research Development Program of China (2015CB856401); the Program for Shanghai Outstanding Academic Leaders (to ZLH), the Shanghai Municipal Science and Technology Major Project (2018SHZDZX01), and the National Key Research and Development Program of China (2018YFC1313600).

**Conflict of interest** The authors claim that there are no conflicts of interest.

**Open Access** This article is licensed under a Creative Commons Attribution 4.0 International License, which permits use, sharing, adaptation, distribution and reproduction in any medium or format, as long as you give appropriate credit to the original author(s) and the source, provide a link to the Creative Commons licence, and indicate if changes were made. The images or other third party material in this article are included in the article's Creative Commons licence, unless indicated otherwise in a credit line to the material. If material is not included in the article's Creative Commons licence and your intended use is not permitted by statutory regulation or exceeds the permitted use, you will need to obtain permission directly from the copyright holder. To view a copy of this licence, visit <http://creativecommons.org/licenses/by/4.0/>.

## References

1. Aldes LD. Subcompartmental organization of the ventral (protruder) compartment in the hypoglossal nucleus of the rat. *J Comp Neurol* 1995, 353: 89–108.
2. Altschuler SM, Bao X, Miselis RR. Dendritic architecture of hypoglossal motoneurons projecting to extrinsic tongue musculature in the rat. *J Comp Neurol* 1994, 342: 538–550.
3. Berger AJ, Bayliss DA, Bellingham MC, Umemiya M, Viana F. Postnatal development of hypoglossal motoneuron intrinsic properties. *Adv Exp Med Biol* 1995, 381: 63–71.
4. Fregosi RF. Respiratory related control of hypoglossal motoneurons—knowing what we do not know. *Respir Physiol Neurobiol* 2011, 179: 43–47.
5. Sokoloff AJ. Topographic segregation of genioglossus motoneurons in the neonatal rat. *Neurosci Lett* 1993, 155: 102–106.
6. Kinney HC. Brainstem mechanisms underlying the sudden infant death syndrome: evidence from human pathologic studies. *Dev Psychobiol* 2009, 51: 223–233.
7. Horner RL. Motor control of the pharyngeal musculature and implications for the pathogenesis of obstructive sleep apnea. *Sleep* 1996, 19: 827–853.
8. Horton GA, Fraigne JJ, Torontali ZA, Snow MB, Lapierre JL, Liu H, *et al.* Activation of the hypoglossal to tongue musculature motor pathway by remote control. *Sci Rep* 2017, 7: 45860.
9. Horner RL. Emerging principles and neural substrates underlying tonic sleep-state-dependent influences on respiratory motor activity. *Philos Trans R Soc Lond B Biol Sci* 2009, 364: 2553–2564.
10. Zhang GH, Liu ZL, Zhang BJ, Geng WY, Song NN, Zhou W, *et al.* Orexin A activates hypoglossal motoneurons and enhances genioglossus muscle activity in rats. *Br J Pharmacol* 2014, 171: 4233–4246.
11. Liu ZL, Wu X, Luo YJ, Wang L, Qu WM, Li SQ, *et al.* Signaling mechanism underlying the histamine-modulated action of hypoglossal motoneurons. *J Neurochem* 2016, 137: 277–286.
12. Fay RA, Norgren R. Identification of rat brainstem multisynaptic connections to the oral motor nuclei using pseudorabies virus. III. Lingual muscle motor systems. *Brain Res Brain Res Rev* 1997, 25: 291–311.
13. Rukhadze I, Kubin L. Mesopontine cholinergic projections to the hypoglossal motor nucleus. *Neurosci Lett* 2007, 413: 121–125.
14. Borke RC, Nau ME, Ringler RL, Jr. Brain stem afferents of hypoglossal neurons in the rat. *Brain Res* 1983, 269: 47–55.
15. Travers JB, Rinaman L. Identification of lingual motor control circuits using two strains of pseudorabies virus. *Neuroscience* 2002, 115: 1139–1151.
16. Wickersham IR, Finke S, Conzelmann KK, Callaway EM. Retrograde neuronal tracing with a deletion-mutant rabies virus. *Nat Methods* 2007, 4: 47–49.
17. Gong S, Doughty M, Harbaugh CR, Cummins A, Hatten ME, Heintz N, *et al.* Targeting Cre recombinase to specific neuron populations with bacterial artificial chromosome constructs. *J Neurosci* 2007, 27: 9817–9823.
18. Rossi J, Balthasar N, Olson D, Scott M, Berglund E, Lee CE, *et al.* Melanocortin-4 receptors expressed by cholinergic neurons regulate energy balance and glucose homeostasis. *Cell Metab* 2011, 13: 195–204.
19. Taniguchi H, He M, Wu P, Kim S, Paik R, Sugino K, *et al.* A resource of Cre driver lines for genetic targeting of GABAergic neurons in cerebral cortex. *Neuron* 2011, 71: 995–1013.
20. Zhang Z, Wang HJ, Wang DR, Qu WM, Huang ZL. Red light at intensities above 10 lx alters sleep–wake behavior in mice. *Light Sci Appl* 2017, 6: e16231.
21. Chen ZK, Yuan XS, Dong H, Wu YF, Chen GH, He M, *et al.* Whole-brain neural connectivity to lateral pontine tegmentum GABAergic neurons in mice. *Front Neurosci* 2019, 13: 375.
22. Yuan XS, Wei HH, Xu W, Wang L, Qu WM, Li RX, *et al.* Whole-brain monosynaptic afferent projections to the cholecystokinin neurons of the suprachiasmatic nucleus. *Front Neurosci* 2018, 12: 807.
23. Hu R, Jin S, He X, Xu F, Hu J. Whole-brain monosynaptic afferent inputs to basal forebrain cholinergic system. *Front Neuroanat* 2016, 10: 98.
24. Chen L, Yin D, Wang TX, Guo W, Dong H, Xu Q, *et al.* Basal forebrain cholinergic neurons primarily contribute to inhibition of electroencephalogram delta activity, rather than inducing behavioral wakefulness in mice. *Neuropsychopharmacology* 2016, 41: 2133–2146.
25. Luo YJ, Li YD, Wang L, Yang SR, Yuan XS, Wang J, *et al.* Nucleus accumbens controls wakefulness by a subpopulation of neurons expressing dopamine D1 receptors. *Nat Commun* 2018, 9: 1576.
26. Franklin KBJ, Paxinos G. *Mouse Brain Atlas in Stereotaxic Coordinates*, Compact 2nd Edition. San Diego, CA: Academic Press, 2001.
27. Wilensky AE, Schafe GE, Kristensen MP, LeDoux JE. Rethinking the fear circuit: the central nucleus of the amygdala is required for the acquisition, consolidation, and expression of Pavlovian fear conditioning. *J Neurosci* 2006, 26: 12387–12396.
28. Han W, Tellez LA, Rangel MJ, Jr., Motta SC, Zhang X, Perez IO, *et al.* Integrated control of predatory hunting by the central nucleus of the amygdala. *Cell* 2017, 168: 311–324.

29. Snow MB, Fraigne JJ, Thibault-Messier G, Chuen VL, Thomasian A, Horner RL, *et al.* GABA cells in the central nucleus of the amygdala promote cataplexy. *J Neurosci* 2017, 37: 4007–4022.
30. Burgess CR, Oishi Y, Mochizuki T, Peever JH, Scammell TE. Amygdala lesions reduce cataplexy in orexin knock-out mice. *J Neurosci* 2013, 33: 9734–9742.
31. He F, Ai H, Wang M, Wang X, Geng X. Altered neuronal activity in the central nucleus of the amygdala induced by restraint water-immersion stress in rats. *Neurosci Bull* 2018, 34: 1067–1076.
32. Van Daele DJ, Fazan VP, Agassandian K, Cassell MD. Amygdala connections with jaw, tongue and laryngo-pharyngeal premotor neurons. *Neuroscience* 2011, 177: 93–113.
33. Yamashita T, Yamanaka A. Lateral hypothalamic circuits for sleep-wake control. *Curr Opin Neurobiol* 2017, 44: 94–100.
34. Stuber GD, Wise RA. Lateral hypothalamic circuits for feeding and reward. *Nat Neurosci* 2016, 19: 198–205.
35. Burbidge S, Stewart I, Placzek M. Development of the neuroendocrine hypothalamus. *Compr Physiol* 2016, 6: 623–643.
36. Barbier M, Chometton S, Peterschmitt Y, Fellmann D, Risold PY. Paraventricular and calbindin nuclei in the posterior lateral hypothalamus are the major hypothalamic targets for projections from the central and anterior basomedial nuclei of the amygdala. *Brain Struct Funct* 2017, 222: 2961–2991.
37. Chometton S, Pedron S, Peterschmitt Y, Van Waes V, Fellmann D, Risold PY. A premammillary lateral hypothalamic nuclear complex responds to hedonic but not aversive tastes in the male rat. *Brain Struct Funct* 2016, 221: 2183–2208.
38. Stanek Et, Cheng S, Takatoh J, Han BX, Wang F. Monosynaptic premotor circuit tracing reveals neural substrates for oro-motor coordination. *Elife* 2014, 3: e02511.
39. Travers JB, Yoo JE, Chandran R, Herman K, Travers SP. Neurotransmitter phenotypes of intermediate zone reticular formation projections to the motor trigeminal and hypoglossal nuclei in the rat. *J Comp Neurol* 2005, 488: 28–47.
40. Travers JB, Norgren R. Afferent projections to the oral motor nuclei in the rat. *J Comp Neurol* 1983, 220: 280–298.
41. Yamamoto T. Brain regions responsible for the expression of conditioned taste aversion in rats. *Chem Senses* 2007, 32: 105–109.
42. Remmers JE, deGroot WJ, Sauerland EK, Anch AM. Pathogenesis of upper airway occlusion during sleep. *J Appl Physiol Respir Environ Exerc Physiol* 1978, 44: 931–938.
43. Yang CF, Feldman JL. Efferent projections of excitatory and inhibitory preBotzinger Complex neurons. *J Comp Neurol* 2018, 526: 1389–1402.
44. Lindsey BG, Nuding SC, Segers LS, Morris KF. Carotid bodies and the integrated cardiorespiratory response to hypoxia. *Physiology (Bethesda)* 2018, 33: 281–297.
45. Reddy MK, Patel KP, Schultz HD. Differential role of the paraventricular nucleus of the hypothalamus in modulating the sympathoexcitatory component of peripheral and central chemoreflexes. *Am J Physiol Regul Integr Comp Physiol* 2005, 289: R789–R797.
46. Fukushi I, Yokota S, Okada Y. The role of the hypothalamus in modulation of respiration. *Respir Physiol Neurobiol* 2019, 265: 172–179.
47. Horner RL. Respiratory motor activity: influence of neuromodulators and implications for sleep disordered breathing. *Can J Physiol Pharmacol* 2007, 85: 155–165.
48. Weber F, Chung S, Beier KT, Xu M, Luo L, Dan Y. Control of REM sleep by ventral medulla GABAergic neurons. *Nature* 2015, 526: 435–438.
49. Boissard R, Gervasoni D, Schmidt MH, Barbagli B, Fort P, Luppi PH. The rat ponto-medullary network responsible for paradoxical sleep onset and maintenance: a combined microinjection and functional neuroanatomical study. *Eur J Neurosci* 2002, 16: 1959–1973.
50. Luppi PH, Clement O, Sapin E, Gervasoni D, Peyron C, Leger L, *et al.* The neuronal network responsible for paradoxical sleep and its dysfunctions causing narcolepsy and rapid eye movement (REM) behavior disorder. *Sleep Med Rev* 2011, 15: 153–163.
51. Anacleit C, Lin JS, Vetrivelan R, Krenzer M, Vong L, Fuller PM, *et al.* Identification and characterization of a sleep-active cell group in the rostral medullary brainstem. *J Neurosci* 2012, 32: 17970–17976.
52. Anacleit C, Ferrari L, Arrigoni E, Bass CE, Saper CB, Lu J, *et al.* The GABAergic parafacial zone is a medullary slow wave sleep-promoting center. *Nat Neurosci* 2014, 17: 1217–1224.
53. Su YT, Gu MY, Chu X, Feng X, Yu YQ. Whole-brain mapping of direct inputs to and axonal projections from GABAergic neurons in the parafacial zone. *Neurosci Bull* 2018, 34: 485–496.



# Plasticity of Sniffing Pattern and Neural Activity in the Olfactory Bulb of Behaving Mice During Odor Sampling, Anticipation, and Reward

Penglai Liu<sup>1</sup> · Tiantian Cao<sup>1</sup> · Jinshan Xu<sup>1</sup> · Xingfeng Mao<sup>1</sup> · Dejuan Wang<sup>1</sup> · Anan Li<sup>1</sup>

Received: 12 August 2019 / Accepted: 15 October 2019 / Published online: 27 January 2020  
© Shanghai Institutes for Biological Sciences, CAS 2020

**Abstract** The olfactory bulb (OB) is the first relay station in the olfactory system. In the OB, mitral/tufted cells (M/Ts), which are the main output neurons, play important roles in the processing and representation of odor information. Recent studies focusing on the function of M/Ts at the single-cell level in awake behaving mice have demonstrated that odor-evoked firing of single M/Ts displays transient/long-term plasticity during learning. Here, we tested whether the neural activity of M/Ts and sniffing patterns are dependent on anticipation and reward in awake behaving mice. We used an odor discrimination task combined with *in vivo* electrophysiological recordings in awake, head-fixed mice, and found that, while learning induced plasticity of spikes and beta oscillations during odor sampling, we also found plasticity of spikes, beta oscillation, sniffing pattern, and coherence between sniffing and theta oscillations during the periods of anticipation and/or reward. These results indicate that the activity of M/Ts plays important roles not only in odor representation but also in salience-related events such as anticipation and reward.

**Keywords** Olfactory bulb · *In vivo* electrophysiological recording · Go/no-go · Odor representation

Penglai Liu and Tiantian Cao have contributed equally to this work.

**Electronic supplementary material** The online version of this article (<https://doi.org/10.1007/s12264-019-00463-9>) contains supplementary material, which is available to authorized users.

✉ Anan Li  
anan.li@xzhmu.edu.cn

<sup>1</sup> Jiangsu Key Laboratory of Brain Disease and Bioinformatics, Research Center for Biochemistry and Molecular Biology, Xuzhou Medical University, Xuzhou 221004, China

## Introduction

As the sensory system that detects chemicals in the environment, olfaction is crucial for survival. Importantly, olfactory dysfunction is common in many neurodegenerative diseases including Parkinson's disease [1–3]. The olfactory bulb (OB) is one of the most important odor information-processing centers in the olfactory system. It receives direct axonal input from the olfactory sensory neurons that express olfactory receptors and interact directly with odorants [4]. The OB is critically involved in the representation of many aspects of an odor, including its identity, intensity, duration, and other timing information [4–7]. While the OB sends this information to higher centers such as the anterior olfactory nucleus and piriform cortex *via* mitral/tufted cells (M/Ts), which are the main output neurons of the OB, it also receives extensive feedback and centrifugal inputs [4, 8]. For example, cholinergic, serotonergic, and noradrenergic innervation are extensive in the OB [9–11]. Since these modulatory systems play important roles in learning and memory and the plasticity of neurons in many brain areas, the odor representation by the OB is likely to be dramatically plastic and dependent on learning and task demands [12–17].

As an important olfactory center, the OB contains neurons that respond to odors by increasing or decreasing their firing rate in both anesthetized and awake states [18–21]. Interestingly, in awake behaving rodents, some neurons in the OB change their firing dramatically in response to other odor-related events such as light-on and a water reward but not the odor stimulus [22]. These findings indicate that the neural activity of OB neurons is rather complex, since it might carry key information not only on odor but also about internal brain states such as anticipation and reward. Unfortunately, the excellent pioneering work

did not explore this important issue intensively and only very few responsive units were recorded [22]. Importantly, other than single units, local field potentials (LFPs), and sniffing signals that play key roles in olfactory perception [13, 23, 24], might also be plastic and dependent on behavioral context during an odor discrimination task within and/or outside the odor-sampling period. However, direct evidence is still lacking.

Here, we tested whether the sniffing pattern and neural activity in the OB show learning-dependent plasticity during odor sampling, anticipation, and water reward when the mice perform a go/no-go odor discrimination task in a head-fixed state. We found that while some of these critical signals showed learning-dependent plasticity during odor sampling, other signals showed such plasticity during anticipation and/or reward.

## Materials and Methods

### Animals

Eleven male C57BL/6J mice (8–16 weeks old) were housed in a vivarium under a 12/12 light/dark cycle with lights on at 08:00. Experiments were performed during the light cycle. Food and water were available *ad libitum* except during the behavioral procedure when water could be received in the experimental chamber. All experimental procedures were carried out in accordance with protocols approved by the Xuzhou Medical University Institutional Animal Care and Use Committee.

### Implantation of Tetrodes

As in previous studies [25], mice were briefly anesthetized with pentobarbital (0.09 mg/g body weight, *i.p.*). Then, after the mouse was mounted in a stereotaxic frame, the fur on the scalp from the midline of the orbits to the midpoint between the ears was removed. A hole was drilled above the right OB (AP, 4.0 mm; ML, 1.0 mm) for the implantation of tetrodes.

For single-cell spiking and LFP recordings, tetrodes were implanted into the OB. Each tetrode consisted of four polyimide-coated nichrome wires (RO-800, Sandvik AB, Sandviken, Sweden), which were connected to a 16-channel electrode interface board (EIB-16, Neuralynx Inc.). The tetrodes were lowered to the mitral cell layer at an average depth between 1.8 mm and 2.0 mm [13, 20]. One stainless-steel screw, which was connected to ground as the reference electrode, was inserted into the bone (1 mm posterior to bregma and 1 mm from the midline). To ensure optimal placement of the tetrodes, spiking recordings were made during implantation. The signals recorded from the

tetrodes were amplified (Plexon DigiAmp; bandpass, 1 Hz–5000 Hz, 2000 × gain), and sampled at 40 kHz by a Plexon Omniplex recording system. The tetrodes were finally sealed to the bone by dental acrylic. To fit the mice for the head-fixed recording system, an aluminum head plate was attached to the skull with two screws and dental cement.

### Spike and LFP Recordings

After at least 7 days of recovery from the surgery, recordings were performed in the awake, head-fixed mice. The mice were head-fixed with two horizontal bars and were able to maneuver on a head-fixed go/no-go system (Thinkerbiotech, Nanjing, China). The procedure for spike recordings was similar to that for recordings made during the tetrode implantation described above. For LFP recordings, the signals were amplified (2000 × gain; Plexon DigiAmp), filtered at 0.1 Hz–300 Hz, and sampled at 1 kHz. Spikes or LFP signals along with other event markers, including odor stimulation and licking, were recorded *via* the same Plexon Omniplex recording system.

### Sniffing Measurement

We implanted a cannula into one nasal cavity and connected it to a pressure sensor [Model No. 24PCEFA6-G(EA), 0 psi–0.5 psi; Honeywell] to measure sniffing. Implantation of the cannula was performed as in previous studies [5, 13, 20]. The pressure transients were amplified (100 × gain, Plexon DigiAmp) and sampled at 1 kHz by the Plexon Omniplex recording system. Each sniff was detected at the point of transition from exhalation to inhalation.

### Odor Presentation

The odors were presented by an odor delivery system (Thinkerbiotech). Four odor pairs, isoamyl acetate *vs* 2-heptanone, phenyl acetate *vs* benzaldehyde, acetophenone *vs* octyl aldehyde, and 1-nonanol *vs* 2-undecanone (Sinopharm Chemical Reagent Co., Shanghai, China) were used. All odorants were dissolved in mineral oil at 1% *v/v* dilution. During the odor delivery period, a stream of nitrogen at 100 mL/min flowed over the odor oil, and then was diluted to 1/20 by an olfactometer. Charcoal-filtered air at a constant rate of 1 L/min was delivered to the nose of the mouse to eliminate the effect of airflow.

### The Go/No-go Behavioral Tasks

After the mice recovered from surgery for at least 1 week, they underwent a series of behavioral tasks. The water

supply was removed from the mouse's cage and the behavioral training began two days later if the weight of the mouse was 80%–85% of that before deprivation. Mice were trained to perform the go/go task before the go/no-go task. During the go/go task, mice learned to lick a tube to get a drop of water (20  $\mu$ L) when either of the odor pair was present. Then the mice began to perform the go/no-go task in which they had to discriminate the two odors correctly to receive a water reward [13, 20]. The mice had to lick the tube when a rewarded odor (S+) was presented and not to lick when the unrewarded odor (S-) was presented. According to the responses of the mice to the odor presentation, if an S+ was presented and the mouse responded with licking (Hit), the water reward was delivered through the lickport; if they did not lick with the S+ (Miss), or the S- was delivered, no water reward was given regardless of the mouse's actions (false alarm [FA] or correct rejection [CR], see Fig. 1C). Thus, Hit and CR were correct trials, and Miss and FA were incorrect trials. The electrophysiological signals and sniffing signals were simultaneously recorded during all tasks.

### Data Analysis

For the go/no-go task, the performance of mice was calculated on each training day (one session). Further analysis was evaluated in blocks of 20 trials and the

behavioral performance of each block was calculated separately. Usually mice performed 6–10 blocks in each session (Fig. 1D).

For offline spike sorting and statistics of single-cell spiking data, similar to previous studies, single units were sorted and identified by principal component analysis with Offline Sorter V4 software (Plexon) [20, 25, 26]. To generate peristimulus time histograms, the spikes 3 s before and 7 s after the odor stimulation in each trial were extracted and the spike firing rate was averaged with a bin-width of 100 ms. The spontaneous firing rate (2 s before odor stimulation) and the odor-evoked firing rate (during the 2 s odor stimulation) were calculated by averaging the spikes during the 2 s periods. We used multivariate permutation tests to determine whether an odor evoked a significant response. Excitatory, inhibitory, and non-responses were classified based on the *P* values and comparison of the firing rate between baseline and the odor-evoked response.

For analysis of LFP signals, a program written in MatLab (The MathWorks) was used. Similar to previous studies [1, 13, 25, 27], we divided LFP signals into 4 frequency bands: theta (2 Hz–12 Hz), beta (15 Hz–35 Hz), low gamma (36 Hz–65 Hz), and high gamma (66 Hz–95 Hz). However, we only focused on the beta and high gamma bands for further analysis since odors usually evoke strong and reliable responses within these two frequency

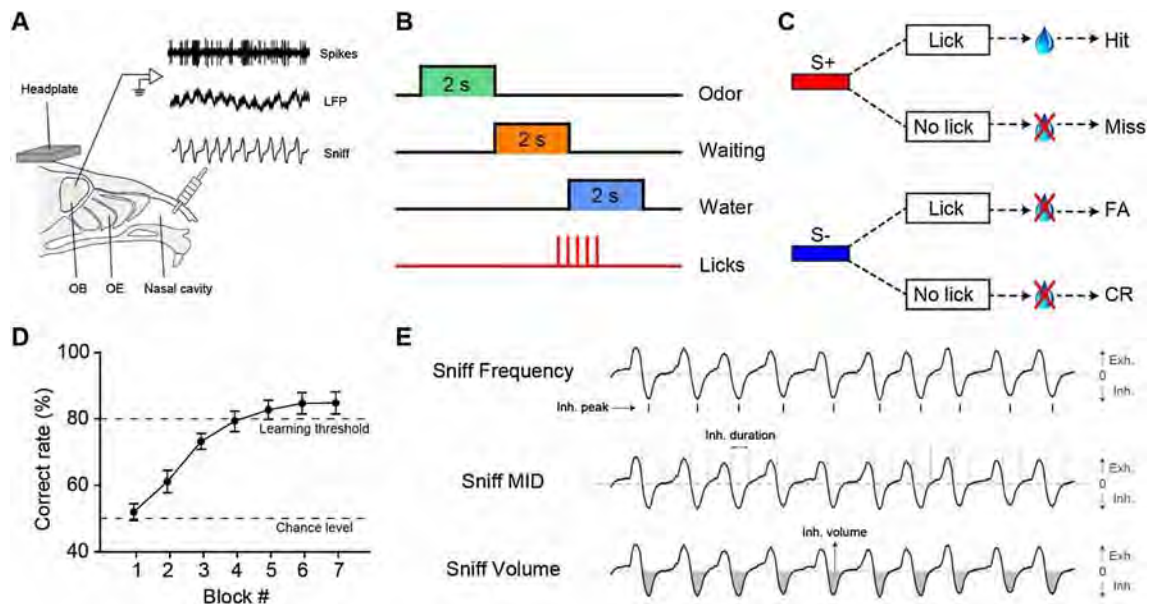


**Fig. 1** Paradigm for data recording and behavioral task. **A** Diagram of the recording setup for spikes, LFPs, and sniffs (OB, olfactory bulb; OE, olfactory epithelium; LFP, local field potential). **B** Schematic of the go/no-go task sequence. An odor is applied for 2 s followed by 2 s waiting time and then the water reward is given. **C** Trial structure of the go/no-go task (FA, false alarm; CR, correct rejection). **D** The odor discrimination performance during the go/no-go task across all

sessions ( $n = 13$  animal-odor pairs from 6 mice). The mean correct response across sessions is plotted for each block (20 trials). The chance level and learning threshold are indicated by dashed lines. Data are presented as the mean  $\pm$  SEM. **E** Diagrams showing extraction of sniffing frequency, mean inhalation duration (MID), and inhalation (Inh.) volume from example nasal flow trace.

bands [1, 25]. For odor-evoked responses, the data 4 s prior to and 8 s after the onset of odor stimulation were selected for further analysis. Spectral power was computed using the MatLab wavelet method, *cwt*, with Morlet wavelets. For each trial, the baseline was normalized to 1, and all the trials for each odor were averaged for further analysis.

To test the significance of differences between learning and learned (proficient) states, the Shapiro–Wilk test was first used to determine whether samples had a normal distribution. In the case of a normal distribution, the paired *t*-test was applied; in the case of a non-normal distribution, the Wilcoxon signed ranks test was used.

## Results

### Sniffing Pattern Shows Plasticity in the Water Reward Period During the Learning Process of the Go/No-go Task

The go/no-go task is extensively used as an olfactory discrimination model in rodents [13, 20, 28, 29]. During this task, animals usually sample the odors for 2 s and a water reward is obtained at the end of the odor delivery if the mice lick for the rewarded odor. This experimental design is sufficient for studying odor representation and reward; however, there is no clear time window in which to study anticipation. Thus, we inserted a 2 s waiting time between odor stimulation and water reward (Fig. 1A–C) and this waiting time represented anticipation by the mice if they expected a reward during this trial. During the task, the sniffing and neural activity from the OB, including spikes from single units and LFPs were recorded (Fig. 1A). In general, mice took  $\sim 5$  blocks (100 trials) to learn to discriminate the odors ( $> 80\%$  correct, Fig. 1D). To investigate how sniffing signals changed during the go/no-go task, we analyzed different aspects of the signals: sniffing frequency, mean inhalation duration (MID), and volume (Fig. 1E).

Representative sniffing signals during the go/no-go task are shown in Fig. 2A. For both learning ( $< 80\%$  correct, left) and proficient ( $> 80\%$  correct, right) states, the sniffing frequency began to increase at the late stage of odor stimulation, peaked during the waiting period, and then began to recover (Fig. 2B). Interestingly, in the learning state, S+ and S– trials showed similar sniffing frequencies during the odor stimulation and water reward periods but showed significantly different sniffing frequencies during the waiting period (Fig. 2B, left and Table S1). However, in the proficient state, S+ and S– trials only showed similar sniffing frequencies during the odor stimulation period and showed significantly different

sniffing frequencies during both the waiting and reward periods (Fig. 2B, right and Table S1).

Besides sniffing frequency, we also analyzed sniffing MID and volume, which are critical parameters of the pattern. Corresponding to sniffing frequency, the MID and volume began to decrease in the late stage of odor stimulation, descended to a trough during the waiting period, and then began to recover (Fig. 2C, D) in both the learning and proficient states. Similar to the results for sniffing frequency, S+ and S– trials showed significantly different MIDs during the waiting period (Fig. 2C, left, Table S2) in the learning stage and during the waiting and reward periods in the proficient stage (Fig. 2C, right, Table S2). However, for sniffing volume, S+ and S– trials only showed a significant difference during the reward period in the proficient state and not at any period in the learning state (Fig. 2D, Table S3). All together, these results indicate that the patterns of the sniffing signals are modulated in the reward period depending on the learning process of the go/no-go task.

During the go/no-go task, the learning state occurred in early trials while the proficient state occurred late in the session (Fig. 1D). This raises the question of whether the difference in the reward period between these behavioral states is due to general behavioral state differences such as thirst. To address this question, we analyzed the data focusing on S+ and S– during the early trials (first 30 trials) and the late trials (last 30 trials) of the go/go task where animals also received water and become satiated (see Materials and Methods). The sniffing signals in all the periods were similar for the odor 1 and odor 2 trials during both the early and late trials (Fig. 2E). Further analysis indicated that although the sniffing signals changed during different periods and these also occurred in the go/no-go task, no significant difference was found between odors 1 and 2 during any period, or in either early or late trials (Fig. 2F–H). Therefore, the change in sniffing pattern during the go/no-go task is established by learning-related plasticity as opposed to behavioral states such as thirst that differ between the beginning and end of the session.

### Coherence Between Theta Oscillation and Sniffing in the Odor Sampling Period is Plastic During the Learning Process of the Go/No-go Task

The theta oscillation of the LFP recorded in the OB is strongly correlated with sniffing, and the correlation varies during different olfactory-related behaviors [13, 30, 31]. To test whether this correlation changed during the learning process of the go/no-go task, we recorded the sniffing signals and LFP signals simultaneously (Figs. 1A and 3A). In the learning state, the coherence between sniffing and theta oscillation showed no significant change during the

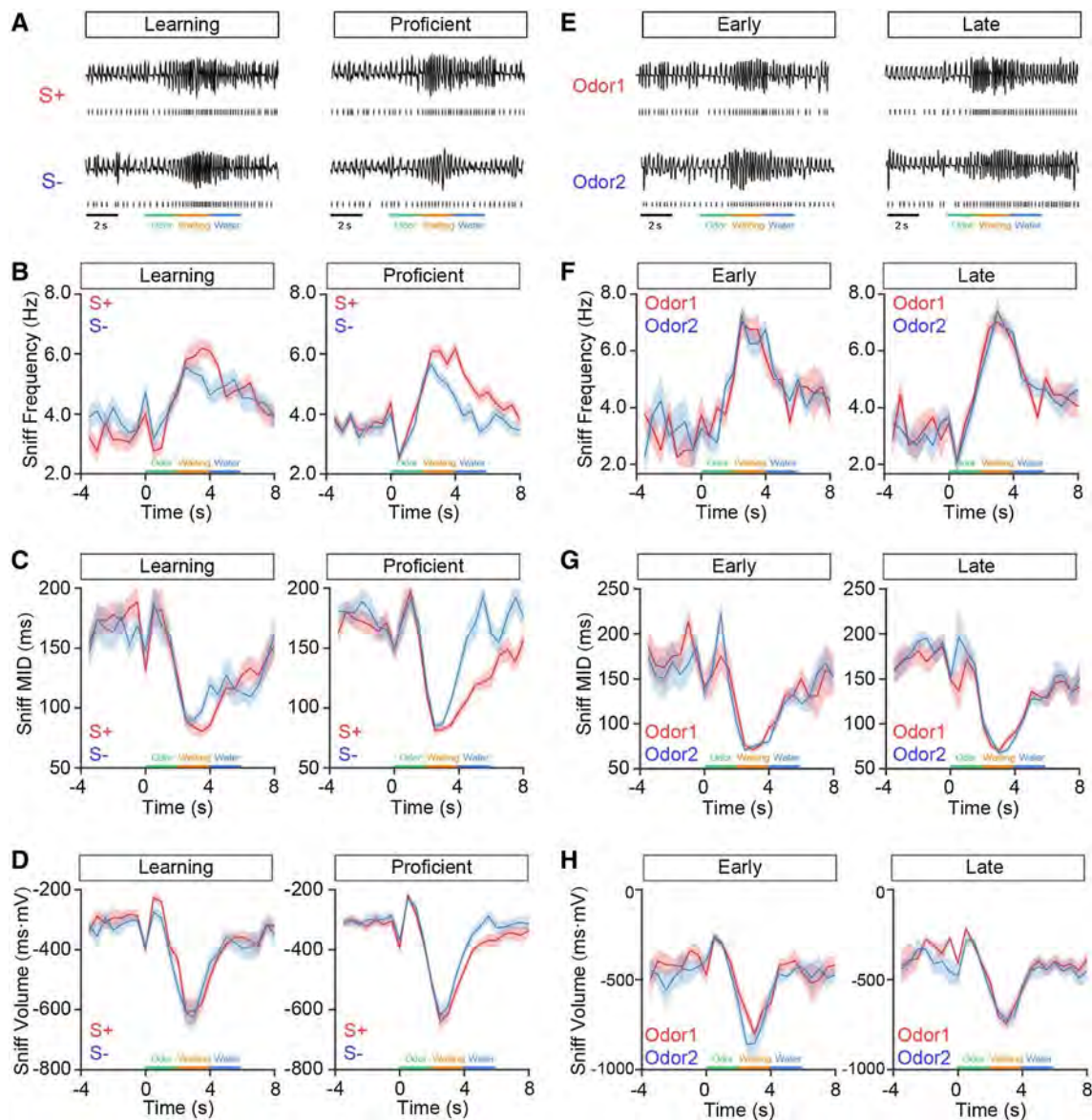


**Fig. 2** Sniffing pattern changes emerge across task learning. **A, E** Raw sniffing traces of responding to one odor pair (phenyl acetate vs 2-butanone) from a representative mouse during the go/no-go task (**A**) and the go/go task conditions (**E**) (S+ and Odor1, phenyl acetate; S– and odor2, 2-butanone). **B, F** Trial-averaged sniffing frequency to

one odor pair (phenyl acetate vs 2-butanone) from a representative mouse during the go/no-go task (**B**) and the go/go task conditions (**F**). **C, G** As for **B** and **F** but for mean inhalation duration (MID) of sniffing. **D, H** As for **B** and **F** but for sniffing volume. Data are presented as the mean  $\pm$  SEM.

odor stimulation, waiting, or reward period compared with baseline ( $-4$  s to  $0$  s, Fig. 3B, C, left; paired  $t$ -test,  $t = 0.77, 0.40,$  and  $-0.16$ ;  $P = 0.47, 0.70,$  and  $0.87$  for odor, waiting, and reward periods, respectively). However, in the proficient state, the coherence increased at the beginning of odor stimulation and then began to recover (Fig. 3B, C, right). Further comparison between S+ and S– trials showed no significant difference during any period in the learning stage (Fig. 3C, left, Table S4), but a significant difference was found during the odor period in the proficient state (Fig. 3C, right, Table S4). Moreover,

data from the go/go experiment showed that the coherence was neither significant between baseline and any event period nor between S+ and S– trials at an early or late state (Fig. 3D, E, Table S4). Thus, these results indicate that the coherence between theta oscillation and sniffing in the odor sampling period is plastic during the learning process of the go/no-go task.

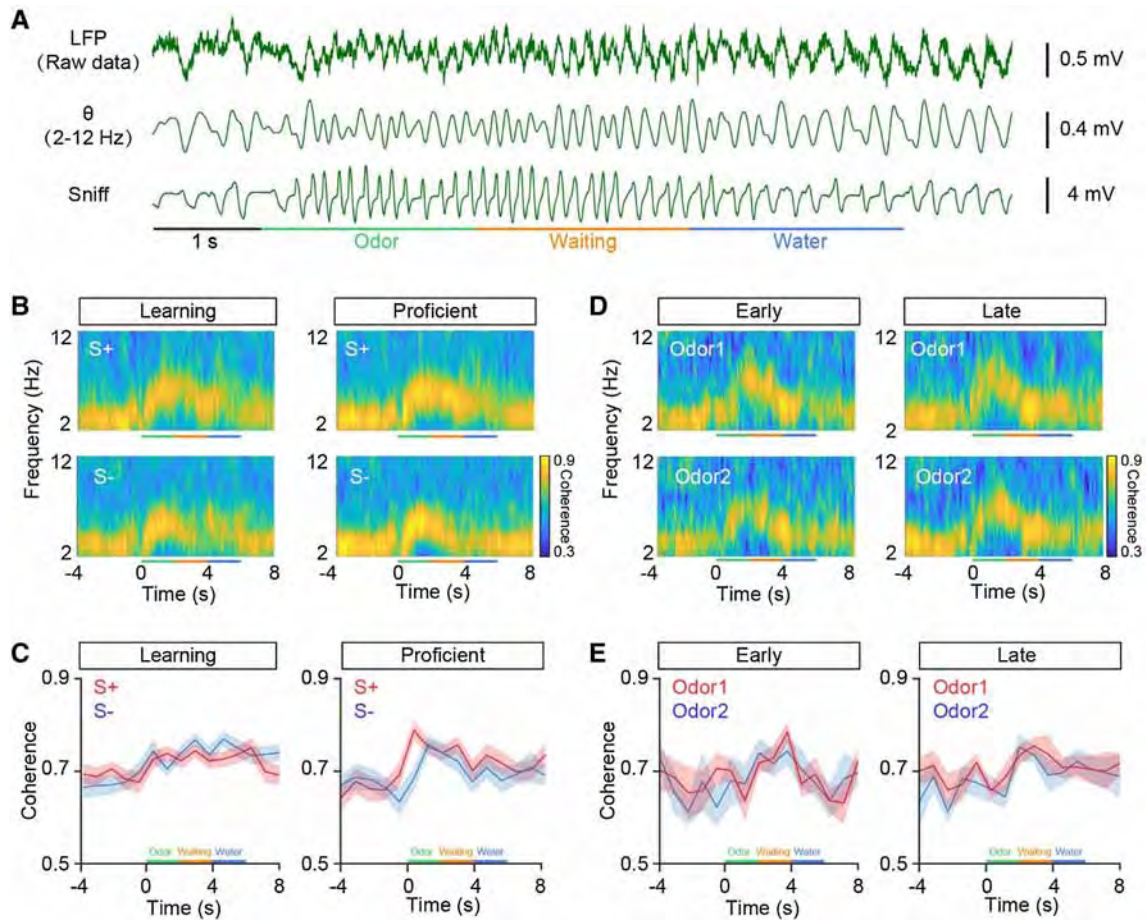


**Fig. 3** Coherence between sniffing and theta oscillations under go/no-go and go/go task conditions. **A** Raw traces (upper) and filtered theta (middle) oscillations of the LFP signals and sniff (lower) responses to one odor (phenyl acetate) from a representative mouse during the go/no-go task. **B, D** Coherence spectra between sniffing and theta oscillations responding to one odor pair (phenyl acetate vs

2-butanone) from a representative mouse during go/no-go (**B**) and go/go (**D**) task conditions (S+ and odor 1, phenyl acetate; S- and odor 2, 2-butanone). **C, E** Trial-averaged coherence between sniff and theta oscillations to one odor pair for example in **B** and **D**. Data are presented as the mean  $\pm$  SEM.

### Power of LFP Beta Oscillation Shows Plasticity for Anticipation and Reward During the Learning Process of the Go/No-go Task

In both anesthetized and awake rodents, odor evokes strong increases in beta oscillations in the OB [19, 25, 32, 33], and these oscillations are critically involved in olfactory learning and perception [34, 35]. Next, we explored whether the beta oscillations changed during learning of the go/no-go task. Similar to previous studies, we found that odor evoked increased responses during the odor stimulation (Fig. 4A, B). Generally, there was no significant difference between S+ and S- trials during any event period in the learning state, but significant differences were found during the waiting and reward periods in the proficient state (Fig. 4C, Table S5). Data from the go/go experiment showed that the power of beta oscillations did not significantly differ between S+ and S- trials during

any event period, either early or late (Fig. 4D–F, Table S5). Thus, these results indicate that the beta oscillation is plastic for the anticipation and reward during the learning process of the go/no-go task.

During the go/no-go task, for S+, the behavioral outputs were mainly Hits and there were few Miss trials (73/617, 11.8%), since we trained the mice to learn the go/go task before the go/no-go task. For S-, the behavioral outputs were FA and CR. However, FA and CR reflect anticipation differently, and the difference would be evident from the power of the LFP beta oscillation. Thus, we performed further analysis to compare the beta power for Hit, CR, and FA. We found that the beta power during the waiting period for Hit and FA trials, which represent anticipation, were similar, and were significantly stronger than CR trials, which represent no anticipation (Fig. S1). This result provides further evidence that the power of beta oscillation reflects anticipation.

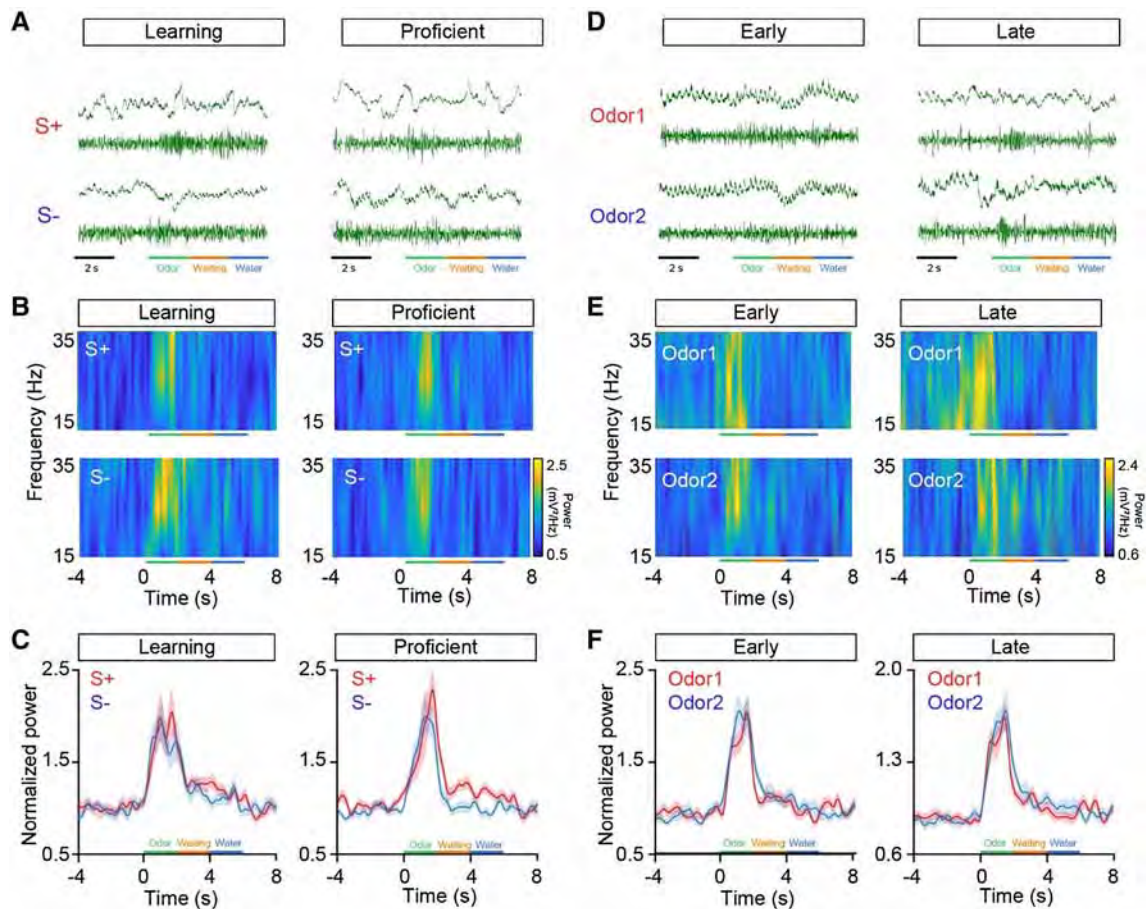


**Fig. 4** Odor-evoked beta responses under go/no-go and go/go task conditions. **A, D** Raw traces (upper) and filtered beta (lower) oscillations of LFP signals responding to one odor pair (phenyl acetate vs 2-butanone) from a representative mouse during the go/no-go (**A**) and go/go (**D**) task conditions (S+ and odor 1, phenyl acetate; S– and odor 2, 2-butanone). **B, E** Power spectra of beta responding to

one odor pair (phenyl acetate vs 2-butanone) from a representative mouse during the go/no-go (**B**) and go/go (**E**) task conditions (S+ and odor 1, phenyl acetate; S– and odor 2, 2-butanone). **C, F** Trial-averaged normalized power of beta responses to the odor pair in **B** and **E**. Data are presented as the mean  $\pm$  SEM.

### The Power of LFP Gamma Oscillation is Stable During the Learning Process of the Go/No-go Task

Besides beta oscillations, gamma oscillations also play important roles in olfactory learning [34, 35]. We then investigated whether the gamma oscillations changed during learning of the go/no-go task. Similar to previous studies in awake animals [32], we found that odor evoked dramatically decreased responses during odor stimulation (Fig. 5A, B). However, no significant difference between S+ and S– trials was found during any event period in either the learning or the proficient stage (Fig. 5B, C, Table S6). Data from the go/go experiment showed similar results (Fig. 5D–F, Table S6). Therefore, these data indicate that the gamma oscillation is stable and shows no plasticity for odor stimulation, anticipation, or reward during the learning process of the go/no-go task.

### The Firing of Single M/Ts Shows Plasticity in the Odor Sampling and Water Reward Periods During Learning of the Go/No-go Task

Finally, we recorded spikes from M/Ts, which are the major output neurons of the OB and play important roles in odor representation. Single M/T units were identified by tetrode recording (Fig. 6A). As in previous studies [13, 20], we recorded strong spontaneous firing of M/Ts, and odors evoked both excitatory and inhibitory responses (Fig. 6B). The proportions of each type of response during the learning and proficient states are shown in Fig. 6C. We then investigated whether the single cell firing changed during learning of the go/no-go task (Fig. 7A, B). Both S+ and S– evoked strong inhibitory responses during odor stimulation and the firing peaked in the waiting period in both the learning and proficient states (Fig. 7C, D). Interestingly, in the proficient state, there was a significant difference between S+ and S– during the odor sampling

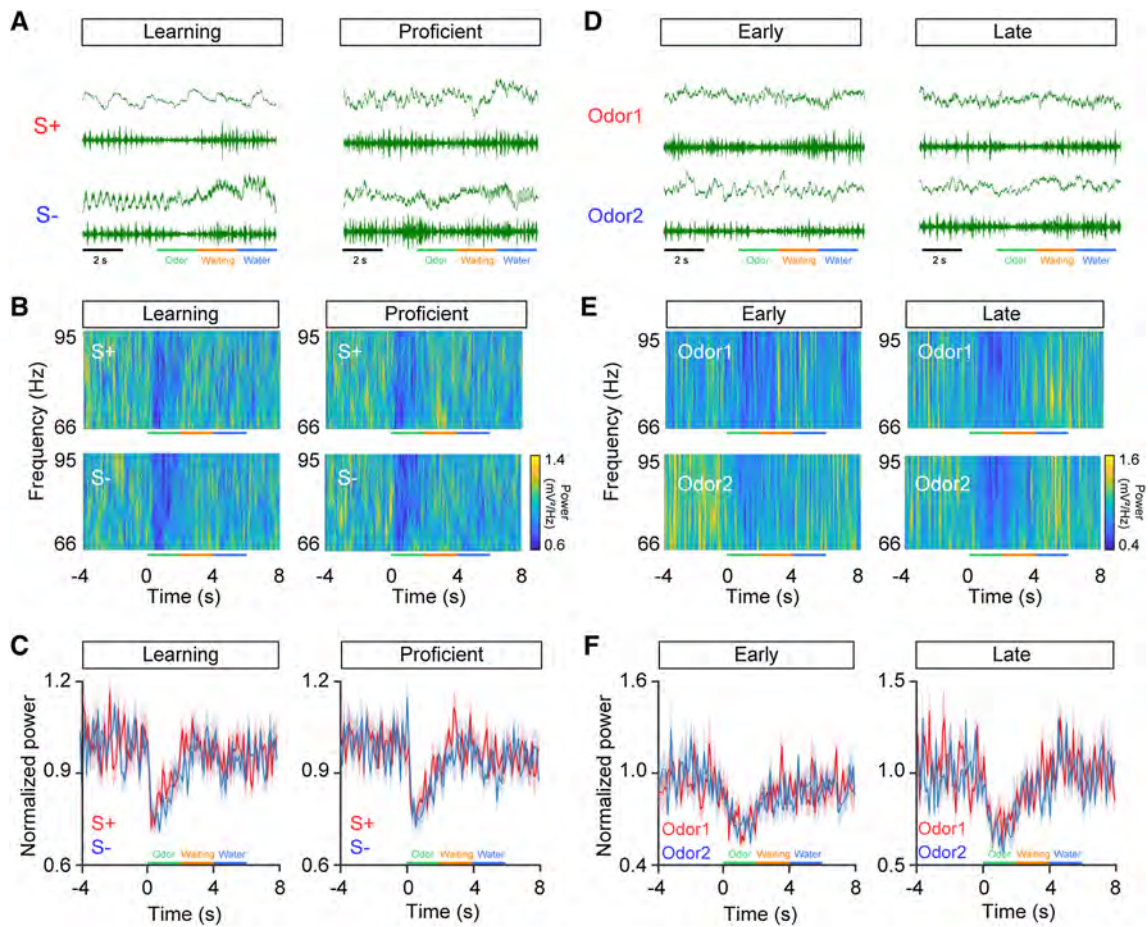


**Fig. 5** Odor-evoked high gamma responses under go/no-go and go/go task conditions. **A, D** Raw traces (upper) and filtered high gamma (lower) oscillations of the LFP signals responding to one odor pair (phenyl acetate vs 2-butanone) from a representative mouse during go/no-go (**A**) and go/go (**D**) task conditions (S+ and odor 1, phenyl acetate; S– and odor 2, 2-butanone). **B, E** Power spectra of high

gamma responding to one odor pair (phenyl acetate vs 2-butanone) from a representative mouse during go/no-go (**B**) and go/go (**E**) task conditions (S+ and odor 1, phenyl acetate; S– and odor 2, 2-butanone). **C, F** Trial-averaged normalized power of high gamma responses to the odor pair in **B** and **F**. Data are presented as the mean  $\pm$  SEM.

period across all the cell-odor pairs (Fig. 7E). No significant difference was found between S+ and S– during the waiting period in either the learning or proficient state (Fig. 7F). Similar to the odor sampling period, during the reward period there was a significant difference between S+ and S– across all the cell-odor pairs in the proficient state (Fig. 7G). These results indicate that the firing of single M/Ts is plastic for the odor response and the reward during the learning process of the go/no-go task. Data from the go/go experiment showed that the firing of single M/Ts did not significantly differ between S+ and S– trials during any event period either early or late (Fig. 7H–J).

## Discussion

The OB is the first relay station in the olfactory system; it receives direct input from the olfactory sensory neurons in which the olfactory receptors are located. However, recent studies in awake behaving rodents have demonstrated that the odor responses of the neurons in the OB are largely dependent on behavioral and brain states [4, 17, 36–39]. In the present study, we found that both the sniffing pattern and neural activity in the OB were plastic during the learning process. The plasticity not only occurred during odor sampling, which is correlated with olfactory information, but also occurred during the anticipation and reward periods. Specifically, learning-induced plasticity of single unit spikes and sniffing/theta oscillation coherence occurred during odor sampling; plasticity of beta oscillation, sniffing frequency, and MID occurred during anticipation of the reward; and plasticity of single unit spikes

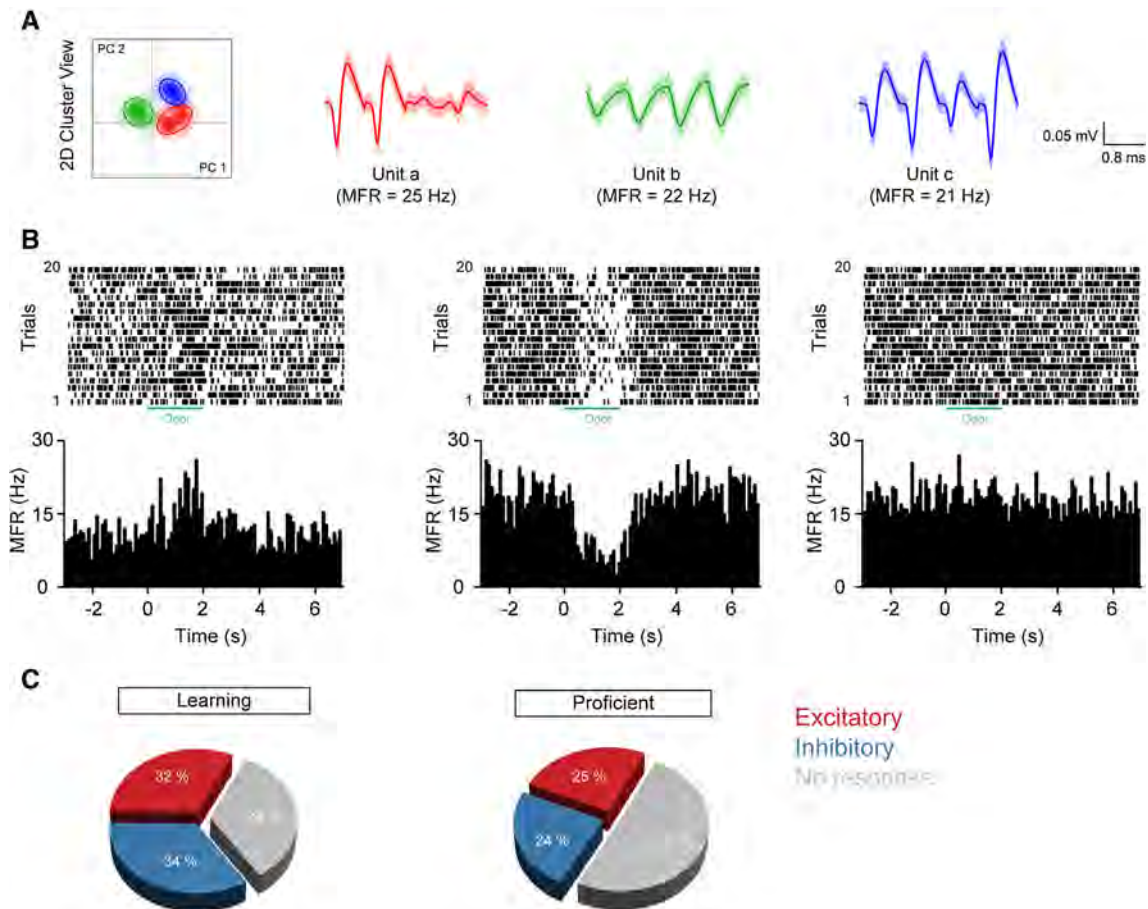


**Fig. 6** M/T spikes recorded from the OB of awake mice. **A** Example of spike sorting using principal component analysis scan clustering of extracellular voltage recordings by tetrodes, resulting in the separation of three units (a, b, and c). **B** Three examples of firing induced by one odor (phenyl acetate) during the go/go task. From left to right:

excitatory response, inhibitory response, and no response. Upper, raster plots; lower, peristimulus time histograms of the firing rate; green lines, odor stimulation (2 s). **C** Pie charts showing the percentages of excitatory (red), inhibitory (blue), or no response (gray) under the go/no-go task conditions.

and sniffing frequency, MID, and volume occurred during the water reward (Fig. 8). These findings provide direct evidence that signals such as single units, LFPs, and sniffing, which play key roles in olfactory perception, show plasticity and are behavioral context-dependent during an odor discrimination task within and/or outside the odor sampling period.

The go/no-go task was initially designed for free-moving rodents [28], and recently it has been extensively used in head-fixed mice [14, 17, 23, 40]. Odor-evoked LFP responses during the learning process of the go/no-go task have been investigated in many studies of free-moving but not head-fixed rodents [13, 32, 33, 41, 42]. Behavioral studies have reported similar odor-discrimination performance under these two conditions [43], indicating that the odor-processing strategy is similar in the two conditions. However, the neural activity may differ because of differences in behavioral status and the level of stress. Moreover, odor sampling is vastly different under the two

conditions since the sampling in the head-fixed state is relatively stable while in the free-moving state it is variable due to the movements of the mice [4]. Thus, it is not unexpected that the results from our study in the head-fixed state differ somewhat from previous studies in the free-moving state.

As regards the LFP, odor-evoked increases in beta response and decreases in gamma response were recorded both here and in previous studies [32, 34]. However, while the odor-evoked plasticity of both beta and gamma oscillations during the learning process has been found in previous studies [32], we only found that the beta but not the gamma oscillations were plastic during learning. This difference is likely due to the different behavioral conditions. Future studies are needed to test this by recording LFPs in mice that perform the go/no-go task in both free-moving and head-fixed states. Similar studies have compared the odor-evoked responses in different olfactory tasks (go/no-go vs 2-alternative choice) [42].

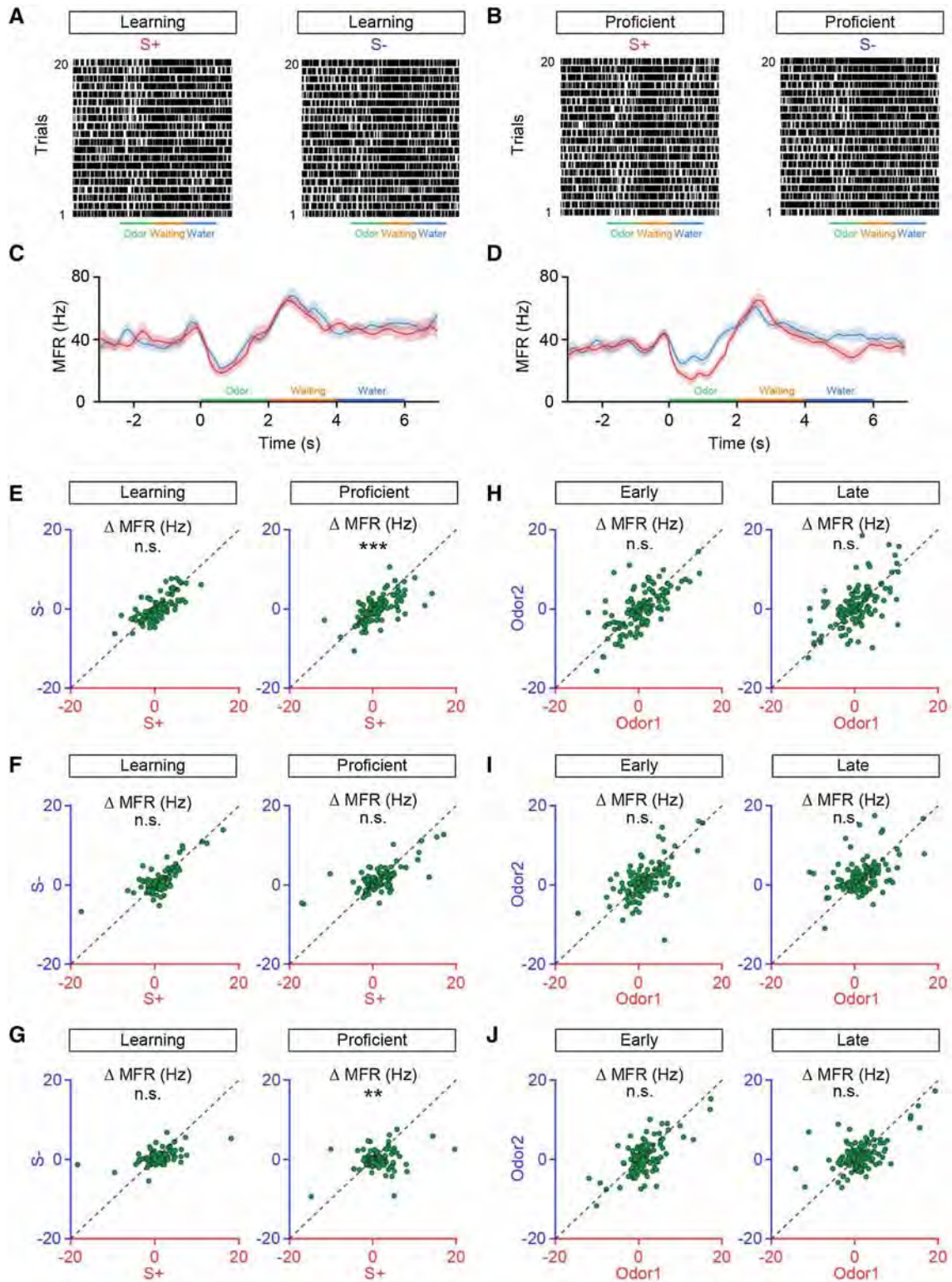


**Fig. 7** Learning-induced plasticity of spikes during the odor sampling and reward periods. **A, B** Raster plots of firing induced by S+ and S− in the learning state (**A**) and the proficient state (**B**) during the go/no-go task from a representative unit (S+, phenyl acetate; S−, 2-butanone). **C, D** Trial-averaged peristimulus time histograms for the example in **A** and **B**, smoothed by a Gaussian filter with a standard deviation of 1500 ms. **E** Comparison of the changes in mean firing rate ( $\Delta$ MFR) between S+ and S− in the learning state [left: paired *t*-test,  $P = 0.073$  ( $df = 118$ ,  $t = 1.810$ )] and the proficient state [right: paired *t*-test,  $***P < 0.001$  ( $df = 118$ ,  $t = 3.454$ )] during the odor sampling period of the go/no-go task for all units and odors ( $n = 119$ , 9 mice and 8 odors). The dashed line shows the diagonal, where the  $\Delta$ MFR in S+ equals that in S−. **F** As for **E** but for the waiting period [left: paired *t*-test,  $P = 0.913$  ( $df = 118$ ,  $t = 0.109$ ); right: paired *t*-test,  $P = 0.826$  ( $df = 118$ ,  $t = -0.220$ )]. **G** As for **E** but for the reward period [left: paired *t*-test,  $P = 0.284$  ( $df = 118$ ,  $t = 1.077$ ); right: paired *t*-test,  $**P = 0.004$  ( $df = 118$ ,  $t = 2.977$ )]. **H** Comparison of the  $\Delta$ MFR between odor 1 and odor 2 early [left: paired *t*-test,  $P = 0.241$  ( $df = 133$ ,  $t = 1.178$ )] and late [right: paired *t*-test,  $P = 0.189$  ( $df = 133$ ,  $t = -1.321$ )] in the odor sampling period of the go/no-go task for all units and odors ( $n = 134$ , 10 mice with 8 odors). The dashed line shows the diagonal, where  $\Delta$ MFR for odor 1 equals that for odor 2. **I** As for **H** but for the waiting period [left: paired *t*-test,  $P = 0.462$  ( $df = 133$ ,  $t = 0.738$ ); right: paired *t*-test,  $P = 0.094$  ( $df = 133$ ,  $t = -1.686$ )]. **J** As for **H** but for the reward period [left: paired *t*-test,  $P = 0.113$  ( $df = 133$ ,  $t = 1.595$ ); right: paired *t*-test,  $P = 0.810$  ( $df = 133$ ,  $t = 0.241$ )].

Interestingly, consistent with previous studies that have revealed that the spikes of single M/Ts show plasticity to the odor during learning, and the odor-evoked spikes are more divergent after the mice learn to discriminate the odor pair in the free-moving go/no-go task [13, 21, 29], our study demonstrated that learning-induced plasticity of single unit spikes occurred during odor sampling. These

results indicate that the plasticity of M/T spiking during the learning process is reliable and independent of behavioral conditions such as free-moving or head-fixed. In addition, besides spikes, the coherence between sniffing and LFP theta oscillation also showed plasticity during odor sampling in the learning process, but this has not been reported in previous studies. The sniffing pattern and LFP theta oscillation are strongly but not completely correlated in awake rodents [13, 31, 44], and their coherence varies from moment to moment [30, 31]. However, the functional significance of the coherence remains elusive. Our data suggest that this coherence at least plays important roles in the olfactory learning process during the go/no-go task in head-fixed mice.

Besides odor sampling, a previous study has reported that other odor-related events, such as light signals and door openings during an olfactory discrimination task, also evoke significant changes of M/T firing [22]. We further confirmed and extended this finding, showing that both the sniffing pattern and neural activity in the OB responded to anticipation and/or reward that were odor-related events in the go/no-go task. Although the neural plasticity of M/Ts responding to odors during the learning process has been extensively investigated by both electrophysiological recording in free-moving rodents and single-cell imaging in head-fixed mice [13, 14, 21, 29, 36, 40], no study has tested whether the neural response to odor-related events shows similar plasticity during learning. Thus, our study provides the first evidence that, while odor-related events evoke neural responses in the OB and sniffing pattern changes, these signals also show plasticity during the

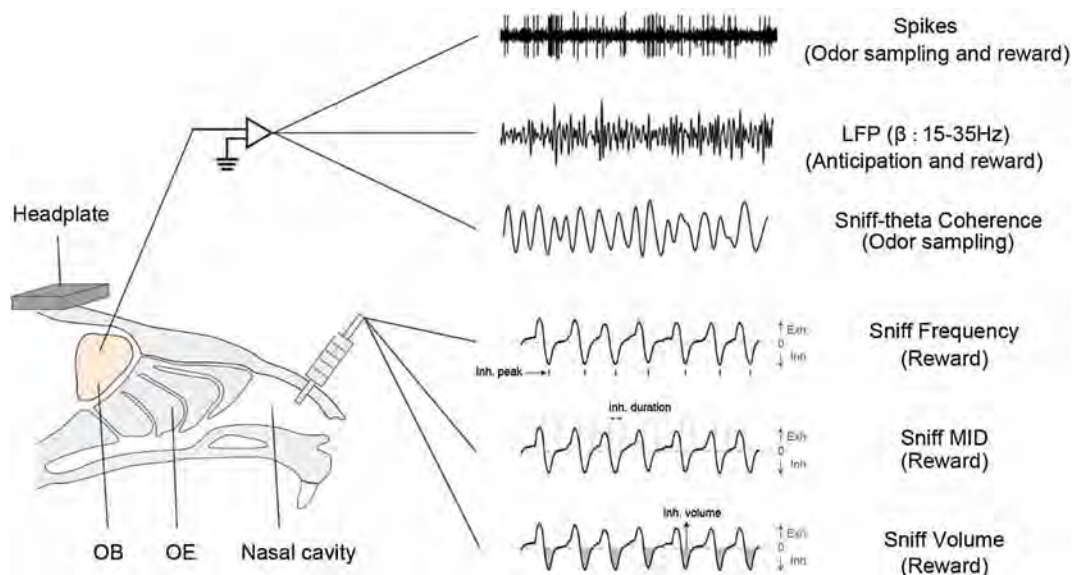


**Fig. 8** Diagram showing the results indicating that learning-induced plasticity of spikes and beta oscillations occurred during odor sampling, and plasticity of spikes, beta oscillations, sniffing patterns,

and coherence between sniffing and theta oscillations occurred during the period of anticipation and/or reward (OB, olfactory bulb; OE, olfactory epithelium).

learning process, at least in the head-fixed go/no-go paradigm.

The response and plasticity of neurons to odor-related events are linked to higher cognitive functions since they are associated with leaning and reward [45, 46]. It is surprising that neural activity in the OB shows this property since the OB is the first relay station in the olfactory system that receives direct input from the olfactory periphery [4, 47]. Therefore, higher brain centers must be involved in the mechanisms by which neural activity in the OB and the sniffing pattern show plasticity during the learning process. While the OB receives direct input from olfactory sensory neurons, it also receives intense cortical feedback and modulatory innervation from a wide range of higher brain centers [9–11]. Some of these centers are critically involved in learning, motivation, anticipation, and reward. For example, cholinergic and noradrenergic inputs to the OB are important for learning [29, 48, 49], and serotonergic inputs to the OB likely play crucial roles in reward and anticipation [50, 51]. In addition, the sniffing pattern usually changes during exploratory behavior and other non-olfactory events [24]. A recent study has reported that the prefrontal cortex and sniffing pattern are strongly correlated during freezing behavior [52], suggesting that the sniffing pattern is modulated by higher brain centers that play important roles in learning, motivation, and reward. Therefore, the learning-induced plasticity of the sniffing pattern and neural activity in the OB responding to odor stimulation and odor-related events is the result of complex interactions between the olfactory system and other centers involved in higher brain functions.

In addition, although both the sniffing pattern and neural activity in the OB showed plasticity during the learning process, it is likely that the change of sniffing signals makes a major contribution since the neural activity in the OB is largely modulated by sniffing patterns in both anesthetized and awake rodents [24]. For example, theta and gamma oscillations in the OB LFP are tightly coupled with the sniffing pattern [35], and the firing of single units recorded from M/T cells is precisely locked to a specific phase of the sniffing cycle [53]. Importantly, a recent study using patch clamping in awake behaving mice has revealed that the activity of tufted cells is modulated by active sniffing [23]. Therefore, the changes of neural activity in the OB during the learning process might also be due to the different sniffing strategies adopted during the different learning states.

In summary, we investigated the sniffing pattern and neural activity in the OB responding to odor and odor-related events in the learning process of the go/no-go task in head-fixed mice. Our results revealed the occurrence of plasticity of the sniffing pattern and neural activity in the

OB of behaving mice during odor sampling, anticipation, and reward. These findings are important for understanding the function of the OB beyond representing olfactory information in awake behaving rodents.

**Acknowledgements** This work was supported by the National Natural Science Foundation of China (31571082, 31872771 and 31700895), the Natural Science Foundation of the Jiangsu Higher Education Institutions of China (16KJA180007), and the Natural Science Foundation of Jiangsu Province (BK20170260). We thank Siqi Jing and Lingzhi Zhang for technical assistance.

**Conflict of interest** The authors declare that they have no competing financial interests.

## References

- Zhang W, Sun C, Shao Y, Zhou Z, Hou Y, Li A. Partial depletion of dopaminergic neurons in the substantia nigra impairs olfaction and alters neural activity in the olfactory bulb. *Sci Rep* 2019, 9: 254.
- Jin H, Zhang JR, Shen Y, Liu CF. Clinical significance of REM sleep behavior disorders and other non-motor symptoms of Parkinsonism. *Neurosci Bull* 2017, 33: 576–584.
- Fullard ME, Morley JF, Duda JE. Olfactory dysfunction as an early biomarker in Parkinson's disease. *Neurosci Bull* 2017, 33: 515–525.
- Li A, Rao X, Zhou Y, Restrepo D. Complex neural representation of odour information in the olfactory bulb. *Acta Physiol (Oxf)* 2020, 228: e13333.
- Li A, Gire DH, Bozza T, Restrepo D. Precise detection of direct glomerular input duration by the olfactory bulb. *J Neurosci* 2014, 34: 16058–16064.
- Roland B, Deneux T, Franks KM, Bathellier B, Fleischmann A. Odor identity coding by distributed ensembles of neurons in the mouse olfactory cortex. *Elife* 2017, 6.
- Chong E, Rinberg D. Behavioral readout of spatio-temporal codes in olfaction. *Curr Opin Neurobiol* 2018, 52: 18–24.
- Wen P, Rao X, Xu L, Zhang Z, Jia F, He X, *et al.* Cortical organization of centrifugal afferents to the olfactory bulb: mono- and trans-synaptic tracing with recombinant neurotropic viral tracers. *Neurosci Bull* 2019, 35: 709–723.
- Fletcher ML, Chen WR. Neural correlates of olfactory learning: Critical role of centrifugal neuromodulation. *Learn Mem* 2010, 17: 561–570.
- Linster C, Cleland TA. Neuromodulation of olfactory transformations. *Curr Opin Neurobiol* 2016, 40: 170–177.
- Lizbinski KM, Dacks AM. Intrinsic and extrinsic neuromodulation of olfactory processing. *Front Cell Neurosci* 2017, 11: 424.
- Restrepo D, Doucette W, Whitesell JD, McTavish TS, Salcedo E. From the top down: flexible reading of a fragmented odor map. *Trends Neurosci* 2009, 32: 525–531.
- Li A, Gire DH, Restrepo D. Upsilon spike-field coherence in a population of olfactory bulb neurons differentiates between odors irrespective of associated outcome. *J Neurosci* 2015, 35: 5808–5822.
- Chu MW, Li WL, Komiyama T. Balancing the robustness and efficiency of odor representations during learning. *Neuron* 2016, 92: 174–186.
- Gire DH, Restrepo D, Sejnowski TJ, Greer C, De Carlos JA, Lopez-Mascaraque L. Temporal processing in the olfactory system: can we see a smell? *Neuron* 2013, 78: 416–432.

16. Abraham NM, Vincis R, Lagier S, Rodriguez I, Carleton A. Long term functional plasticity of sensory inputs mediated by olfactory learning. *Elife* 2014, 3: e02109.
17. Koldaeva A, Schaefer AT, Fukunaga I. Rapid task-dependent tuning of the mouse olfactory bulb. *Elife* 2019, 8: e43558.
18. Rinberg D, Koulakov A, Gelperin A. Sparse odor coding in awake behaving mice. *J Neurosci* 2006, 26: 8857–8865.
19. Li A, Gong L, Xu F. Brain-state-independent neural representation of peripheral stimulation in rat olfactory bulb. *Proc Natl Acad Sci U S A* 2011, 108: 5087–5092.
20. Li A, Guthman EM, Doucette WT, Restrepo D. Behavioral status influences the dependence of odorant-induced change in firing on prestimulus firing rate. *J Neurosci* 2017, 37: 1835–1852.
21. Doucette W, Restrepo D. Profound context-dependent plasticity of mitral cell responses in olfactory bulb. *PLoS Biol* 2008, 6: e258.
22. Kay LM, Laurent G. Odor- and context-dependent modulation of mitral cell activity in behaving rats. *Nat Neurosci* 1999, 2: 1003–1009.
23. Jordan R, Fukunaga I, Kollo M, Schaefer AT. Active sampling state dynamically enhances olfactory bulb odor representation. *Neuron* 2018, 98: 1214–1228.
24. Wachowiak M. All in a sniff: olfaction as a model for active sensing. *Neuron* 2011, 71: 962–973.
25. Sun C, Tang K, Wu J, Xu H, Zhang W, Cao T, *et al.* Leptin modulates olfactory discrimination and neural activity in the olfactory bulb. *Acta Physiol (Oxf)* 2019: e13319.
26. Jeanne JM, Sharpee TO, Gentner TQ. Associative learning enhances population coding by inverting interneuronal correlation patterns. *Neuron* 2013, 78: 352–363.
27. Zhou Y, Wang X, Cao T, Xu J, Wang D, Restrepo D, *et al.* Insulin modulates neural activity of pyramidal neurons in the anterior piriform cortex. *Front Cell Neurosci* 2017, 11: 378.
28. Slotnick B, Restrepo D. Olfactometry with mice. *Curr Protoc Neurosci* 2005, Chapter 8: Unit 8 20.
29. Doucette W, Gire DH, Whitesell J, Carmean V, Lucero MT, Restrepo D. Associative cortex features in the first olfactory brain relay station. *Neuron* 2011, 69: 1176–1187.
30. Khan AG, Sarangi M, Bhalla US. Rats track odour trails accurately using a multi-layered strategy with near-optimal sampling. *Nat Commun* 2012, 3: 703.
31. Nguyen Chi V, Muller C, Wolfenstetter T, Yanovsky Y, Draguhn A, Tort AB, *et al.* Hippocampal respiration-driven rhythm distinct from theta oscillations in awake mice. *J Neurosci* 2016, 36: 162–177.
32. Ravel N, Chabaud P, Martin C, Gaveau V, Hugues E, Tallon-Baudry C, *et al.* Olfactory learning modifies the expression of odour-induced oscillatory responses in the gamma (60–90 Hz) and beta (15–40 Hz) bands in the rat olfactory bulb. *Eur J Neurosci* 2003, 17: 350–358.
33. Martin C, Gervais R, Hugues E, Messaoudi B, Ravel N. Learning modulation of odor-induced oscillatory responses in the rat olfactory bulb: a correlate of odor recognition? *J Neurosci* 2004, 24: 389–397.
34. Martin C, Ravel N. Beta and gamma oscillatory activities associated with olfactory memory tasks: different rhythms for different functional networks? *Front Behav Neurosci* 2014, 8: 218.
35. Kay LM. Olfactory system oscillations across phyla. *Curr Opin Neurobiol* 2015, 31: 141–147.
36. Kato HK, Chu MW, Isaacson JS, Komiya T. Dynamic sensory representations in the olfactory bulb: modulation by wakefulness and experience. *Neuron* 2012, 76: 962–975.
37. Ross JM, Fletcher ML. Learning-dependent and -independent enhancement of mitral/tufted cell glomerular odor responses following olfactory fear conditioning in awake mice. *J Neurosci* 2018, 38: 4623–4640.
38. Fontanini A, Katz DB. Behavioral states, network states, and sensory response variability. *J Neurophysiol* 2008, 100: 1160–1168.
39. Carlson KS, Gadziola MA, Dauster ES, Wesson DW. Selective attention controls olfactory decisions and the neural encoding of odors. *Curr Biol* 2018, 28: 2195–2205.
40. Yamada Y, Bhaukaurally K, Madarasz TJ, Pouget A, Rodriguez I, Carleton A. Context- and output layer-dependent long-term ensemble plasticity in a sensory circuit. *Neuron* 2017, 93: 1198–1212.
41. Gourevitch B, Kay LM, Martin C. Directional coupling from the olfactory bulb to the hippocampus during a go/no-go odor discrimination task. *J Neurophysiol* 2010, 103: 2633–2641.
42. Frederick DE, Brown A, Tacopina S, Mehta N, Vujovic M, Brim E, *et al.* Task-dependent behavioral dynamics make the case for temporal integration in multiple strategies during odor processing. *J Neurosci* 2017, 37: 4416–4426.
43. Abraham NM, Guerin D, Bhaukaurally K, Carleton A. Similar odor discrimination behavior in head-restrained and freely moving mice. *PLoS One* 2012, 7: e51789.
44. Rojas-Libano D, Frederick DE, Egana JI, Kay LM. The olfactory bulb theta rhythm follows all frequencies of diaphragmatic respiration in the freely behaving rat. *Front Behav Neurosci* 2014, 8: 214.
45. Calu DJ, Roesch MR, Stalnaker TA, Schoenbaum G. Associative encoding in posterior piriform cortex during odor discrimination and reversal learning. *Cereb Cortex* 2007, 17: 1342–1349.
46. Roesch MR, Stalnaker TA, Schoenbaum G. Associative encoding in anterior piriform cortex versus orbitofrontal cortex during odor discrimination and reversal learning. *Cereb Cortex* 2007, 17: 643–652.
47. Gelperin A, Ghatpande A. Neural basis of olfactory perception. *Ann N Y Acad Sci* 2009, 1170: 277–285.
48. Ogg MC, Ross JM, Bendahmane M, Fletcher ML. Olfactory bulb acetylcholine release dishabituates odor responses and reinstates odor investigation. *Nat Commun* 2018, 9: 1868.
49. Ma M, Luo M. Optogenetic activation of basal forebrain cholinergic neurons modulates neuronal excitability and sensory responses in the main olfactory bulb. *J Neurosci* 2012, 32: 10105–10116.
50. Liu ZX, Zhou JF, Li Y, Hu F, Lu Y, Ma M, *et al.* Dorsal raphe neurons signal reward through 5-HT and glutamate. *Neuron* 2014, 81: 1360–1374.
51. Luo M, Li Y, Zhong W. Do dorsal raphe 5-HT neurons encode “beneficialness”? *Neurobiol Learn Mem* 2016, 135: 40–49.
52. Moberly AH, Schreck M, Bhattarai JP, Zweifel LS, Luo W, Ma M. Olfactory inputs modulate respiration-related rhythmic activity in the prefrontal cortex and freezing behavior. *Nat Commun* 2018, 9: 1528.
53. Fukunaga I, Berning M, Kollo M, Schmaltz A, Schaefer AT. Two distinct channels of olfactory bulb output. *Neuron* 2012, 75: 320–329.



# Social Isolation in Male Rats During Adolescence Inhibits the Wnt/ $\beta$ -Catenin Pathway in the Prefrontal Cortex and Enhances Anxiety and Cocaine-Induced Plasticity in Adulthood

Santiago Cuesta<sup>1,2,3</sup> · Alejandrina Funes<sup>1,2</sup> · Alejandra M. Pacchioni<sup>1,2</sup>

Received: 28 June 2019 / Accepted: 1 December 2019 / Published online: 20 February 2020  
© Shanghai Institutes for Biological Sciences, CAS 2020

**Abstract** In adult animals, it is well established that stress has a proactive effect on psychostimulant responses. However, whether only a short period of stress during adolescence can also affect cocaine responses later in life and what mechanisms are involved are unknown. Here, we showed that 5 days of social isolation during rat adolescence had a long-term impact on anxiety-like behaviors, cocaine-induced conditioned place preference, and the expression of sensitization during adulthood. At the molecular level, social isolation decreased the activity of the Wnt/ $\beta$ -catenin pathway in the prefrontal cortex (PFC). Furthermore, after the expression of cocaine sensitization, isolated rats showed an increase in this pathway in the nucleus accumbens. Together, these findings suggest that, adolescent social isolation by altering the Wnt/ $\beta$ -catenin pathway in the developing PFC might increase the cocaine responses during adulthood, introducing this pathway as a novel neuroadaptation in the cortical-accumbens connection that may mediate a stress-induced increase in vulnerability to drugs.

**Keywords** Social isolation · Adolescence · Cocaine vulnerability · Wnt/ $\beta$ -catenin pathway

## Introduction

Adolescence is a transitional period of social behavior development, risk-taking, and preparation for the independence of adulthood [1]. This transition to adulthood involves, among other biological processes, a strong refinement of different brain structures and circuitries [2, 3]. Because of the heightened plasticity during adolescence, this period of brain maturation is particularly responsive to different genetic and environmental factors that can increase the risk for developing mental illness [3, 4]. Among other factors, negative social environments have been shown to strongly disturb adolescent brain development, leading to long-lasting neurobiological changes that raise the risk for psychiatric disorders later in life, including drug addiction [5–9]. Indeed, experiments using animal models have shown that the emotional stress induced by social isolation (SI) during adolescence is associated with increased rates of acquisition of cocaine self-administration, increased motivation for cocaine, and enhanced vulnerability to drug-associated behaviors in adulthood [10, 11]. However, most of these studies used long isolation periods, generally lasting more than 15 days in different stages of adolescence [11–14], and only a few focused on the impact of a brief period of adolescent SI on adult behaviors [15–18]. This is particularly intriguing, because it has been shown that in rats, only five days of SI from postnatal days 30 to 35 (P30–P35) produces deficits in memory and learning, as well as structural changes in the cortex [15, 16] that could predict affective disorders in adulthood such as drug abuse.

In past years, the canonical Wnt pathway has been shown to participate in the deleterious effects of social defeat stress [19, 20]. Wnt factors are secreted proteins that, once they reach their membrane receptor Frizzled, can

✉ Alejandra M. Pacchioni  
Pacchioni.am@gmail.com

<sup>1</sup> Área Toxicología, Departamento de Ciencias de los Alimentos y del Medioambiente, Facultad de Ciencias Bioquímicas y Farmacéuticas, Universidad Nacional de Rosario, Suipacha 531, 2000 Rosario, Santa Fe, Argentina  
<sup>2</sup> Consejo Nacional de Investigaciones Científicas y Técnicas, Rosario, Argentina  
<sup>3</sup> Present Address: Department of Microbiology, University of Texas Southwestern Medical Center, Dallas, TX 75390, USA

activate three different pathways, which diverge at the level of Dishevelled, the first intracellular effector. The canonical Wnt or Wnt/ $\beta$ -catenin signaling pathway is one of these three branches [21–23]. Its activation leads to the inhibitory phosphorylation of glycogen synthase kinase 3 $\beta$  (GSK3 $\beta$ ), allowing the stabilization of  $\beta$ -catenin and its subsequent entry into the nucleus where it promotes gene expression [22, 24, 25]. In the absence of Wnt, GSK3 $\beta$  phosphorylates  $\beta$ -catenin, marking it for degradation by the proteasome [26]. Notably, apart from contributing to the detrimental effects of social defeat, this pathway has also been linked to the dopaminergic and glutamatergic changes found in rodent models of schizophrenia [27–29]. Furthermore, we have identified the canonical Wnt pathway among the short- and long-term molecular changes associated with cocaine-induced sensitization in areas such as the prefrontal cortex (PFC) and the nucleus accumbens (NAcc) [30, 31]. All together, this evidence raises the possibility of a role of the canonical Wnt pathway in mediating the long-term effects of stress on drug vulnerability. Therefore, in this study we assessed whether a brief period of emotional stress induced by SI during adolescence can alter  $\beta$ -catenin levels in brain areas strongly associated with addiction and modify the behavioral responses to cocaine during adulthood.

## Methods

### Experimental Animals

A total of 145 male Wistar rats (P21–P23) were purchased from the Vivarium of the Facultad de Ciencias Bioquímicas y Farmacéuticas, Universidad Nacional de Rosario (FCByF-UNR, Argentina). Usually 2 or 3 litters were used at a time. They were housed in mixed groups of 3 or 4 assigned by block randomization. These groups then underwent the same experimental procedure, and the rats in each cage were selected to be part of the isolated or the non-isolated groups by simple randomization. None of the rats were discarded. Rats were housed in a colony room with food and water *ad libitum*.

All experiments were conducted during the light period of a 12 h light/dark cycle, specifically between 09:00 and 16:00 and were performed according to the National Institutes of Health guidelines. The experimental protocol was approved by the Institutional Animal Care and Use Committee at the FCByF-UNR (D.R. No. 301/2013).

### Drugs

Cocaine hydrochloride was purchased from Droguería Saporiti (Buenos Aires, Argentina) and dissolved in saline.

### Experimental Design

At P30, half of the rats were isolated until P35 (isolated group) and the other half was left in their home cages (non-isolated group). At the end of the SI period, the rats were housed with their previous group-mates. Rats were euthanized 1 (P36,  $n = 11$ ), 10 (P45,  $n = 14$ ), or 23 days (P58,  $n = 10$ ) after SI for molecular analysis (Fig. 1A). The remaining rats were left undisturbed until P59 or P60 to evaluate their responses to cocaine either in the conditioned place preference (CPP) test or after a sensitization paradigm. The day after the end of the sensitization paradigm, some animals were euthanized for molecular studies. Each animal underwent only one experimental procedure. Control and treated animals were run simultaneously.

### Stress by SI

The SI protocol was performed as in previous studies [15, 16]. Briefly, rats at P30 were individually housed in small cages ( $14 \times 18 \times 21 \text{ cm}^3$ ) with free access to food and water. The cages were separated by pieces of wood that prevented visual contact and were placed in the colony room. After 5 days of SI, on P35, the rats were relocated to group cages with their previous mates. The non-isolated animals remained undisturbed in their home cages during the whole experiment.

### Behavioral Tests

#### Motor Activity Cages

The testing apparatus consisted of an acrylic box ( $43 \times 43 \times 30 \text{ cm}^3$ ) equipped with 8 infrared photocell beams located 3 cm above the floor. Interruption of any beam resulted in a photocell count. Rats were individually placed in the boxes and their activity was recorded for an hour (habituation) and for another hour after cocaine injection. The apparatus and its software were developed by Laboratorio de Investigación Aplicada y Desarrollo, Facultad de Ciencias Exactas, Físicas y Naturales (Universidad Nacional de Córdoba, Argentina).

#### Open Field Test

On P60, the total activity and time spent in the center of the arena were recorded for 1 h during habituation on day 1 of the sensitization paradigm (i.e. first exposure to the apparatus) (Fig. 2). The software divided the cage into 81 squares (area,  $1,849 \text{ cm}^2$ ) according to the intersections of the beams, and 25 of these squares formed the center of the arena (area,  $570.3 \text{ cm}^2$ ) where the external border was

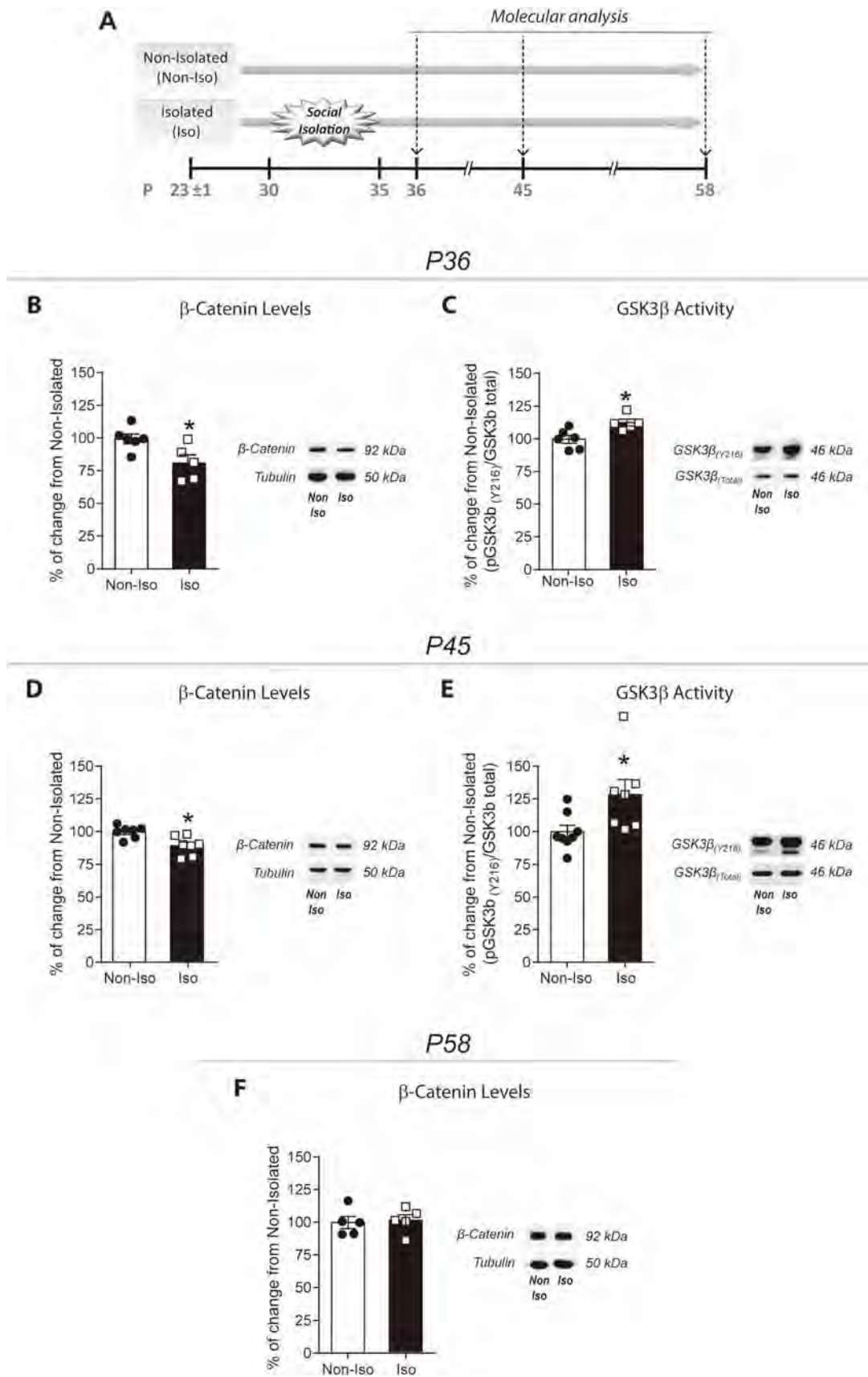


**Fig. 1** Adolescent social isolation leads to long-term changes in Wnt/ $\beta$ -catenin pathway activity. **A** Schematic of the different groups evaluated. **B–F** Protein levels of  $\beta$ -catenin and GSK3 $\beta$  in the PFC at P36 (**B, C**), P45 (**D, E**) and P58 (**F**) (\* $P < 0.05$ ).

equidistant from the border of the cage. The time spent in the center of the arena reflects approach–avoidance of novel stimuli, is considered a reliable index of anxiety, responds to anxiolytic agents, and is sensitive to stress-induced anxiety states. In addition, assessment of the total activity is a guide to the exploratory response to a novel environment [32].

### Cocaine Sensitization

Cocaine-induced sensitization was measured as before [31], with modifications. On P60, rats in each group were individually placed in the locomotor activity cages for habituation. At the end of habituation, all rats received six cocaine injections (5 or 15 mg/kg i.p., once daily) on P60–P64 and P87, and the total activity was recorded on P60 (day 1, D1), P64 (D5), and P87 (D28) after the injection. Between the injections on D5 and D28 the rats were left undisturbed in their home cages. On P88, 24 h after the last injection, rats were sacrificed, and their brains were removed (Fig. 3A).

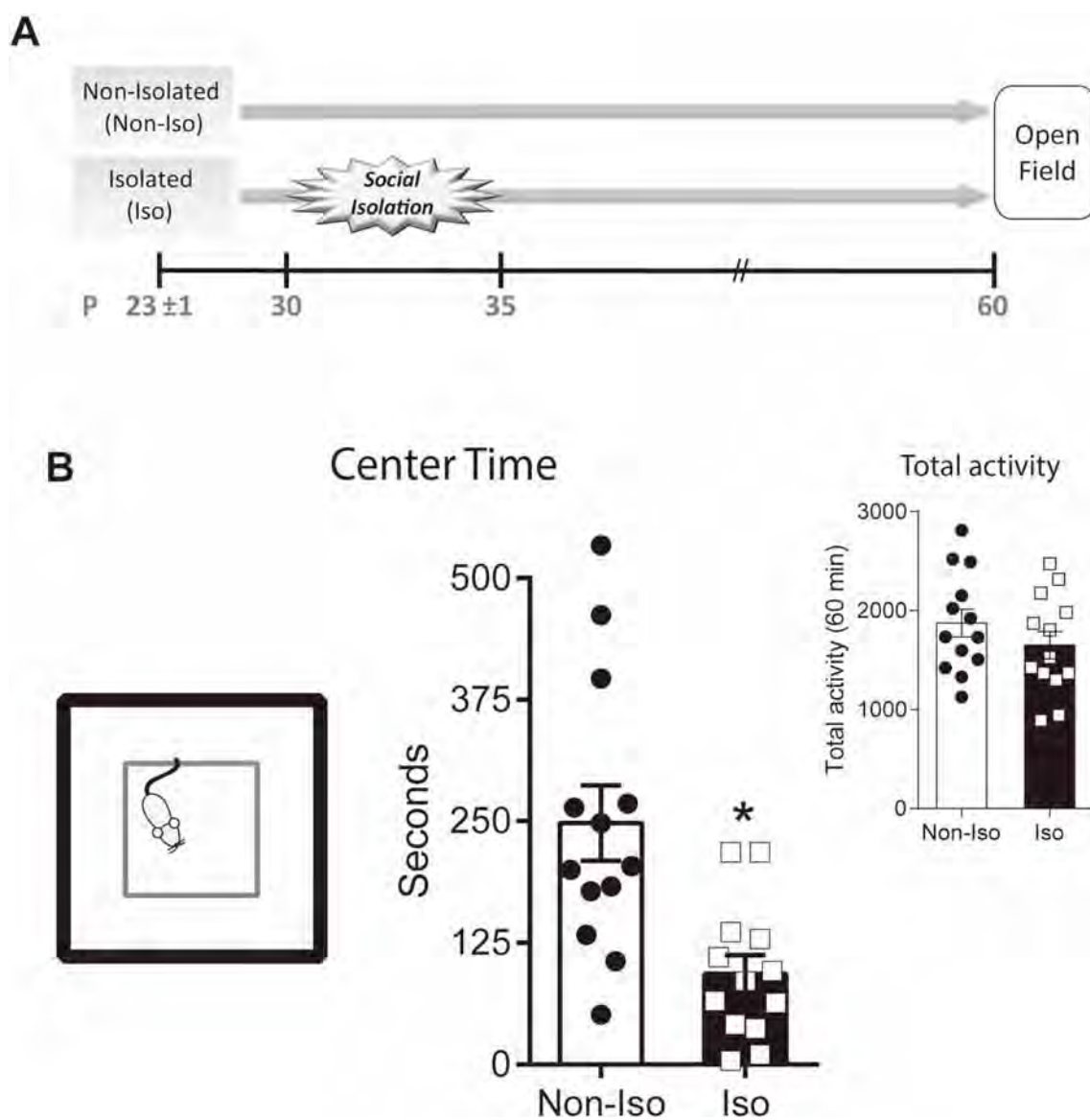
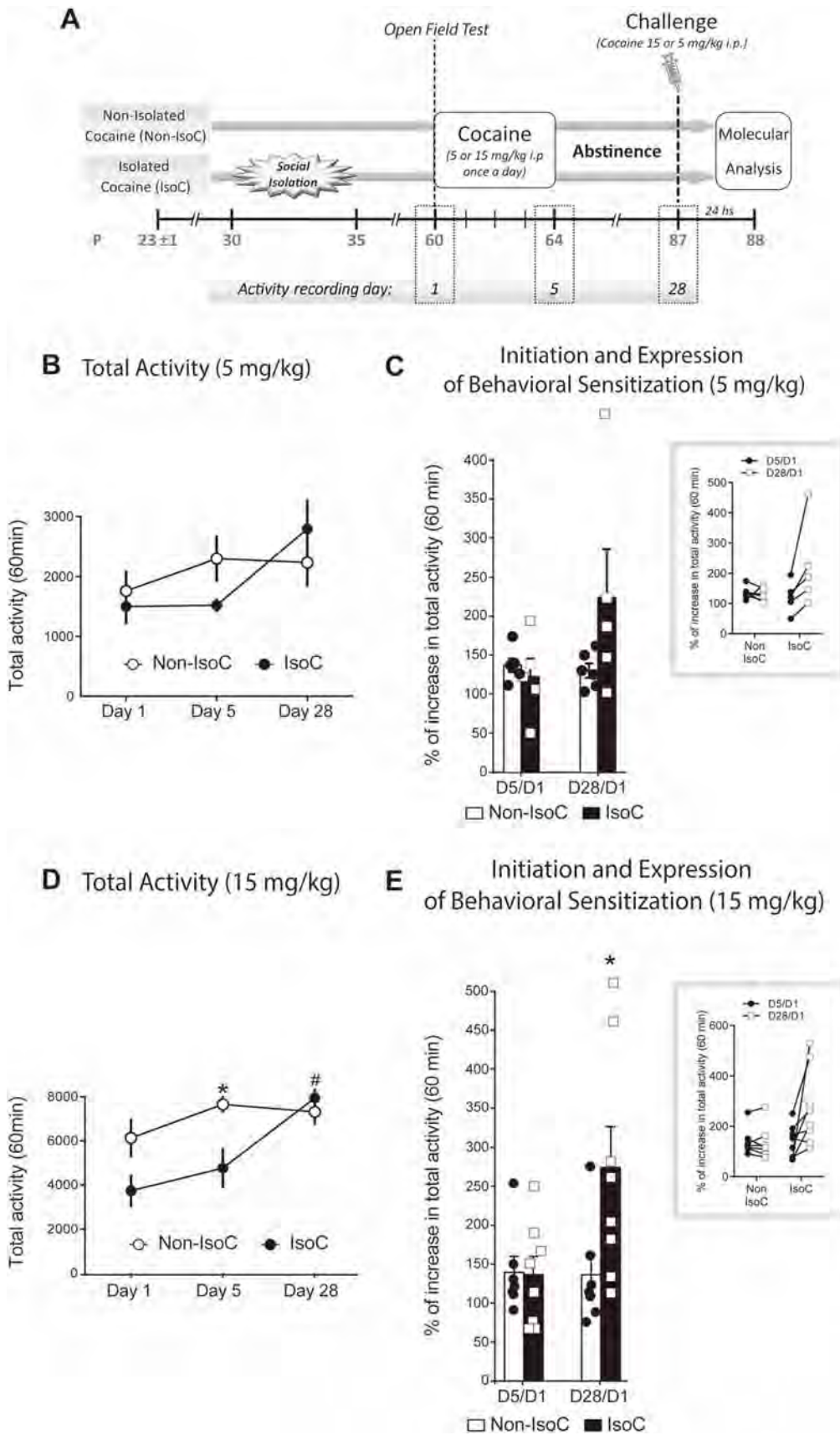


**Fig. 2** Adolescent social isolation increases anxiety-like behaviors in adulthood. **A** Schematic of the different groups evaluated. **B** Socially isolated rats during adolescence spent less time in the center of a novel open field environment in adulthood (\* $P < 0.05$  vs non-isolated group).



◀ **Fig. 3** Social isolation during adolescence facilitates cocaine-induced expression of sensitization during adulthood. **A** Schematic of the different groups evaluated. **B** Total locomotor activity during 60 min after 5 mg/kg cocaine injection on D1, D5, and D28. **C** No significant differences were found in the initiation (percentage increase in activity between D5 and D1) or expression (percentage increase in activity between D28 and D1) of behavioral sensitization (inset, increase across time in the behavioral response of each isolated and non-isolated rat). **D** Total locomotor activity during 60 min after cocaine injection on D1, D5, and D28 ( $\#P < 0.05$  vs total activity on D1 and D5 in the isolated group;  $*P < 0.05$  vs total activity on D5 in the isolated group; Sidak's *post hoc* test). **E** Percentage increase for initiation (D5/D1) as well as for expression (D28/D1) of sensitization (inset, increase across time in the behavioral response for each isolated and non-isolated rat;  $*P < 0.05$  vs non-isolated group).

Behavioral sensitization has been conceptualized as occurring in two distinct temporal domains: initiation and expression. Behaviorally, initiation is defined by changes observed between the first and last injection of the treatment, while expression is defined by the changes in motor activity caused by a period of forced abstinence (for reviews see [33, 34]). In our experimental setup, initiation was evaluated by comparing the total activity on D5 to that on D1 (D5/D1), while expression was evaluated as D28/D1. The criterion for cocaine-induced sensitization was set as a minimum of a 20% increase in the total activity count [35]. Since the percentage increase represented changes in a rat's individual response during treatment, the above setup allowed the evaluation of individual vulnerability.

#### *Cocaine Conditioned Place Preference and Cocaine-Primed Test*

The rewarding property of cocaine was assessed using a place preference procedure and apparatus described previously [36]. Briefly, the apparatus consisted of an acrylic box ( $43 \times 43 \times 30$  cm<sup>3</sup>) divided into two compartments by a removable divider. One of the compartments was white and had bedding on the floor, and the other was black with wire mesh on the floor. This design yielded a strongly biased preference ( $\sim 70\%$  of the rats preferred the black compartment). The procedure consisted of 6 sequential phases: habituation, pre-conditioning test (Pre-Test), conditioning, post-conditioning test (Post-Test), abstinence, and cocaine-primed test. Each test lasted 15 min. During habituation (P59), Pre-Test (P60), Post-Test (P69), and the cocaine-primed test (P90) each rat could explore both compartments. The time spent in each compartment during the Pre-Test was recorded to establish the individual preference, which was used to assign the conditioning conditions in a non-counterbalanced way. On P59, a total of 94 non-isolated and isolated rats were habituated to the apparatus, and on P60 the Pre-Test was done.

Cocaine conditioning was conducted over an 8-day period (P61–P68). Rats were brought into the conditioning room, injected with cocaine (0.5, 1, or 5 mg/kg i.p.) and restricted to the non-preferred compartment; or with saline (1 ml/kg i.p.) and placed in their preferred compartment. Each conditioning session lasted 20 min. The Post-Test was conducted the day after the last conditioning session (P69). Only the rats conditioned with 5 mg/kg cocaine were left undisturbed until P90 when they received a cocaine-priming injection (5 mg/kg i.p.) and were returned to the CPP apparatus to test the persistence of the cocaine conditioning effect (Fig. 5A). Place conditioning was quantified as an increase in the time spent on the drug-paired side compared with the Pre-Test and referred to as the CPP score (in seconds). Meanwhile, a separate group of animals received a saline injection before each conditioning session either in the preferred or the non-preferred compartment (Saline group) to facilitate the interpretation of the biased place conditioning paradigm results [37, 38].

#### *Euthanasia*

At the end of each experiment, rats were anesthetized with ketamine/xylazine (85/2.5 mg/kg, i.p.) and then decapitated with a small-animal guillotine. For the experiments where brain areas were used for molecular analysis, anesthesia was not applied because it could differentially affect the protein and mRNA expression levels [39–42]. To minimize stress, the decapitation was fast, and the sharpness of the guillotine was frequently checked. It is important to note that this study was not pre-registered, and that the procedures were not performed blindly.

#### **Tissue Preparation**

All the brain areas evaluated were dissected according to Heffner, Hartman, Seiden [43] using a rat brain matrix. Tissue was stored at  $-80^{\circ}\text{C}$  until analysis. At analysis, tissue was homogenized on ice with RIPA buffer supplemented with phosphatase and protease inhibitors (2  $\mu\text{g}/\text{mL}$  aprotinin; 2  $\mu\text{g}/\text{mL}$  leupeptin; 1  $\mu\text{g}/\text{mL}$  pepstatin; 100  $\mu\text{g}/\text{mL}$  PMSF; 1 mmol/L  $\text{Na}_3\text{VO}_4$ ; 50 mmol/L NaF), and centrifuged for 5 min at 13,000 g. Protein concentrations were measured using the Lowry assay.

#### **Western Blotting**

Protein extracts from total homogenates were heated to  $80^{\circ}\text{C}$  for 5 min with Laemmli buffer as a reducing treatment. Samples (total homogenate: 10  $\mu\text{g}/\text{lane}$ ) were run in 10% SDS-polyacrylamide gel and transferred to a nitrocellulose membrane, which was incubated overnight with the primary antibody  $\beta$ -catenin (1:10,000, BD

Biosciences, San Jose, CA, Cat# 610154, RRI-D:AB\_397555) or phospho-GSK3 $\beta$ -Y216 (1:8000; BD Biosciences, San Jose, CA, Cat# 612312, RRI-D:AB\_399627) followed by secondary horseradish peroxidase-conjugated antibody (Sigma, St. Louis, MO). Reactivity was detected using enhanced chemiluminescence and quantified using the ImageJ (National Institutes of Health, Bethesda, MD). Total homogenate blots were also incubated with anti-tubulin (1:14,000; Sigma) or total GSK3 $\beta$  (1:1,000; BD Biosciences Cat# 610201, RRID: AB\_397600) to correct for differences in protein loading.

### Data Analysis

Statistical comparisons were performed in Prism 6 (GraphPad Software, La Jolla, CA, RRID:SCR\_002798). The distribution of data was determined with the Shapiro-Wilk and/or Kolmogorov-Smirnov normality test and Welch's correction. No sample size calculations were performed. To determine outliers in each experimental group we performed the Grubbs' test in Prism (RRID:SCR\_002798) and none were identified. When ANOVA was applied, isolation was a between-group factor, while time (injection days or test) was a within-group factor. These main factors were applied for data expressed as counts in 60 min, CPP score, or time spent on the drug-side, while in Fig. 4B the main factors were isolation and cocaine dose, both between-groups factors. ANOVA was followed by a *post-hoc* test for multiple comparisons (Sidak's or Fisher's Least Significant

Difference). Student's *t*-test or the unpaired Mann-Whitney test (nonparametric) was used when necessary. Results are expressed as the mean  $\pm$  SEM. Significance was set at  $P < 0.05$  in all cases.

## Results

### SI During Adolescence Changes Wnt/ $\beta$ -Catenin Pathway Activity in PFC

In adult mice it has been shown that the Wnt/ $\beta$ -catenin pathway is involved in the response to social defeat [20]. Therefore, we decided to investigate whether 5 days of SI during adolescence (P30–P35) can also modify the activity of the canonical pathway at different time points after the isolation ends. To do that, we evaluated the levels of  $\beta$ -catenin as a readout for canonical Wnt signaling [25] in the PFC and NAcc at 24 h (P36), 10 days (P45), and 23 days (P58) after the end of isolation. We found significantly lower  $\beta$ -catenin levels in the PFC of isolated than in non-isolated rats 24 h after the end of isolation (Fig. 1B; P36,  $t_9 = 3.418$ ,  $P < 0.01$ ). Notably, this reduction was still evident 10 days after the end of the stress (Fig. 1D; P45,  $t_{12} = 3.253$ ,  $P < 0.01$ ). At P58, the  $\beta$ -catenin levels were similar to controls (Fig. 1F;  $t_8 = 0.2604$ ,  $P = 0.801$ ). To confirm that the changes in  $\beta$ -catenin in the PFC at P36 and P45 were associated with alterations in the activity of the canonical Wnt pathway, we measured the activation levels of the upstream regulator GSK3 $\beta$  at these time-points. We

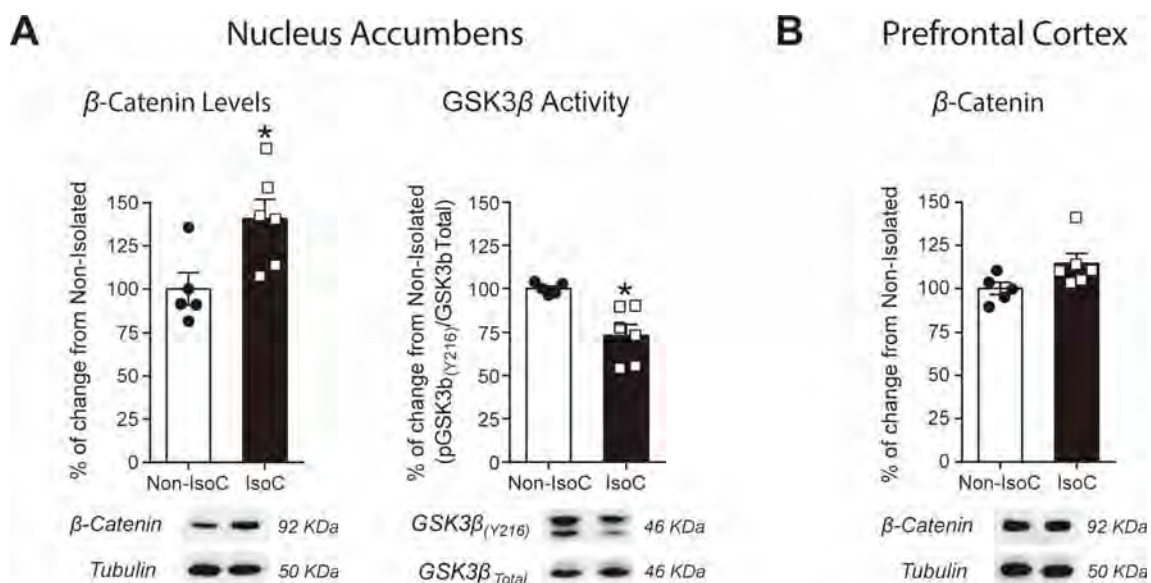


**Fig. 4** Adolescent isolated males show increased activity of the Wnt/ $\beta$ -catenin pathway in the NAcc after cocaine-induced expression of sensitization during adulthood. **A** Twenty-four hours after the expression of sensitization, isolated rats showed higher levels of  $\beta$ -

catenin together with lower levels of GSK3 $\beta$  activation in the NAcc. **B** No significant differences in the levels of  $\beta$ -catenin were found between control and stressed animals in the PFC after the expression of behavioral sensitization ( $*P < 0.05$  vs non-isolated group).

found significantly greater GSK3 $\beta$  activation [revealed by the level of phosphorylation in the activation site (Y216)] in isolated than in non-isolated rats at both time-points (Fig. 1C: P36  $t_9 = 3.104$ ,  $P < 0.05$  and Fig. 1E: P45,  $t_{12} = 2.224$ ,  $P < 0.05$ ), with no change in the expression of total GSK3 $\beta$  (P36,  $t_9 = 1.420$ ,  $P = 0.19$ ; P45,  $t_{12} = 0.39$ ,  $P = 0.70$ ). Together, these results suggest that, indeed, adolescent SI affects the activity of the canonical Wnt pathway.

The evaluation of  $\beta$ -catenin levels in the NAcc 24 h after the end of the isolation (P36) revealed no significant change (percentage change: non-isolated:  $100 \pm 8.32$ ; isolated:  $111.1 \pm 12.77$ ;  $t_{4,448} = 0.1676$ ,  $P = 0.8743$ , unpaired  $t$  test with Welch's correction).

These results indicate that the exposure to SI early in adolescence leads to a reduction in the activity of the canonical Wnt pathway particularly in the PFC, and this lasted for at least 10 days after the end of the stress, affecting the function and development of the PFC and altering different behaviors during adulthood.

### Five Days of Adolescent SI Increases Anxiety-Like Behaviors in Adulthood

To determine whether the emotional stress induced by SI during adolescence modifies behaviors in adulthood, we started by analyzing the response to a novel environment exhibited by isolated and non-isolated rats. We measured the total activity as well as the time spent in the center of an arena as an indication of anxiety [32], and found that less time was spent in the center of the open field by the isolated than by the non-isolated rats (Fig. 2B:  $t_{17,52} = 3.583$ ,  $P < 0.01$ , unpaired  $t$  test with Welch's correction), while there was no difference between the groups in total activity (Fig. 2B;  $t_{24} = 1.133$ ,  $P = 0.2682$ ). These findings strongly suggest that a short period of SI during adolescence can lead to long-lasting effects on anxiety-like behaviors in adulthood.

### Adolescent SI Facilitates Cocaine-Induced Sensitization During Adulthood: Possible Role of the Wnt/ $\beta$ -Catenin Pathway

The decrease in the activity of the Wnt/ $\beta$ -catenin pathway found after SI resembles the inhibition in the PFC the day after the last cocaine injection in animals that show behavioral sensitization, as we previously described [31]. Thus, we hypothesized that the activity of the Wnt/ $\beta$ -catenin pathway is a common target involved in the proactive effect of stress on drug-induced sensitization. To test this, we submitted either control or isolated (from P30 to P35) rats to a sensitization paradigm starting at P60, when the maturation of the dopaminergic innervation to the PFC is complete [44]. The rats received 5 injections of

cocaine (5 or 15 mg/kg, i.p., once per day) and were left undisturbed for 23 days, when they were challenged with another cocaine injection. Total activity was measured at D1 (P60), D5 (P64), and D28 (P87) (Fig. 3A). No significant differences were found in the overall activity between saline and cocaine animals with 5 mg/kg cocaine (Fig. 3B; significant effect of time,  $F_{2,18} = 7.64$ ,  $P < 0.01$  and time  $\times$  stress interaction,  $F_{2,18} = 4.28$ ,  $P < 0.05$ , two-way ANOVA). At this dose, there were no differences between groups when the percentages of increase in the initiation (D5/D1) were evaluated (Fig. 3C,  $t_9 = 0.649$ ,  $P = 0.54$ ). Regarding the expression (D28/D1), the rats isolated during adolescence showed greater increases in activity than the control group; however, these results did not reach statistical significance (Fig. 3C;  $t_{4,18} = 1.489$ ,  $P = 0.21$ , unpaired  $t$ -test with Welch's correction). The behavioral data after 15 mg/kg cocaine for both groups across the treatment are shown in Fig. 3D. Note that at this dose, while the behavioral activity rose between D1 and D5 in both groups, the response of the non-isolated rats on D5 was similar to that displayed after a cocaine challenge on D28. In contrast, the isolated rat group showed a significant increase in the cocaine-induced activity from D5 to D28. Two-way ANOVA revealed a significant effect of time ( $F_{2,26} = 11.23$ ,  $P < 0.0003$ ) as well as a significant time  $\times$  stress interaction ( $F_{2,26} = 5.58$ ,  $P < 0.01$ ). The percentage increases for the initiation (D5/D1) as well as for the expression (D28/D1) of sensitization are shown in Fig. 3E. We found that while there was no significant effect of stress on the initiation of behavioral sensitization (D5/D1:  $U = 27$ ,  $P = 0.9305$ , Mann–Whitney test), the rats isolated during adolescence showed markedly stronger expression of cocaine sensitization than non-isolated rats (D28/D1:  $U = 9$ ,  $P < 0.05$ , Mann–Whitney test).

The percentage increase represents changes in the individual responses through time (D1, D5, and D28). Therefore, these results suggest that the stress induced by SI during adolescence has a greater impact on the response to cocaine after a period of abstinence. In other words, while adolescent isolation seems not to affect the initiation of cocaine-induced sensitization during adulthood, it increases the individual vulnerability to its expression after a period of abstinence.

At the molecular level, we found that 24 h after the expression of sensitization to 15 mg/kg cocaine, the isolated rats showed higher levels of  $\beta$ -catenin in the NAcc, together with lower levels of GSK3 $\beta$  activation (Fig. 4A;  $\beta$ -catenin  $t_9 = 2.718$ ,  $P < 0.05$ ; GSK3 $\beta$   $t_9 = 3.674$ ,  $P < 0.01$ ). No changes were found in the total GSK3 $\beta$  expression ( $t_9 = 0.44$ ,  $P = 0.67$ ). In the PFC,  $\beta$ -catenin levels were similar in both groups (Fig. 4B;  $U = 4$ ,  $P = 0.052$ , Mann–Whitney test). No significant changes were found in the NAcc after 5 mg/kg cocaine (percentage

increase in  $\beta$ -catenin levels: Non-Isolated  $100.0 \pm 14.5$ ; Isolated  $120.3 \pm 12.6$ ;  $t_9 = 1.032$ ,  $P = 0.33$ ). These results show that a brief period of SI during adolescence enhances the likelihood of behavioral sensitization to cocaine during adulthood in a dose-response manner, as well as increasing the  $\beta$ -catenin levels in the NAcc.

### Five Days of Adolescent SI Induces Long-Term Effects on the Rewarding Properties of Cocaine During Adulthood

Greater cocaine rewarding effects have been shown in anxious rats [45]. Therefore, considering that we found an increase in anxiety-like behaviors in adult rats stressed during adolescence, we decided to assess whether adolescent SI can also alter the adult response to the rewarding properties of cocaine tested in a CPP paradigm. Rats were isolated for 5 days from P30 to P35 and then returned to their previous mates until adulthood, when a dose-response curve for the rewarding properties of cocaine was evaluated by CPP (Fig. 5A). The differences between the time spent on the drug-paired side during Post-test and Pre-Test trials (CPP score) for different cocaine doses (0.5, 1, and 5 mg/kg, i.p.) in non-isolated and isolated animals are shown in Fig. 5B. We found significant effects of the stress and the cocaine dose on the CPP score (Fig. 5B; two-way ANOVA main effect of stress,  $F_{1,89} = 6.02$ ,  $P < 0.05$  and dose,  $F_{3,89} = 8.087$ ,  $P < 0.0001$ ). Furthermore, *post hoc* analysis showed that, in contrast to the non-isolated group, isolated animals developed CPP at the lower cocaine doses (0.5 mg/kg and 1 mg/kg i.p.) with a CPP score significantly higher than that of the non-isolated group ( $P < 0.05$ , 0 mg/kg vs 0.5 and 1 mg/kg cocaine). At 5 mg/kg i.p., both groups developed CPP. Together, these results show that a brief period of SI in adolescence produces a shift to the left in the dose-response curve for cocaine, increasing the rewarding effects of cocaine during adulthood.

Considering that we found a significant difference between isolated and non-isolated rats during the expression of behavioral sensitization, we decided to test the persistence of CPP after a period of abstinence in some of the animals that received 5 mg/kg of cocaine. On P90, after 3 weeks of forced abstinence, rats received a cocaine priming injection (5 mg/kg) before the test (cocaine-primed test) (Fig. 5C). Two-way ANOVA revealed a significant main effect of the test ( $F_{1,13} = 17.281$ ,  $P < 0.01$ ; inset,  $F_{2,26} = 21.97$ ,  $P < 0.001$ ) with significant differences between isolated and non-isolated rats during the cocaine-primed test ( $P < 0.05$ ). Importantly, both the CPP score and the time spent in the drug-paired compartment during the cocaine-primed test were significantly higher in the isolated rats than in the non-isolated rats, revealing that only previously-isolated animals

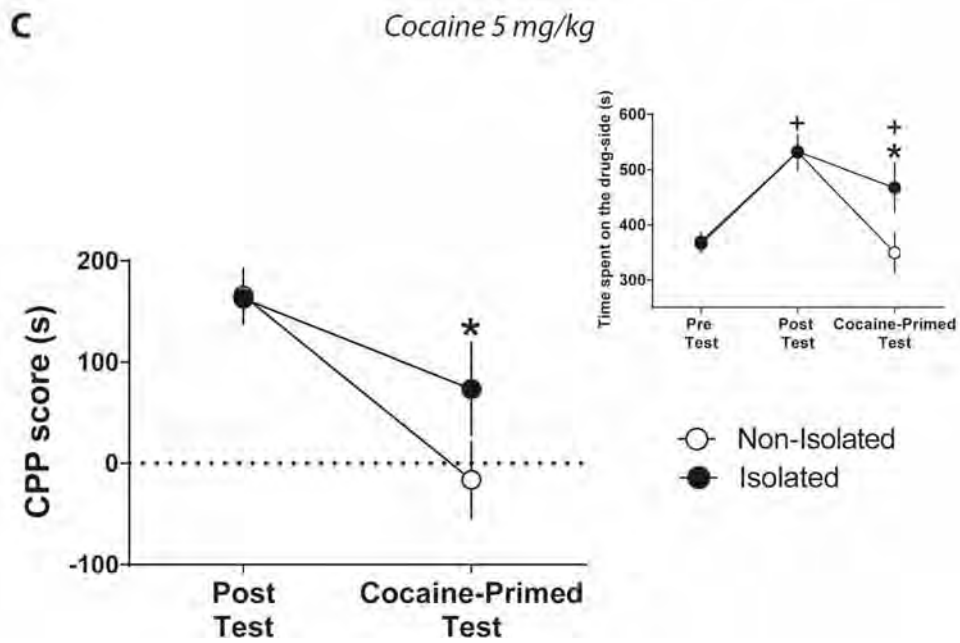
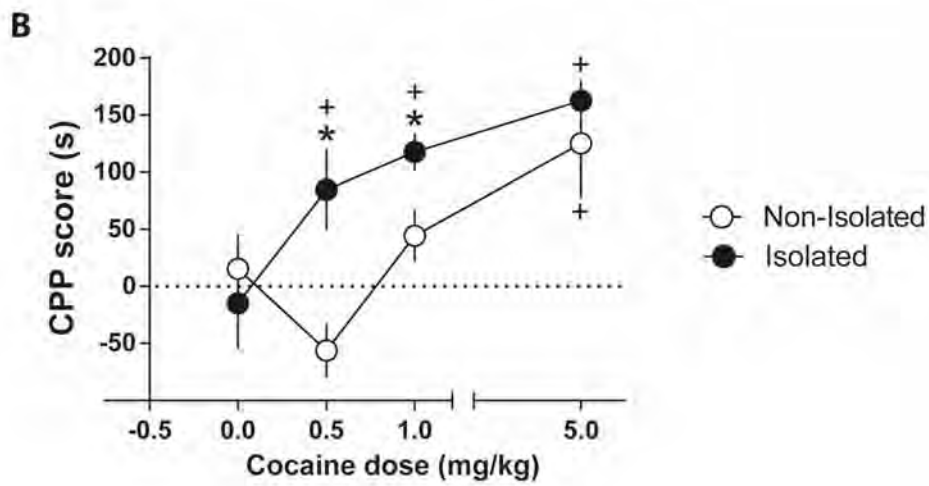
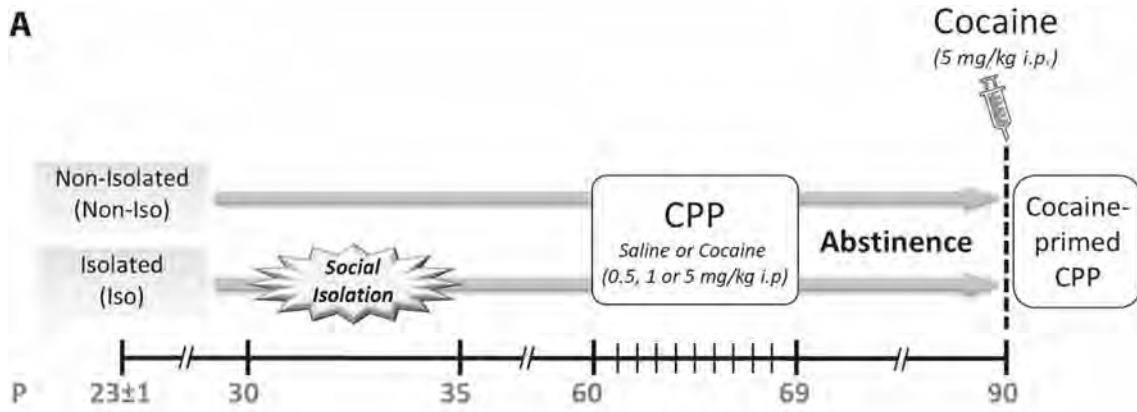
maintained a preference for the drug-paired side after receiving 5 mg/kg of cocaine.

All together, these results suggest that a short period of SI during adolescence not only leads to a long-lasting increase in sensitivity to the rewarding properties of cocaine but also that this persists after a period of forced abstinence.

### Discussion

The present study reveals that 5 days of SI during adolescence leads to molecular changes in the Wnt/ $\beta$ -catenin pathway not only after the stress but also after the expression of cocaine-induced sensitization. Furthermore, this short period of isolation affects anxiety-related behaviors during adulthood and increases CPP responses to cocaine. We postulate the Wnt/ $\beta$ -catenin pathway as another molecular neuroadaptation that may be involved in the stress-induced long-term effects on vulnerability to drugs of abuse. Our main findings showed that a brief period of adolescent SI induces: (1) changes in the activity of the Wnt/ $\beta$ -catenin pathway in the PFC that persist after the isolation ends; (2) high levels of anxiety-like behaviors during adulthood; (3) behavioral sensitization following forced abstinence; (4) changes in the Wnt/ $\beta$ -catenin pathway in the NAcc after cocaine challenge; (5) an increase in the acquisition of CPP to low (or subthreshold) doses of cocaine that are ineffective in control animals; and (6) a longer persistence of CPP in a cocaine-primed test.

The PFC is one of the brain areas most vulnerable to stress during adolescence, both in humans [46] and in animals [15], most likely because it is still undergoing extensive maturation [47, 48]. Here, we found for the first time that adolescent SI alters the expression of canonical Wnt pathway effectors in the PFC, a change that lasts at least for 10 days after the end of the stress. Notably, a decrease in  $\beta$ -catenin together with an increase in the activity of GSK-3 $\beta$  has also been reported in the PFC of teenage suicide victims [48], suggesting a critical role of the Wnt signaling pathway in the effects of stress on the developing brain. How this decrease alters the maturation of the PFC remains to be established. In neurons,  $\beta$ -catenin regulates synapse formation and function as well as axon growth and branching [23, 49]. Therefore, it is possible that the stress-induced reduction of  $\beta$ -catenin during adolescence affects the protracted maturation of the PFC circuitry, leading to long-term changes in PFC function. In line with this hypothesis, it has been reported that the same SI protocol alters the expression of structural proteins (e.g. spinophilin, synaptophysin, and myelin basic protein) mainly in the PFC [15], with some protein levels remaining altered until P60 [16]. While the mechanism behind the



◀ **Fig. 5** Social isolation during adolescence increases cocaine rewarding properties in adulthood. **A** Schematic of the experimental procedures. **B** Social isolation during adolescence shifted the CPP cocaine dose-response curve left during adulthood [results are expressed as the mean  $\pm$  SEM of the difference in the time spent on the drug-paired side during the Post-Test and Pre-Test (CPP score) for each cocaine dose (0, 0.5, 1, and 5 mg/kg i.p.);  $^+P < 0.05$  vs dose 0 for the same pretreatment;  $*P < 0.05$  vs non-isolated at the same dose, Fisher's LSD test]. **C** The cocaine-primed test during adulthood revealed that only socially isolated rats exposed to 5 mg/kg cocaine showed CPP persistence. The results are expressed as the mean  $\pm$  SEM of the difference in the time spent on the drug-paired side during the Post-Test or during the cocaine-primed test and the Pre-Test (CPP score). Inset, the mean  $\pm$  SEM of the time spent on the drug-paired side during the Pre, Post, and cocaine-primed tests for rats previously conditioned with 5 mg/kg i.p cocaine ( $*P < 0.05$  vs non-isolated group;  $^+P < 0.05$  vs Pre-Test group; Fisher's LSD test).

reduction in  $\beta$ -catenin levels after stress remains to be determined, it might involve the activation of dopamine 2 receptors (D2Rs). Briefly, it has been reported that while the systemic administration of D2R agonists decreases the activity of the pathway, D2R antagonists activate it [27, 28]. Like other stressors [8, 9, 50, 51], SI modifies dopaminergic activity in the PFC, so D2Rs could be responsible for the reduction in the Wnt/ $\beta$ -catenin pathway. In line with this hypothesis, preliminary results from our group have shown that daily injections of a D2R antagonist during the isolation period prevent the changes in the Wnt/ $\beta$ -catenin pathway.

Alterations in the function of the PFC are strongly associated with general anxiety disorders [52, 53] and here we found that rats that were socially isolated during adolescence showed higher levels of anxiety in adulthood than non-isolated animals. Similar results have been reported in adult animals exposed to SI for 1 h daily (with constant changes of cage partners) between P30 and P45 [18]. Notably, no effect on anxiety was reported immediately after the end of the adolescent stress exposure [15, 18], suggesting that such exposure has a greater impact on long-term rather than short-term behaviors involving the PFC. Recently, it has been shown that anxiety levels are predicted by cocaine responses in CPP, with high levels of anxiety linked to stronger responses [54, 55]. Therefore, we cannot rule out the possibility that the increase in the sensitivity to cocaine-induced CCP we found is partially driven by a stress-induced long-term increase in anxiety.

The changes of  $\beta$ -catenin in the PFC after adolescent SI resemble those we reported after cocaine treatment, where the activity of the canonical Wnt pathway on the day after the last injection in sensitized animals was inhibited, with no changes in the NAcc [31]. Furthermore, preventing this cocaine-induced reduction of  $\beta$ -catenin in the PFC hinders the later expression of cocaine-induced sensitization [30],

suggesting that such a reduction in  $\beta$ -catenin has a long-term impact on the neuronal circuits that allow the expression of cocaine sensitization. Our present results suggest a similar pattern for the effects induced by stress in cocaine responses, with isolated animals showing a reduction in the activity of the Wnt/ $\beta$ -catenin pathway only in the PFC, and displaying exacerbated cocaine sensitization in adulthood compared to non-isolated animals. Moreover, the increase in  $\beta$ -catenin levels we found in the NAcc of isolated rats after the expression of sensitization is also consistent with our previous report, showing that activation of the Wnt/ $\beta$ -catenin pathway in the NAcc is strongly associated with the expression of the behavioral sensitization phenomenon, with no changes after chronic cocaine injection in non-sensitized rats or after repeated saline injections [30]. While this is the first demonstration that previous stress exposure has a long-lasting impact on the activity of the pathway that may exacerbate the cocaine response later in life, it is not the first piece of evidence showing that the Wnt pathway is associated with stress [20, 56]. Indeed, it has been demonstrated in adult mice that while the inactivation of the canonical Wnt pathway in the NAcc can be linked to social defeat-induced depression-like behaviors, the overexpression of  $\beta$ -catenin might mediate stress resilience [20, 56]. Furthermore, 10 days of optogenetic stimulation of the PFC leads to modifications in the canonical Wnt pathway in the NAcc similar to those induced by social defeat, suggesting that changes in the PFC-to-NAcc connection could mediate future maladaptive responses to social stressors such as depressive-like behaviors [56]. It is important to note that, similar to our results, these authors did not find changes in the total levels of  $\beta$ -catenin in the NAcc after social defeat. Together, these results support a role of canonical Wnt pathway activity in the interplay between the PFC and the NAcc underlying the long-term effects on individual vulnerability to drugs induced by stress. Although our previous results support this idea in the context of cocaine plasticity [30, 31], further experiments are needed to evaluate whether preventing stress-induced  $\beta$ -catenin reduction in the PFC can prevent the increase in the vulnerability to develop behavioral sensitization to cocaine.

A particular feature of the behavioral sensitization model is the possibility of studying individual responses to a drug across time. This characteristic allowed us to discern a proactive effect of stress on drug responses that was not revealed when analyzing the absolute behavioral activity elicited by the psychostimulant. Specifically, our behavioral data showed that a cocaine challenge after a period of abstinence induced higher rates of expression of the behavioral sensitization to cocaine (D28/D1) in socially isolated rats, without showing significant differences in locomotor activity on D28 or D1 when comparing both

adolescent experiences. This same scenario has been reported after 15 days of adolescent chronic social stress (from P30 to P45) [57]. That study showed that, in spite of displaying similar locomotor activity in response to an amphetamine challenge, only previously-stressed animals expressed behavioral sensitization during adulthood [57], reinforcing the hypothesis that early life stress has an impact on the response to a psychostimulant later in life.

Our behavioral studies also revealed that only 5 days of SI during a period with a high level of social play behaviors can increase the reinforcing properties of cocaine during adulthood. We demonstrated that adolescent SI has a long-term impact on CPP acquisition as well as on its persistence after cocaine priming following a period of forced abstinence. In line with this, it has been shown that another stressor, social defeat, between P35 and P39 increases amphetamine induced-CPP during adulthood [58], supporting the idea that the adolescent brain is particularly vulnerable to the effects of stress, which alters the rewarding properties of different psychostimulants later in life. Whether this increase in the acquisition and persistence of CPP is a consequence of the reduction of the canonical Wnt pathway that we found after adolescent SI and/or involves changes in  $\beta$ -catenin need to be determined.

CPP studies can be performed using different experimental designs. The selection of biased CPP apparatus with a non-counterbalanced design was based on the literature [37, 38, 59]. Briefly, Cunningham *et al.* [59] showed that previous unconditioned side-preference could hinder the CPP measurement in a biased apparatus. In contrast, the use of a non-counterbalanced design in a biased apparatus has been shown to reduce the ceiling effects caused by previous side-preference [37, 59]. A downside of the non-counterbalanced design in a biased apparatus is the possibility of a false-positive result due to a drug's anxiolytic effect or the repeated exposure to the non-preferred side, which could help to overcome the initial aversion [37]. However, considering that cocaine is anxiogenic [60] rather than anxiolytic, that we have found place conditioning with (Cocaine-Primed Test) and without (Post-Test) cocaine, and that we did not find CPP in the saline group, the chances of a false positive are very low.

An interesting observation that deserves further investigation is related to the effects of abstinence in stressed and non-stressed animals. The data shown here using both CPP and behavioral sensitization clearly demonstrated an important impact of adolescent SI on the effects of cocaine after a period of abstinence, which suggests that abstinence triggers a distinct molecular mechanism in isolated animals that would render them highly susceptible to re-exposure to the psychostimulant.

Finally, it is important to highlight that the data presented here demonstrate that SI during adolescence has a long-term impact on cocaine responses in male rats. Further research is necessary to determine if the same responses occur in female rats, and to evaluate whether these effects can also be seen after adult SI.

## Conclusions

Based on our results and on previous evidence, we postulate that Wnt/ $\beta$ -catenin is another molecular mechanism involved in the proactive effect of adolescent stress on responses to drugs of abuse later in life [9, 61]. Remarkably, this is one of a few studies showing that SI during adolescence can impact cocaine-induced CPP as well as the expression of sensitization even 50 days after the end of the stress. Future studies will help to clarify the actual role of the canonical Wnt pathway and its relevance to the vulnerability of individuals to drugs.

**Acknowledgements** We thank Florencia Cerchiara and Patricia Rivera Podesta for their assistance with technical English. This work was supported by Consejo Nacional de Investigaciones Científicas y Técnicas (CONICET, PIP 112-201001-00243), Secretaría de Ciencia, Tecnología e Innovación Productiva de la Prov. Santa Fe (SeCTel, 2010-058-12), and Universidad Nacional de Rosario (UNR, BIO 295).

**Conflict of interest** The authors claim that there are no conflicts of interest.

## References

1. van Duijvenvoorde ACK, Peters S, Braams BR, Crone EA. What motivates adolescents? Neural responses to rewards and their influence on adolescents' risk taking, learning, and cognitive control. *Neurosci Biobehav Rev* 2016, 70: 135–147.
2. Caballero A, Granberg R, Tseng KY. Mechanisms contributing to prefrontal cortex maturation during adolescence. *Neurosci Biobehav Rev* 2016, 70: 4–12.
3. Lin Y, Li M, Zhou Y, Deng W, Ma X, Wang Q, *et al.* Age-related reduction in cortical thickness in first-episode treatment-naïve patients with schizophrenia. *Neurosci Bull* 2019, 35: 688–696.
4. Fuhrmann D, Knoll LJ, Blakemore SJ. Adolescence as a sensitive period of brain development. *Trends Cogn Sci* 2015, 19: 558–566.
5. Braun K, Bock J. The experience-dependent maturation of prefronto-limbic circuits and the origin of developmental psychopathology: implications for the pathogenesis and therapy of behavioural disorders. *Dev Med Child Neurol* 2011, 53 Suppl 4: 14–18.
6. Cacioppo JT, Hawkley LC. Perceived social isolation and cognition. *Trends Cogn Sci* 2009, 13: 447–454.
7. Baarendse PJ, Counotte DS, O'Donnell P, Vanderschuren LJ. Early social experience is critical for the development of cognitive control and dopamine modulation of prefrontal cortex function. *Neuropsychopharmacology* 2013, 38: 1485–1494.

8. Burke AR, McCormick CM, Pellis SM, Lukkes JL. Impact of adolescent social experiences on behavior and neural circuits implicated in mental illnesses. *Neurosci Biobehav Rev* 2017, 76: 280–300.
9. Burke AR, Miczek KA. Stress in adolescence and drugs of abuse in rodent models: role of dopamine, CRF, and HPA axis. *Psychopharmacology (Berl)* 2014, 231: 1557–1580.
10. Fosnocht AQ, Lucerne KE, Ellis AS, Olimpo NA, Briand LA. Adolescent social isolation increases cocaine seeking in male and female mice. *Behav Brain Res* 2019, 359: 589–596.
11. Baarendse PJ, Limpens JH, Vanderschuren LJ. Disrupted social development enhances the motivation for cocaine in rats. *Psychopharmacology (Berl)* 2014, 231: 1695–1704.
12. Karkhanis AN, Leach AC, Yorgason JT, Uneri A, Barth S, Niere F, *et al.* Chronic social isolation stress during peri-adolescence alters presynaptic dopamine terminal dynamics via augmentation in accumbal dopamine availability. *ACS Chem Neurosci* 2019, 10: 2033–2044.
13. Yajie D, Lin K, Baoming L, Lan M. Enhanced cocaine self-administration in adult rats with adolescent isolation experience. *Pharmacol Biochem Behav* 2005, 82: 673–677.
14. Phillips GD, Howes SR, Whitelaw RB, Robbins TW, Everitt BJ. Isolation rearing impairs the reinforcing efficacy of intravenous cocaine or intra-accumbens d-amphetamine: impaired response to intra-accumbens D1 and D2/D3 dopamine receptor antagonists. *Psychopharmacology (Berl)* 1994, 115: 419–429.
15. Leussis MP, Andersen SL. Is adolescence a sensitive period for depression? Behavioral and neuroanatomical findings from a social stress model. *Synapse* 2008, 62: 22–30.
16. Leussis MP, Lawson K, Stone K, Andersen SL. The enduring effects of an adolescent social stressor on synaptic density, part II: poststress reversal of synaptic loss in the cortex by adinazolam and MK-801. *Synapse* 2008, 62: 185–192.
17. McCormick CM, Robarts D, Kopeikina K, Kelsey JE. Long-lasting, sex- and age-specific effects of social stressors on corticosterone responses to restraint and on locomotor responses to psychostimulants in rats. *Horm Behav* 2005, 48: 64–74.
18. McCormick CM, Smith C, Mathews IZ. Effects of chronic social stress in adolescence on anxiety and neuroendocrine response to mild stress in male and female rats. *Behav Brain Res* 2008, 187: 228–238.
19. Dias C, Feng J, Sun H, Shao NY, Mazei-Robison MS, Damez-Werno D, *et al.* beta-catenin mediates stress resilience through Dicer1/microRNA regulation. *Nature* 2014, 516: 51–55.
20. Wilkinson MB, Dias C, Magida J, Mazei-Robison M, Lobo M, Kennedy P, *et al.* A novel role of the WNT-dishevelled-GSK3beta signaling cascade in the mouse nucleus accumbens in a social defeat model of depression. *J Neurosci* 2011, 31: 9084–9092.
21. Anastas JN, Moon RT. WNT signalling pathways as therapeutic targets in cancer. *Nat Rev Cancer* 2013, 13: 11–26.
22. Clevers H, Nusse R. Wnt/beta-catenin signaling and disease. *Cell* 2012, 149: 1192–1205.
23. Oliva CA, Vargas JY, Inestrosa NC. Wnts in adult brain: from synaptic plasticity to cognitive deficiencies. *Front Cell Neurosci* 2013, 7: 224.
24. Nusse R, Clevers H. Wnt/beta-catenin signaling, disease, and emerging therapeutic modalities. *Cell* 2017, 169: 985–999.
25. Metcalfe C, Bienz M. Inhibition of GSK3 by Wnt signalling—two contrasting models. *J Cell Sci* 2011, 124: 3537–3544.
26. Maguschak KA, Ressler KJ. The dynamic role of beta-catenin in synaptic plasticity. *Neuropharmacology* 2012, 62: 78–88.
27. Alimohamad H, Rajakumar N, Seah YH, Rushlow W. Antipsychotics alter the protein expression levels of beta-catenin and GSK-3 in the rat medial prefrontal cortex and striatum. *Biol Psychiatry* 2005, 57: 533–542.
28. Alimohamad H, Sutton L, Mouyal J, Rajakumar N, Rushlow WJ. The effects of antipsychotics on beta-catenin, glycogen synthase kinase-3 and dishevelled in the ventral midbrain of rats. *J Neurochem* 2005, 95: 513–525.
29. Sutton LP, Rushlow WJ. Regulation of Akt and Wnt signaling by the group II metabotropic glutamate receptor antagonist LY341495 and agonist LY379268. *J Neurochem* 2011, 117: 973–983.
30. Cuesta S, Batuecas J, Severin MJ, Funes A, Rosso SB, Pacchioni AM. Role of Wnt/beta-catenin pathway in the nucleus accumbens in long-term cocaine-induced neuroplasticity: a possible novel target for addiction treatment. *J Neurochem* 2017, 140: 114–125.
31. Cuesta S, Severin MJ, Batuecas J, Rosso SB, Pacchioni AM. Wnt/beta-catenin pathway in the prefrontal cortex is required for cocaine-induced neuroadaptations. *Addict Biol* 2017, 22: 933–945.
32. Hiroi R, Neumaier JF. Differential effects of ovarian steroids on anxiety versus fear as measured by open field test and fear-potentiated startle. *Behav Brain Res* 2006, 166: 93–100.
33. Steketeer JD, Kalivas PW. Drug wanting: behavioral sensitization and relapse to drug-seeking behavior. *Pharmacol Rev* 2011, 63: 348–365.
34. Pierce RC, Kalivas PW. A circuitry model of the expression of behavioral sensitization to amphetamine-like psychostimulants. *Brain Res Brain Res Rev* 1997, 25: 192–216.
35. Pierce RC, Bell K, Duffy P, Kalivas PW. Repeated cocaine augments excitatory amino acid transmission in the nucleus accumbens only in rats having developed behavioral sensitization. *J Neurosci* 1996, 16: 1550–1560.
36. Pacchioni AM, Vallone J, Worley PF, Kalivas PW. Neuronal pentraxins modulate cocaine-induced neuroadaptations. *J Pharmacol Exp Ther* 2009, 328: 183–192.
37. Bardo M, Bevins R. Conditioned place preference: what does it add to our preclinical understanding of drug reward? *Psychopharmacology* 2000, 153: 31–43.
38. Tzschentke TM. Measuring reward with the conditioned place preference (CPP) paradigm: update of the last decade. *Addict Biol* 2007, 12: 227–462.
39. Cui X, Li J, Li T, Ji F, Bu X, Zhang N, *et al.* Propofol and ketamine-induced anesthetic depth-dependent decrease of CaMKII phosphorylation levels in rat hippocampus and cortex. *J Neurosurg Anesthesiol* 2009, 21: 145–154.
40. Tedesco V, Ravagnani C, Bertoglio D, Chiamulera C. Acute ketamine-induced neuroplasticity: ribosomal protein S6 phosphorylation expression in drug addiction-related rat brain areas. *Neuroreport* 2013, 24: 388–393.
41. Silva Pereira V, Elfving B, Joca SRL, Wegener G. Ketamine and aminoguanidine differentially affect Bdnf and Mtor gene expression in the prefrontal cortex of adult male rats. *Eur J Pharmacol* 2017, 815: 304–311.
42. Li Y, Xu J, Xu Y, Zhao XY, Liu Y, Wang J, *et al.* Regulatory effect of general anesthetics on activity of potassium channels. *Neurosci Bull* 2018, 34: 887–900.
43. Heffner TG, Hartman JA, Seiden LS. A rapid method for the regional dissection of the rat brain. *Pharmacol Biochem Behav* 1980, 13: 453–456.
44. Naneix F, Marchand AR, Di Scala G, Pape JR, Coutureau E. Parallel maturation of goal-directed behavior and dopaminergic systems during adolescence. *J Neurosci* 2012, 32: 16223–16232.
45. Pelloux Y, Costentin J, Duterte-Boucher D. Anxiety increases the place conditioning induced by cocaine in rats. *Behav Brain Res* 2009, 197: 311–316.
46. Andersen SL, Teicher MH. Desperately driven and no brakes: Developmental stress exposure and subsequent risk for substance abuse. *Neurosci Biobehav Rev* 2009, 33: 516–524.

47. Spear LP. Adolescent brain development and animal models. *Ann N Y Acad Sci* 2004, 1021: 23–26.
48. Ren X, Rizavi HS, Khan MA, Dwivedi Y, Pandey GN. Altered Wnt signalling in the teenage suicide brain: focus on glycogen synthase kinase-3beta and beta-catenin. *Int J Neuropsychopharmacol* 2013, 16: 945–955.
49. Dickins EM, Salinas PC. Wnts in action: from synapse formation to synaptic maintenance. *Front Cell Neurosci* 2013, 7: 162.
50. Abercrombie ED, Keefe KA, DiFrischia DS, Zigmond MJ. Differential effect of stress on in vivo dopamine release in striatum, nucleus accumbens, and medial frontal cortex. *J Neurochem* 1989, 52: 1655–1658.
51. Cabib S, Puglisi-Allegra S. Different effects of repeated stressful experiences on mesocortical and mesolimbic dopamine metabolism. *Neuroscience* 1996, 73: 375–380.
52. Ball TM, Ramsawh HJ, Campbell-Sills L, Paulus MP, Stein MB. Prefrontal dysfunction during emotion regulation in generalized anxiety and panic disorders. *Psychol Med* 2013, 43: 1475–1486.
53. Page CE, Coutellier L. Adolescent stress disrupts the maturation of anxiety-related behaviors and alters the developmental trajectory of the prefrontal cortex in a sex- and age-specific manner. *Neuroscience* 2018, 390: 265–277.
54. Ladron de Guevara-Miranda D, Pavon FJ, Serrano A, Rivera P, Estivill-Torres G, Suarez J, *et al.* Cocaine-conditioned place preference is predicted by previous anxiety-like behavior and is related to an increased number of neurons in the basolateral amygdala. *Behav Brain Res* 2016, 298: 35–43.
55. Prast JM, Schardl A, Sartori SB, Singewald N, Saria A, Zernig G. Increased conditioned place preference for cocaine in high anxiety related behavior (HAB) mice is associated with an increased activation in the accumbens corridor. *Front Behav Neurosci* 2014, 8: 441.
56. Dias C, Dietz D, Mazei-Robison M, Sun H, Dames-Werno D, Ferguson D, *et al.* Dishevelled-2 regulates cocaine-induced structural plasticity and Rac1 activity in the nucleus accumbens. *Neurosci Lett* 2015, 598: 23–28.
57. Mathews IZ, Mills RG, McCormick CM. Chronic social stress in adolescence influenced both amphetamine conditioned place preference and locomotor sensitization. *Dev Psychobiol* 2008, 50: 451–459.
58. Burke AR, Watt MJ, Forster GL. Adolescent social defeat increases adult amphetamine conditioned place preference and alters D2 dopamine receptor expression. *Neuroscience* 2011, 197: 269–279.
59. Cunningham CL, Ferree NK, Howard MA. Apparatus bias and place conditioning with ethanol in mice. *Psychopharmacology (Berl)* 2003, 170: 409–422.
60. DeVries AC, Pert A. Conditioned increases in anxiogenic-like behavior following exposure to contextual stimuli associated with cocaine are mediated by corticotropin-releasing factor. *Psychopharmacology (Berl)* 1998, 137: 333–340.
61. Miczek KA, Yap JJ, Covington HE, 3rd. Social stress, therapeutics and drug abuse: preclinical models of escalated and depressed intake. *Pharmacol Ther* 2008, 120: 102–128.



# Aloin Protects Against Blood–Brain Barrier Damage After Traumatic Brain Injury in Mice

Yao Jing<sup>1</sup> · Dian-Xu Yang<sup>1</sup> · Wei Wang<sup>1</sup> · Fang Yuan<sup>1</sup> · Hao Chen<sup>1</sup> · Jun Ding<sup>1</sup> · Zhi Geng<sup>2</sup> · Heng-Li Tian<sup>1</sup>

Received: 10 July 2019 / Accepted: 6 December 2019 / Published online: 25 February 2020  
© Shanghai Institutes for Biological Sciences, CAS 2020

**Abstract** Aloin is a small-molecule drug well known for its protective actions in various models of damage. Traumatic brain injury (TBI)-induced cerebral edema from secondary damage caused by disruption of the blood–brain barrier (BBB) often leads to an adverse prognosis. Since the role of aloin in maintaining the integrity of the BBB after TBI remains unclear, we explored the protective effects of aloin on the BBB using *in vivo* and *in vitro* TBI models. Adult male C57BL/6 mice underwent controlled cortical impact injury, and mouse brain capillary endothelial bEnd.3 cells underwent biaxial stretch injury, then both received aloin treatment. In the animal experiments, we found 20 mg/kg aloin to be the optimum concentration to decrease cerebral edema, decrease disruption of the BBB, and improve neurobehavioral performance after cortical impact injury. In the cellular studies, the optimum concentration of 40 µg/mL aloin reduced apoptosis and reversed the loss of tight junctions by reducing the reactive oxygen species levels and changes in mitochondrial membrane potential after stretch injury. The mechanisms may be that aloin downregulates the phosphorylation of

p38 mitogen-activated protein kinase, the activation of p65 nuclear factor-kappa B, and the ratios of B cell lymphoma (Bcl)-2-associated X protein/Bcl-2 and cleaved caspase-3/caspase-3. We conclude that aloin exhibits these protective effects on the BBB after TBI through its anti-oxidative stress and anti-apoptotic properties in mouse brain capillary endothelial cells. Aloin may thus be a promising therapeutic drug for TBI.

**Keywords** Aloin · Blood–brain barrier · Traumatic brain injury · Oxidative stress · Apoptosis

## Introduction

Traumatic brain injury (TBI) is a crucial factor in disability and even death in young adults world-wide [1]. About 5.3 million people in the USA and ~ 7.7 million people in Europe are living with TBI-induced death and disabilities [2]. The population-based mortality from TBI in China is estimated to be ~ 13 per 100,000 [3]. Whether these patients die or survive with disability, the economic consequences of TBI are enormous [4].

TBI involves primary injury and secondary damage. The initial primary injury is caused by direct mechanical damage to brain tissue and tends to be irreversible. As a consequence of the injury, a cascade of effects is initiated, involving disruption of the blood–brain barrier (BBB), apoptosis, oxidative stress, formation of brain edema, and so on, leading to secondary damage [1, 2]. Some treatments are currently available to reduce the severity of secondary damage, but few are effective [5, 6].

The BBB is the major functional barrier in the central nervous system. It inhibits the extravasation of intravascular contents such as toxic substances, pathogens, and blood

Yao Jing and Dian-Xu Yang have contributed equally to this work.

✉ Jun Ding  
djdjdoc@126.com

✉ Zhi Geng  
gengzhi1998@163.com

✉ Heng-Li Tian  
tianhlsh@126.com

<sup>1</sup> Department of Neurosurgery, Shanghai Jiao Tong University Affiliated Sixth People's Hospital, Shanghai 200233, China

<sup>2</sup> Department of Neurology, Shanghai Jiao Tong University Affiliated Sixth People's Hospital, Shanghai 200233, China

cells into the brain parenchyma, and pumps out cerebral waste materials so that the balance of the biochemical environment is maintained to ensure basic neural functions [7, 8]. Cerebrovascular endothelial cells (ECs) are the main components of the BBB and are connected by the continuous intercellular tight junctions (TJs), mainly consisting of zonula occludens (ZO) and occludin [9, 10]. After TBI, the function of the BBB is disrupted as a result of breakage of the continuous intercellular TJs, triggering secondary damage [7]. Therefore, ensuring the protection of the BBB is considered a promising therapeutic strategy for reducing secondary brain damage.

Aloin, an anthraquinone glycoside, is one of the major active ingredients extracted from *Aloe* species [11]. According to previous studies, aloin has shown anti-aging activity in a D-galactose-induced mouse model [12], anti-oxidative stress and anti-apoptotic activity in oxygen- and glucose-deprivation-induced PC12 cell injury [13], an anti-tumor growth effect in human colorectal cancer [14], and immunomodulatory and anti-inflammatory responses in both a lipopolysaccharide-activated human umbilical vein EC model and a model of ultraviolet B-induced paw sunburn in rats [11, 15]. However, there is little evidence that aloin has a protective action on the BBB after TBI, and if so, what the possible mechanism may be.

In this study, we aimed to explore the protective effects of aloin on the BBB in TBI models *in vivo* and *in vitro* and to investigate the possible underlying mechanisms.

## Materials and Methods

### Experimental Animals and Protocols

We used adult male C57BL/6 mice weighing 20–25 g and aged 8–10 weeks (Shanghai SLAC Laboratory Animal Corp., Shanghai). The use of animals was approved by the Institutional Animal Care and Use Committee of Shanghai Jiao Tong University, Shanghai, China, and the animal experiments were performed according to the Guidelines for Laboratory Animal Research of Shanghai Jiao Tong University. Aloin (> 97% pure) was from Sigma (St. Louis, MO) and diluted in a mixture of dimethyl sulfoxide and normal saline. First, the animals were randomly divided into sham-operated, TBI, TBI+vehicle, and TBI+aloin (10, 20, and 30 mg/kg) groups to determine the optimum concentration of aloin by measuring brain water content. Subsequently, based on the results, we randomly divided the remaining mice into three groups: sham-operated, TBI+vehicle, and TBI+aloin (optimum concentration). Each group contained 6 or 12 mice (12 for the neurobehavioral tests only) in each experiment. The vehicle or aloin was injected intraperitoneally 30 min

before TBI was induced and then injected once daily until the experiments were finished. Except for the mice used in behavioral tests, mice were euthanized 3 days after TBI model completion, and brain tissue was collected for further analyses.

Controlled cortical impact (CCI) was adopted as the TBI model. After each C57BL/6 mouse was anesthetized with ketamine (75 mg/kg) and xylazine (10 mg/kg), we fixed its head in a stereotaxic frame, and a heating pad was placed under its body to maintain a temperature of  $\sim 37^{\circ}\text{C}$ . Then, a midline incision  $\sim 10$  mm long was made on the scalp under aseptic conditions. The skin and fascia were retracted and a bone window 4 mm in diameter was made by a trephine at the center of the right parietal bone, 1 mm lateral to the sagittal suture. Extreme care was required during this operation. If the dural integrity was compromised, the mouse was excluded from the study. At that point, the treatment of the sham-operated group was complete. Then, the TBI model was created using a CCI device (PinPoint Precision Cortical Impactor PCI3000; Hatteras Instruments Inc., Cary, NC), which has been used in previous studies [16, 17]. A rounded steel impactor tip 3 mm in diameter was placed precisely on the exposed intact dura, and the cortical surface was struck vertically at an impact velocity of 1.5 m/s, a deformation depth of 1.5 mm, and a dwell time of 100 ms. The injured cortical surface was compressed with sterile cotton until the bleeding was controlled. The cranial defects in these mice, including the sham-operated group, were sealed with sterile bone wax, and the incisions were closed with interrupted 6–0 silk sutures under aseptic conditions. All animals were placed in heated cages to regain full consciousness, and then returned to their home cages.

### Measurement of Brain Water Content and Brain Edema

The brain water content of mice was measured using the wet-dry method. In brief, 3-mm coronal sections of the ipsilateral cortex, centered on the impact site, were used to evaluate the water content. The sections were immediately weighed to obtain the wet weight, and then dried for 24 h in an oven ( $100^{\circ}\text{C}$ ) to determine the dry weight. Brain water content was calculated as follows:  $(\text{wet weight} - \text{dry weight}) / \text{dry weight} \times 100\%$ .

Magnetic resonance imaging (MRI) of mouse heads was performed with a 3.0 T scanner (Excite; Siemens Signa, Buffalo Grove, IL) 3 days after TBI. The parameters of the T2-weighted MRI were as follows: repetition time, 3670 ms; echo time, 97 ms; slice thickness, 0.9 mm; field of view,  $70 \times 70 \text{ mm}^2$ ; and number of excitations, 1.5. The volume of the brain edema lesion, including the contusion area, was assessed from coronal T2-weighted scans using

ImageJ software (National Institutes of Health, Bethesda, MD) by a physician proficient in neuroimaging.

### Analysis of Evans Blue (EB) Extravasation

The extravasation of EB was used to assess the degree of BBB damage 3 days after TBI. EB dye (2%) was injected intravenously at 4 mL/kg, and then 2 h later the mice were perfused through the heart with normal saline to completely wash out the intravascular dye. After the brain was removed, it was divided into two hemispheres and weighed immediately. Subsequently, each hemisphere was homogenized in 50% trichloroacetic acid and centrifuged for 20 min at 12,000×g. The supernatant was transferred into 3 volumes of ethanol and the EB content of the cerebral hemispheres was assessed by a spectrophotometer (Bio-Tek, Winooski, VT) at 610 nm, and then quantified as micrograms per gram of brain tissue.

### Neurological Severity Score Determination

The modified neurological severity score (mNSS) was adopted to assess the neurological status of mice before TBI and at 1, 3, 7, and 14 days after TBI. As described in a previous report [18], the mNSS includes motor, sensory, balance, and reflex tests, for which a normal score is 0 and the maximal deficit score is 14 points. One point is awarded for deficiencies in each of the categories listed above; the higher the score, the more severe the neurological injury.

The rotarod test was used to assess motor coordination as previously described [19]. Briefly, each mouse was trained on the rod at speeds that accelerated from 0 to 40 rounds/min within 5 min for 3 days. Each training day included 3 trials. Before TBI, the mean value for 3 trials was calculated as the baseline value for each mouse. After TBI, the rotarod test time data were collected at 1, 3, 7, and 14 days.

The spatial learning and memory of mice were evaluated by a Morris water maze test [20]. The apparatus was a circular tank with warm water which contained white lime to make the water opaque. The pool was divided into 4 quadrants with visual cues, and a platform 10 cm in diameter was submerged 1 cm below the surface of the water in one quadrant. On training days (14–18 days after TBI), each mouse received 4 training trials per day; the starting positions were randomly selected from among the 4 quadrants. Mice were allowed 60 s to find the platform. If they failed to locate the platform within 60 s, they were manually guided to it and allowed to stay there for 15 s; this result was recorded as 60 s. The mean time per training day were recorded for comparison. On the test day (19 days after TBI), the probe trial was conducted in the absence of

the platform. Each mouse was put into the quadrant opposite to the normal location of the platform and allowed to swim freely for 60 s. The latency to the platform location, the number of crossings, and the time spent in the target quadrant were recorded. All the neurobehavioral tests were assessed by an investigator who was blinded to the experimental design.

### Experimental Cell Design

The bEnd.3 mouse brain capillary ECs were from the American Type Culture Collection (Manassas, VA). They were cultured in Dulbecco's modified Eagle's medium (DMEM; Gibco Laboratories, Grand Island, NY) containing 10% fetal bovine serum and 1% penicillin/streptomycin in a 37°C humidified incubator infused with a mixture of 5% CO<sub>2</sub> and 95% air [21]. First, we explored the effects on cell viability of different concentrations of aloin using a Cell Counting Kit-8 (CCK-8) assay (Dojindo, Tokyo). Next, we randomly divided the cells into control, stretch injury (SI), SI+vehicle, and SI+aloin (10, 20, 40, 60, and 80 µg/mL) groups to determine the optimum concentration of aloin using a lactate dehydrogenase (LDH) release assay. Finally, according to the results, the bEnd.3 cells were randomly divided into three groups: control, SI+vehicle, and SI+aloin (optimum concentration). The vehicle and aloin solutions were added 30 min before SI of cells, which were then cultured for an appropriate time after SI for most of the subsequent biological tests. Each experiment was repeated 6 times.

Mechanical SI of bEnd.3 cells was used to simulate TBI *in vitro*. The cells were seeded at  $0.5 \times 10^5$  cells/cm<sup>2</sup> onto BioFlex® 6-well culture plates (Flexcell International Corp., Burlington, NC) with collagen-coated Silastic membranes. After the cells were cultured overnight, a biaxial SI was induced in cells using the Cell Injury Controller II system (Virginia Commonwealth University, Richmond, VA). This instrument released a 50-ms burst of nitrogen gas to cause a 7.5-mm downward deformation of the Silastic membrane and the adherent cells, analogous to the mechanical stress exerted on brain tissue by rotational acceleration and deceleration injury [2, 22, 23].

### Cell Viability Assay

The bEnd.3 cells were seeded into 96-well plates at  $1 \times 10^4$  per well and cultured overnight. The different concentrations of aloin (10, 20, 40, 60, and 80 µg/mL) were administered to the cells, which were cultured for 4.5 h. After 10 µL of the CCK-8 reaction solution was added into each well, the cells were conventionally incubated for 2 h. The absorbance of each well was then measured at 450 nm using a spectrophotometer.

### LDH Release Assay

LDH release from bEnd.3 cells was determined using a cytotoxicity detection kit (Roche, Mannheim). The 100  $\mu$ L supernatant from each group was transferred into 96-well plates. After adding 100  $\mu$ L reaction solution to each well, the mixed samples were incubated for 30 min in the dark at 25°C. The LDH release was determined as the absorbance of each well at 490 nm measured using a spectrophotometer.

### Terminal Deoxynucleotidyl Transferase-mediated dUTP Nick-end Labeling (TUNEL) Assay

Samples of bEnd.3 cells from the control, SI+vehicle, and SI+aloin groups were collected to count the apoptotic cells by TUNEL assay using the *in-situ* cell death detection kit, TMR red (Roche, Diagnostics, Basel). Briefly, after immersion in 4% paraformaldehyde for 30 min and 0.3% TritonX-100 for 10 min, the samples were allowed to react with the TUNEL mixture solution for 1 h at 37°C, and then stained with 4',6-diamidino-2-phenylindole (DAPI; 1:1000; Beyotime Biotechnology, Nantong, Jiangsu) for 5 min in the dark. Apoptotic cells were observed and recorded under a confocal fluorescence microscope (Leica TCS SP5 II; Zeiss, Jena, Germany). The apoptosis rate was calculated as follows: apoptotic cells/all cells in a field  $\times$  100%.

### Immunostaining

Brain cryosections 20  $\mu$ m thick and Silastic membranes with bEnd.3 cells were fixed in cold anhydrous methanol. After penetration with 0.3% TritonX-100 and blocking with 10% bovine serum albumin, the samples were incubated overnight with the following primary antibodies at 4°C: rabbit anti-ZO-1 (1:200; Life Technologies, Carlsbad, CA)/goat anti-CD31 (1:200; R&D Systems, Minneapolis, MN) and mouse anti-occludin (1:200; Invitrogen, Carlsbad, CA)/goat anti-CD31 (1:200) double-staining for tissue; rabbit anti-ZO-1 (1:200) and mouse anti-occludin (1:200) single-staining for cells. Subsequently, the samples were incubated with the mixed corresponding secondary antibodies (1:400) for 1 h, and the cells were stained with DAPI (1:1000) for 10 min in the dark at room temperature. Immunofluorescence images were captured using the fluorescence microscope.

### Western Blot Analysis

The brain tissue samples and bEnd.3 cells were lysed in a mixed lysis buffer at the same protein concentration. After denaturation, equal volumes were separated by sodium

dodecyl sulfate-polyacrylamide gel electrophoresis and transferred to a polyvinylidene difluoride membrane. The membrane was blocked with 5% skimmed milk powder for 1 h and then incubated at 4°C overnight with antibodies against the following: ZO-1 and occludin (1:1000); p38, phospho-p38 (p-p38), p65, phospho-p65 (p-p65), B cell lymphoma (Bcl)-2, Bcl-2-associated X protein (Bax), cleaved caspase-3, and caspase-3 (1:1000; Cell Signaling Technology, Beverly, MA);  $\beta$ -actin,  $\beta$ -tubulin, and GAPDH (1:1000; Abcam, Cambridge). After washing 3 times, the membrane was incubated with corresponding horseradish peroxidase-conjugated secondary antibodies (1:5000) for 1 h at room temperature. Protein signals were measured using a gel imaging system (Millipore, Billerica, MA) with the enhanced chemiluminescence reagent (Pierce, Rockford, IL), and then the results were analyzed with Quantity One software (BioRad, Hercules, CA).

### Measurement of Intracellular Reactive Oxygen Species (ROS)

The intracellular ROS generation of bEnd.3 cells was assessed using a DCFH-DA Assay Kit (Beyotime Biotechnology, Nantong, China). Briefly, 1 mL of 10  $\mu$ mol/L DCFH-DA diluent was added to a BioFlex<sup>®</sup> 6-well culture plate, and then the cells were incubated for 20 min in the dark at 37°C. After washing the wells 3 times with DMEM, the fluorescence intensity was measured with a fluorescence spectrophotometer (Horiba Scientific, Piscataway, NJ), a fluorescence microscope, and a flow cytometer (BD Biosciences, San Jose, CA) at an excitation wavelength of 488 nm and an emission wavelength of 525 nm.

### Determination of Mitochondrial Membrane Potential ( $\Delta\Psi_m$ )

The  $\Delta\Psi_m$  of bEnd.3 cells was assessed using a JC-1 assay kit (Beyotime Biotechnology). Briefly, 1 mL DMEM and 1 mL JC-1 reaction solution were added to a BioFlex<sup>®</sup> 6-well culture plate, and then the cells were incubated for 20 min in the dark at 37°C. After washing the wells twice with JC-1 buffer,  $\Delta\Psi_m$  fluorescence images were captured on the fluorescence microscope, and the  $\Delta\Psi_m$  fluorescence intensity was determined by flow cytometry. Red fluorescence indicated healthy cells with a normal  $\Delta\Psi_m$ , while green fluorescence indicated potentially apoptotic cells with a low  $\Delta\Psi_m$ . The ratio of red to green fluorescence was used to quantify the differences in  $\Delta\Psi_m$  in the different groups of bEnd.3 cells.

## Statistical Analysis

All data are expressed as the mean  $\pm$  standard deviation (SD). Comparisons among multiple groups were assessed by one-way analysis of variance followed by Tukey's *post-hoc* test, and differences between two groups were determined by the unpaired Student's *t* test.  $P < 0.05$  was considered to be statistically significant. Statistical analyses were demonstrated on IBM SPSS version 20 (SPSS Inc., Chicago, IL). Quantified bar graphs of the data were created in GraphPad Prism version 6 (GraphPad Software, San Diego, CA).

## Results

### Aloin Reduces Brain Edema by Protecting the BBB after TBI in Mice

Brain water content is one of the most important indicators of the severity of edema after TBI, and we found that the water content markedly increased after TBI in mice. To determine the optimum concentration of aloin for the mouse TBI model, we measured the brain water content using the wet-dry method for each of the different concentrations of aloin (10, 20, and 30 mg/kg) at 3 days after TBI. There were no differences between the TBI and vehicle groups ( $82.14\% \pm 0.29\%$  vs  $82.17\% \pm 0.22\%$ ), or the 20 mg/kg and 30 mg/kg aloin groups ( $79.77\% \pm 0.38\%$  vs  $79.87\% \pm 0.38\%$ ) (both  $P > 0.05$ ). There was a significant reduction in the 10 mg/kg aloin

group compared with the vehicle group ( $80.92\% \pm 0.25\%$  vs  $82.17\% \pm 0.22\%$ ), as well as in the 20 mg/kg aloin group compared with the 10 mg/kg aloin group ( $79.77\% \pm 0.38\%$  vs  $80.92\% \pm 0.25\%$ ) (both  $P < 0.01$ ; Fig. 1A). Therefore, 20 mg/kg was used as the optimum concentration for further experiments.

The brain edema lesions were directly visualized as high intensity areas contoured by white lines on contiguous coronal T2-weighted scans (Fig. 1B). The lesion areas were evident in the vehicle group and were significantly smaller after treatment with aloin at 3 days post-TBI. These results were consistent with the statistical analyses ( $24.67\% \pm 3.93\%$  vs  $14.83\% \pm 3.13\%$ ,  $P < 0.01$ ; Fig. 1B).

The extent of damage to the BBB influenced the severity of brain edema as previously described [2]. We assayed the images of EB extravasation to assess the permeability of the BBB. Statistical analyses revealed that aloin treatment significantly reduced EB leakage at 3 days after TBI, indicating that TBI-induced BBB damage is attenuated by aloin ( $5.69 \pm 0.56 \mu\text{g/g}$  vs  $8.06 \pm 0.59 \mu\text{g/g}$ ,  $P < 0.01$ ; Fig. 1C).

### Aloin Alleviates the Disruption of TJ Proteins of the BBB in the Pericontusional Areas after TBI in Mice

TJ proteins, including ZO-1 and occludin, play important roles in maintaining the functions of the BBB. TBI led to the loss of ZO-1 and occludin in the pericontusional areas.

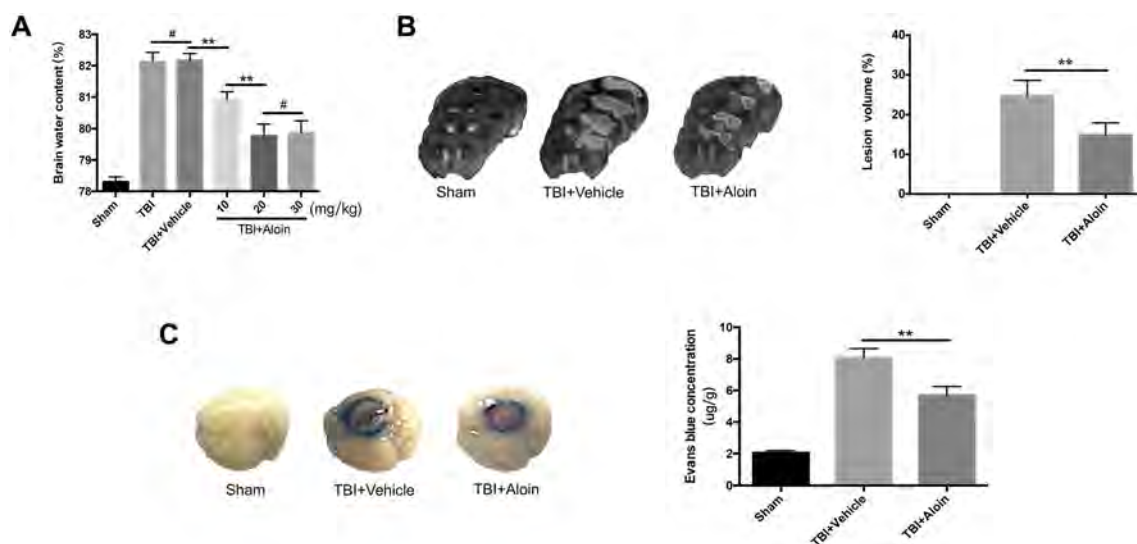
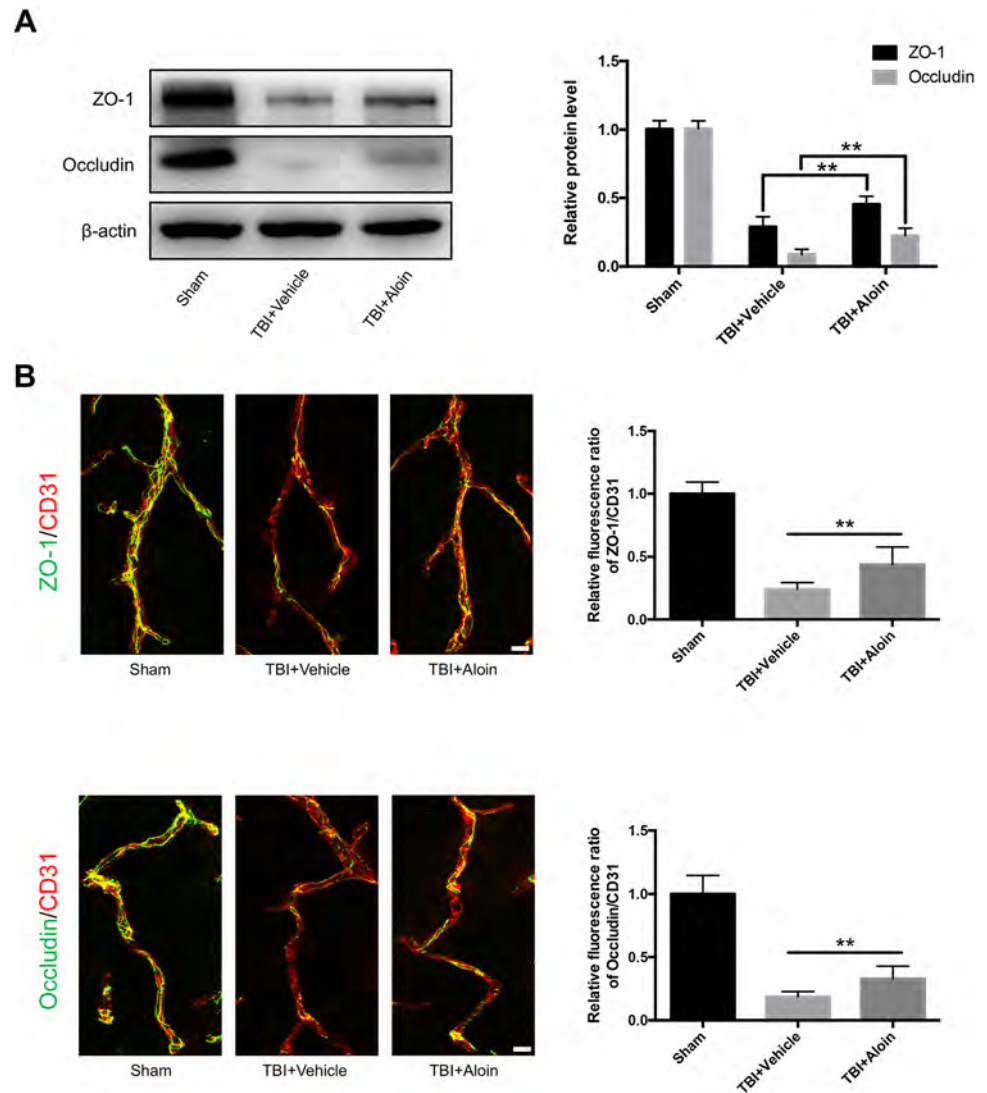


**Fig. 1** Aloin attenuates TBI-induced brain edema caused by damage to the BBB in mice. **A** Brain water content in different groups at 3 days post-TBI. **B** Representative coronal T2-weighted MRI scans and brain lesion volumes in sham, TBI+vehicle, and TBI+aloin groups at 3 days after TBI (white contours indicate areas of edema).

**C** Representative images of EB extravasation and statistics for EB content in the three groups at 3 days after TBI (blue areas indicate EB extravasation).  $n = 6/\text{group}$ , data are presented as the mean  $\pm$  SD,  $**P < 0.01$ ,  $\#P < 0.05$ .

**Fig. 2** Aloin alleviates the loss of TJ proteins in the BBB in the pericontusional area 3 days after experimental TBI in mice.

**A** Representative western blots and levels of ZO-1 and occludin in the sham, TBI+vehicle, and TBI+aloin groups. **B** Representative co-stained immunofluorescence and levels of ZO-1/CD31 and occludin/CD31 in the three groups (scale bars, 75  $\mu\text{m}$ ).  $n = 6/\text{group}$ , data are presented as the mean  $\pm$  SD.  $**P < 0.01$ , aloin vs vehicle group.



Western blot analyses revealed that the levels of ZO-1 and occludin were much higher in the aloin-treated group than in the vehicle-treated group at 3 days after TBI (both  $P < 0.01$ ) (Fig. 2A). At the same time, double immunostaining for ZO-1/CD31 and occludin/CD31 revealed continuous ZO-1 and occludin staining along the EC margin of the cerebral capillaries in the sham group. Gaps and losses were present in the vehicle group, but they were fewer after aloin treatment (both  $P < 0.01$ ; Fig. 2B).

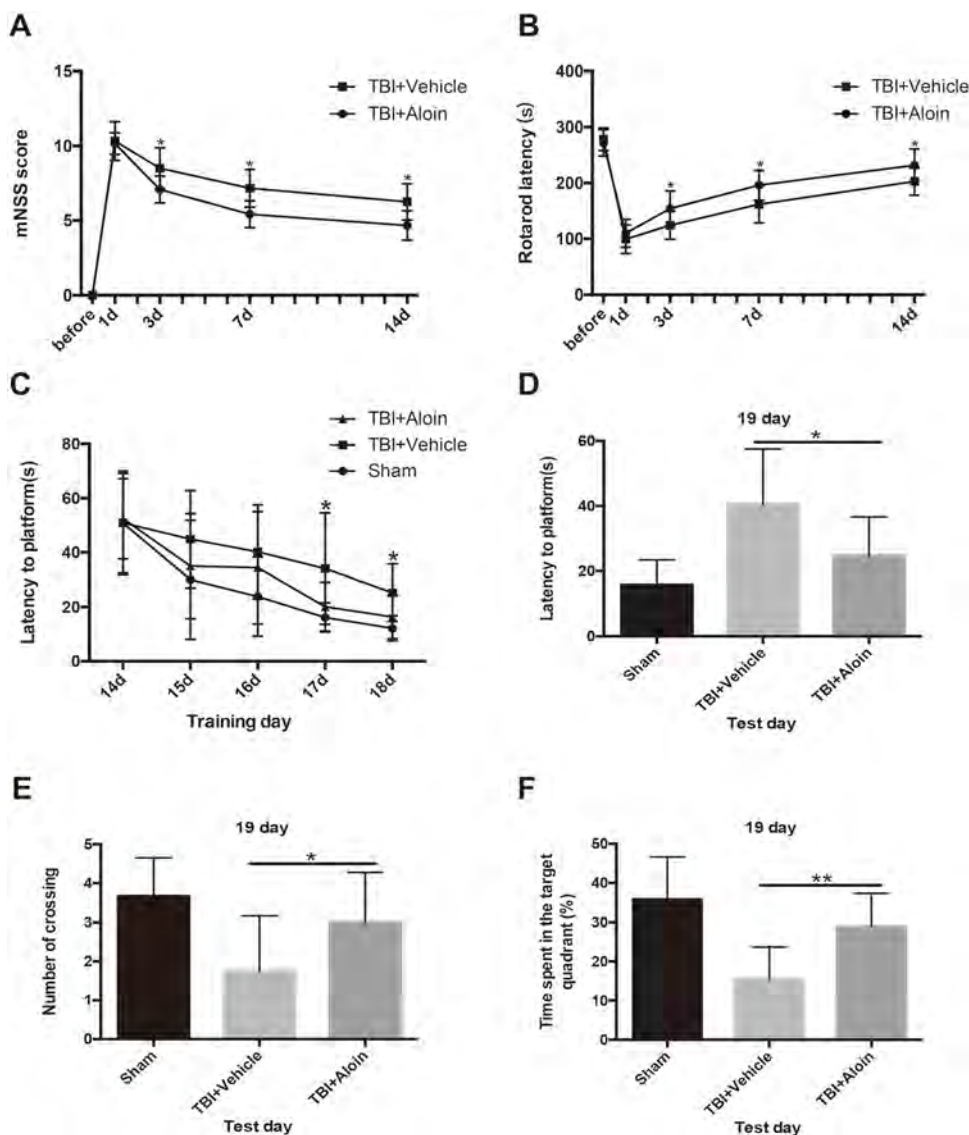
### Aloin Improves Recovery from Neurological Deficits after TBI in Mice

Neurological deficits were present after TBI in mice, and we explored the effects of aloin on the recovery of neurological functions using the mNSS, rotarod test, and Morris water maze test. The results of the mNSS, which included motor, sensory, balance, and reflex tests, were

lower in the aloin group than in the vehicle group at 3, 7, and 14 days after TBI (all  $P < 0.05$ ; Fig. 3A). In the rotarod test, which focused on motor coordination, the durations that mice stayed on the rod in the aloin group were longer than those in the vehicle group at 3, 7, and 14 days post-TBI (all  $P < 0.05$ ; Fig. 3B), consistent with the mNSS data.

The Morris water maze was used to assess spatial learning and memory. In the training trials, the aloin group exhibited a shorter latency than the vehicle group at 17 and 18 days after TBI (both  $P < 0.05$ ; Fig. 3C). In the probe trials, the neurobehavioral outcomes of latency to the platform, number of crossings, and time spent in the target quadrant were better in the aloin group than in the vehicle group at 19 days after TBI ( $P < 0.05$ ,  $P < 0.05$ , and  $P < 0.01$ , respectively; Fig. 3D–F).

**Fig. 3** Aloin improves neurological functions after experimental TBI in mice. **A, B** mNSS (A), and rotarod latency (B) before TBI and at 1, 3, 7, and 14 days after TBI in the TBI + vehicle and TBI + aloin groups. **C** Morris water maze training results during 14–18 days after TBI in the sham, TBI + vehicle, and TBI + aloin groups. **D–F** Time of first arrival at the platform (D), number of times crossing the platform (E), and percentage of time in the platform quadrant (F) in the Morris water maze 19 days after TBI in the three groups. *n* = 12/group, data are presented as the mean ± SD, \**P* < 0.05, \*\**P* < 0.01, aloin vs vehicle group.



**Aloin Decreases Apoptosis, and Protects the Integrity of TJ Proteins in bEnd.3 Cells after Stretch Injury**

To explore the cytotoxicity of aloin, we used CCK-8 assays to evaluate the viability of bEnd.3 cells at different concentrations (10, 20, 40, 60, and 80 µg/mL) for 4.5 h. There were no differences between the control, 10 µg/mL, 20 µg/mL, and 40 µg/mL aloin (all *P* > 0.05). With increasing aloin concentrations, cell viability continuously declined (*P* < 0.05 for both 40 vs 60 µg/mL and 60 vs 80 µg/mL; Fig. 4A). In addition, the release of LDH, an apoptosis-associated index, increased significantly after SI and was used to determine the optimum concentration of aloin at 4 h post-SI. Consistent with the CCK-8 assays, 40 µg/mL was the optimum concentration and this was used in subsequent experiments (Fig. 4B).

TUNEL and DAPI double-positive cells verified as apoptotic cells were detected in the control and SI groups. The statistical analyses revealed that the apoptosis rates were significantly lower after aloin treatment than in the vehicle-treated group at 4 h post-SI (*P* < 0.01; Fig. 4C).

Immunostaining and western blot analyses showed that the ZO-1 and occludin expression levels increased after aloin treatment compared with the vehicle-treated group at 4 h post-SI (all *P* < 0.01; Fig. 5A, B).

**Aloin Attenuates Intracellular ROS Generation after Stretch Injury of bEnd.3 Cells**

After SI, a great deal of ROS occurred in bEnd.3 cells, as assessed by DCFH-DA. The level of ROS reached its highest point 2 h after SI. Aloin (40 µg/mL) noticeably reduced the ROS production at 1 h, 2 h, and 4 h after SI (all

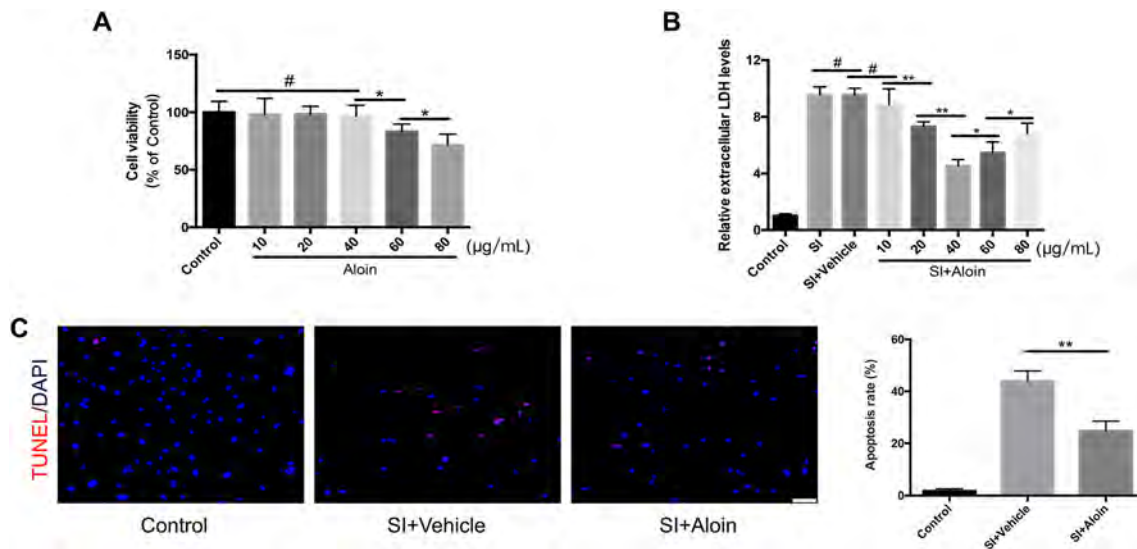


**Fig. 4** Aloin reduces the damage to bEnd.3 cells by experimental SI. **A** Cell viability at different concentrations of aloin after 4.5 h assessed by CCK-8. **B** Effects of different concentrations of aloin on cells 4 h after SI assessed by LDH release. **C** Representative TUNEL

staining of apoptotic cells and quantified apoptosis rate at 4 h after SI in control, SI+vehicle, and SI+aloin groups (scale bar, 75 µm).  $n = 6/\text{group}$ , data are presented as the mean  $\pm$  SD,  $*P < 0.05$ ,  $**P < 0.01$ ,  $\#P > 0.05$ .

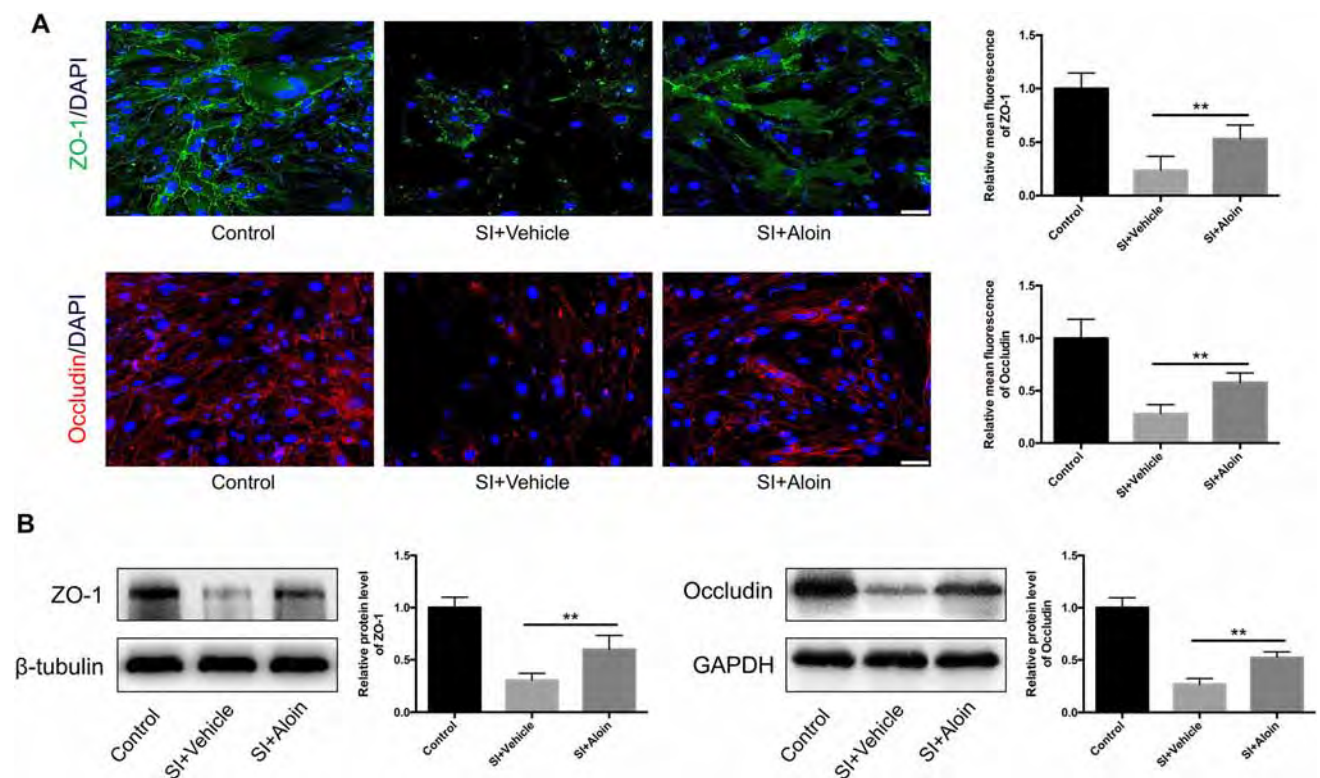


**Fig. 5** Aloin alleviates the loss of TJ proteins after experimental SI in bEnd.3 cells. **A** Representative immunofluorescence images and quantification of ZO-1 and occludin proteins 4 h after SI in the three groups (scale bars, 30 µm). **B** Representative western blots and

quantification of ZO-1 and occludin proteins 4 h after SI in the three groups.  $n = 6/\text{group}$ , data are presented as the mean  $\pm$  SD,  $**P < 0.01$ , aloin vs vehicle group.

$P < 0.01$ ). There were no differences among 20, 40, and 60 µg/mL aloin at 1 h after SI (both  $P > 0.05$ ), and the 40 µg/mL aloin had the optimum effect compared with

20 µg/mL (both  $P < 0.01$ ) and 60 µg/mL ( $P < 0.01$ ,  $P < 0.05$ ) at 2 h and 4 h after SI, so we used 40 µg/mL aloin in subsequent assays (Fig. 6A). The DCFH

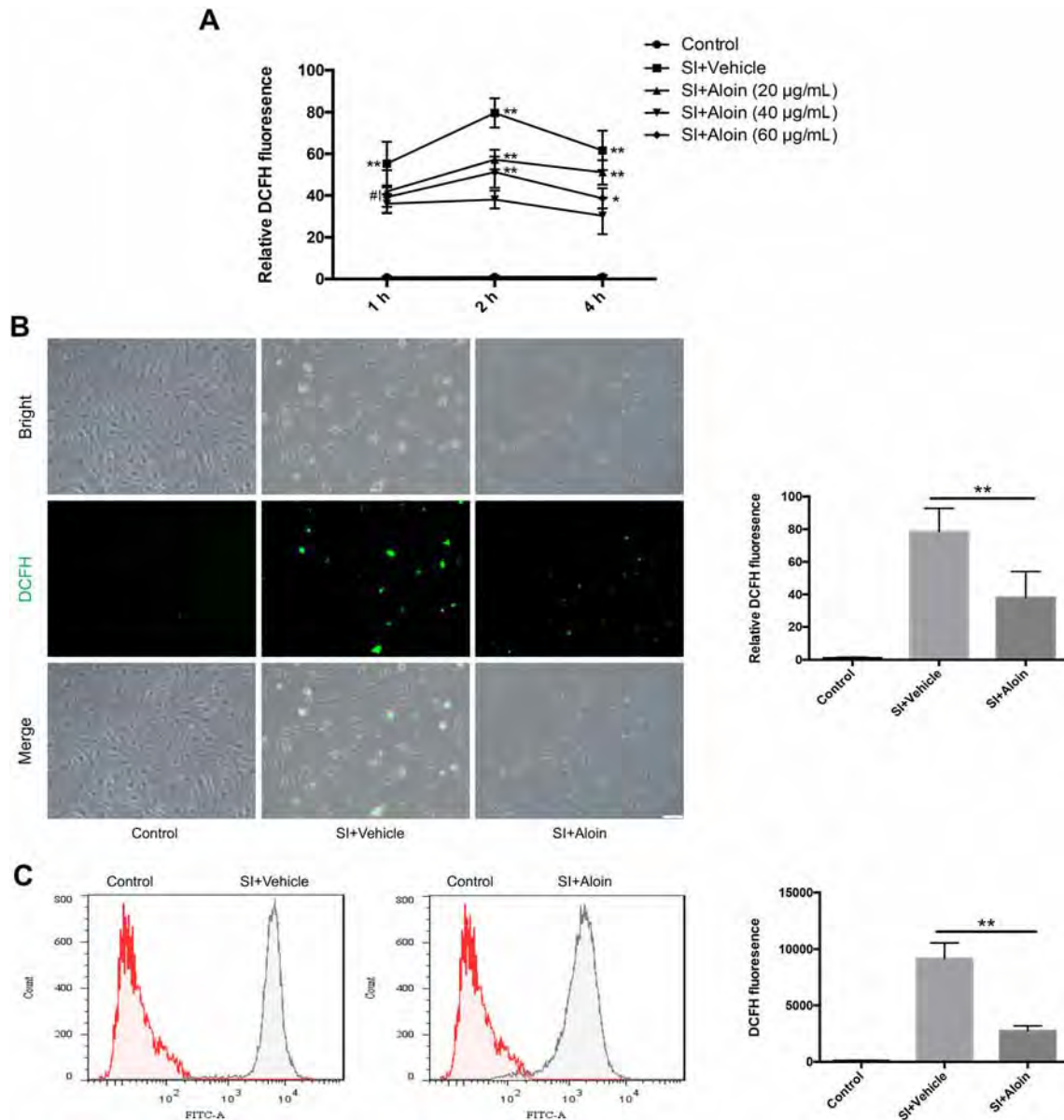


**Fig. 6** Aloin decreases intracellular ROS generation after experimental SI in bEnd.3 cells, as detected by DCFH-DA. **A** ROS levels at different time points post-SI after treatment with different concentrations of aloin. **B** Representative intracellular ROS fluorescence images with bright field and quantification 2 h after SI in the control,

SI+vehicle, and SI+aloin groups (scale bar, 75 µm). **C** Representative fluorescence intensity using flow cytometry and quantification 2 h after SI in the three groups.  $n = 6/\text{group}$ , data are presented as the mean  $\pm$  SD, \* $P < 0.05$ , \*\* $P < 0.01$ , # $P > 0.05$ .

fluorescence analyses showed that the relative ROS level of each cell after aloin treatment was markedly lower than in the vehicle-treated group 2 h post-SI ( $P < 0.01$ ; Fig. 6B), and similar results were found using flow cytometry (Fig. 6C). The DCFH fluorescence intensity of all cells in the aloin-treated group decreased significantly compared with the vehicle-treated group ( $P < 0.01$ ).

### Aloin Protects against the Changes in Mitochondrial Membrane Potential after Stretch Injury of bEnd.3 Cells

The changes in  $\Delta\Psi_m$  from red to green fluorescence after SI in bEnd.3 cells were detected by the JC-1 kit and showed that the relatively lower  $\Delta\Psi_m$  of each cell in the vehicle-treated group was remarkably reversed after aloin treatment ( $P < 0.01$ ; Fig. 7A). Consistent with the above

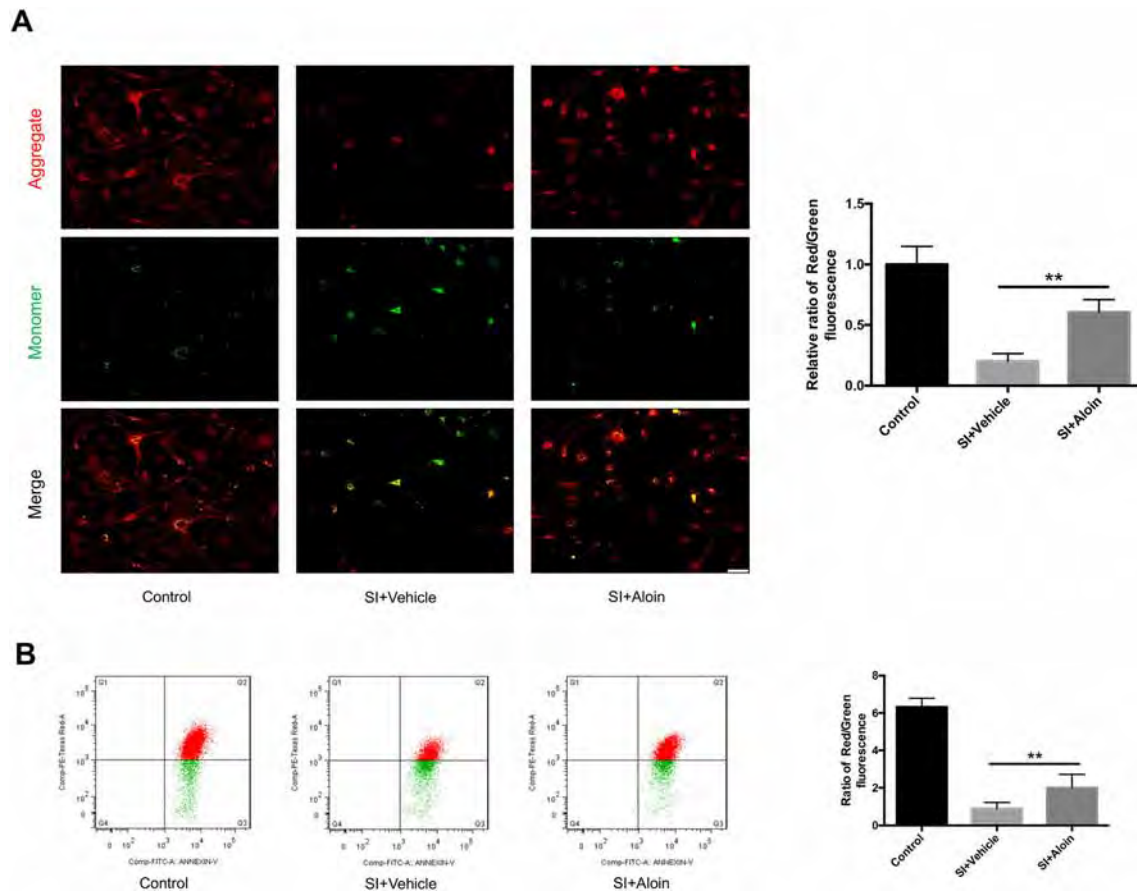


**Fig. 7** Aloin protects against the changes in  $\Delta\Psi_m$  after SI in bEnd.3 cells. **A** Representative  $\Delta\Psi_m$  fluorescence images and red/green fluorescence ratios 2 h after SI in the control, SI + vehicle, and SI + aloin groups (scale bar, 75  $\mu\text{m}$ ). **B** Representative fluorescence

intensity using flow cytometry and red/green fluorescence ratios 2 h after SI in the three groups.  $n = 6/\text{group}$ , data are presented as the mean  $\pm$  SD,  $**P < 0.01$ , aloin vs vehicle group.

results, the flow cytometry-based analyses of the red/green fluorescence ratio revealed that aloin significantly increased the levels of  $\Delta\Psi_m$  at 2 h post-SI ( $P < 0.01$ ; Fig. 7B).

#### Aloin Regulates Mitogen-Activated Protein Kinase (MAPK), Nuclear Factor-kappa B (NF- $\kappa\text{B}$ ), and Apoptosis-Associated Pathways to Reduce the Damage in Mice Post-TBI and in bEnd.3 Cells after Stretch Injury

To determine the effects of aloin on the MAPK, NF- $\kappa\text{B}$ , and apoptosis-associated pathways in the *in vivo* and *in vitro* TBI models, we used western blot analyses. In the animal model, aloin remarkably decreased the high levels of p-p38/p38 in the MAPK pathway and p-p65/p65 in the NF- $\kappa\text{B}$  pathway induced by TBI after 3 days (both  $P < 0.01$ ; Fig. 8A, B). Furthermore, in the mitochondrial apoptotic pathways, the ratios of Bax/Bcl-2 and cleaved caspase-3/caspase-3 were clearly lower in the aloin-treated group than in the vehicle group (both  $P < 0.01$ ; Fig. 8C).

In the cell-injury model, the levels of phosphorylation of p38 and p65 were elevated at 2 h after SI, while they were reversed by aloin treatment (both  $P < 0.05$ ; Fig. 9A, B). Meanwhile, the ratios of Bax/Bcl-2 and cleaved caspase-3/caspase-3 increased remarkably at 2 h after SI, and aloin reduced these ratios (both  $P < 0.01$ ; Fig. 9C, D).

#### Discussion

TBI is a public health problem that leads to high rates of disability and mortality in modern-day society [24]. Therefore, to explore the pathogenesis and possible therapies, several TBI models in mice have been developed over time to simulate human TBI, such as the fluid percussion injury model [25], the weight-drop-based injury model [26], the penetrating brain injury model [27], and the blast brain injury model [28]. In our study, the CCI model was used due to its strong operability and high accuracy compared with the above models. We were able to manually control the impact parameters to obtain different

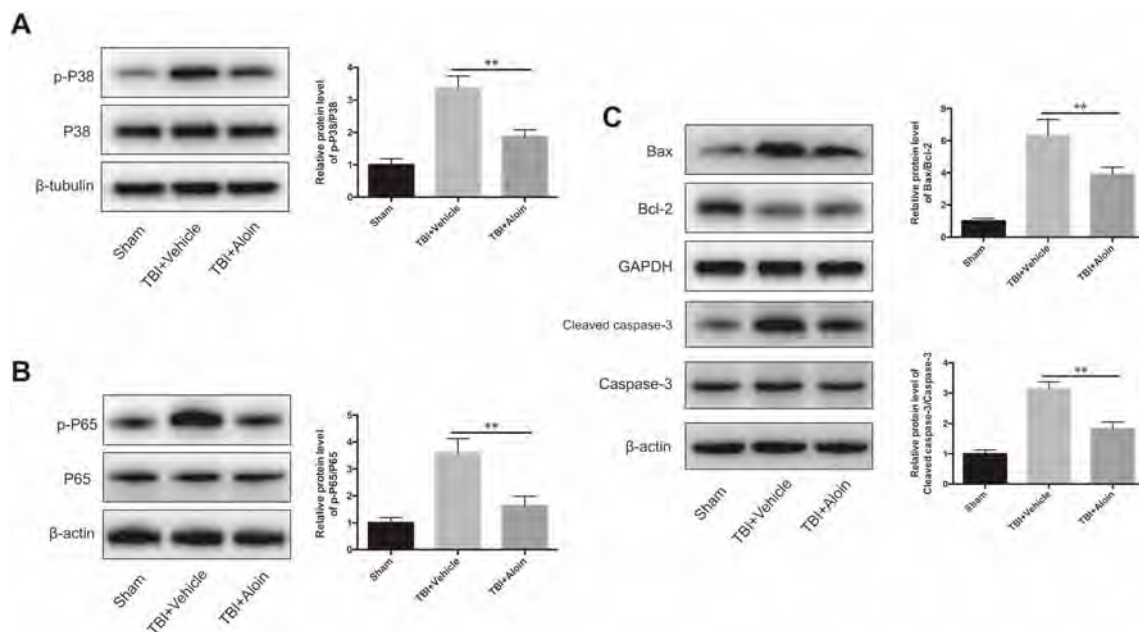


**Fig. 8** Aloin regulates MAPK, NF- $\kappa$ B, and apoptosis-associated pathways in mouse TBI models. **A–C** Representative western blots of p-P38 and P38 (**A**), p-P65 and P65 (**B**), and Bax, Bcl-2, cleaved caspase-3, and caspase-3 proteins (**C**), along with their quantifications

3 days after TBI in the sham, TBI+vehicle, and TBI+aloin groups.  $n = 6/\text{group}$ , data are presented as the mean  $\pm$  SD,  $**P < 0.01$ , aloin vs vehicle group.

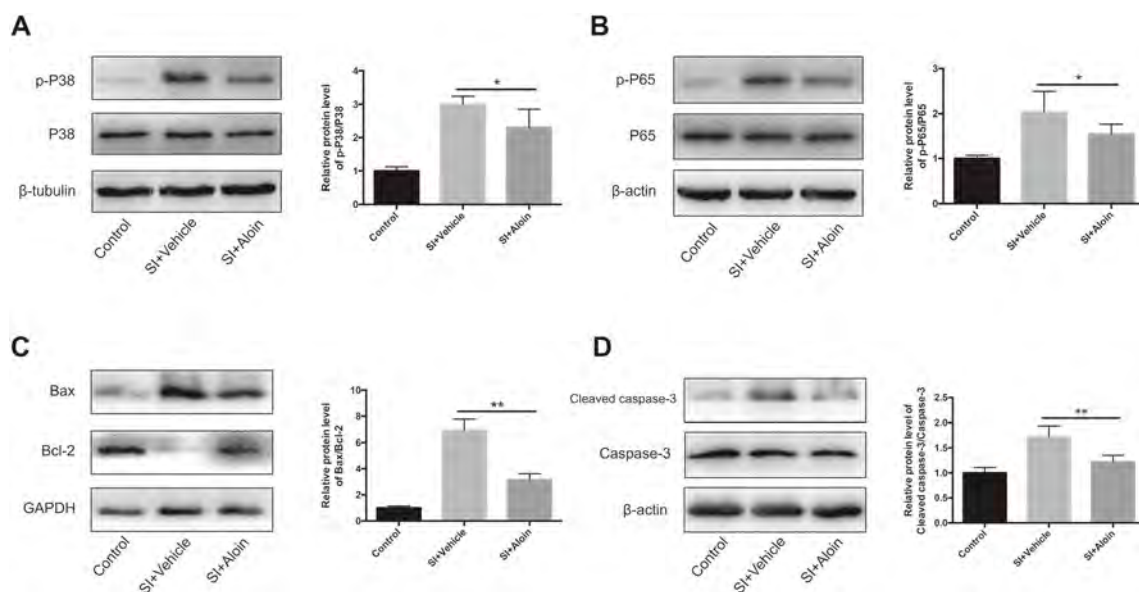


**Fig. 9** Aloin regulates MAPK, NF- $\kappa$ B, and apoptosis-associated pathways after experimental stretch injury in bEnd.3 cells. **A–D** Representative western blots of p-P38 and P38 (**A**), p-P65 and P65 (**B**), and Bax, Bcl-2 (**C**), cleaved caspase-3, and caspase-3 proteins

(**D**), along with quantifications at 2 h after SI in the control, SI+vehicle, and SI+aloin groups.  $n = 6/\text{group}$ , data are presented as the mean  $\pm$  SD,  $*P < 0.05$ ,  $**P < 0.01$ , aloin vs vehicle group.

degrees of pathological brain injury. According to a previous report [29], moderate TBI was created in mice for our experiments.

After TBI, the reversible secondary damage is an important target for therapy [30]. Disruption of the BBB is a crucial part of this secondary damage, leading to the

generation of vasogenic brain edema. The more severe the BBB damage, the more edema forms [31]. Aloin, a small molecule, has been used and explored in our studies of its anti-apoptosis [13] and anti-oxidative stress response [15] properties. At the optimum treatment concentration of 20 mg/kg, aloin significantly reduced the volume of edema

after TBI, and attenuated the BBB damage as evidenced by the extravasation of EB. Furthermore, the integrity of the BBB is maintained mainly by the TJ proteins ZO-1 and occludin in ECs [32]. The loss of these proteins in the pericontusional area post-TBI was reversed by aloin, reducing the permeability of the BBB.

TBI-induced secondary damage inhibits the recovery of neurological deficits [33]. In this study, the mNSS, rotarod test, and Morris water maze test were used to comprehensively assess the recovery of neurological functions. The motor, sensory, balance, and reflex functions in mice are evaluated by the mNSS and the rotarod test [34], while spatial learning and memory are examined by the Morris water maze test [34, 35]. Clearly, aloin improved the neurobehavioral performance of mice after TBI.

In the animal TBI model, we found that aloin regulated the MAPK, NF- $\kappa$ B, and apoptosis-associated pathways. To further investigate the possible underlying mechanism of action of aloin in TBI therapy, we used an SI model in bEnd.3 cells similar to the moderate TBI, which is usually used to explore the properties of the BBB *in vitro* [36]. Based on the cell viability and LDH release tests, 40  $\mu$ g/mL aloin had the best therapeutic effect. This concentration significantly reduced the apoptosis and minimized the loss of the TJ proteins ZO-1 and occludin in bEnd.3 cells after SI. Potentially, aloin protects the integrity of TJ proteins by alleviating the apoptosis of cerebrovascular ECs after TBI.

Excessive ROS accumulation in cells is associated with oxidative stress, which exacerbates secondary damage [8]. ROS include superoxide anion, hydroxyl radical, hydrogen peroxide, and hypochlorous acid. However, the most common intracellular free radical after TBI is the superoxide anion, which attacks DNA, protein, transcription factor, and membrane lipid, leading to cell damage and apoptosis [8, 37]. Aloin inhibited the generation of excessive ROS in bEnd.3 cells after SI as determined by DCFH-DA. Consistent with previous studies [12, 38], we found that the high levels of ROS directly activated the MAPK and NF- $\kappa$ B signaling pathways. MAPKs, which belong to the highly-conserved family of serine/threonine protein kinases, mainly include the ERK, JNK, and p38 subgroups [39]. The phosphorylation of MAPKs is induced by the stimulation of intracellular ROS and is associated with apoptosis [6, 8, 40]. NF- $\kappa$ B, a family of DNA-binding proteins, is widely known to play an important role in the pathology of neuroinflammation after TBI [5, 12]. NF- $\kappa$ B in the cytoplasm is activated and phosphorylated by ROS, then translocated into the nucleus, where it induces inflammatory factors and apoptosis [6, 41]. The results from our studies demonstrated that aloin blocked the phosphorylation of p38 MAPK and the activation of p65 NF- $\kappa$ B. Taken together, apoptosis was alleviated post-TBI

based on the action of aloin to remarkably decrease the levels of ROS that regulate MAPK and NF- $\kappa$ B.

After TBI, the decreased normal mitochondrial populations lead to abundant ROS, which aggravate the mitochondrial damages [37, 42]. We also found that the low  $\Delta\Psi_m$  post-SI in bEnd.3 cells was significantly reversed by aloin to prevent apoptosis. In addition, the endogenous mitochondria-related apoptosis pathways that are activated after TBI include Bax, Bcl-2, and cleaved caspase-3 [2, 8]. Bax, a pro-apoptotic protein, and Bcl-2, an anti-apoptotic protein, were detected on the membrane of mitochondria. A high ratio of Bax/Bcl-2 induces the release of cytochrome c from the mitochondria into the cytoplasm, which promotes the activation of caspase-3 [43, 44] and cleaved caspase-3 is a key player in the final execution phase of apoptotic [45–47]. We found that aloin inhibited the apoptotic pathway *via* significant reductions of the ratios of Bax/Bcl-2 and cleaved caspase-3/caspase-3.

There were some limitations to this study. First, cerebral edema is mainly regarded as the vasogenic edema caused by disruption of the BBB. However, some investigators argue that cytotoxic edema is also an important part of cerebral edema, coexisting with vasogenic edema [48]. We found no evidence for a relationship between aloin and cytotoxic edema. Second, we created a model of moderate TBI only and used it to investigate the protective effects of aloin on the BBB. Other TBI models of different severity (both milder and more severe) need to be established for future investigations. Third, we only assessed some of the protein factors in the MAPK, NF- $\kappa$ B, and apoptosis-associated pathways, and the effects of aloin on the other signaling pathways need to be explored in further experiments. Last, the interactions between ROS,  $\Delta\Psi_m$ , and signal pathways are complex. More detailed analyses would be valuable in the future.

## Conclusions

In summary, our results demonstrated that aloin protects against disruption of the BBB to reduce the vasogenic edema resulting from secondary injury in a TBI model in mice. Subsequently, we showed that aloin attenuates the loss of TJs in ECs, and this was consistent with the experimental evidence *in vitro*. A possible mechanism is that aloin influences intracellular ROS generations and changes the  $\Delta\Psi_m$  by regulating the MAPK, NF- $\kappa$ B, and apoptosis-associated pathways to reduce the apoptosis of ECs. Aloin improves the recovery of neurological deficits and might be a promising therapeutic drug for TBI.

**Acknowledgements** We thank Prof. Guo-yuan Yang (School of Biomedical Engineering and Med-X Research Institute of Shanghai

Jiao Tong University, Shanghai, China) for guidance in experiments. This work was supported by the National Natural Science Foundation of China (81671207, 81701895, and 81501048) and the Shanghai Jiao Tong University Medicine-Engineering Research Fund (YG2016QN20).

**Conflict of interest** The authors declare no competing interests.

## References

- Needham EJ, Helmy A, Zanier ER, Jones JL, Coles AJ, Menon DK. The immunological response to traumatic brain injury. *J Neuroimmunol* 2019, 332: 112–125.
- Yang DX, Jing Y, Liu YL, Xu ZM, Yuan F, Wang ML, *et al.* Inhibition of transient receptor potential vanilloid 1 attenuates blood–brain barrier disruption after traumatic brain injury in mice. *J Neurotrauma* 2019, 36: 1279–1290.
- Jiang JY, Gao GY, Feng JF, Mao Q, Chen LG, Yang XF, *et al.* Traumatic brain injury in China. *Lancet Neurol* 2019, 18: 286–295.
- Zhang L, Wang H, Zhou X, Mao L, Ding K, Hu Z. Role of mitochondrial calcium uniporter-mediated  $\text{Ca}^{2+}$  and iron accumulation in traumatic brain injury. *J Cell Mol Med* 2019, 23: 2995–3009.
- Liu YL, Yuan F, Yang DX, Xu ZM, Jing Y, Yang GY, *et al.* Adjudin attenuates cerebral edema and improves neurological function in mice with experimental traumatic brain injury. *J Neurotrauma* 2018, 35: 2850–2860.
- Xu ZM, Yuan F, Liu YL, Ding J, Tian HL. Glibenclamide attenuates blood–brain barrier disruption in adult mice after traumatic brain injury. *J Neurotrauma* 2017, 34: 925–933.
- Michinaga S, Koyama Y. Dual roles of astrocyte-derived factors in regulation of blood–brain barrier function after brain damage. *Int J Mol Sci* 2019, 20: 571.
- Liu YL, Xu ZM, Yang GY, Yang DX, Ding J, Chen H, *et al.* Sesamin alleviates blood–brain barrier disruption in mice with experimental traumatic brain injury. *Acta Pharmacol Sin* 2017, 38: 1445–1455.
- Luissint AC, Artus C, Glacial F, Ganeshamoorthy K, Couraud PO. Tight junctions at the blood brain barrier: physiological architecture and disease-associated dysregulation. *Fluids Barriers CNS* 2012, 9: 23.
- Hu HM, Li B, Wang XD, Guo YS, Hui H, Zhang HP, *et al.* Fluoxetine is neuroprotective in early brain injury *via* its anti-inflammatory and anti-apoptotic effects in a rat experimental subarachnoid hemorrhage model. *Neurosci Bull* 2018, 34: 951–962.
- Lee W, Yang S, Lee C, Park EK, Kim KM, Ku SK, *et al.* Aloin reduces inflammatory gene iNOS *via* inhibition activity and p-STAT-1 and NF- $\kappa$ B. *Food Chem Toxicol* 2019, 126: 67–71.
- Zhong J, Wang F, Wang Z, Shen C, Zheng Y, Ma F, *et al.* Aloin attenuates cognitive impairment and inflammation induced by d-galactose *via* down-regulating ERK, p38 and NF- $\kappa$ B signaling pathway. *Int Immunopharmacol* 2019, 72: 48–54.
- Chang R, Zhou R, Qi X, Wang J, Wu F, Yang W, *et al.* Protective effects of aloin on oxygen and glucose deprivation-induced injury in PC12 cells. *Brain Res Bull* 2016, 121: 75–83.
- Pan Q, Pan H, Lou H, Xu Y, Tian L. Inhibition of the angiogenesis and growth of Aloin in human colorectal cancer *in vitro* and *in vivo*. *Cancer Cell Int* 2013, 13: 69.
- Silva MA, Trevisan G, Hoffmeister C, Rossato MF, Boligon AA, Walker CIB, *et al.* Anti-inflammatory and antioxidant effects of *Aloe saponaria* Haw in a model of UVB-induced paw sunburn in rats. *J Photochem Photobiol B* 2014, 133: 47–54.
- Yuan F, Xu ZM, Lu LY, Nie H, Ding J, Ying WH, *et al.* SIRT2 inhibition exacerbates neuroinflammation and blood–brain barrier disruption in experimental traumatic brain injury by enhancing NF- $\kappa$ B p65 acetylation and activation. *J Neurochem* 2016, 136: 581–593.
- Sarkar C, Zhao Z, Aungst S, Sabirzhanov B, Faden AI, Lipinski MM. Impaired autophagy flux is associated with neuronal cell death after traumatic brain injury. *Autophagy* 2014, 10: 2208–2222.
- Tang G, Liu Y, Zhang Z, Lu Y, Wang Y, Huang J, *et al.* Mesenchymal stem cells maintain blood–brain barrier integrity by inhibiting aquaporin-4 upregulation after cerebral ischemia. *Stem Cells* 2014, 32: 3150–3162.
- Ni H, Yang S, Siaw-Debrah F, Hu J, Wu K, He Z, *et al.* Exosomes derived from bone mesenchymal stem cells ameliorate early inflammatory responses following traumatic brain injury. *Front Neurosci* 2019, 13: 14.
- Vorhees CV, Williams MT. Morris water maze: procedures for assessing spatial and related forms of learning and memory. *Nat Protoc* 2006, 1: 848–858.
- Jing Y, Zhang L, Xu ZM, Chen H, Ju SM, Ding J, *et al.* Phosphatase actin regulator-1 (PHACTR-1) knockdown suppresses cell proliferation and migration and promotes cell apoptosis in the bEnd.3 mouse brain capillary endothelial cell line. *Med Sci Monit* 2019, 25: 1291–1300.
- Xu Z, Liu Y, Yang D, Yuan F, Ding J, Chen H, *et al.* Sesamin protects SH-SY5Y cells against mechanical stretch injury and promoting cell survival. *BMC Neurosci* 2017, 18: 57.
- Ahmed SM, Rzigalinski BA, Willoughby KA, Sitterding HA, Ellis EF. Stretch-induced injury alters mitochondrial membrane potential and cellular ATP in cultured astrocytes and neurons. *J Neurochem* 2000, 74: 1951–1960.
- Fang J, Zhu Y, Wang H, Cao B, Fei M, Niu W, *et al.* Baicalin protects mice brain from apoptosis in traumatic brain injury model through activation of autophagy. *Front Neurosci* 2018, 12: 1006.
- Bhowmick S, D’Mello V, Caruso D, Wallerstein A, Abdul-Muneer PM. Impairment of pericyte-endothelium crosstalk leads to blood–brain barrier dysfunction following traumatic brain injury. *Exp Neurol* 2019, 317: 260–270.
- Wang ZF, Gao C, Chen W, Gao Y, Wang HC, Meng Y, *et al.* Salubrinal offers neuroprotection through suppressing endoplasmic reticulum stress, autophagy and apoptosis in a mouse traumatic brain injury model. *Neurobiol Learn Mem* 2019, 161: 12–25.
- Cernak I, Wing ID, Davidsson J, Plantman S. A novel mouse model of penetrating brain injury. *Front Neurol* 2014, 5: 209.
- Sajja VSSS, Jablonska A, Haughey N, Bulte JWM, Stevens RD, Long JB, *et al.* Sphingolipids and microRNA changes in blood following blast traumatic brain injury: an exploratory study. *J Neurotrauma* 2018, 35: 353–361.
- Washington PM, Forcelli PA, Wilkins T, Zapple DN, Parsadian M, Burns MP. The effect of injury severity on behavior: a phenotypic study of cognitive and emotional deficits after mild, moderate, and severe controlled cortical impact injury in mice. *J Neurotrauma* 2012, 29: 2283–2296.
- Huang SX, Qiu G, Cheng FR, Pei Z, Yang Z, Deng XH, *et al.* Berberine protects secondary injury in mice with traumatic brain injury through anti-oxidative and anti-inflammatory modulation. *Neurochem Res* 2018, 43: 1814–1825.
- Wang D, Xu X, Wu YG, Lyu L, Zhou ZW, Zhang JN. Dexmedetomidine attenuates traumatic brain injury: action pathway and mechanisms. *Neural Regen Res* 2018, 13: 819–826.
- Hao FL, Han XF, Wang XL, Zhao ZR, Guo AH, Lu XJ, *et al.* The neurovascular protective effect of alogliptin in murine MCAO

- model and brain endothelial cells. *Biomed Pharmacother* 2019, 109: 181–187.
33. Rehman SU, Ahmad A, Yoon GH, Khan M, Abid MN, Kim MO. Inhibition of c-Jun N-terminal kinase protects against brain damage and improves learning and memory after traumatic brain injury in adult mice. *Cereb Cortex* 2018, 28: 2854–2872.
  34. Gao C, Qian Y, Huang J, Wang D, Su W, Wang P, *et al.* A three-day consecutive fingolimod administration improves neurological functions and modulates multiple immune responses of CCI mice. *Mol Neurobiol* 2017, 54: 8348–8360.
  35. Xie BS, Wang YQ, Lin Y, Mao Q, Feng JF, Gao GY, *et al.* Inhibition of ferroptosis attenuates tissue damage and improves long-term outcomes after traumatic brain injury in mice. *CNS Neurosci Ther* 2019, 25: 465–475.
  36. Zhou Q, Wang YW, Ni PF, Chen YN, Dong HQ, Qian YN. Effect of tryptase on mouse brain microvascular endothelial cells *via* protease-activated receptor 2. *J Neuroinflammation* 2018, 15: 248.
  37. Abdul-Muneer PM, Chandra N, Haorah J. Interactions of oxidative stress and neurovascular inflammation in the pathogenesis of traumatic brain injury. *Mol Neurobiol* 2015, 51: 966–979.
  38. Yuan F, Liu R, Hu M, Rong X, Bai L, Xu L, *et al.* JAX2, an ethanol extract of *Hyssopus cuspidatus* Boriss, can prevent bronchial asthma by inhibiting MAPK/NF- $\kappa$ B inflammatory signaling. *Phytomedicine* 2019, 57: 305–314.
  39. Tao L, Li D, Liu H, Jiang F, Xu Y, Cao Y, *et al.* Neuroprotective effects of metformin on traumatic brain injury in rats associated with NF- $\kappa$ B and MAPK signaling pathway. *Brain Res Bull* 2018, 140: 154–161.
  40. Zhang L, Zhang L, Liu H, Jiang F, Wang H, Li D, *et al.* Inhibition of Epac2 attenuates neural cell apoptosis and improves neurological deficits in a rat model of traumatic brain injury. *Front Neurosci* 2018, 12: 263.
  41. Wang X, Lan YL, Xing JS, Lan XQ, Wang LT, Zhang B. Alantolactone plays neuroprotective roles in traumatic brain injury in rats *via* anti-inflammatory, anti-oxidative and anti-apoptosis pathways. *Am J Transl Res* 2018, 10: 368–380.
  42. Azarashvili T, Stricker R, Reiser G. The mitochondria permeability transition pore complex in the brain with interacting proteins—promising targets for protection in neurodegenerative diseases. *Biol Chem* 2010, 391: 619–629.
  43. Chae IH, Park KW, Kim HS, Oh BH. Nitric oxide-induced apoptosis is mediated by Bax/Bcl-2 gene expression, transition of cytochrome c, and activation of caspase-3 in rat vascular smooth muscle cells. *Clin Chim Acta* 2004, 341: 83–91.
  44. Yang J, Liu XS, Bhalla K, Kim CN, Ibrado AM, Cai J, *et al.* Prevention of apoptosis by Bcl-2: Release of cytochrome c from mitochondria blocked. *Science* 1997, 275: 5303.
  45. Knoblach SM, Nikolaeva M, Huang X, Fan L, Krajewski S, Reed JC, *et al.* Multiple caspases are activated after traumatic brain injury: evidence for involvement in functional outcome. *J Neurotrauma* 2002, 19: 1155–1170.
  46. Cheng G, Kong RH, Zhang LM, Zhang JN. Mitochondria in traumatic brain injury and mitochondrial-targeted multipotential therapeutic strategies. *Br J Pharmacol* 2012, 167: 699–719.
  47. Wang X, Li S, Ma J, Wang C, Chen A, Xin Z, *et al.* Effect of gastrodin on early brain injury and neurological outcome after subarachnoid hemorrhage in rats. *Neurosci Bull* 2019, 35: 461–470.
  48. Globler NK, Sprague S, Ahmad S, Mayfield KG, Fletcher LM, Digicaylioglu MH, *et al.* Acetazolamide treatment prevents redistribution of astrocyte aquaporin 4 after murine traumatic brain injury. *Neurosci J* 2019, 2019: 1–12.



# EPAC Negatively Regulates Myelination *via* Controlling Proliferation of Oligodendrocyte Precursor Cells

Zhen-Zhen Gao<sup>1</sup> · Ying-Cong Li<sup>2</sup> · Chong-Yu Shao<sup>2</sup> · Jian Xiao<sup>1</sup> · Ying Shen<sup>2</sup>  · Liang Zhou<sup>2,3</sup>

Received: 3 July 2019 / Accepted: 5 January 2020 / Published online: 17 April 2020  
© Shanghai Institutes for Biological Sciences, CAS 2020

**Abstract** Increasing evidence suggests that a cyclic adenosine monophosphate (cAMP)-dependent intracellular signal drives the process of myelination. Yet, the signal transduction underlying the action of cAMP on central nervous system myelination remains undefined. In the present work, we sought to determine the role of EPAC (exchange protein activated by cAMP), a downstream effector of cAMP, in the development of the myelin sheath using EPAC1 and EPAC2 double-knockout (EPAC<sup>dKO</sup>) mice. The results showed an age-dependent regulatory effect of EPAC1 and EPAC2 on myelin development, as their deficiency caused more myelin sheaths in postnatal early but not late adult mice. Knockout of EPAC promoted the proliferation of oligodendrocyte precursor cells and had diverse effects on myelin-related transcription factors, which in turn increased the expression of myelin-related proteins. These results indicate that EPAC proteins are negative regulators of myelination and may be promising targets for the treatment of myelin-related diseases.

**Keywords** EPAC · Proliferation · Oligodendrocyte · Myelination · Transcription factor

## Introduction

In the central nervous system (CNS), oligodendrocytes (OLs) provide electrical insulation and trophic support for neurons by myelinating axons [1]. OL precursor cells (OPCs), which are generated from the neural tube during CNS development, differentiate into OLs and migrate throughout the CNS [2]. The transition of OLs from proliferative to differentiated stages is a highly coordinated process and is critical for understanding myelin formation and the repair of demyelinating diseases. To date, more and more molecules have been shown to play important roles in the development of the myelin sheath, including axonally-expressed ligands [3–5], nuclear transcription factors [6–10], and mitogens [11–15].

Cyclic adenosine monophosphate (cAMP) is a key regulator of metabolic activity, survival, proliferation, and differentiation in a variety of cell types. Increasing evidence suggests that a cAMP-dependent intracellular signal drives the process of myelination. For example, an increase or decrease in cAMP level in dorsal root ganglion neurons results in suppressed or enhanced myelination, respectively [16]; and enhanced intracellular cAMP prevents the demyelination in the corpus callosum of mice induced by cuprizone [17]. Yet, the signal transduction underlying the action of cAMP on CNS myelination remains undefined.

cAMP controls complex cellular processes primarily through the activation of two downstream effectors, PKA (protein kinase A) and EPAC (exchange protein activated by cAMP) [18]. The catalytic subunits of PKA

Zhen-Zhen Gao and Ying-Cong Li contributed equally to this work.

✉ Ying Shen  
yshen@zju.edu.cn

✉ Liang Zhou  
zllzlj@zju.edu.cn

<sup>1</sup> Molecular Pharmacology Research Center, School of Pharmaceutical Sciences, Wenzhou Medical University, Wenzhou 325035, China

<sup>2</sup> Department of Neurobiology, Zhejiang University School of Medicine, Hangzhou 310058, China

<sup>3</sup> Key Laboratory of Brain Science, Guizhou Institution of Higher Education, Zunyi Medical University, Zunyi 563000, China

phosphorylate and modulate the activity of cytosolic and nuclear substrates [18]. EPAC directly transduces cAMP signals as a guanine nucleotide exchange factor for the small GTP-binding protein Rap1 [18]. However, their potential roles in the proliferation and differentiation of OPCs are still elusive. In the present work, we sought to examine the role of EPAC in the development of the myelin sheath using EPAC1 and EPAC2 double-knockout (EPAC<sup>dKO</sup>) mice. Our results showed that EPAC deficiency caused a developmentally-dependent increase of myelin sheaths, which may be due to increased proliferation of OPCs. We also showed that EPAC had diverse effects on myelin-related transcription factors, which in turn increased the expression of myelin-related proteins.

## Materials and Methods

### Animals

The experiments in the present work were approved by the Animal Experimentation Ethics Committee of Zhejiang University. Original breeding pairs of EPAC<sup>dKO</sup> mice were obtained from Prof. Youmin Lu [19]. The resulting offspring were genotyped using PCR of genomic DNA. Mice were kept at the Experimental Animal Center of Zhejiang University under temperature-controlled conditions on a 12:12 h light/dark cycle. All experiments were performed blind to genotype in littermates of either sex.

### Antibodies and Reagents

Antibodies against EPAC1, EPAC2, cyclin D1, and cyclin-dependent kinase 4 (CDK4) were from Cell Signaling (Danvers, MA). Antibodies against 2',3'-cyclic nucleotide 3'-phosphodiesterase (CNP), myelin basic protein (MBP), Olig2, TCF4, SOX2, SOX10, CC-1, and GAPDH were from Millipore (Billerica, MA). Antibodies against GPR17, myelin regulatory factor (Mrf), Lamin B, yin-yang 1 (YY1), and CDK5 were from Santa Cruz (Dallas, TX). The antibody against Ki67 was from Abcam (Cambridge, UK). Myelin-associated glycoprotein (MAG) antibody, IgG antibody, and Alexa Fluor-conjugated secondary antibodies were from Invitrogen (Carlsbad, CA). Horseradish peroxidase-conjugated secondary antibodies for immunoblotting were from GE Healthcare (Waukesha, WI). Proteinase inhibitor was from Merck Chemicals (Darmstadt, Germany).

### Western Blotting

Protein assays were performed using Western blots as in previous work [20]. Primary antibodies and their dilutions

used for Western blots were EPAC1 (1:1000), EPAC2 (1:1000), cyclin D1 (1:500), CDK5 (1:500), MBP (1:5,000), MAG (1:2000), CNP (1:5000), TCF4 (1:1000), Mrf (1:1000), YY1 (1:200), SOX10 (1:1000), SOX2 (1:1000), GPR17 (1:2000), LaminB (1:500), and GAPDH (1:10000). The signals on films were scanned and quantitated using ImageJ 1.42q (NIH, Bethesda, MD).

### Immunohistochemistry

Immunohistochemistry was performed as in our previous work [20]. Secondary antibodies were diluted at 1:1000. The dilutions of primary antibodies were MBP (1:500), Olig2 (1:500), Ki67 (1:1000), and CC-1 (1:1000).

### Electron Microscopy (EM)

EM studies were performed as in previous work [20, 21] using a Philips CM100 microscope (FEI). ImageJ was used to measure the ratio of axonal diameter to fiber diameter (*g*-ratio).

### Statistics

Excel 2003 (Microsoft), the SPSS 16.0 statistical program (SPSS), and Igor Pro 6.0 (Wavemetrics), were used for data analysis. Statistical differences were determined using unpaired two-sided Student's *t*-test. The accepted level of significance was  $P < 0.05$ . "*n*" represents the number of animals or cultures tested. Data in the text and figures are presented as the mean  $\pm$  SEM.

## Results

### Expression of EPAC Proteins in Developing Brain

To investigate the roles of EPAC proteins in OL development, we first examined their expression in the postnatal brain. Equal amounts of proteins from mouse brain homogenates at different ages (birth to 4 months) were resolved by SDS-PAGE and immunoblotted with antibodies recognizing EPAC1, EPAC2, and MBP, a vital marker protein of OL maturation. We found that the expression of EPAC1 and EPAC2 increased with age and was roughly proportional to MBP expression (Fig. 1A). However, the changing progress of EPAC1 and EPAC2 appeared different: EPAC1 started to slow down after P30 while EPAC2 increased constantly throughout (Fig. 1A). Since *in vivo* Western blotting could not distinguish EPAC proteins from different types of neural cells, we further used *in vitro* cultures to determine the presence of EPACs in OPCs and mature OLs. Rat OPCs were collected from glial cultures

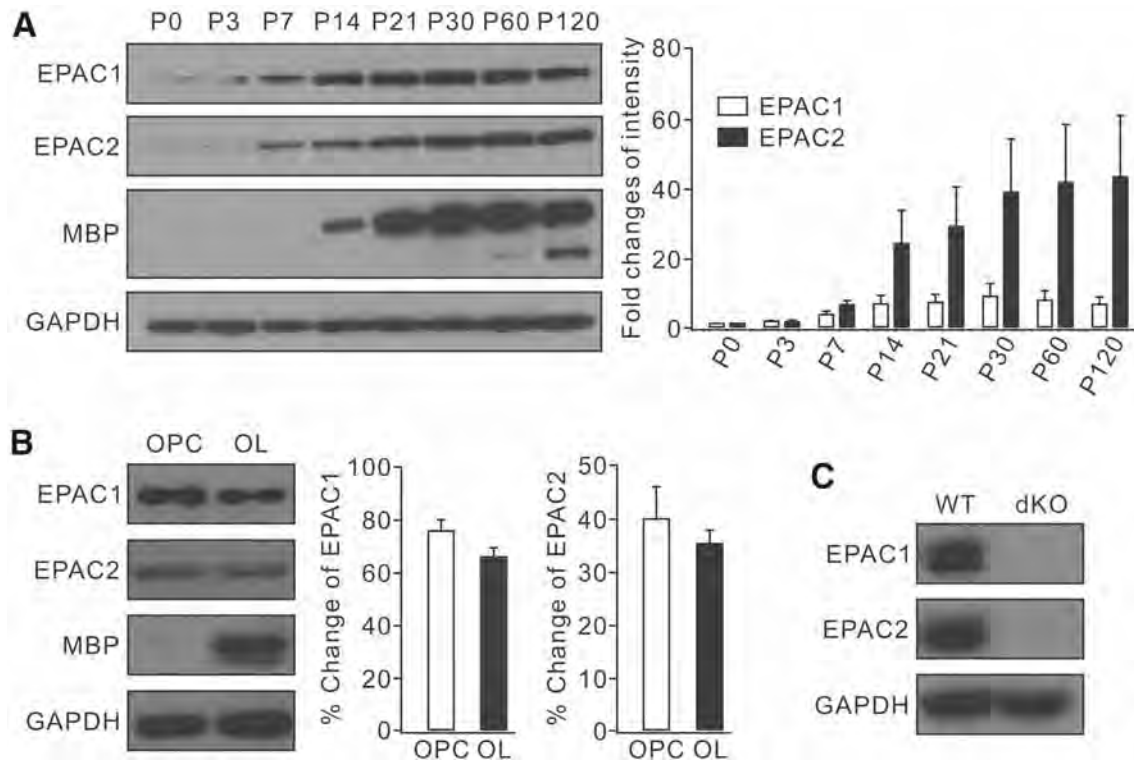


**Fig. 1** Expression of EPAC proteins in the brain. **A** Western blots of one out of six independent experiments showing the expressions of EPAC1, EPAC2, and MBP in the brain from postnatal mice. The signal intensities of EPAC1 and EPAC2 were divided by that of GAPDH, the loading control. The ratios were normalized to P0 and fold changes are shown in the histogram. **B** Expression of EPAC1, EPAC2, and MBP in cultured OPCs and OLs. Three-day triiodothyronine treatment was used to stimulate OPC differentiation into

mature OLs. GAPDH was the internal control. EPAC1 and EPAC2 were normalized to the corresponding GAPDH and their percentage changes are shown in the bar graphs. EPAC1: 75%  $\pm$  4% (OPC) and 66%  $\pm$  4% (OL) ( $P > 0.05$ ). EPAC2: 40%  $\pm$  6% (OPC) and 35%  $\pm$  3% (OL) ( $P > 0.05$ ). The experiment was repeated 4 times. **C** Western blots of EPAC1 and EPAC2 in the brain from WT and EPAC<sup>dKO</sup> mice (P14). The experiment was repeated 4 times.

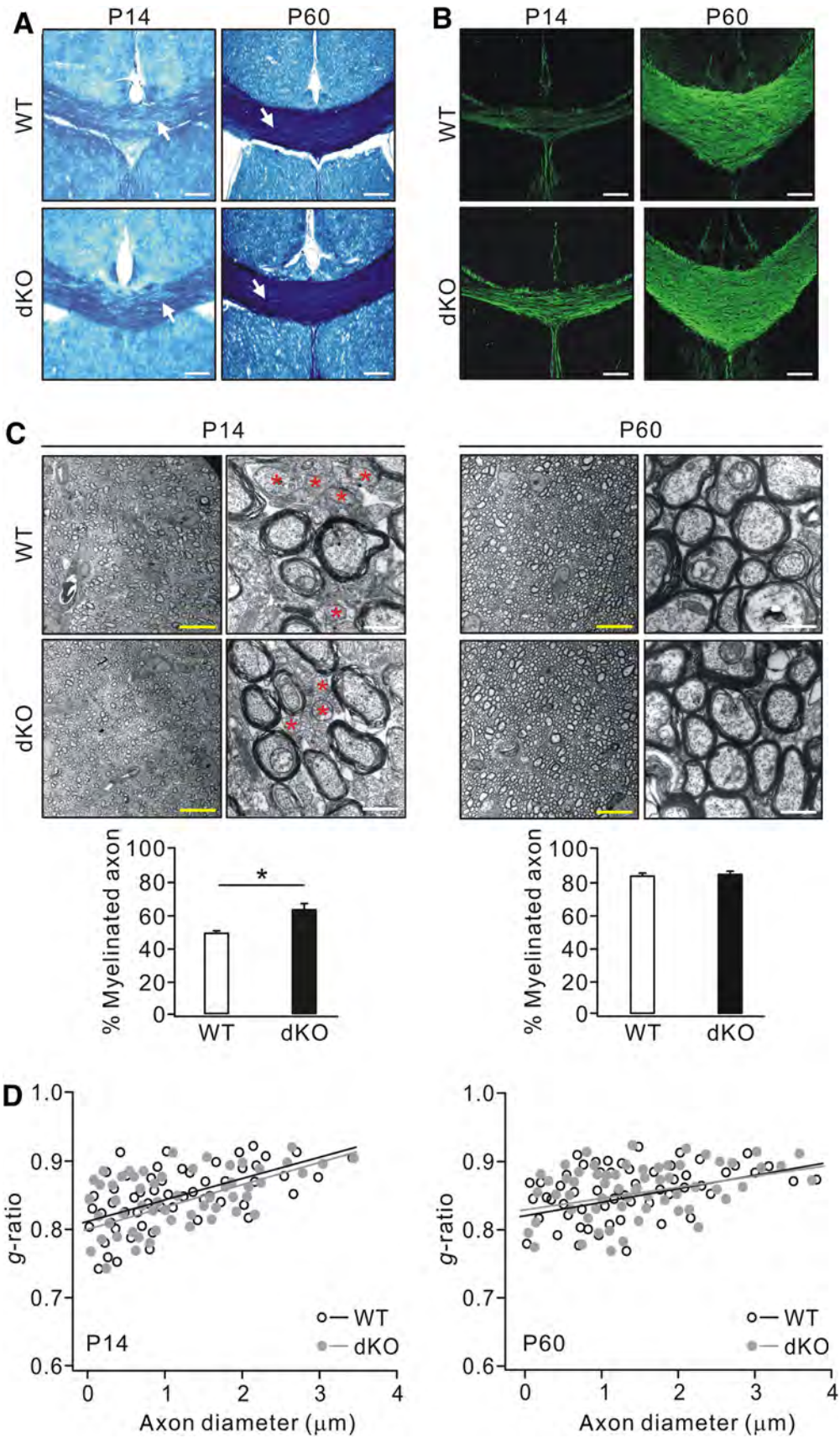
by shaking procedures and triiodothyronine was added to cultures and incubated for 3 days to allow OPC differentiation [21, 22]. Both EPAC1 and EPAC2 were abundantly expressed in OPC cultures (Fig. 1B). Triiodothyronine promoted OPC differentiation, as indicated by the expression of MBP (Fig. 1B). The expression of EPAC1 and EPAC2 was slightly lower in mature OLs than in OPCs, but there was no significance between two types of cell (Fig. 1B).

### EPAC Deficiency Accelerates CNS Myelination

We next generated EPAC<sup>dKO</sup> mice to evaluate their roles in CNS myelination. The deletion of EPACs was confirmed by Western blotting using mouse brain tissues (Fig. 1C). EPAC<sup>dKO</sup> mice were viable and did not exhibit gait abnormality during adulthood.

Several experiments were conducted to investigate whether the ablation of EPACs affects CNS myelination. First, eriochrome cyanine staining showed that EPAC<sup>dKO</sup> mice (P14) had a significantly higher density of white

matter tracts of the corpus callosum than wild-type (WT) mice (Fig. 2A). Interestingly, the knock-out effect was age-dependent because the tracts displayed no difference between WT and EPAC<sup>dKO</sup> mice at P60. Second, immunohistochemical staining indicated that EPAC<sup>dKO</sup> mice had more MBP-positive fibers than WT mice at P14 (Fig. 2B). Similarly, the intensity of MBP staining in EPAC<sup>dKO</sup> mice was close to that in WT mice at P60 (Fig. 2B). Third, we examined myelin sheaths in the cerebral cortex from WT and EPAC<sup>dKO</sup> littermates using EM. The number of myelinated axons was significantly higher in EPAC<sup>dKO</sup> than in WT mice at P14 (Fig. 2C). This phenotype again faded away in EPAC<sup>dKO</sup> mice by P60 (Fig. 2C). Together, these results suggest that EPAC proteins act as negative regulators and their deficiency accelerates the progress of CNS myelination. To investigate whether other phenotypes occur in parallel with the reduced percentage of myelinated axons, we measured the thickness of myelin sheaths by morphometric quantification. The results showed that the g-ratios of optic nerves in EPAC<sup>dKO</sup> mice did not differ from those in WT mice at both P14 and P60 (Fig. 2D).



◀ **Fig. 2** EPAC ablation increases myelination at P14 but not P60. **A** Cyanine staining showing myelin tracts (arrows) in the corpus callosum of WT and EPAC<sup>dKO</sup> mice at P14 and P60 (scale bars, 200  $\mu$ m). **B** Immunohistochemistry reveals an increase of MBP-positive fibers in the corpus callosum of EPAC<sup>dKO</sup> mice compared with WT mice at P14, but not at P60 (scale bars, 200  $\mu$ m). **C** EM images from optic nerves of WT and EPAC<sup>dKO</sup> mice at P14 and P60 (red asterisks, unmyelinated axons; yellow scale bars, 10  $\mu$ m; white scale bars, 1  $\mu$ m). Bar graphs in the lower panel show percentages of myelinated axons. P14: 48%  $\pm$  1% (WT) and 62%  $\pm$  2% (EPAC<sup>dKO</sup>);  $n = 4$ /group, \* $P < 0.05$ . P60: 83%  $\pm$  1% (WT) and 84%  $\pm$  1% (EPAC<sup>dKO</sup>);  $n = 4$ /group. **D** Relationships between axonal diameters and  $g$ -ratios of WT and EPAC<sup>dKO</sup> mice at P14 and P60. In mice at P14, the regression equations were  $y = 0.032x + 0.81$  (WT;  $n = 56$ ) and  $y = 0.033x + 0.80$  (EPAC<sup>dKO</sup>;  $n = 61$ ) ( $P > 0.05$ ). For mice at P60, the regression equations were  $y = 0.02x + 0.82$  (WT;  $n = 60$ ) and  $y = 0.016x + 0.83$  (EPAC<sup>dKO</sup>;  $n = 70$ ) ( $P > 0.05$ ).

### EPAC Deficiency Promotes the Proliferation of OPCs

To investigate how EPAC deficiency affects the progress of CNS myelination, we counted the number of OLs in WT and EPAC<sup>dKO</sup> mice using antibodies selective for OLs. Our results showed that the total number of OL lineage cells, as indicated by Olig2 staining, significantly increased in the corpus callosum of EPAC<sup>dKO</sup> mice at P14 (Fig. 3A). Moreover, the number of differentiated OLs, which were stained by both CC-1 and Olig2, was 23% higher in EPAC<sup>dKO</sup> mice than in WT mice at P14 (Fig. 3A). These results suggested that EPAC deficiency affects myelination through promoting OPC proliferation. The proliferative capacity of OPCs was further assessed by analyzing Ki67, which is expressed in active phases of the cell cycle. Immunohistochemical staining showed that there were more proliferating OLs (Ki67+/Olig2+) in the corpus callosum of EPAC<sup>dKO</sup> mice than in WT mice at P14 (Fig. 3B), confirming that EPACs contribute to OPC proliferation. The expression of Olig2 and CC-1 was also evaluated in EPAC<sup>dKO</sup> mice at P60. Statistical results showed that, at this age, the total numbers of Olig2+ and differentiated CC-1+/Olig2+ OLs were normal in the corpus callosum of EPAC<sup>dKO</sup> mice (Fig. 3C). The percentage of CC-1+/Olig2+ cells among Olig2+ cells was unchanged as well in EPAC<sup>dKO</sup> mice compared with WT mice at P60 (Fig. 3C). Thus, these results provided further evidence showing the age-dependent regulation of myelination by EPACs.

### EPACs Regulate Early Expression of Myelin-specific Proteins

Myelin-related proteins appear in OLs prior to the onset of myelination and are continuously produced by OLs during

anabolism and catabolism of the myelin sheath [23]. Myelin-related proteins are not only major components of myelin but also characteristic indicators of the myelination capacity. Hence, we examined myelin-specific proteins to define the effects of EPAC-knockout on myelination. Our results showed that the expression of MAG, CNP, and MBP was significantly higher in the cerebral cortex from EPAC<sup>dKO</sup> mice than WT mice at P14 (Fig. 4A). Consistent with the results from immunohistochemistry (Fig. 2), myelin-specific proteins were generally not affected by EPAC deletion at P21 and P60, with one exception that CNP expression increased at P21 (Fig. 4A).

Myelin maturation is earlier in the spinal cord than the cerebral cortex. Do EPAC proteins also regulate myelination in the spinal cord? To address this question, we examined MAG, CNP, and MBP in the spinal cord at three postnatal stages (P4, P14, and P21), and found that their expression was increased at P4 but unchanged at P14 and P21 in EPAC<sup>dKO</sup> mice compared with WT mice (Fig. 4B). The changes of myelin-specific proteins induced by EPAC ablation in the spinal cord were consistent with those in the cerebral cortex, strengthening the idea that the effect of EPACs on myelination is age-dependent.

How are myelin proteins regulated by EPACs? We assessed the mRNA levels of myelin-related genes in EPAC<sup>dKO</sup> mice to answer this question. Our results showed that the mRNA levels of MAG, CNP, MBP, and PLP were significantly higher in EPAC<sup>dKO</sup> mice than in WT mice at P14 (Fig. 4C), implying that EPAC ablation up-regulates the transcription of myelin-related genes.

### Effects of EPAC Ablation on Transcription Factors and Cell Cycle-associated Proteins

A number of transcriptional regulators are critical for OPC differentiation and maturation. For example, SOX10, Olig2, Mrf, and YY1 promote OPC differentiation [24] whereas SOX6 arrests it [25]. Thus, the next question was whether EPACs modulate the expression of myelination-related transcription factors. In EPAC<sup>dKO</sup> mice at P14, we found that the expression of TCF4 and YY1 increased and that of GPR17 was reduced. However, the expression of the other transcription factors, Mrf, SOX10, and SOX2 was not changed by EPAC ablation (Fig. 5A, B). Since EPAC deficiency promoted the proliferation of OPCs (Fig. 3), we examined the expression of cell cycle-associated proteins and found that the total expression of several critical proteins essential to the cell cycle, including cyclin D1, CDK4, and CDK5, was not changed in EPAC<sup>dKO</sup> mice compared with WT mice at P14 (Fig. 5C). Taken together, these results suggest that EPAC ablation has complex effects on transcription factors and cell cycle-associated proteins.

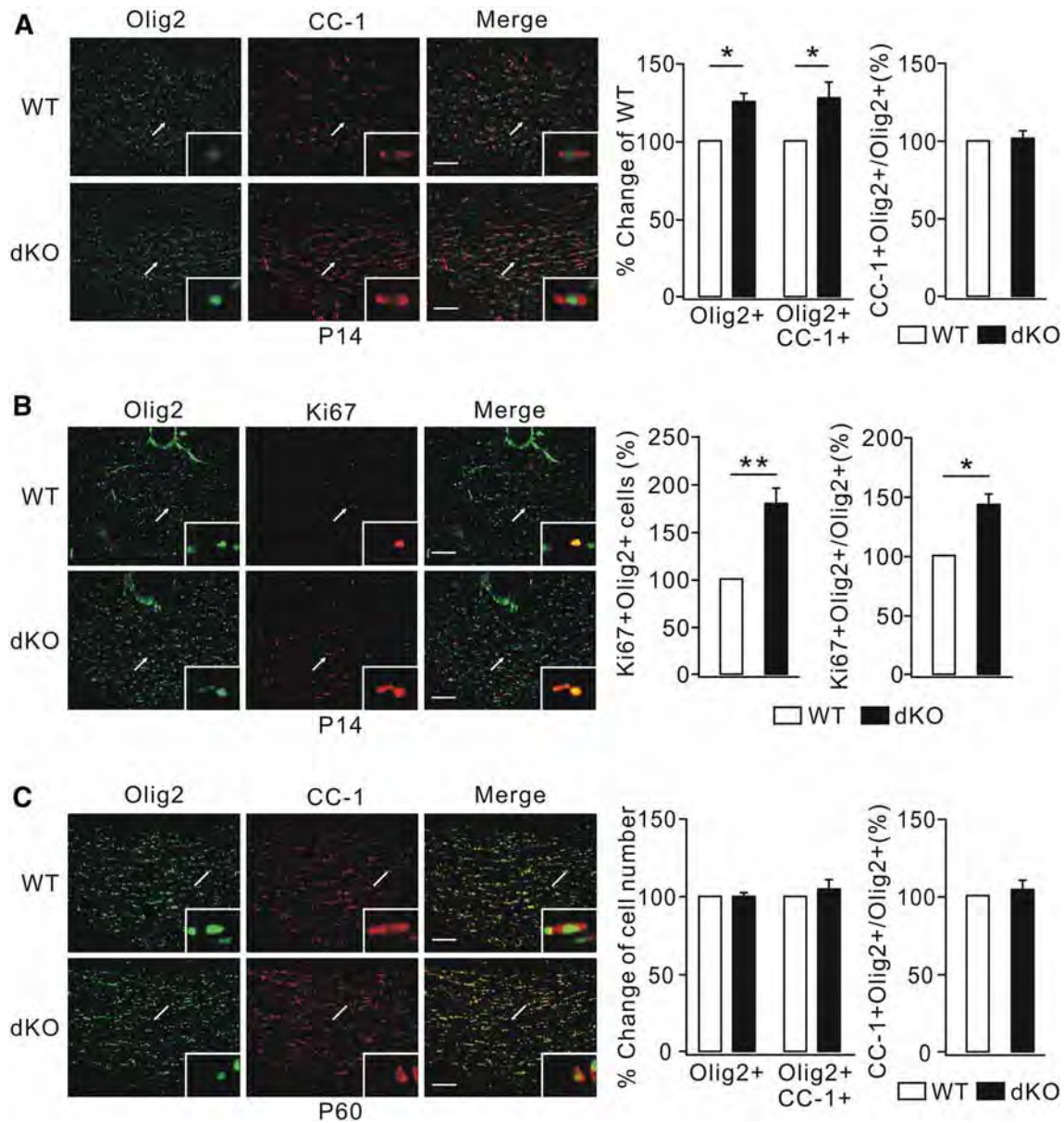


**Fig. 3** EPAC ablation promotes OPC proliferation. **A** Double-staining of Olig2 and CC1 showing total (Olig2+) and differentiated (CC-1 + Olig2+) OLs in the corpus callosum from WT and EPAC<sup>dKO</sup> mice at P14. Higher magnifications in boxes show the cells stained by Olig2 and CC-1 (arrows). Scale bars, 100  $\mu$ m. The numbers of Olig2+ and CC-1+Olig2+ cells of EPAC<sup>dKO</sup> mice were normalized to those of WT mice and the percentage changes (Olig2: 126%  $\pm$  5%,  $n = 4$ /group,  $P < 0.05$ ; CC-1 + Olig2+: 128%  $\pm$  10%,  $n = 4$ /group,  $P < 0.05$ ) are shown in the bar graphs. The ratio of CC-1 + Olig2+/Olig2+ cells of EPAC<sup>dKO</sup> mice was normalized to that of WT mice and the percentage change (102%  $\pm$  5%,  $n = 4$ /group,  $P > 0.05$ ) is also shown in bar graphs. **B** Double-staining of Olig2 and Ki67 showing total (Olig2+) and proliferating (Ki67+Olig2+) OLs in the corpus callosum from WT and EPAC<sup>dKO</sup> mice at P14. Higher magnifications in boxes show the cells stained by both Olig2 and Ki67 (arrows). Scale bars, 100  $\mu$ m. The number of Ki67 + Olig2+ cells of EPAC<sup>dKO</sup> mice was normalized to that of WT mice and the

percentage change (180%  $\pm$  16%,  $n = 4$ /group,  $P < 0.01$ ) is shown in the bar graph. The ratio of Ki67 + Olig2+/Olig2+ cells of EPAC<sup>dKO</sup> mice was normalized to that of WT mice and the percentage change (144%  $\pm$  8%,  $n = 4$ /group,  $P < 0.05$ ) is also shown in the bar graphs. **C** Double-staining of Olig2 and CC1 showing total (Olig2+) and differentiated (CC-1 + Olig2+) OLs in the corpus callosum from WT and EPAC<sup>dKO</sup> mice at P60. Higher magnifications in boxes show the cells stained by both Olig2 and CC-1 (arrows). Scale bars, 100  $\mu$ m. The numbers of Olig2+ and CC-1 + Olig2+ cells of EPAC<sup>dKO</sup> mice were normalized to those of WT mice and the percentage changes (Olig2: 100%  $\pm$  2%,  $n = 4$ /group,  $P > 0.05$ ; CC-1 + Olig2+: 105%  $\pm$  6%,  $n = 4$ /group,  $P > 0.05$ ) are shown in the bar graphs. The ratio of CC-1 + Olig2+/Olig2+ cells of EPAC<sup>dKO</sup> mice was normalized to that of WT mice and the percentage change (105%  $\pm$  6%,  $n = 4$ /group,  $P > 0.05$ ) is also shown in the bar graphs. \* $P < 0.05$ . \*\* $P < 0.01$ .

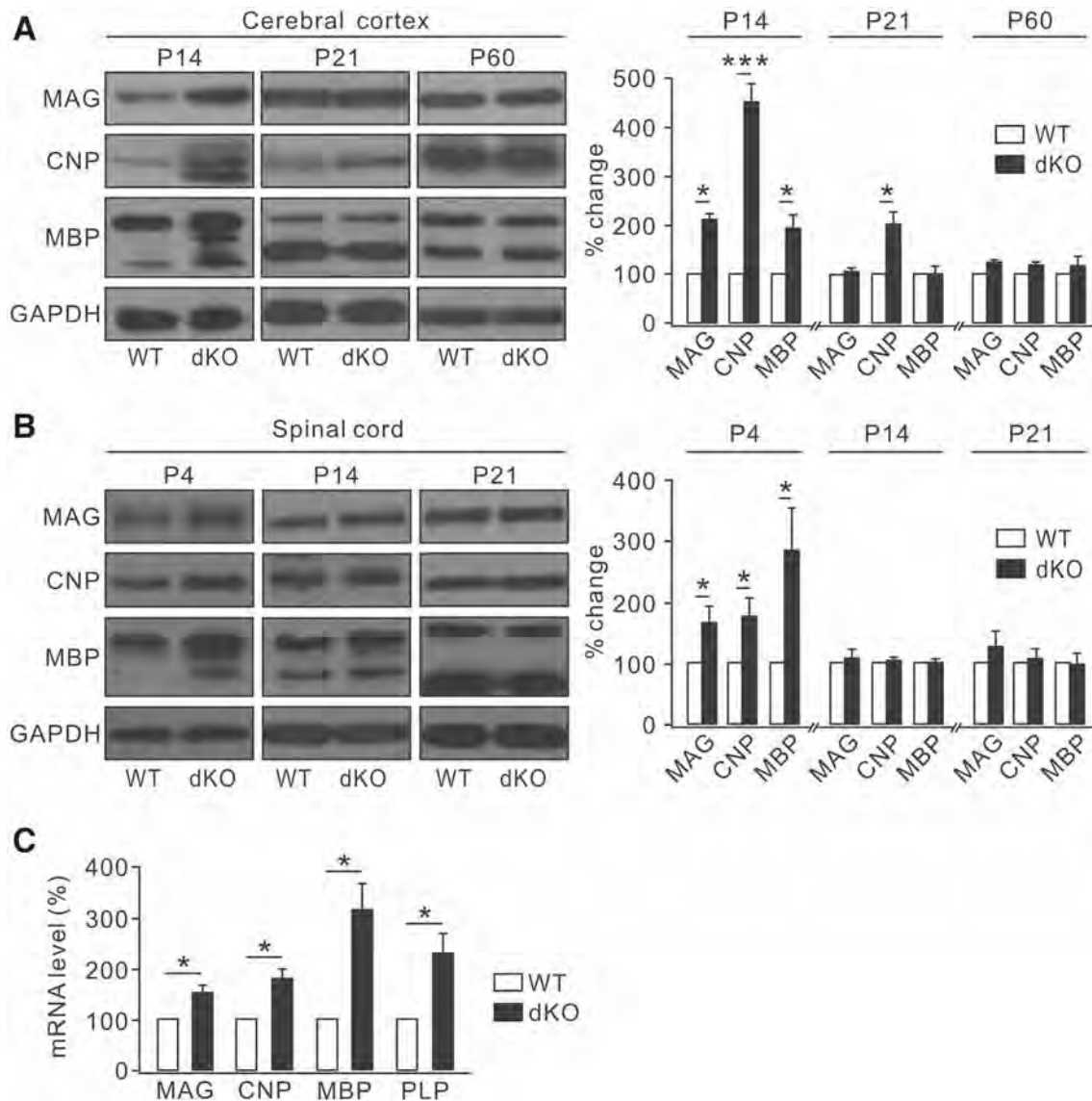


**Fig. 4** Effects of EPAC deletion on myelin-specific proteins. **A** Western blots of protein expression in the cerebral cortex of WT and EPAC<sup>dKO</sup> mice at P14. The protein levels of EPAC<sup>dKO</sup> mice were normalized to those of WT mice and the percentage changes are shown in the bar graphs on the right. **B** Western blots of protein expression in the spinal cord of WT and EPAC<sup>dKO</sup> mice at P14. The protein levels in EPAC<sup>dKO</sup> mice were normalized to those in WT mice and the percentage changes are shown in the bar graphs on the

right. **C** mRNA levels of myelin genes were quantified by the comparative Ct method using WT and EPAC<sup>dKO</sup> mice at P14. The ratios of myelin genes *versus* control GAPDH of EPAC<sup>dKO</sup> mice were calculated, normalized to those of WT mice, and percentage changes are shown in the bar graphs. The percentage changes in EPAC<sup>dKO</sup> mice were 152% ± 15% (MAG), 179% ± 19% (CNP), 314% ± 52% (MBP), and 228% ± 40% (PLP).  $n = 4/\text{group}$ . \* $P < 0.05$ . \*\*\* $P < 0.001$ .

## Discussion

The present work reveals new roles of EPACs in the CNS by showing an age-dependent regulatory effect of EPAC1 and EPAC2 on myelin development, as their deficiency caused more myelin sheaths in early postnatal (P14) but not late adult (P60) mice. Furthermore, we found that EPAC deletion promoted the proliferation of OPCs through immunohistochemical staining. Finally, we showed that EPACs had diverse effects on myelin-related transcription

factors, which in turn increased the expression of myelin-related proteins. Together, our results indicate that EPAC proteins are negative regulators of myelination and may be promising for the treatment of myelin-related diseases.

The cAMP-mediated signaling pathway, which includes the downstream effectors EPAC and PKA, regulates a multitude of physiological and pathological processes [18]. EPAC and PKA not only share homologous cAMP-binding domains but also possess unique domains, such as a Ras exchange motif as well as Ras association and CDC25-

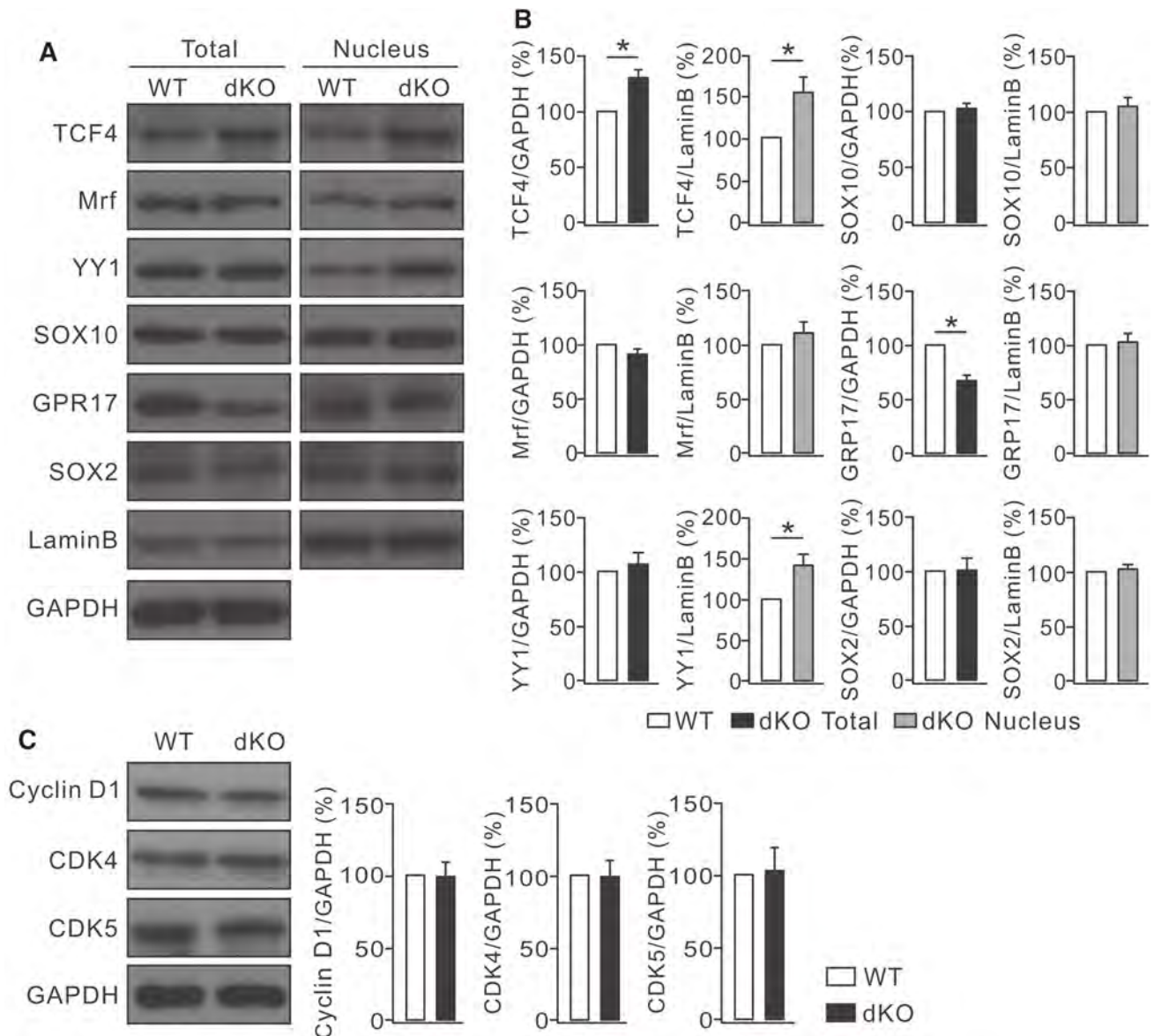


**Fig. 5** Effects of EPAC deletion on transcription factors and cell cycle-related proteins. **A** Total and nuclear expression of transcription factors in the cerebral cortex from WT and EPAC<sup>dKO</sup> mice (P14). Lysates were immunoblotted with antibodies against TCF4, Mrf, YY1, SOX10, GPR17, SOX2, LaminB, and GAPDH. **B** Percentage changes in ratios of transcription factors *versus* control GAPDH

(total) or LaminB (nucleus) of EPAC<sup>dKO</sup> mice normalized to those of WT mice. **C** Brain lysates from WT and EPAC<sup>dKO</sup> mice (P14) were immunoblotted with antibodies against Cyclin D1, CDK4, CDK5, and GAPDH. Histograms show percentage changes in the ratios of proteins *vs* control GAPDH of EPAC<sup>dKO</sup> mice normalized to those of WT mice. \**P* < 0.05.

homology domains [18]. Previously, a study reported that elevated intracellular cAMP controls the proliferation and differentiation of cultured Schwann cells (SCs) [26]. Their results suggest that proliferation requires PKA activation and differentiation into myelin-forming cells requires EPAC activation in SCs [26]. Thus, the balance between EPAC and PKA may switch the action of cAMP between proliferation and myelinating phenotypes in SCs and possibly in OLs. Although the conclusion that EPAC is required for SC differentiation has been drawn [26, 27], it should be noted that the actions of PKA and EPAC in SCs

are still paradoxical. For example, the same work shows that EPAC activation alone is not sufficient to drive a full differentiation response and there is no clear correlation between the application of PKA analogs and the induction of differentiation [26]. Considering that EPACs and PKA share homologous domains, it cannot be excluded that the analogs may fail to distinguish them and may operate in an integrated manner to achieve a net physiological effect. In other words, results derived from pharmacological treatments in cultured SCs are not sufficient to oppose our finding showing that EPAC proteins promote the

proliferation of OLs. Now, it is of interest to investigate how EPACs regulate the myelination process in the peripheral nervous system using EPAC double-knockout mice. In addition, a higher density of OPCs might cause more differentiation *in vitro* [28]. Thus, more evidence is needed to exclude potential side-effects of OPC proliferation.

Many proteins are involved in the cell cycle of eukaryotic cells, which comprises the G1, S, G2, and mitosis phases. As key factors, cyclin and cyclin-dependent protein kinases affect cell proliferation, differentiation, and apoptosis by regulating the length of the cell cycle. Cyclin D1 and CDK4 are positive regulators of the G1/S phase and accelerate cell division [29, 30]. CDK5 interacts with regulatory subunits such as p35 and P39 to regulate cell proliferation and apoptosis. In order to determine how EPAC deletion causes the increased proliferation of OPCs, we assessed the expression of cyclin D1, CDK4, and CDK5. Our results showed that their expression did not differ between EPAC<sup>dKO</sup> and WT mice. However, these results are not enough to rule out the potential regulation of the cell cycle by EPACs, because the phosphorylation of cyclin protein kinases as well as other factors included in the cell cycle may be subject to regulation by EPAC. Alternatively, EPAC may synergistically enhance the activation of neuregulin co-receptor ErbB2-ErbB3 [31] and the downstream MEK-ERK and Akt pathways [32]. It has been shown that cAMP is able to induce the phosphorylation of ErbB2 on a threonine residue, Thr-686, and in turn enhances tyrosine phosphorylation of ErbB2 and ErbB3, activation of ERK and Akt, and cell proliferation [31].

We showed that EPAC proteins are negative regulators of CNS myelination, which makes them unique. We previously reported that the GSK3 $\beta$ - $\beta$ -catenin signaling is a positive regulator of OPC differentiation by increasing the expression of the positive transcription factors SOX10, Olig2, Mrf, and YY1 [22]. In contrast, the present work showed that EPAC deletion did not influence the expression of most transcription factors, suggesting the distinct roles of negative and positive regulators of transcription factors. In fact, very little is known about how transcription factors are regulated *via* cAMP sensing [33].

To conclude, the results presented here indicated that EPAC proteins play important roles in OPC proliferation and myelination. A major remaining challenge is to explore how EPAC proteins act at the early stage of myelin development. The answer to this question will unveil the functional connection of EPAC proteins to CNS myelination and provide a potential target for the treatment of demyelinating diseases, for which a negative regulator of myelination may be more effective, as previously shown for LINGO-1 [5]. In addition, we could not exclude the

possibility that abnormalities in other types of cells may indirectly impair the development of myelin. The mice with specific deletion of EPAC 1 and EPAC2 in OL lineage cells are a better model for a clear conclusion.

**Acknowledgements** We thank Prof. You-Min Lu (Huazhong University of Science and Technology, Wuhan, China) for providing the original EPAC1 and EPAC2 knockout mice and the Core Facilities of Zhejiang University Institute of Neuroscience for technical assistance. This work was supported by the National Key Research and Development Program of Ministry of Technology and Science of China (2017YFA0104200), the National Natural Science Foundation of China (31560273, 81625006, 31571051, and 81571098), and the Natural Science Foundation of Zhejiang Province, China (Z15C090001).

**Conflict of interest** The authors claim that there are no conflicts of interest.

## References

1. Simons M, Nave KA. Oligodendrocytes: myelination and axonal support. *Cold Spring Harb Perspect Biol* 2015, 8: a020479.
2. Rowitch DH. Glial specification in the vertebrate neural tube. *Nat Rev Neurosci* 2004, 5: 409–419.
3. Wang S, Sdrulla AD, diSibio G, Bush G, Nofziger D, Hicks C, *et al.* Notch receptor activation inhibits oligodendrocyte differentiation. *Neuron* 1998, 21: 63–75.
4. Charles P, Hernandez MP, Stankoff B, Aigrot MS, Colin C, Rougon G, *et al.* Negative regulation of central nervous system myelination by polysialylated-neural cell adhesion molecule. *Proc Natl Acad Sci U S A* 2000, 97: 7585–7590.
5. Mi S, Miller RH, Lee X, Scott ML, Shulag-Morskaya S, Shao Z, *et al.* LINGO-1 negatively regulates myelination by oligodendrocytes. *Nat Neurosci* 2005, 8: 745–751.
6. Fu H, Qi Y, Tan M, Cai J, Takebayashi H, Nakafuku M, *et al.* Dual origin of spinal oligodendrocyte progenitors and evidence for the cooperative role of Olig2 and Nkx2.2 in the control of oligodendrocyte differentiation. *Development* 2002, 129: 681–693.
7. Arnett HA, Fancy SP, Alberta JA, Zhao C, Plant SR, Kaing S, *et al.* bHLH transcription factor Olig1 is required to repair demyelinated lesions in the CNS. *Science* 2004, 306: 2111–2115.
8. Battiste J, Helms AW, Kim EJ, Savage TK, Lagace DC, Mandyam CD, *et al.* Ascl1 defines sequentially generated lineage-restricted neuronal and oligodendrocyte precursor cells in the spinal cord. *Development* 2007, 134: 285–293.
9. He Y, Dupree J, Wang J, Sandoval J, Li J, Liu H, *et al.* Casaccia-Bonnel P The transcription factor YinYang 1 is essential for oligodendrocyte progenitor differentiation. *Neuron* 2007, 55: 217–230.
10. Emery B, Agalliu D, Cahoy JD, Watkins TA, Dugas JC, Mulinylaw SB, *et al.* Myelin gene regulatory factor is a critical transcriptional regulator required for CNS myelination. *Cell* 2009, 138: 172–185.
11. Pringle NP, Mudhar HS, Collarini EJ, Richardson WD. PDGF receptors in the rat CNS: during late neurogenesis, PDGF alpha-receptor expression appears to be restricted to glial cells of the oligodendrocyte lineage. *Development* 1992, 115: 535–551.
12. Spassky N, de Castro F, Le Bras B, Heydon K, Quéraud-LeSaux F, Bloch-Gallego E, *et al.* Directional guidance of oligodendroglial migration by class 3 semaphorins and netrin-1. *J Neurosci* 2002, 22: 5992–6004.

13. Tsai HH, Macklin WB, Miller RH. Netrin-1 is required for the normal development of spinal cord oligodendrocytes. *J Neurosci* 2006, 26: 1913–1922.
14. Filipovic R, Zecevic N. The effect of CXCL1 on human fetal oligodendrocyte progenitor cells. *Glia* 2008, 56: 1–15.
15. Furusho M, Ishii A, Bansal R. Signaling by FGF receptor 2, not FGF receptor 1, regulates myelin thickness through activation of ERK1/2-MAPK, which promotes mTORC1 activity in an Akt-independent manner. *J Neurosci* 2017, 37: 2931–2946.
16. Malone M, Gary D, Yang IH, Miglioretti A, Houdayer T, Thakor N, *et al.* Neuronal activity promotes myelination via a cAMP pathway. *Glia* 2013, 61: 843–854.
17. Vakilzadeh G, Khodaghohi F, Ghadiri T, Darvishi M, Ghaemi A, Noorbakhsh F, *et al.* Protective effect of a cAMP analogue on behavioral deficits and neuropathological changes in cuprizone model of demyelination. *Mol Neurobiol* 2015, 52:130–141.
18. Cheng X, Ji Z, Tsalkova T, Mei F. Epac and PKA: a tale of two intracellular cAMP receptors. *Acta Biochim Biophys Sin* 2008, 40: 651–662.
19. Yang Y, Shu X, Liu D, Shang Y, Wu Y, Pei L, *et al.* EPAC null mutation impairs learning and social interactions via aberrant regulation of miR-124 and Zif268 translation. *Neuron* 2012, 73: 774–788.
20. Xie YJ, Zhou L, Wang Y, Jiang NW, Cao S, Shao CY, *et al.* Leucine-rich glioma inactivated 1 promotes oligodendrocyte differentiation and myelination via TSC-mTOR signaling. *Front Mol Neurosci* 2018, 11: 231.
21. Zou J, Zhou L, Du XX, Ji Y, Xu J, Tian J, *et al.* Rheb1 is required for mTORC1 and myelination in postnatal brain development. *Dev Cell* 2011, 20: 97–108.
22. Zhou L, Shao CY, Xu SM, Ma J, Xie YJ, Zhou L, *et al.* GSK3 $\beta$  promotes the differentiation of oligodendrocyte precursor cells via  $\beta$ -catenin-mediated transcriptional regulation. *Mol Neurobiol* 2014, 50: 507–519.
23. Sternberger NH, Itoyama Y, Kies MW, Webster HD. Myelin basic protein demonstrated immunocytochemically in oligodendroglia prior to myelin sheath formation. *Proc Natl Acad Sci U S A* 1978, 75: 2521–2524.
24. Emery B. Regulation of oligodendrocyte differentiation and myelination. *Science* 2010, 330: 779–782.
25. Stolt CC, Schlierf A, Lommes P, Hillgärtner S, Werner T, Kosian T, *et al.* SoxD proteins influence multiple stages of oligodendrocyte development and modulate SoxE protein function. *Dev Cell* 2006, 11: 697–709.
26. Bacallao K, Monje PV. Opposing roles of PKA and EPAC in the cAMP-dependent regulation of schwann cell proliferation and differentiation. *PLoS One* 2013, 8: e82354.
27. Bacallao K, Monje PV. Requirement of cAMP signaling for Schwann cell differentiation restricts the onset of myelination. *PLoS One* 2015,10: e0116948.
28. Rosenberg SS, Kelland EE, Tokar E, De la Torre AR, Chan JR. The geometric and spatial constraints of the microenvironment induce oligodendrocyte differentiation. *Proc Natl Acad Sci U S A* 2008,105: 14662–14667.
29. Cai D, Latham VM Jr, Zhang X, Shapiro GI. Combined depletion of cell cycle and transcriptional cyclin-dependent kinase activities induces apoptosis in cancer cells. *Cancer Res* 2006, 66: 9270–9280.
30. Yeh CT, Lu SC, Chen TC, Peng CY, Liaw YF. Aberrant transcripts of the cyclin-dependent kinase-associated protein phosphatase in hepatocellular carcinoma. *Cancer Res* 2000, 60: 697–700.
31. Monje PV, Athauda G, Wood PM. Protein kinase A-mediated gating of neuregulin-dependent ErbB2-ErbB3 activation underlies the synergistic action of cAMP on Schwann cell proliferation. *J Biol Chem* 2008, 283: 34087–34100.
32. Monje PV, Bartlett Bunge M, Wood PM. Cyclic AMP synergistically enhances neuregulin-dependent ERK and Akt activation and cell cycle progression in Schwann cells. *Glia* 2006, 53: 649–659.
33. Sands WA, Palmer TM. Regulating gene transcription in response to cyclic AMP elevation. *Cell Signal* 2008, 20: 460–466.



LETTER TO THE EDITOR

## Empathic Contagious Pain and Consolation in Laboratory Rodents: Species and Sex Comparisons

Rui Du<sup>1</sup> · Wen-Jun Luo<sup>1</sup> · Kai-Wen Geng<sup>1</sup> · Chun-Li Li<sup>1,2</sup> · Yang Yu<sup>1,2</sup> · Na Wei<sup>1,2</sup> · Jun Chen<sup>1,2</sup>

Received: 18 October 2019 / Accepted: 8 December 2019 / Published online: 17 January 2020  
© Shanghai Institutes for Biological Sciences, CAS 2020

### Dear Editor,

In the past five years, we have developed a behavioral model of empathy for pain in rats [1–5]. Experimentally, at least two types of behaviors associated with empathy for pain in rats can be identified, based on the evolutionary notion of the Russian doll model [6]. One has been referred to as an observer's empathic consolation, which is driven by social interaction with a demonstrator in pain [3, 7–9]; the other is referred to as observational contagious pain (OCP or empathic transfer of pain) from a distressed object to a witnessing subject [1–3, 5]. Briefly, the consolation in rat observers has been identified as allolicking and allogrooming behaviors toward a familiar conspecific in pain during a 30-min priming dyadic social interaction (PDSI) [3, 8, 9]. Allolicking can be defined as an observer's sustained licking action at a demonstrator's injury site, while allogrooming can be defined as an observer's head contact with the head or body of a demonstrator in pain, accompanied by rhythmic head movement [3, 4, 8]. The bouts of allolicking and allogrooming behaviors can be captured by video recorder

and analyzed qualitatively and quantitatively off-line (see Supplementary Methods) [4]. Meanwhile, OCP, also referred to as empathic pain hypersensitivity in our previous reports, has been identified qualitatively and quantitatively as lowered pain threshold or increased pain sensitivity in a rat observer after the PDSI with a demonstrator in pain [1–3]. OCP remains unchanged for at least 5 h after the PDSI [2, 3]. Although allogrooming behavior can be seen in both familiar and unfamiliar conspecifics during the PDSIs, allolicking behavior and OCP can only be seen in a familiar observer, suggesting that the establishment of familiarity among conspecifics is essential to the induction of empathic responses to another's pain in rats [2, 3, 5]. However, the model has only been validated in male but not female rats. Moreover, so far a mouse model of empathy for pain has not been available although models of observational fear learning have been well established [5]. Whether species and sex differences exist for this paradigm is unknown. Thus, to answer the above common questions, we further designed and studied the behavioral parameters associated with OCP and consolation qualitatively and quantitatively in both male and female mice and rats.

In this study, male and female C57BL/6 (B6) mice and Sprague-Dawley albino rats were used. Regardless of species, the dyads of animals used for social interaction, which were of the same sex and familiar to each other, were designed as two paradigms: (1) CO<sub>naive</sub>-CD<sub>naive</sub>, a control paradigm for dyadic social interaction between a naive cagemate observer and a naive cagemate demonstrator; and (2) CO<sub>naive</sub>-CD<sub>pain</sub>, an experimental paradigm for dyadic social interaction between a naive cagemate observer and a cagemate demonstrator in pain (for details see Supplementary Methods and Fig. S1) [4]. The mouse and rat observers in the CO<sub>naive</sub>-CD<sub>pain</sub> paradigm both

Rui Du and Wen-Jun Luo have contributed equally to this work.

**Electronic supplementary material** The online version of this article (<https://doi.org/10.1007/s12264-020-00465-y>) contains supplementary material, which is available to authorized users.

✉ Jun Chen  
junchen@fmmu.edu.cn; junchen\_ibsp2015@yeah.net

<sup>1</sup> Institute for Biomedical Sciences of Pain, Tangdu Hospital, The Fourth Military Medical University, Xi'an 710038, China

<sup>2</sup> Key Laboratory of Brain Stress and Behavior, People's Liberation Army, Xi'an 710038, China

showed more consolation behaviors toward a conspecific in pain than the observers in the CO<sub>naive</sub>-CD<sub>naive</sub> paradigm (Fig. 1A–D for mice, Fig. 2A–D for rats, and Supplementary Tables S1–S2). Generally, both mouse and rat observers had a shorter latency and spent more time and visit counts engaged in allolicking and allogrooming when witnessing a conspecific in pain (Figs. 1A–D, 2A–D). Interestingly, the mouse observers also had allo-mouth sniffing behavior, but in contrast the rat observers did not (Supplementary Tables S1–S2). Both mouse and rat observers showed allo-tail sniffing and self-grooming

behaviors as previously described (Supplementary Tables S1–S2) [7].

There were no species differences in consolation (latency, total time, and visit count of allolicking and allogrooming) between mice and rats in either males or females (Table S3). Species differences between mice and rats were not revealed in allo-tail sniffing in terms of latency and total time in either males or females (Table S3). Although male mice had more visit counts than male rats ( $P = 0.002$ , Mann-Whitney U test), no species difference was found between female mice and rats for allo-tail sniffing counts (Table S3). As for non-social

**Fig. 1** Empathic consolation and observational contagious pain in male and female mouse observers. **A–D** Latency (**A**), time course (**B**), total time (**C**), and visit counts (**D**) when the mouse observers engaged in allolicking and allogrooming behaviors during 30-min priming dyadic social interactions (PDSIs) with a cagemate demonstrator of the same sex in pain. **E, F** Examples of stimulus-response curves (SRCs) prior to (BL) and 60 min after a PDSI in male (m) and female (f) mouse observers in the CO<sub>naive</sub>-CD<sub>naive</sub> and CO<sub>naive</sub>-CD<sub>pain</sub> paradigms. **G** Time courses of changes in von Frey intensity (g) for half maximal response from the SRCs of mouse observers in the CO<sub>naive</sub>-CD<sub>naive</sub> and CO<sub>naive</sub>-CD<sub>pain</sub> paradigms (BL, baseline;  $n = 12$  males,  $n = 12$  females; mean  $\pm$  SEM; \* $P < 0.05$ , CO<sub>naive</sub>-CD<sub>pain</sub> vs CO<sub>naive</sub>-CD<sub>naive</sub>; # $P < 0.05$  female vs male in the CO<sub>naive</sub>-CD<sub>pain</sub> paradigm, two-tailed Mann-Whitney U test). See supplementary Tables S1, S3 and S4 for details.

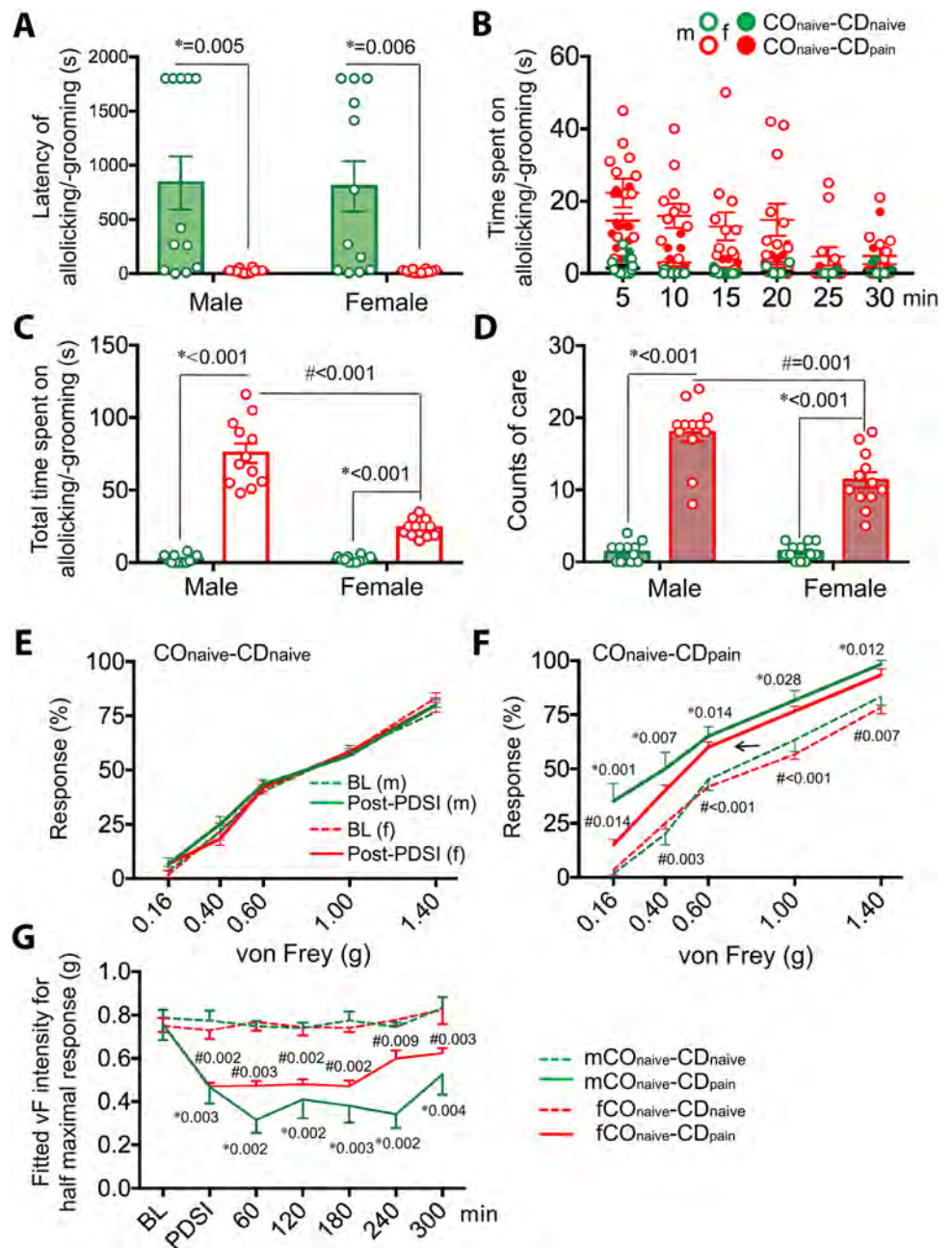
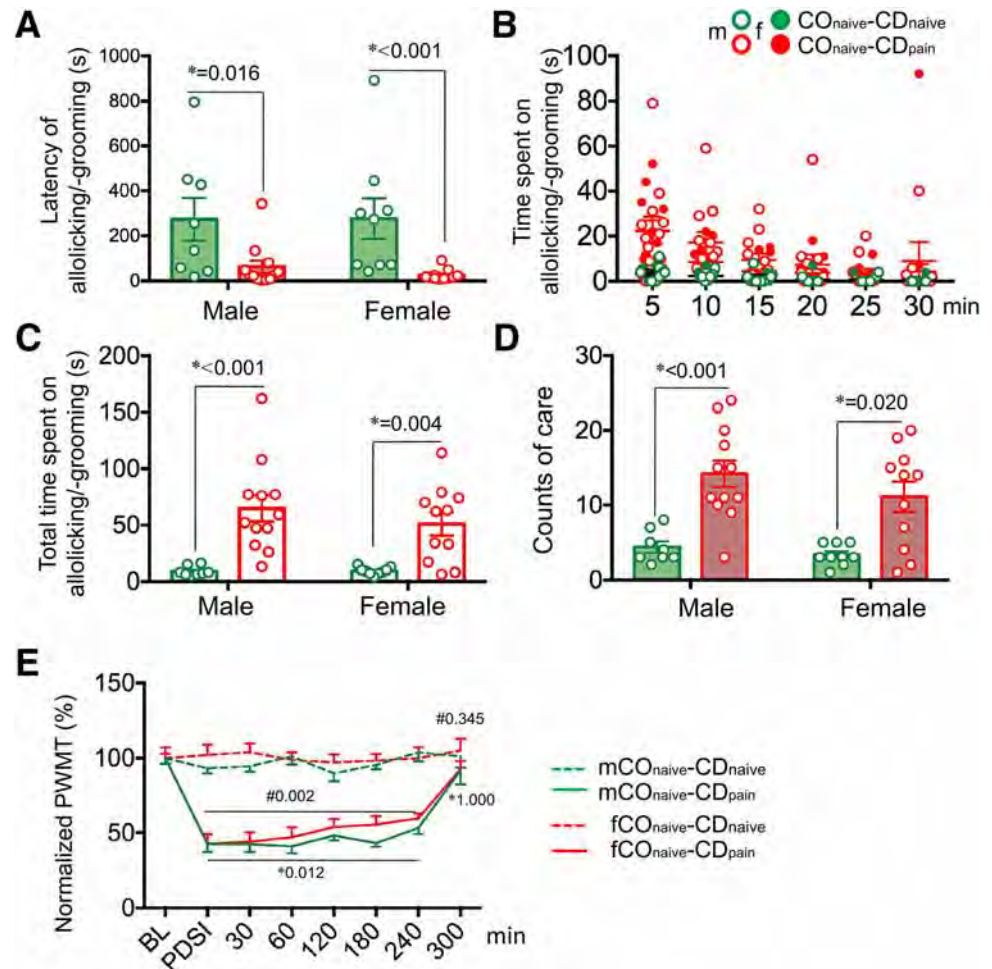


**Fig. 2** Empathic consolation and observational contagious pain in male and female rat observers. **A–D** Latency (A), time course (B), total time (C), and visit counts (D) when the rat observers engaged in allolicking and allogrooming behaviors during 30-min PDSI with a cagemate demonstrator of the same sex in pain. **E** Time courses of changes in paw withdrawal mechanical threshold (g) of rat observers in the CO<sub>naive</sub>–CD<sub>naive</sub> and CO<sub>naive</sub>–CD<sub>pain</sub> paradigms (BL, baseline;  $n = 8–12$  males,  $n = 9–11$  females; mean  $\pm$  SEM;  $*P < 0.05$ , CO<sub>naive</sub>–CD<sub>pain</sub> vs CO<sub>naive</sub>–CD<sub>naive</sub>; two-tailed Mann-Whitney *U* test). See supplementary Tables S2, S3 and S4 for details.



behavior, rats of both sexes spent more time on self-grooming than mice of both sexes (Table S3, mice vs. rats:  $P = 0.017$  for males and  $P = 0.016$  for females, Mann-Whitney *U* test) although the counts showed no species difference. Moreover, rats of both sexes had a shorter latency in self-grooming than mice of both sexes although a statistically significant species difference was only seen in males (Table S3,  $P = 0.001$ , Mann-Whitney *U* test). Taking the latency and time course data together, we found that both mouse and rat observers, either male or female, were likely to approach a conspecific in pain as quickly as possible and spent more time on consolation and social behaviors than on self-grooming behavior (Figs. 1A, 1B, 2A, 2B, and Tables S1 and S2).

In mice, a distinct sex difference was found in both empathic consolation and general social behaviors in terms of time and counts, but there was no sex difference for latency (Fig. 1A–D and Table S1). Male mice spent more time and had higher visit counts than females in allolicking/allogrooming and allo-mouth/allo-tail sniffing toward a conspecific in pain during the first 20 min of PDSIs (Fig. 1C, D and Table S1), while there was no sex

difference in self-grooming in terms of latency, time, and count (Table S1). In rats, no sex difference was seen in either empathic consolation or general social behavior in terms of latency, time, and count (Fig. 2A–D and Table S2). Although female rats had a relatively shorter latency than males ( $P = 0.019$ , Mann-Whitney *U* test), no sex difference was seen in time and count for self-grooming behavior (Table S2).

Similar to our previous and present reports on rats [1–4], OCP also occurred in naive mouse observers in the CO<sub>naive</sub>–CD<sub>pain</sub> paradigm after 30-min PDSI (Fig. 1F–G and Fig. S2G–L), but OCP was not identified in mouse observers in the CO<sub>naive</sub>–CD<sub>naive</sub> paradigm (Fig. 1E and Fig. S2A–F). Both male and female mouse observers presented long-term mechanical pain hypersensitivity after a PDSI with a conspecific in pain, as evidenced by a significant leftward shift of the stimulus-response curves from baseline (Fig. 1F and Fig. S2G–L) and a lower paw withdrawal threshold (von Frey intensity for half maximal response; Fig. 1G). The OCP identified in the mouse observers in the CO<sub>naive</sub>–CD<sub>pain</sub> paradigm did not

disappear after a PDSI until 240 min in females and 300 min in males (Fig. 1G and Fig. S2G–L).

Generally, no species difference in OCP was revealed between mice and rats of either sex in terms of magnitude and time course under the same experimental condition, procedure, and paradigm (Figs. 1E–G, 2E, and Fig. S2).

No sex difference was revealed in OCP between male and female observers in either mice or rats in terms of magnitude and time course under the same experimental condition, procedure and paradigm for up to 180 min after a PDSI (Figs. 1E–G, 2E, and Fig. S2). However, the empathic mechanical pain hypersensitivity in mouse observers was maintained relatively longer in males than in females (Fig. 1G and Fig. S2). No sex difference was found in OCP between rat male and female observers during the whole time of observation (Fig. 2E).

Finally, because we had reported that the spontaneous pain-related behaviors in the demonstrators play a very important role in the elicitation of empathic responses in the observers [3], we also rated the total time that the distressed demonstrators spent on injured paw licking behaviors in mice and rats of both sexes (Fig. S3). The results showed no differences in pain indices between mouse and rat demonstrators of both sexes although female mice spent more time in paw licking than males (Fig. S3).

From the evolutionary point of view, empathy has been proposed to be hierarchical in mammals, evolving from a very low stage (motor mimicry and emotional contagion) to a relatively higher stage (empathic concern and consolation), and finally to the highest stage (perspective-taking, mentalizing, theory of mind, and targeted-help) from lower animals to human beings [6]. Although several emerging lines of evidence support the existence of emotional contagion in lower mammals [5, 10, 11], answers to questions of whether they are able to recognize, understand, share, and care for others are still controversial due to the lack of direct experimental evidence [3, 8, 12]. In a series of reports on empathy for pain in rats and mice, including the present study, we have provided strong experimental evidence for the existence of both emotional contagion and empathic consolation in laboratory rodents [1–5, 9]. Before our findings, empathic consolation had only been reported in a special sub-species of wild rodent—the socially monogamous, biparental prairie vole [8], although emotional contagion of pain or observational fear learning has been increasingly evidenced [5, 6, 10, 13]. Taken together, it has been demonstrated experimentally that lower mammals such as rodents exhibit both a lower stage (emotional contagion, i.e., OCP here) and a relatively higher stage of empathy (empathic concern and consolation), supporting the theoretical Russian-doll model for the evolution of empathy in mammals [6]. Moreover, the finding that social familiarity plays essential roles in the

induction of empathy for pain in rodents also supports Darwin's assertion that "with all animals, sympathy is directed solely towards the members of the same community, and therefore towards known, and more or less beloved members, but not to all the individuals of the same species" [5, 14].

In the past century, empathy has been mostly studied outdoors in non-human primates and other non-laboratory animals [6, 11]. Therefore, discovering, developing and validating laboratory animal models of empathy are critical for opening a new field of science—the neuroscience of empathy. Here, we have developed a laboratory rodent model of empathy for pain in both mice and rats using a set of novel behavioral parameters for both qualitative and quantitative assessment. We have identified and validated two behavioral components of empathy for pain in a laboratory rodent model: (1) consolation and (2) observational contagious pain.

To make qualitative and quantitative assessments of consolation, we successfully identified allolicking and allogrooming behaviors in naive observers during PDSIs with familiar conspecifics in pain. To determine whether the observer's allolicking and allogrooming behaviors are selective or specific to the injury and pain of the object, we also evaluated general social behavior (allo-mouth and allo-tail sniffing) and non-social behavior (self-grooming) in the observers. In each type of targeted behavior, four parameters (latency, time course, total time, and visit count) were quantified. The results clearly showed that there were no species differences between mice and rats for allolicking and allogrooming behaviors in males or females, suggesting that laboratory rodents can be motivated to perform empathic consolation when witnessing their familiars in a painful or distressing condition. Mice and rats are likely as sharing and caring as humans. Our data showed that both mouse and rat observers began to approach a familiar conspecific in pain after a short delay when witnessing the event and then engaged longer in allolicking the injury site and allogrooming the body of the injured partner. In contrast, the same animals had a longer latency and a lower count in either self-grooming or allo-tail and allo-mouth sniffing, suggesting that laboratory rodents have a strong ability to rapidly recognize and understand the distressing condition of others. And this process is likely to motivate visiting, sharing, and caring for the injured object at the expense of loss of observers' time in environmental exploration and self-grooming. Because self-grooming is predominant among the usual behaviors of rodents (> 40% of waking time) [7], the loss of time in self-grooming and gain of time in allolicking and allogrooming during PDSIs strongly imply the existence of prosocial and altruistic behaviors in rodent observers while witnessing a familiar in pain.

It is interesting to note that there was a sex difference between male and female mice in visit counts and total time of allolicking and allogrooming as well as allo-mouth and allo-tail sniffing; however, no such difference was seen in rats. Although the female mouse observers spent less time engaged in allogrooming but more time on allolicking toward the injury site in the distressed object, the sex difference in consolation in mice is not likely to be only caused by the sex difference in allogrooming, since general social behaviors (allo-mouth and allo-tail sniffing) also showed a sex difference. The sex difference in observer consolation in mice is not likely to be caused by a sex difference in the paw-licking behavior of injured demonstrators, because female observers engaged in less consolation toward the female demonstrators with more pain while male observers engaged in more consolation toward male demonstrators with less pain. Generally, the male has more consolation and more social behaviors than the female in mice. Moreover, rats spent equivalent amounts of time and visit counts in allolicking, allogrooming, and allo-tail sniffing in males and females. Unlike mice, the rat observers spent less time engaged in allo-mouth sniffing although there was no difference in the time spent allo-tail sniffing in the two species.

As noted above, although mice and rats have different sensitivity to mechanical stimuli, standardized measurements revealed no species and sex differences in OCP. Similar to our previous reports on male rats [2, 3], here the rat observers showed no sex difference in OCP between males and females after PDSIs with a familiar conspecific in pain. The paw withdrawal threshold of both sexes was lowered by > 50% immediately after a PDSI, and this lowered threshold remained unchanged until 300 min later. A relatively long-term decrease in mechanical threshold was identified on both sides of the hind paws and was in parallel between males and females in the rat observers. Similarly, OCP was also identified in mouse observers of both sexes immediately after a PDSI by showing leftward shift of the stimulus-response curves from baseline. This leftward shift remained unchanged between male and female mice until 240 min after the PDSI. Moreover, the intensity for the half maximal response in mice that is equivalent to the mechanical threshold in rats also showed a separation of the time effect between male and female at 240 min after the PDSI. Because the male observers had a longer time course in both the consolation and OCP than the females, this may reflect a stronger correlation between the two empathic behaviors in mice. Although sex differences in pain are well established [15], the sex difference in empathic contagious pain in mice is not likely due to a sex difference in mechanical pain sensitivity because the stimulus-response curves for the observers in the CO<sub>naive</sub>-CD<sub>naive</sub> paradigm (for both pre- and post-PDSI) and the baseline of the CO<sub>naive</sub>-CD<sub>pain</sub> paradigm nicely overlapped between males and females.

In summary, our results demonstrated that both mice and rats have OCP and consolation when witnessing a conspecific in pain, although a sex difference may exist in mice. This further supports an evolutionary view of empathy—that social animals, including laboratory rodents, are gregarious in nature and may also have the ability to feel, recognize, understand, and share the distressed state of another.

**Acknowledgements** The authors are grateful to YQ Yu, W Sun, Y Wang, YJ Yin, RR Wang, Y Yang, and F Yang for cooperation and XL Wang for animal support. This work was supported by grants from the National Natural Science Foundation of China (81571072 and 31600855).

**Conflict of interest** The authors have no conflicts of interest to declare.

## References

- Li Z, Lu YF, Li CL, Wang Y, Sun W, He T, *et al.* Social interaction with a cagemate in pain facilitates subsequent spinal nociception via activation of the medial prefrontal cortex in rats. *Pain* 2014, 155: 1253–1261.
- Lü YF, Yang Y, Li CL, Wang Y, Li Z, Chen J. The locus coeruleus–norepinephrine system mediates empathy for pain through selective up-regulation of P2X3 receptor in dorsal root ganglia in rats. *Front Neural Circuits* 2017, 11: 66.
- Li CL, Yu Y, He T, Wang RR, Geng KW, Du R, *et al.* Validating rat model of empathy for pain: effects of pain expressions in social partners. *Front Behav Neurosci* 2018, 12: 242.
- Yu Y, Li CL, Du R, Chen J. Rat model of empathy for pain. *Bio-protocol* 2019, 9: e3266.
- Chen J. Empathy for distress in humans and rodents. *Neurosci Bull* 2018, 34: 216–236.
- de Waal FBM, Preston SD. Mammalian empathy: behavioural manifestations and neural basis. *Nat Rev Neurosci* 2017, 18: 498–509.
- Kalueff AV, Stewart AM, Song C, Berridge KC, Graybiel AM, Fentress JC. Neurobiology of rodent self-grooming and its value for translational neuroscience. *Nat Rev Neurosci* 2016, 17: 45–59.
- Burkett JP, Andari E, Johnson ZV, Curry DC, de Waal FB, Young LJ. Oxytocin-dependent consolation behavior in rodents. *Science* 2016, 351: 375–378.
- Lu YF, Ren B, Ling BF, Zhang J, Xu C, Li Z. Social interaction with a cagemate in pain increases allogrooming and induces pain hypersensitivity in the observer rats. *Neurosci Lett* 2018, 662: 385–388.
- Mogil JS. Social modulation of and by pain in humans and rodents. *Pain* 2015, 156 Suppl 1: S35–41.
- Panksepp J, Panksepp JB. Toward a cross-species understanding of empathy. *Trend Neurosci* 2013, 36: 489–496.
- Langford DJ, de C Williams AC. The caring, sharing rat? *Pain* 2014, 155: 1183–1184.
- Langford DJ, Cramer SE, Shehzad Z, Smith SB, Sotocinal SG, Levenstadt JS, *et al.* Social modulation of pain as evidence for empathy in mice. *Science* 2006, 312: 1967–1970.
- Darwin C. *The Descent of Man*. 2nd edition. London: Penguin Group, 1871.
- Fillingim RB. *Sex, Gender, and Pain*. Seattle: IASP Press, 2000.



LETTER TO THE EDITOR

# Low-frequency Stimulation at the Subiculum is Anti-convulsant and Anti-drug-resistant in a Mouse Model of Lamotrigine-resistant Temporal Lobe Epilepsy

Yeping Ruan<sup>1</sup> · Cenglin Xu<sup>2</sup> · Jile Lan<sup>1</sup> · Jiazhen Nao<sup>2</sup> · Shuo Zhang<sup>2</sup> · Fei Fan<sup>2</sup> · Yi Wang<sup>2</sup> · Zhong Chen<sup>1,2</sup>

Received: 24 October 2019 / Accepted: 10 December 2019 / Published online: 10 March 2020  
© Shanghai Institutes for Biological Sciences, CAS 2020

## Dear Editor,

Epilepsy is a common neurological disease. About 30% of epileptic patients develop resistance to antiepileptic drugs (AEDs), and are considered to have refractory or drug-resistant epilepsy [1]. Based on the time course over which drug-resistance develops, refractory epilepsy can be further divided into an early-onset type (drug-resistance more likely innate and correlated with gene mutations) and a delayed-onset type (drug-resistance emerges after a period of medication) [2]. The latter usually displays a more complex constellation of pathological findings, often associated with mesial temporal sclerosis [3]. Longitudinal neuroimaging studies have shown that the degree of brain atrophy is more extensive in patients with the delayed-onset type than in those with an early onset [4]. After repeated trials with unsuccessful drug treatments, uncontrolled seizures, along with other complications including impaired memory, often put patients' health at risk. At that time, even epilepsy surgery adds limited value to the

treatment of these patients. Thus, an alternative therapeutic strategy is urgently needed for patients with delayed-onset refractory epilepsy.

Deep brain stimulation (DBS), with either a low or a high frequency, is a promising treatment for refractory epilepsy. In particular, low-frequency stimulation (LFS), with mild and relatively safe characteristics, is more suitable for epileptic patients than high-frequency stimulation [5]. The therapeutic effect of LFS largely depends on the stimulus parameters and brain targets. The subiculum is a crucial output region of the hippocampus, and has been shown to be hyperexcitable in both patients and animals with temporal lobe epilepsy (TLE) [6]. More importantly, specific 1-Hz interictal spikes originate in the subiculum of patients with refractory TLE [7]. We previously reported that 1-Hz LFS at the subiculum significantly retards kindling acquisition and inhibits recurrent seizures in rats [8]. Further study has verified the anti-convulsant efficacy of LFS in animal models with early-onset refractory TLE. Moreover, drug resistance can be reversed by LFS treatment [9]. However, whether LFS at the subiculum is a promising treatment for delayed-onset refractory TLE is still unclear.

The lamotrigine (LTG)-resistant kindled rodent is one of the most widely-used animal models that resemble delayed-onset refractory epilepsy [10]. Kindled rats or mice exposed to a sub-therapeutic dose of LTG during the kindling process subsequently show LTG resistance. Thus, in this study, we established this classic hippocampal kindled LTG-resistant TLE model and evaluated the therapeutic efficacy of LFS at the subiculum in this model.

The LTG-resistant TLE model was established with rapid hippocampal kindling in mice [11]. The mice were divided into two groups based on their afterdischarge threshold. The LTG group received a sub-therapeutic dose

---

**Electronic supplementary material** The online version of this article (<https://doi.org/10.1007/s12264-020-00482-x>) contains supplementary material, which is available to authorized users.

---

Yeping Ruan and Cenglin Xu have contributed equally to this work.

---

✉ Zhong Chen  
chenzhong@zju.edu.cn

<sup>1</sup> College of Pharmaceutical Science, Zhejiang Chinese Medical University, Hangzhou 310000, China

<sup>2</sup> Key Laboratory of Medical Neurobiology of National Health Commission and Chinese Academy of Medical Sciences, Institute of Pharmacology and Toxicology, College of Pharmaceutical Sciences, Zhejiang University, Hangzhou 310000, China

of LTG while the vehicle group received vehicle, along with kindling (Fig. 1). The kindling acquisition process was not altered by LTG: both the progression of behavioral

seizure stage and mean afterdischarge duration (ADD) showed no difference between the two groups (Fig. 1B, C). Once mice were fully kindled (three consecutive stage 5

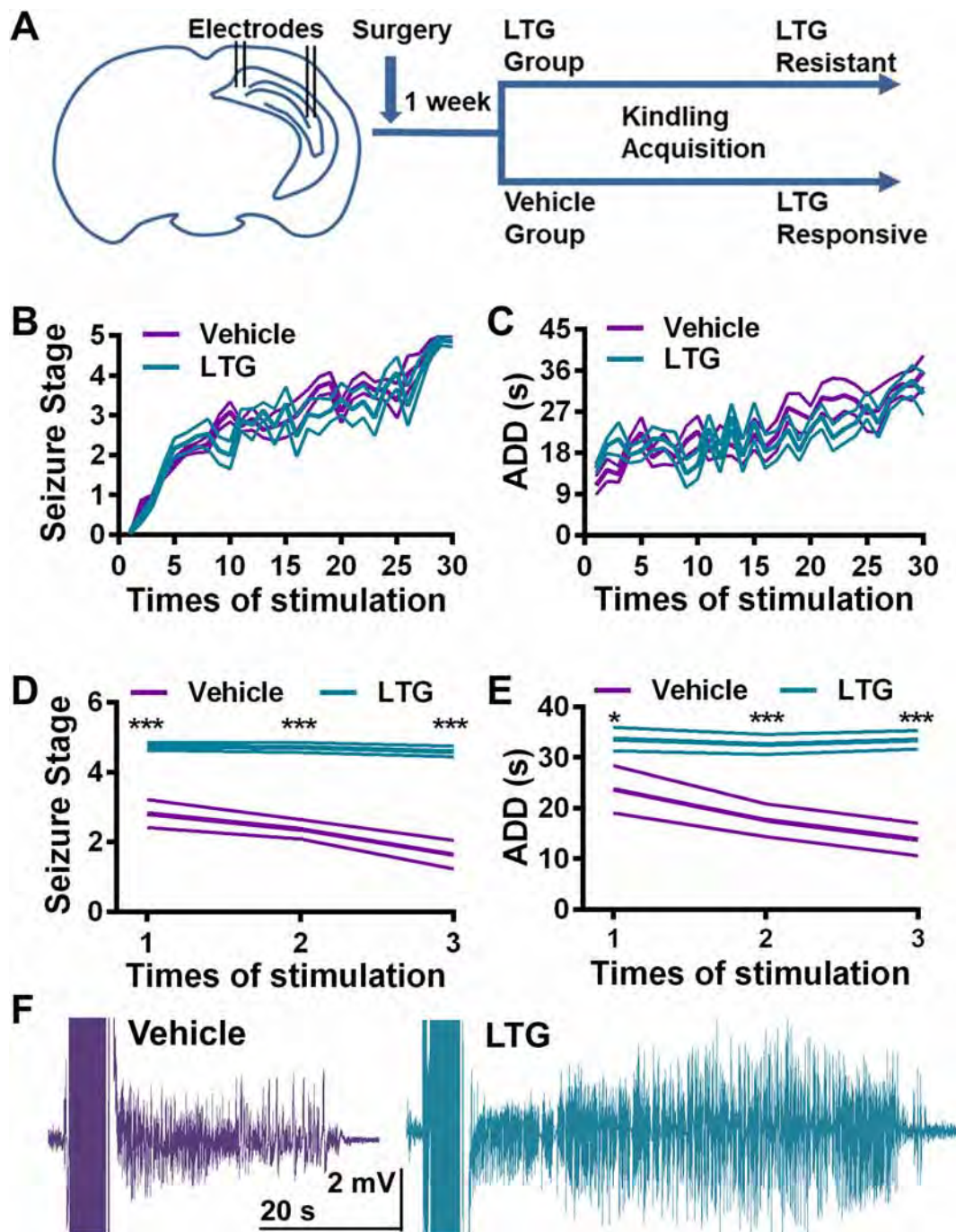


**Fig. 1** Establishment of a mouse model of TLE with delayed-onset lamotrigine (LTG) resistance. **A** Schematic of the establishment of the LTG-resistant TLE model. Electrodes were implanted into the CA3 and subiculum of C57 mice, which were then divided into two groups, one receiving a sub-therapeutic dose of LTG and the other receiving vehicle along with kindling acquisition. **B, C** The progression of seizure stage (**B**) and afterdischarge duration (ADD) (**C**) showed no differences between vehicle and LTG groups. **D, E** LTG at a

therapeutic dose had an anti-convulsant effect in the vehicle but not in the LTG group ( $n = 11$  for vehicle,  $n = 18$  for LTG). LTG treatment significantly lowered the seizure stage (**D**,  $***P < 0.001$ , unpaired  $t$  test) and shortened the ADD (**E**,  $*P = 0.047$ ,  $***P < 0.001$ , unpaired  $t$  test) in kindled mice of the vehicle group compared with the LTG group. **F** Representative seizure EEGs under LTG treatment from the vehicle and LTG groups.

seizures), the anti-convulsant effect of LTG was determined 3 times. LTG significantly alleviated the seizure severity in the vehicle group compared with the LTG group. Mice in the vehicle group only showed focal seizures (less than stage 3), while mice in the LTG group had generalized seizures (GSs, stages 4 and 5) after LTG treatment (Fig. 1D). The ADD was also shorter in the vehicle group (Fig. 1E). Thus, mice in the LTG group were considered to be LTG-resistant.

Then we delivered LFS 10 times (twice daily for 5 days) at the subiculum immediately after each CA3 kindling (Fig. 2A) and found that the seizure severity was alleviated in the LTG group. The incidence of GSs was significantly decreased (Fig. 2B), along with a lower average behavioral seizure stage (Fig. 2C). LFS also extended the average latency to GSs (Fig. 2D) and shortened the average GS duration (Fig. 2E). The average ADD did not change significantly (Fig. 2F). Power spectrum analysis showed that the absolute power of the seizure EEG in the LFS group was lower than that in the sham group (Fig. 2G, H). Further statistical analysis revealed that the absolute power in the delta, theta, and gamma bands was lower in the LFS group than in the sham group (Fig. 2I). We also measured the coastline index, which indicates the amplitude of epileptic EEG spikes, and found that it was significantly lower in the LFS group than in the sham group (Fig. 2J). These results suggested that LFS at the subiculum suppresses the severity of seizure EEGs, indicating that it has anti-convulsant efficacy. To define the time-window of the therapeutic effect of LFS, we analyzed its anti-convulsive action on a daily basis. LFS on the first day had no significant anti-convulsant effect (Fig. 2K–N), but the effect became prominent with time. On day 2, LFS increased the latency to GS (Fig. 2M), while on day 4, LFS reduced the seizure stage and the GS duration (Fig. 2K, L). These results suggested that LFS has a time-dependent cumulative effect, the anti-convulsant action being manifested only in the later period of treatment.

Our previous study showed that LFS at the subiculum reverses early-onset phenytoin resistance [9]. Therefore, in this study we aimed to determine whether long-term LFS also reverses LTG resistance. We tested the effect of LTG after 10 sessions of LFS at the subiculum on LTG-resistant kindled mice. We found that LTG significantly inhibited seizures in terms of the stage (Fig. 2O) and ADD (Fig. 2P). Also, the effectiveness of LTG after LFS was significantly greater than that before LFS (Fig. 2Q). These results suggest that LTG resistance is reversed by LFS at the subiculum.

Delayed-onset drug-resistance in epilepsy has been recognized for decades. In such patients, the brain lesion is often more extensive and the pathological findings more

complicated than in patients with early-onset refractoriness [2, 4]. These features further illustrate the difficulty in treating such patients, even with epilepsy surgery. LFS, as an alternative to epilepsy surgery, provides a promising option. Clinical trials testing its effects on patients with refractory epilepsy have been carried out in different centers, though with contradictory results, possibly due to the different targets for stimulation. Furthermore, accumulating evidence suggests that the subiculum plays a crucial role in epilepsy [7, 12]. In this study, we showed for the first time that LFS at the subiculum had an anti-convulsant effect on TLE mice with delayed-onset LTG resistance. The EEG power in a broad range of frequency bands was decreased by LFS, which might be due to the lower amplitude of synchronized epileptic spikes. This result was further corroborated by coastline analysis. Interestingly, the ADD was not affected, perhaps because the subiculum mediates the propagation rather than the initiation of GSs. Together, these results suggest that LFS at the subiculum might also induce neural desynchronization. Our previous study also showed that only 1-Hz LFS at the subiculum has therapeutic effects on both kindling acquisition and early-onset refractoriness in TLE rats and has a relatively wide time window [8, 9]. Therefore, we consider the subiculum to be an optimal target of LFS for refractory epilepsy.

Delayed-onset drug-resistance is characterized by the diminishing efficacy of AEDs. In the later period of using the medication, patients become completely drug-resistant. Interestingly, we found that, unlike AEDs, LFS lowered the seizure stage and shortened the GS duration in the later period of treatment. In addition, LFS had an earlier effect of extending the latency to GS, probably associated with a delay in seizure propagation, given the role of the subiculum as the main output region of the hippocampus [6]. The distinct features of the therapeutic effects of LFS and AEDs might be due to the differences in their mechanisms of action. Almost all AEDs act on ion channels and postsynaptic receptors to directly reduce the epileptic hyperexcitability, while LFS might have a long-term de-potentialization effect *via* the neural circuits between the subiculum and seizure foci [13], resulting in seizure control. In this way, LFS at the subiculum had a cumulative anti-convulsant effect on delayed-onset drug-resistant TLE.

Our previous study reported that LFS at the subiculum reverses early-onset phenytoin resistance [9]. In line with this, here we further showed that LFS reversed delayed-onset LTG resistance. However, the mechanism underlying this type of resistance remains elusive. An alternative hypothesis proposes the induction of multidrug transporter expression by recurrent seizures, resulting in later drug-resistance [14]. Besides, epilepsy, especially TLE with hippocampal sclerosis, is a progressive condition. Changes in neural circuitry may conceivably lead to delayed-onset

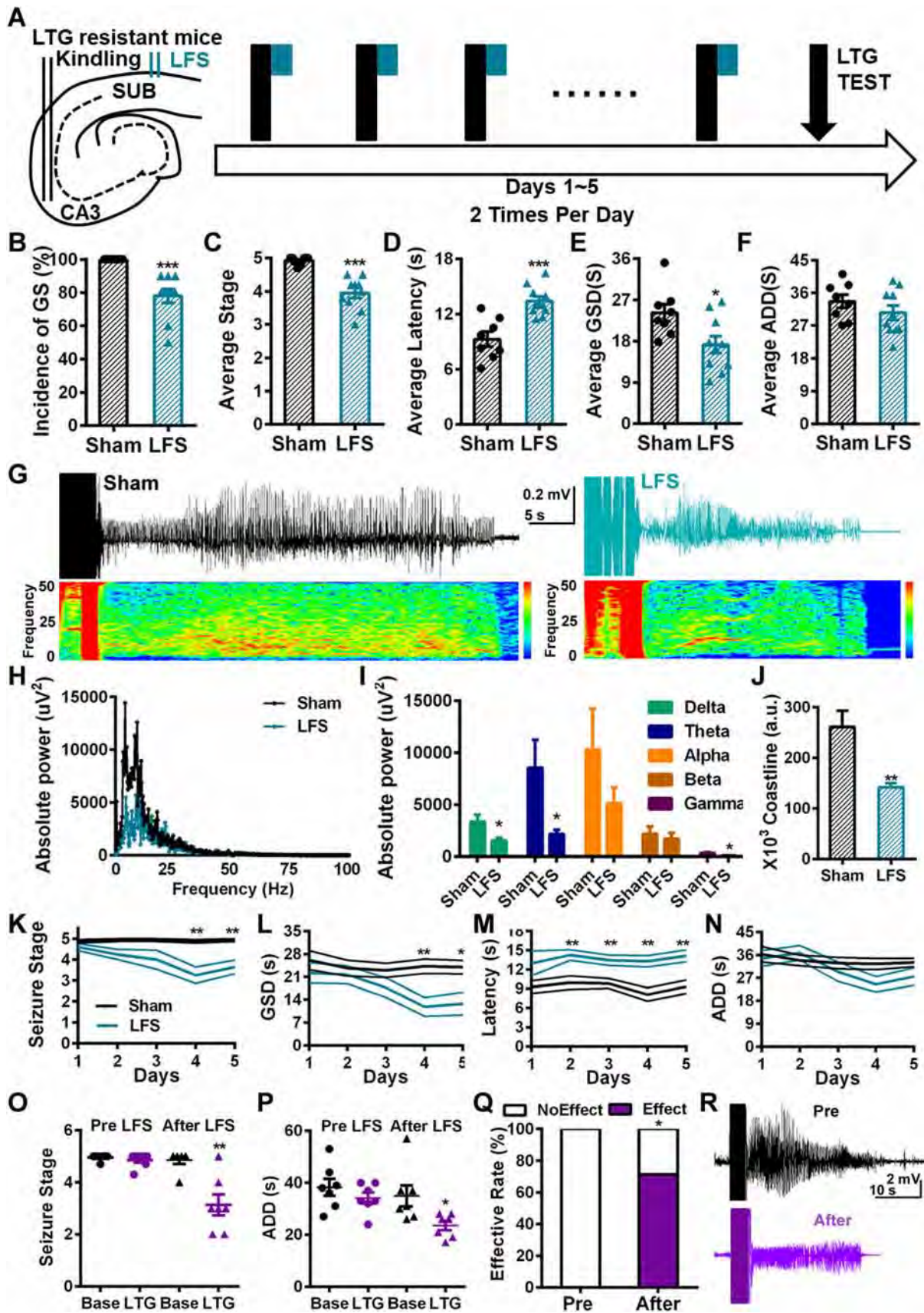


**Fig. 2** The anti-convulsant and anti-drug-resistant effects of LFS at the subiculum. **A** Schematic of LFS treatments. LFS at the subiculum (green) was delivered immediately after kindling stimulation (black) (LTG, lamotrigine). **B–F** LFS at the subiculum significantly alleviated the seizure severity in LTG-resistant kindled mice ( $n = 8$  for sham,  $n = 10$  for LFS). LFS lowered the incidence of GS (**B**) and average seizure stage (**C**), extended the average latency to GS (**D**), and shortened the average GS duration (**E**), but had no effect on the average ADD (**F**). **G** Representative seizure EEGs and spectra of the sham and LFS groups. **H** Representative seizure EEG power spectra of the sham and LFS groups. **I** LFS significantly reduced the absolute power in the delta, theta, and gamma bands ( $n = 8$  for sham,  $n = 10$  for LFS). **J** LFS treatment decreased the coastline index of seizure EEG ( $n = 8$  for sham,  $n = 10$  for LFS). **K** LFS lowered the seizure stage on day 4 of treatment ( $n = 8$  for sham,  $n = 10$  for LFS). **L** LFS shortened the GS duration on day 4 of treatment ( $n = 8$  for sham,  $n = 10$  for LFS). **M** LFS extended the latency to GS on day 2 of treatment ( $n = 8$  for sham,  $n = 10$  for LFS). **N** LFS had no effect on ADDs throughout treatment. **O, P** After 10 LFS sessions, seizure stage (**O**,  $n = 7$ ) was lower, and ADD (**P**,  $n = 7$ ) was shorter in LTG-resistant kindled mice ( $*P < 0.05$ ,  $**P < 0.01$  compared with baseline, paired *t*-test). **Q** The effectiveness of LTG was significantly raised by LFS ( $*P < 0.05$ ,  $\chi^2$  test). **R** Representative seizure EEG at baseline and under LTG treatment after LFS.  $*P < 0.05$ ,  $**P < 0.01$ ,  $***P < 0.001$  compared with sham, unpaired *t* test.

drug-resistance over time [15]. Our results indicated that, besides the drug transport hypothesis, the subiculum might be involved in the altered neural circuits resulting in drug-resistance, since it is reported to be more susceptible to hyperexcitability during the epileptic process [6]. Further circuitry studies combined with multifaceted techniques are needed to uncover the subiculum-mediated mechanisms of delayed-onset drug-resistance.

In conclusion, this study revealed that LFS at the subiculum has an anti-convulsant and anti-drug-resistant effects on delayed-onset LTG resistance in a TLE model. These findings highlight LFS at the subiculum as an effective therapeutic strategy for refractory epilepsy.

**Acknowledgements** This work was supported by grants from the National Natural Science Foundation of China (81703480 and 81603084) and the Fundamental Research Funds for Central Universities, China (2019FZA7016 and 2019QNA5001).

**Conflict of interest** All authors claim that there are no conflicts of interest.

## References

1. Kwan P, Brodie MJ. Early identification of refractory epilepsy. *N Engl J Med* 2000, 342: 314–319.
2. Berg AT, Langfitt J, Shinnar S, Vickrey BG, Sperling MR, Walczak T, *et al.* How long does it take for partial epilepsy to become intractable? *Neurology* 2003, 60: 186–190.
3. Berg AT. The natural history of mesial temporal lobe epilepsy. *Curr Opin Neurol* 2008, 21: 173–178.
4. Bilevicius E, Yasuda CL, Silva MS, Guerreiro CA, Lopes-Cendes I, Cendes F. Antiepileptic drug response in temporal lobe epilepsy: a clinical and MRI morphometry study. *Neurology* 2010, 75: 1695–1701.
5. Burbaud P, Vital A, Rougier A, Bouillot S, Guehl D, Cuny E, *et al.* Minimal tissue damage after stimulation of the motor thalamus in a case of chorea-acanthocytosis. *Neurology* 2002, 59: 1982–1984.
6. Stafstrom CE. The role of the subiculum in epilepsy and epileptogenesis. *Epilepsy Curr* 2005, 5: 121–129.
7. Cohen I, Navarro V, Clemenceau S, Baulac M, Miles R. On the origin of interictal activity in human temporal lobe epilepsy *in vitro*. *Science* 2002, 298: 1418–1421.
8. Zhong K, Wu DC, Jin MM, Xu ZH, Wang Y, Hou WW, *et al.* Wide therapeutic time-window of low-frequency stimulation at the subiculum for temporal lobe epilepsy treatment in rats. *Neurobiol Dis* 2012, 48: 20–26.
9. Xu C, Wang Y, Zhang S, Nao J, Liu Y, Wang Y, *et al.* Subicular pyramidal neurons gate drug resistance in temporal lobe epilepsy. *Ann Neurol* 2019, 86: 626–640.
10. Postma T, Krupp E, Li XL, Post RM, Weiss SRB. Lamotrigine treatment during amygdala-kindled seizure development fails to inhibit seizures and diminishes subsequent anticonvulsant efficacy. *Epilepsia* 2000, 41: 1514–1521.
11. Wang Y, Wang Y, Xu C, Wang S, Tan N, Chen C, *et al.* Direct septum-hippocampal cholinergic circuit attenuates seizure through driving somatostatin inhibition. *Biol Psychiatry* 2019. <https://doi.org/10.1016/j.biopsych.2019.11.014>.
12. de Guzman P, Inaba Y, Biagini G, Baldelli E, Mollinari C, Merlo D, *et al.* Subiculum network excitability is increased in a rodent model of temporal lobe epilepsy. *Hippocampus* 2006, 16: 843–860.
13. Berretta N, Cherubini E. A novel form of long-term depression in the CA1 area of the adult rat hippocampus independent of glutamate receptors activation. *Eur J Neurosci* 1998, 10: 2957–2963.
14. Rizzi M, Caccia S, Guiso G, Richichi C, Gorter JA, Aronica E, *et al.* Limbic seizures induce P-glycoprotein in rodent brain: functional implications for pharmacoresistance. *J Neurosci* 2002, 22: 5833–5839.
15. Wang Y, Chen Z. An update for epilepsy research and antiepileptic drug development: Toward precise circuit therapy. *Pharmacol Ther* 2019, 201: 77–93.



LETTER TO THE EDITOR

# The Role of Frontal and Occipital Cortices in Processing Sustained Visual Attention in Young Adults with Attention-Deficit/Hyperactivity Disorder: A Functional Near-Infrared Spectroscopy Study

Ziyan Wu<sup>1</sup> · Yuyang Luo<sup>2</sup> · Yu Gao<sup>3</sup> · Ying Han<sup>4,5,6,7</sup> · Kai Wu<sup>8,9,10</sup> · Xiaobo Li<sup>1,2,10</sup>

Received: 4 July 2019 / Accepted: 9 January 2020 / Published online: 11 April 2020  
© Shanghai Institutes for Biological Sciences, CAS 2020

## Dear Editor,

Attention deficit/hyperactivity disorder (ADHD), characterized by age-inappropriate symptoms of inattention, hyperactivity, and impulsivity, is a highly prevalent and heritable childhood-onset neurodevelopmental disorder, with impairing symptoms that persist into adulthood in up to 65% of patients [1]. Adults with persistent ADHD symptoms since childhood have been found to have neurocognitive impairments in multiple domains, especially in attention and cognitive control, which significantly contribute to an increased risk of social disability, educational and occupational failure, and other comorbid psychiatric disorders, resulting in significant economic

burdens to the affected individuals, their families, and society [2, 3].

An increasing number of structural and functional neuroimaging studies have focused on investigating the neural correlates of symptom persistence and their associations with the observed cognitive and behavioral impairments in adults with childhood ADHD, which have yielded divergent findings [4–8]. Although the neurobiological substrate operating in ADHD symptom persistence in adulthood is not yet well understood, emerging studies have demonstrated functional alterations in frontal and occipital regions in both children and adults with ADHD [9–12]. For instance, findings of functional magnetic resonance imaging (MRI) studies conducted by our team and others have demonstrated significantly reduced nodal-efficiency in frontal and occipital regions during visual attention information processing in children with ADHD relative to group-matched controls [9]; significantly lower

**Electronic supplementary material** The online version of this article (<https://doi.org/10.1007/s12264-020-00492-9>) contains supplementary material, which is available to authorized users.

✉ Kai Wu  
kaiwu@scut.edu.cn

✉ Xiaobo Li  
xli.aecom@gmail.com; xiaobo.li@njit.edu

<sup>1</sup> Department of Electrical and Computer Engineering, New Jersey Institute of Technology, Newark, NJ 07102, USA

<sup>2</sup> Department of Biomedical Engineering, New Jersey Institute of Technology, Newark, NJ 07102, USA

<sup>3</sup> Department of Psychology, Brooklyn College and the Graduate Center of the City University of New York, Brooklyn, NY 10004, USA

<sup>4</sup> Department of Neurology, XuanWu Hospital of Capital Medical University, Beijing 100053, China

<sup>5</sup> Beijing Institute of Geriatrics, XuanWu Hospital of Capital Medical University, Beijing 100053, China

<sup>6</sup> National Clinical Research Center for Geriatric Disorders, Beijing 100053, China

<sup>7</sup> Center of Alzheimer's Disease, Beijing Institute for Brain Disorders, Beijing 100069, China

<sup>8</sup> Department of Biomedical Engineering, School of Materials Science and Engineering, South China University of Technology, Guangzhou 510003, China

<sup>9</sup> Guangzhou Huiai Hospital, The Affiliated Brain Hospital of Guangzhou Medical University, Guangzhou 510370, China

<sup>10</sup> Guangdong Engineering Technology Research Center for Diagnosis and Rehabilitation of Dementia, Guangzhou 510500, China

**Table 1** Summary of statistics.

Statistical method	Between-group difference	Region of cortical activity/pairwise FC	<i>F</i>	<i>P</i>
ANCOVA	ADHD > NC	Regional cortical activation in the MFG.L.	19.077	<0.001
	ADHD < NC	Pairwise FC between MFG.L. and IOC.L.	10.018	0.003

ANCOVA analysis of covariance; NC normal controls; ADHD attention-deficit/hyperactivity disorder; FC functional connectivity

activations in the inferior frontal gyrus, orbitofrontal cortex, and occipital cortex during cognitive control processing in adults with childhood ADHD relative to healthy controls [10]; and other functional abnormalities associated with frontal and occipital regions in both children and adults with ADHD [11, 12]. Based on these findings, we hypothesized that functional alterations associated with frontal and occipital cortices may exist in adults who were diagnosed with ADHD in childhood, and these abnormalities may significantly contribute to ADHD symptom persistence into adulthood. To test this hypothesis, we investigated (1) regional cortical activations in 6 regions of interest (ROIs), including the bilateral middle frontal gyri (MFG), bilateral calcarine sulci (CS), and bilateral inferior occipital cortices (IOC), evoked by a visual sustained attention task (a detailed description of the task is outlined in our previous study [13]), (2) pairwise functional connectivity (FC) between two given ROIs, and (3) correlations between brain activation/FC measurements and ADHD-related clinical symptom severity scores from the Conners' Adult ADHD Self-Report Rating Scales [14]. Functional near-infrared spectroscopy (fNIRS) was utilized for brain imaging data collection. This is a novel optical neuroimaging modality which allows the noninvasive measurement of brain activity in human subjects [15]. Compared to the commonly used functional MRI technique, fNIRS provides much higher temporal resolution when measuring neural activity. This technique is particularly suitable for examining patients with ADHD who may have difficulty staying still, because it is less susceptible to movement-induced artifacts.

This study was approved by the Institutional Review Board of New Jersey Institute of Technology. Consent forms were signed by all participants. A total of 51 young adults, ranging from 18 to 27 years of age, were involved in this study. Two were excluded from further analysis due to incomplete data. Finally, 18 ADHD patients and 31 group-matched normal controls (NCs) were included in the statistical analyses. Participant recruitment inclusion and exclusion criteria, experimental setup, data acquisition, and individual-level data analyses are detailed in the Supplementary Materials. Group comparisons were carried out using a  $\chi^2$  test for the clinical and demographic characteristics with discrete variables (i.e. gender), and *t*-tests for characteristics with continuous variables (i.e. ADHD

symptom severity scores and fNIRS task performance measures). Imaging measures including regional cortical activation magnitude and pairwise FC between two given ROIs were compared using analysis of covariance by adding age and gender as covariates. Pearson correlations between the brain imaging measures and ADHD symptom severity were analyzed to find brain-behavior association patterns in the ADHD and NC groups. All the group-level analyses were controlled for multiple comparisons using the false discovery rate at  $\alpha = 0.05$  [16].

There were no significant between-group differences in demographic and task-responsive behavioral measures, while the ADHD group had significantly higher inattentive and hyperactive/impulsive symptom severity scores, relative to NCs (Table S1). Group comparisons of the brain imaging measures showed that, relative to controls, ADHD patients had significantly increased regional cortical activation in the left MFG ( $P < 0.001$ ), and significantly decreased inter-regional FC between the MFG and IOC in the left hemisphere ( $P = 0.003$ ) (Table 1, Fig. 1A). These results support our hypothesis of functional alterations associated with frontal and occipital lobes in adults with ADHD. In the literature, functional MRI studies have reported altered neural activations in dorsolateral prefrontal, inferior frontal, orbitofrontal, and inferior, middle, and superior occipital cortices in adults with ADHD performing various cognitive tasks [8, 17–19]. Reduced regional FC within the prefrontal cortex in adults with ADHD relative to controls has also been reported in a resting-state functional MRI study [7]. In addition, structural MRI and diffusion tensor imaging studies have shown significant prefrontal volume reduction [4, 5], increased cortical thickness in the occipital lobe [20], and significantly lower fractional anisotropy in the inferior fronto-occipital fasciculus [3] in adults with ADHD; this may serve as the anatomical basis for the functional abnormalities associated with these areas.

We also found distinct brain-behavior association patterns in the ADHD and NC groups (Table 2, Fig. 1B). In controls, the hyperactive/impulsive symptom severity scores demonstrated a significant negative correlation with the regional cortical activation magnitude in the right MFG ( $r = -0.417$ ;  $P = 0.022$ ) and a significant positive correlation with the FC between the MFG and CS in the left hemisphere ( $r = 0.434$ ;  $P = 0.022$ ), while these patterns

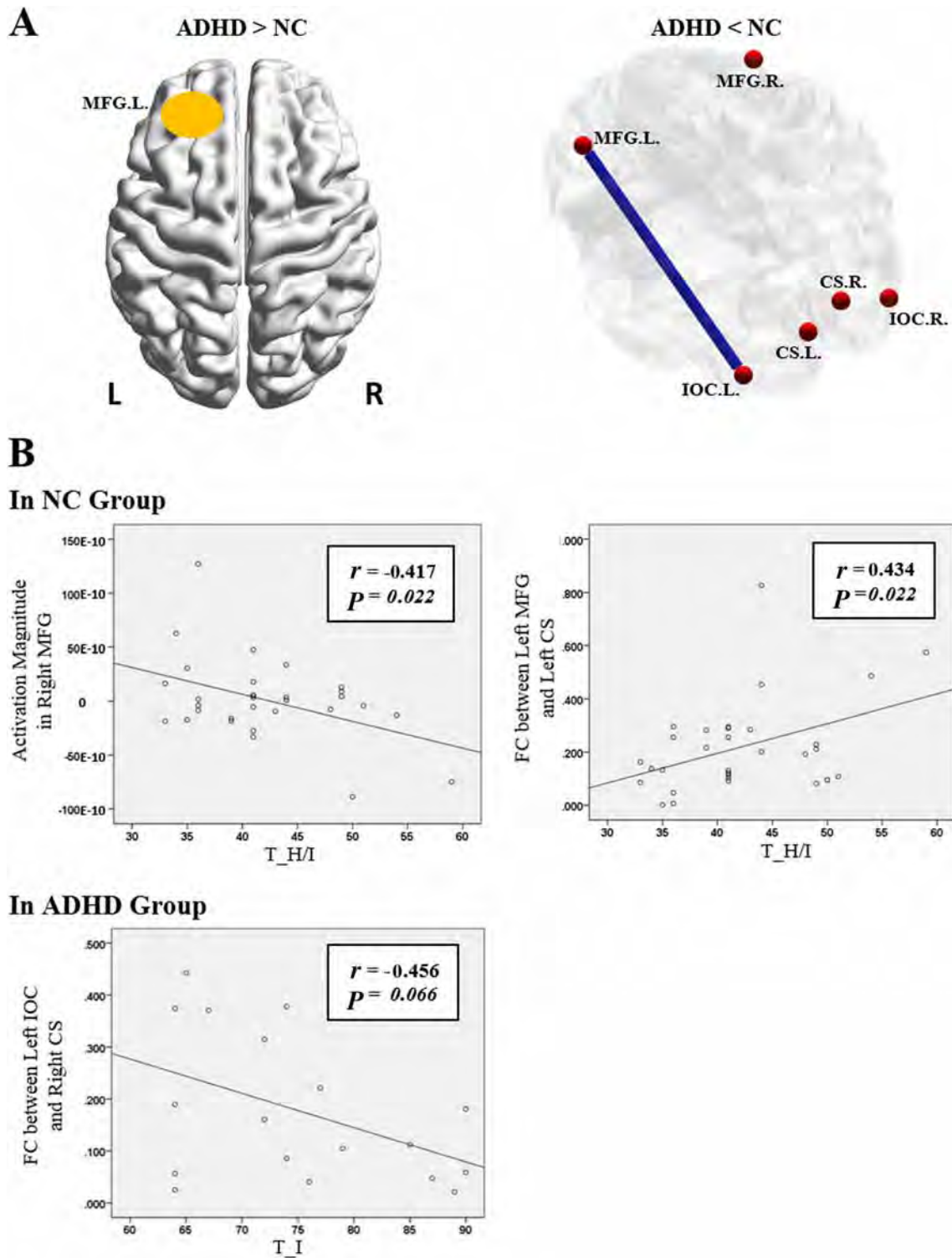


**Fig. 1** A Altered regional cortical activation and functional connectivity in adults with ADHD relative to controls. B Distinct brain-behavior association patterns in the NC and ADHD groups. ADHD attention-deficit/hyperactivity disorder; NC normal control; L left;

R right; MFG middle frontal gyrus; CS calcarine sulcus; IOC inferior occipital cortex; T\_I T-score of ADHD inattentive symptom scale; T\_H/I T-score of ADHD hyperactive/impulsive symptom scale; r strength of correlation; P level of significance.

**Table 2** Brain-behavior association statistics.

Statistical method	Group	Brain-behavior association	<i>r</i>	<i>P</i>
Correlation analysis	NC	T <sub>H/I</sub> & regional cortical activation in MFG.R.	−0.417	0.022
		T <sub>H/I</sub> & pairwise FC between MFG.L. and CS.L.	0.434	0.022
	ADHD	T <sub>I</sub> & pairwise FC between IOC.L. and CS.R.	−0.456	0.066

NC normal controls; ADHD attention-deficit/hyperactivity disorder; T<sub>I</sub> T-score of ADHD inattentive symptom severity scale; T<sub>H/I</sub> T-score of ADHD hyperactive/impulsive symptom severity scale; MFG.L. left middle frontal gyrus; IOC.L. left inferior occipital cortex; MFG.R. right middle frontal gyrus; CS.L. left calcarine sulcus; CS.R. right calcarine sulcus; *r* strength of correlation

were not found in the ADHD group. In adults with ADHD, there was a negative correlation between the inattentive symptom severity scores and inter-regional FC between left IOC and right CS which approached statistical significance ( $r = -0.456$ ;  $P = 0.066$ ), while such a pattern did not exist in controls. Together with results from other studies which demonstrated strong associations between ADHD-related behavioral symptoms and functional abnormalities associated with frontal and occipital regions in ADHD patients [21, 22], our findings suggest that abnormal bilateral-occipital and occipital-frontal functional interactions contribute to the persistent ADHD-related behavioral symptoms in adults with childhood ADHD.

The current study has some limitations. First is the insufficient penetration depth and limited number of optodes provided by fNIRS, as discussed in our previous study [13]. Due to this issue, other cortical and subcortical brain regions involved in the attention processing pathway were not investigated here. Second, the study included both male and female participants. Gender-related differences in neural activity and their associations with behavioral deficits have been discussed in a previous ADHD study [23]. Here, the gender factor was adjusted in our group-level statistical analysis. Due to the limited sample size in the male and female subgroups, we did not conduct gender-specific subgroup comparisons. Future work with a larger sample size is needed to investigate the gender-related neurobiological substrates associated with symptom persistence in male and female ADHD patients.

In conclusion, significantly increased frontal activation and decreased occipital-frontal connectivity in the left hemisphere during visual attentional processing were found in adults with ADHD relative to NCs. Distinct association patterns regarding the positive correlation between hyperactive/impulsive symptoms and occipital-frontal FC in NCs as well as the negative correlation between inattentive symptoms and bilateral-occipital functional interaction in ADHD patients, during visual attention processing further suggest a significant role of the frontal and occipital cortices in the persistence of ADHD-related behavioral symptoms in adults with ADHD. In addition, our study suggests that, considering its much higher temporal

resolution and lower sensitivity to head motion-induced artifacts, fNIRS can be a less expensive alternative to functional MRI for evaluating the cortical functional abnormalities associated with symptom persistence in adults with childhood ADHD.

**Acknowledgements** This work was supported by research grants from the New Jersey Commission on Brain Injury Research (CBIR17PIL012), the National Institutes of Mental Health (MH109791 and MH117368), the New Jersey Institute of Technology Start-up Award to Dr. Xiaobo Li, the National Natural Science Foundation of China (31771074) and the Science and Technology Program of Guangzhou Province, China (201704020168 and 201807010064).

**Conflict of interest** All authors claim that there is no conflict of interest.

## References

- Luo Y, Weibman D, Halperin JM, Li X. A review of heterogeneity in attention deficit/hyperactivity disorder (ADHD). *Front Hum Neurosci* 2019, 13: 42.
- Zhu Y, Jiang X, Ji W. The Mechanism of cortico-striato-thalamo-cortical neurocircuitry in response inhibition and emotional responding in attention deficit hyperactivity disorder with comorbid disruptive behavior disorder. *Neurosci Bull* 2018, 34: 566–572.
- Salomone S, Fleming GR, Bramham J, O’Connell RG, Robertson IH. Neuropsychological deficits in adult ADHD: Evidence for differential attentional impairments, deficient executive functions, and high self-reported functional impairments. *J Atten Disord* 2016, pii:1087054715623045.
- Hesslinger B, Tebartz van Elst L, Thiel T, Haegle K, Hennig J, Ebert D. Frontoorbital volume reductions in adult patients with attention deficit hyperactivity disorder. *Neurosci Lett* 2002, 328: 319–321.
- Seidman LJ, Valera EM, Makris N, Monuteaux MC, Boriell DL, Kelkar K, et al. Dorsolateral prefrontal and anterior cingulate cortex volumetric abnormalities in adults with attention-deficit/hyperactivity disorder identified by magnetic resonance imaging. *Biol Psychiatry* 2006, 60: 1071–1080.
- Pironti VA, Lai MC, Müller U, Dodds CM, Suckling J, Bullmore ET, et al. Neuroanatomical abnormalities and cognitive impairments are shared by adults with attention-deficit/hyperactivity disorder and their unaffected first-degree relatives. *Biol Psychiatry* 2014, 76: 639–647.

7. Mattfeld AT, Gabrieli JD, Biederman J, Spencer T, Brown A, Kotte A, *et al.* Brain differences between persistent and remitted attention deficit hyperactivity disorder. *Brain* 2014, 137: 2423–2428.
8. Wolf RC, Plichta MM, Sambataro F, Fallgatter AJ, Jacob C, Lesch KP, *et al.* Regional brain activation changes and abnormal functional connectivity of the ventrolateral prefrontal cortex during working memory processing in adults with attention-deficit/hyperactivity disorder. *Hum Brain Mapp* 2009, 30: 2252–2266.
9. Xia S, Foxe JJ, Sroubek AE, Branch C, Li X. Topological organization of the “small-world” visual attention network in children with attention deficit/hyperactivity disorder (ADHD). *Front Hum Neurosci* 2014, 8.
10. Schulz KP, Li X, Clerkin SM, Fan J, Berwid OG, Newcorn JH, *et al.* Prefrontal and parietal correlates of cognitive control related to the adult outcome of attention-deficit/hyperactivity disorder diagnosed in childhood. *Cortex* 2017, 90: 1–11.
11. Cubillo A, Halari R, Giampietro V, Taylor E, Rubia K. Fronto-striatal underactivation during interference inhibition and attention allocation in grown up children with attention deficit/hyperactivity disorder and persistent symptoms. *Psychiatry Res* 2011, 193: 17–27.
12. Qian A, Wang X, Liu H, Tao J, Zhou J, Ye Q, *et al.* Dopamine D4 receptor gene associated with the frontal-striatal-cerebellar loop in children with ADHD: A resting-state fMRI study. *Neurosci Bull* 2018, 34: 497–506.
13. Wu Z, Mazzola CA, Catania L, Owoeye O, Yaramothu C, Alvarez T, *et al.* Altered cortical activation and connectivity patterns for visual attention processing in young adults post-traumatic brain injury: A functional near infrared spectroscopy study. *CNS Neurosci Ther* 2018, 24: 539–548.
14. Epstein JN, Johnson D, Conners CK. *Conners’ Adult ADHD Diagnostic Interview for DSM-IV*. North Tonawanda, NY: Multi-Health Systems, 2006.
15. Wang Q, Zhu GP, Yi L, Cui XX, Wang H, Wei RY, *et al.* A review of functional near-infrared spectroscopy studies of motor and cognitive function in preterm infants. *Neurosci Bull* 2020, 36: 321–329.
16. Benjamini YH, Hochberg Y. Controlling the false discovery rate: a practical and powerful approach to multiple testing. *J R Stat Soc Series B Stat Methodol* 1995, 57: 289–300.
17. Cubillo A, Halari R, Smith A, Taylor E, Rubia K. A review of fronto-striatal and fronto-cortical brain abnormalities in children and adults with Attention Deficit Hyperactivity Disorder (ADHD) and new evidence for dysfunction in adults with ADHD during motivation and attention. *Cortex* 2012, 48: 194–215.
18. Banich MT, Burgess GC, Depue BE, Ruzic L, Bidwell LC, Iitt-Laustsen S, *et al.* The neural basis of sustained and transient attentional control in young adults with ADHD. *Neuropsychologia* 2009, 47: 3095–3104.
19. Lei D, Du M, Wu M, Chen T, Huang X, Du X, *et al.* Functional MRI reveals different response inhibition between adults and children with ADHD. *Neuropsychology* 2015, 29: 874–881.
20. Almeida Montes LG, Prado Alcántara H, Martínez García RB, De La Torre LB, Avila Acosta D, Duarte M. Brain cortical thickness in ADHD: age, sex, and clinical correlations. *J Atten Disord* 2013, 17: 641–654.
21. Tomasi D, Volkow ND. Abnormal functional connectivity in children with attention-deficit/hyperactivity disorder. *Biol Psychiatry* 2012, 71: 443–450.
22. Barber AD, Jacobson LA, Wexler JL, Nebel MB, Caffo BS, Pekar JJ, *et al.* Connectivity supporting attention in children with attention deficit hyperactivity disorder. *Neuroimage Clin* 2015, 7: 68–81.
23. Valera EM, Brown A, Biederman J, Faraone SV, Makris N, Monuteaux MC, *et al.* Sex differences in the functional neuroanatomy of working memory in adults with ADHD. *Am J Psychiatry* 2010, 167: 86–94.



## Somatic Mutations Confer Severe Peripheral Neuropathy in POEMS Syndrome-Associated Multicentric Castleman Disease

Qingqing Lin<sup>1,3</sup> · Juying Wei<sup>1,2,3</sup> · Jiejing Qian<sup>1,3</sup> · Liangshun You<sup>1,2,3</sup> · Wenbin Qian<sup>1,2,3</sup>

Received: 19 June 2019 / Accepted: 10 December 2019 / Published online: 12 March 2020  
© Shanghai Institutes for Biological Sciences, CAS 2020

### Dear Editor,

POEMS-associated multicentric Castleman disease (POEMS-MCD) is a subtype of MCD that presents POEMS symptoms (polyneuropathy, organomegaly, endocrinopathy, M protein, and skin changes) as well as the manifestations of MCD. Among these symptoms, polyneuropathy is a critical feature. However, its mechanism remains poorly understood. The present study presents a case of severe peripheral neuropathy in a POEMS-MCD patient. Whole-exome sequencing (WES), three-dimensional modeling, and protein stability analysis demonstrated that the mutation V49G in *PDLIM5* resulted in instability of the protein, which may play a key role in the pathogenesis of peripheral neuropathy in POEMS-MCD.

MCD is a rare lymphoproliferative disorder characterized by polyclonal lymphoproliferation, systemic inflammatory symptoms, and multiple organ system dysfunction. Based on the status of human herpes virus 8 (HHV-8)

infection, MCD is divided into HHV-8-associated and idiopathic forms (HHV-8-negative MCD or iMCD). Recently, a third subtype known as POEMS-associated MCD (POEMS-MCD) has been identified [1, 2]. Although peripheral neuropathy occurs in both MCD and POEMS-MCD, patients with POEMS-MCD tend to show more subtle electrophysiological changes [3]. So far, excessive vascular endothelial growth factor (VEGF) secreted by plasma cells has been proposed as the pathogenesis of the peripheral neuropathy. Local VEGF can promote endothelial hypertrophy and disrupt the blood-nerve barrier; the leaky vessels allow serum components to exert toxic action on the nerves [4]. However, peripheral neuropathy also occurs in a proportion of these patients with normal VEGF levels [5]. In addition, the symptoms of neuropathy persist in some patients even when the VEGF level returns to normal after treatment [6]. These results imply that the peripheral neuropathy of this disease may not be driven entirely by VEGF in all patients. Interestingly, some recent studies have demonstrated that somatic mutations in genes associated with neuronal development play an important role in the pathogenesis of peripheral neuropathy. However, evidence for a role of genetic mutation in the peripheral neuropathy of POEMS-MCD is lacking. In this study, we describe a somatic mutation for severe peripheral neuropathy in a patient with POEMS-MCD.

In July 2014, a 57-year-old man was admitted to the First Affiliated Hospital of Zhejiang University with a one-month history of numbness and weakness in the lower limbs. The numbness gradually spread from the feet up to the knees, and was accompanied by pain in the feet. The medical history and family history were unremarkable. The neurological examination revealed a decrease in muscle strength of the lower limbs (grade 3) [7]. Furthermore, there was hypoaesthesia in the lower legs (below the knee),

Qingqing Lin and Juying Wei contributed equally to this work.

✉ Liangshun You  
youliangshun@zju.edu.cn

✉ Wenbin Qian  
qianwb@zju.edu.cn

<sup>1</sup> Department of Hematology, The First Affiliated Hospital, Zhejiang University School of Medicine, Hangzhou 310003, China

<sup>2</sup> Institute of Hematology, Zhejiang University, Hangzhou 310003, China

<sup>3</sup> Malignant Lymphoma Diagnosis and Therapy Center, The First Affiliated Hospital, Zhejiang University School of Medicine, Hangzhou 310003, China

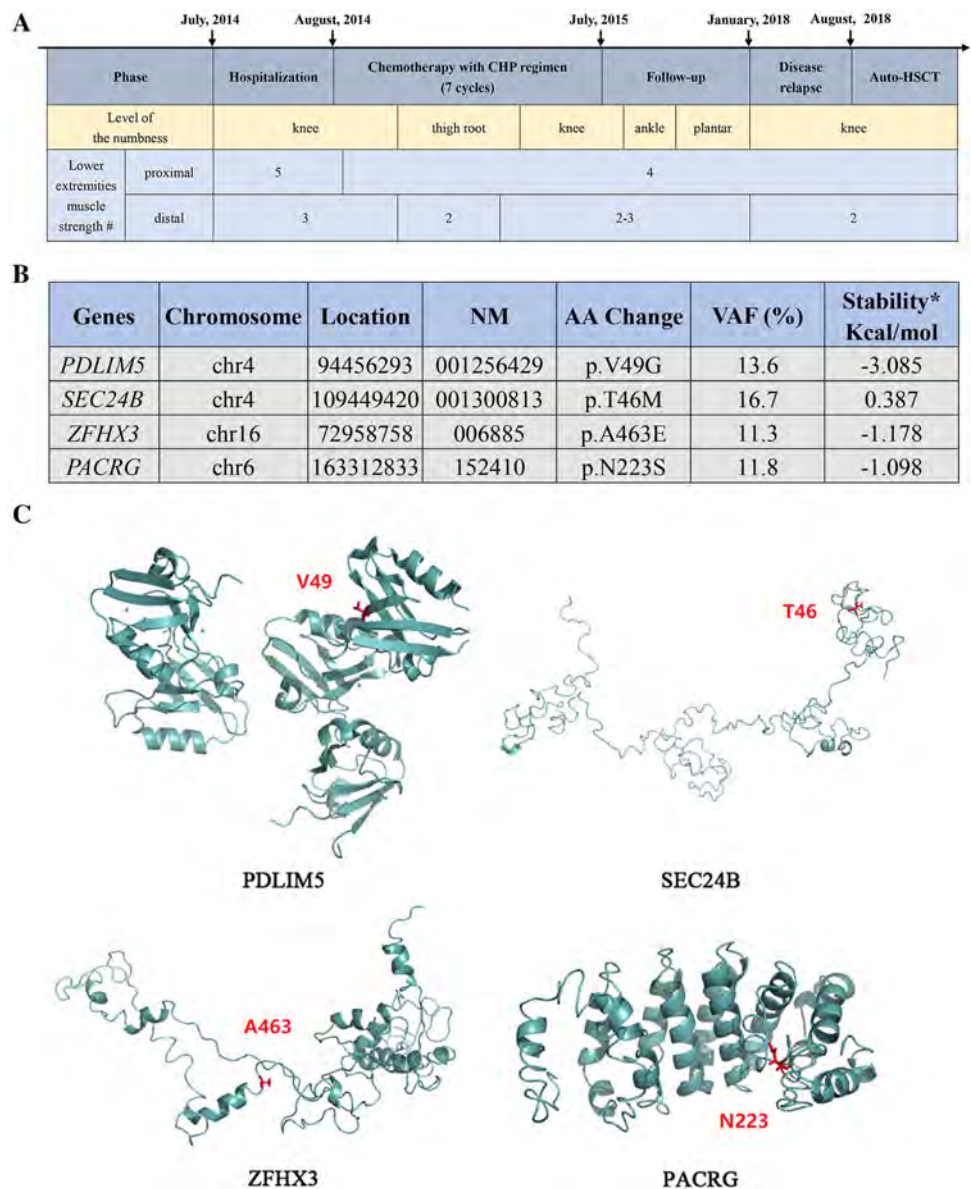
with a predominance on the left side. Other neurological examinations were negative. The laboratory tests revealed thrombocytosis ( $444 \times 10^9/L$ ; normal range,  $101 \times 10^9 - 320 \times 10^9/L$ ), and increased levels of VEGF (583 pg/mL; normal range, 18–160 pg/mL) and thyroid-stimulating hormone (8.21  $\mu IU/mL$ ; normal range, 0.35–4.94  $\mu IU/mL$ ). Ultrasonography manifested multiple lymphadenopathy throughout the body and mild pericardial effusion. Computed tomography of the chest and abdomen revealed no bone lesions. Immunoelectrophoresis revealed a monoclonal IgG/lambda protein. The percentage of bone marrow plasmacytes was 3%. Electromyograms revealed slowed motor conduction velocity and typical signs of axonal injury in the lower limbs, compatible with polyneuropathy. Immunohistochemistry of a right cervical lymph

node proved to be the hyaline vascular variant of Castleman disease. Finally, based on the diagnostic criteria, the patient was diagnosed as having POEMS syndrome with MCD, also known as POEMS-MCD [1, 8]. Although the level of VEGF returned to normal (78 pg/mL; normal range, 18–160 pg/mL) after seven cycles of CHP regimen chemotherapy (including cyclophosphamide, pirarubicin, and dexamethasone), the patient’s peripheral nerve injury persisted. The disease progressed for three years, so autologous hematopoietic stem cell transplantation was performed. Regrettably, there was no improvement in muscle strength in the lower limbs after almost one year of follow-up (Fig. 1A).

In order to explore the possible mechanism underlying the irreversible nerve injury, WES was performed using

**Fig. 1** **A** Schematic of the clinical course. The patient was treated with seven cycles of CHP regimen after a diagnosis of POEMS-MCD. The disease then progressed for 37 months, after which the patient received autologous hematopoietic stem cell transplantation (auto-HSCT). However, the peripheral neurological symptoms failed to significantly improve throughout the entire clinical course. **B** List of variants in genes and their impact on the stability of proteins. **C** Three-dimensional models of the proteins PDLIM5, SEC24B, ZFH3, and PACRG (mutation sites indicated in red).

#Dynamic muscle strength was manually assessed using the modified British Medical Research Council scoring system (from 0, no contraction, to 5, joint can be held against maximum pressure) [7]. \*Positive numbers mean that the protein became more stable, while negative numbers mean that the protein became less stable after the mutation. AA, amino-acid; NM, mRNA reference sequence number; VAF, variant allele frequency.



paraffin-embedded lymph node tissue and a paired saliva sample to identify the acquired genetic alternations. A total of 58 genes with non-silent somatic mutations were identified. Subsequently, functional enrichment analysis was performed in the Gene Oncology database using Kobas. The results revealed that genes with somatic alterations were mainly enriched in neuron development pathways, including *PDLIM5*, *SEC24B*, *ZFHX3*, and *PACRG*, which have been reported in previous studies. Homology modeling and DUET analysis revealed that the V49G mutation in *PDLIM5* resulted in instability of the protein, with a stability of  $-3.085$  Kcal/mol, and this may lead to degradation through the proteasome pathway. In contrast, there were no significant changes in the other proteins (Fig. 1B, C).

*PDLIM5*, also known as the enigma homolog, belongs to the PDZ-LIM protein family and acts as a scaffold protein that carries out a wide range of functions to promote neural development [9]. Previous studies have suggested that *PDLIM5* binds the inhibitor of DNA binding 2, resulting in its sequestration in the cytoplasm and loss of inhibitory effects on nuclear transcription, thereby promoting axonal growth and branching [10]. Ren *et al.* proposed that *PDLIM5* functions in growth cone guidance *via* its interaction with protein kinase C epsilon. Knockdown of *PDLIM5* in cultured neurons prevents the translocation of protein kinase C epsilon, which induces growth-cone collapse and affects neuronal development [11].

In the present study, we revealed for the first time that somatic genetic alterations in genes for neuronal development may be one of the pathogeneses of peripheral neuropathy in patients with POEMS-MCD. Hence, we conclude that such genetic mutations, especially mutation of *PDLIM5*, may lead to unrecoverable peripheral neuropathy even with prompt and creative therapy including microRNA inhibition [12]. This is an important step in understanding the molecular pathogenesis of the disease. From the perspective of precision medicine, large studies are required to replicate and validate these novel targets underlying this uncommon disabling condition.

**Acknowledgements** This work was supported by the National Natural Science Foundation of China (No. 81830006, 81873451,

81670178), and the National Key Research and Development Program of China (No. 2016YFC090150X).

**Conflict of interest** The authors have no conflict of interest to declare.

## References

1. Fajgenbaum DC, Uldrick TS, Bagg A, Frank D, Wu D, Srkalic G, *et al.* International, evidence-based consensus diagnostic criteria for HHV-8-negative/idiopathic multicentric Castleman disease. *Blood* 2017, 129: 1646–1657.
2. Fajgenbaum DC, Shilling D. Castleman Disease Pathogenesis. *Hematol Oncol Clin North Am* 2018, 32: 11–21.
3. Naddaf E, Dispenzieri A, Mandrekar J, Mauermann ML. Clinical spectrum of Castleman disease-associated neuropathy. *Neurology* 2016, 87: 2457–2462.
4. Scarlato M, Previtali SC, Carpo M, Pareyson D, Briani C, Del Bo R, *et al.* Polyneuropathy in POEMS syndrome: role of angiogenic factors in the pathogenesis. *Brain* 2005, 128: 1911–1920.
5. D'Souza A, Hayman SR, Buadi F, Mauermann M, Lacy MQ, Gertz MA, *et al.* The utility of plasma vascular endothelial growth factor levels in the diagnosis and follow-up of patients with POEMS syndrome. *Blood* 2011, 118: 4663–4665.
6. Karam C, Klein CJ, Dispenzieri A, Dyck PJ, Mandrekar J, D'Souza A, *et al.* Polyneuropathy improvement following autologous stem cell transplantation for POEMS syndrome. *Neurology* 2015, 84: 1981–1987.
7. Compston A. Aids to the investigation of peripheral nerve injuries. Medical Research Council: Nerve Injuries Research Committee. His Majesty's Stationery Office: 1942; pp. 48 (iii) and 74 figures and 7 diagrams; with aids to the examination of the peripheral nervous system. By Michael O'Brien for the Guarantors of Brain. Saunders Elsevier: 2010; pp. [8] 64 and 94 Figures. *Brain* 2010, 133: 2838–2844.
8. Dispenzieri A. POEMS Syndrome: 2019 Update on diagnosis, risk-stratification, and management. *Am J Hematol* 2019, 94: 812–827.
9. Krcmery J, Camarata T, Kulisz A, Simon HG. Nucleocytoplasmic functions of the PDZ-LIM protein family: new insights into organ development. *Bioessays* 2010, 32: 100–108.
10. Lasorella A, Iavarone A. The protein ENH is a cytoplasmic sequestration factor for Id2 in normal and tumor cells from the nervous system. *Proc Natl Acad Sci U S A* 2006, 103: 4976–4981.
11. Ren B, Li X, Zhang J, Fan J, Duan J, Chen Y. *PDLIM5* mediates PKCepsilon translocation in PMA-induced growth cone collapse. *Cell Signal* 2015, 27: 424–435.
12. Li WY, Zhang WT, Cheng YX, Liu YC, Zhai FG, Sun P, *et al.* Inhibition of KLF7-targeting microRNA 146b promotes sciatic nerve regeneration. *Neurosci Bull* 2018, 34: 419–437.



REVIEW

# Pathophysiology and Individualized Management of Vasovagal Syncope and Postural Tachycardia Syndrome in Children and Adolescents: An Update

Ying Liao<sup>1</sup> · Junbao Du<sup>1</sup>

Received: 7 August 2019 / Accepted: 31 January 2020 / Published online: 4 May 2020  
© Shanghai Institutes for Biological Sciences, CAS 2020

**Abstract** Vasovagal syncope (VVS) and postural tachycardia syndrome (POTS) are the main forms of orthostatic intolerance in pediatrics and both are underlying causes of neurally-mediated syncope. In recent years, increasing attention has been paid to the management of VVS and POTS in children and adolescents. A number of potential mechanisms are involved in their pathophysiology, but the leading cause of symptoms varies among patients. A few studies thus have focused on the individualized treatment of VVS or POTS based on selected hemodynamic parameters or biomarkers that can predict the therapeutic effect of certain therapies and improve their effectiveness. This review summarizes the latest developments in individualized treatment of VVS and POTS in children and indicates directions for further research in this field.

**Keywords** Vasovagal syncope · Postural tachycardia syndrome · Individualized management · Pathophysiology · Children · Adolescents

## Introduction

Orthostatic intolerance (OI) is common in the pediatric population and is defined as having difficulties in tolerating the upright posture because of several symptoms (e.g., lightheadedness, blurred vision, palpitations, tremor, fatigue, and even syncope) that are relieved by recumbency [1]. Vasovagal syncope (VVS) and postural tachycardia

syndrome (POTS) are the main forms of OI in pediatric patients [1]. VVS is usually triggered by prolonged standing (acute OI) or exposure to mental stress and is manifested as sudden syncopal episodes accompanied by pallor, nausea, diaphoresis, and other symptoms associated with hypotension and/or bradycardia resulting from vagal excitation [2]. A diagnosis of VVS is made mainly based on the typical manifestations noted above, but sometimes a provocative test, the head-up tilt test (HUTT), should be performed to confirm the diagnosis, especially when the patient has atypical signs. A positive response in the HUTT that supports a diagnosis of VVS is that the patient suddenly faints or has pre-syncopal signs during the course of tilting combined with either hypotension (vasoinhibitory type) or bradycardia (cardioinhibitory type), or both (mixed type), and the cutoff values for hypotension and bradycardia vary with age [2]. POTS is a form of chronic OI characterized by an excessive increase in heart rate when moving from the supine to the upright position [2, 3]. The diagnostic criterion for “excessive increase of heart rate” in pediatric patients with POTS refers to an increase in heart rate  $\geq 40$  beats per min (bpm) from the supine to the upright position or the maximum upright heart rate reaches  $\geq 130$  bpm (in children aged 6 to 12 years) or  $\geq 125$  bpm (in adolescents aged 13 to 18 years) within the initial 10 min after standing up in the HUTT or standing test [4]. Both VVS and POTS are underlying causes of neurally-mediated syncope, which is defined as syncope associated with autonomic neural reflexes or autonomic nerve dysfunction and accounts for  $\sim 75\%$  of pediatric syncope cases [2, 4]. The recurrent or sustained symptoms of OI, either frequent syncopal episodes or chronic systemic symptoms, may have negative effects on children’s physical and mental health and significantly lower the quality of the children’s and parents’ lives [1]. In recent years, increasing attention

✉ Junbao Du  
junbaodu1@126.com

<sup>1</sup> Department of Pediatrics, Peking University First Hospital, Beijing 100034, China

has been paid to the management of VVS and POTS in children and adolescents. The Heart Rhythm Society [4], Canadian Cardiovascular Society and Canadian Pediatric Cardiology Association [5], American College of Cardiology/American Heart Association (ACC/AHA) [2], European Society of Cardiology (ESC) [6], and Chinese Pediatric Cardiology Society (CPCS) [3] have successively published guidelines or expert consensus statements on the diagnosis and management of pediatric VVS or POTS. In addition, a number of studies have focused on the individualized treatment of VVS or POTS based on selected hemodynamic parameters or biomarkers that can predict the therapeutic effects of certain therapies to improve their effectiveness. In the following, we review the latest developments in individualized treatment for VVS and POTS in children for the purpose of improving the therapeutic strategy in further clinical studies in this field.

## Pathophysiology and Individualized Management of VVS in Pediatric Patients

### Pathophysiology and Theoretical Basis of Individualized Therapy for VVS

VVS is the most common form of reflex syncope, comprising postural syncope and emotional/stress syncope in response to various triggers. Currently, there are continuing disputes about the pathophysiology of VVS, indicating that the dominant mechanisms causing syncope vary among VVS patients.

When upright, it is a challenge for humans to maintain sufficient cerebral blood flow (CBF) because the heart is lower than the brain and 70% of the blood flow is below heart level. Adequate blood volume and the integrity of cardiovascular and autonomic compensatory mechanisms are essential for tolerance of orthostatic stress [7]. Any impairment in the orthostatic compensatory system can lead to decreased CBF and symptoms of OI. To a certain extent, OI is a “cost” of bipedalism.

Early researchers believed that the key pathological mechanism of VVS was the Bezold-Jarisch reflex, which is induced by an under-filled and hyper-contractile heart [8]. However, increasingly opposing opinions have emerged to challenge this classic theory [9, 10]. According to recent categorizations, the postural VVS patient typically experiences three stages during a syncopal episode based on the hemodynamic data with a positive response during the HUTT (Fig. 1).

In stage I, the blood pressure (BP) is relatively stable. After standing up, a transient fall of BP called initial orthostatic hypotension occurs because of the decreased

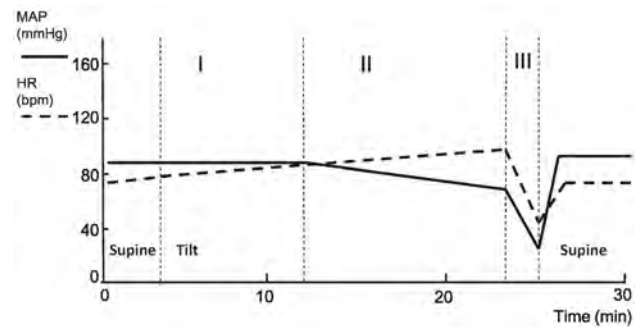


**Fig. 1** Illustration of the three stages of hemodynamic change in pediatric patients with classic postural vasovagal syncope (VVS) during the head-up tilt test (HUTT). Typical changes in mean arterial pressure (MAP; solid line) and heart rate (HR; dashed line) during the HUTT (vertical dashed lines, different stages during the test until a positive response). MAP is maintained relatively stable accompanied by increased HR in stage I. Then MAP decreases slowly while HR increases continuously in stage II. Both MAP and HR fall abruptly in stage III, indicating a positive response of the mixed type. The MAP and HR rise to normal levels soon after the patient returns to the supine position. bpm, beats per minute.

intrathoracic blood volume due to gravity, and the BP can recover in 30–60 s by reflex tachycardia. This initial fall of BP occurs in both healthy people and VVS patients. Then, the BP remains stable by means of increased reflex sympathetic activity and compensatory vasoconstriction, although the sympathetic activity, heart rate, and peripheral vascular resistance increase more in VVS patients than in healthy people. Patients with a relatively insufficient central volume have to exert more effort to compensate for the excessive reduction of inevitable cardiac preload. Patients may feel well or at most experience transient and slight dizziness as well as palpitation at this stage because of the relatively stable BP and mild tachycardia. During this stage, efforts to increase venous return, such as physical counter-pressure maneuvers and external compression on the lower limbs, can be helpful.

In stage II, the BP slowly decreases despite the more obvious tachycardia combined with continuously increasing sympathetic activity and peripheral vascular resistance, leading to the symptoms of pre-syncope. Patients begin to show prodromal manifestations such as weakness, pallor, blurred vision, severe lightheadedness, nausea, and abdominal pain due to the insufficient blood supply. Sweating may also appear as a result of sympathetic activation. The gradual decline of BP reflects the decreased cardiac output, which is believed to be related to the reduction of cardiac preload, vasodilation in selected peripheral vascular beds, and excessive tachycardia in this stage [11, 12]. The inappropriate vasodilation in specific peripheral vascular beds has been shown to play an important role at this stage [1, 13]. However, peripheral vasodilation is not evident in all VVS patients, and the extent of tachycardia can be mild

to moderate in some patients, indicating that the predominant mechanism of the reduction in cardiac output differs among individuals.

In stage III, the CBF suddenly falls, combined with a sharply decreased BP and/or heart rate, leading to a loss of consciousness. A syncopal attack finally occurs at this stage because of a significant decrease in CBF. These abrupt hemodynamic changes have been attributed to the impairment of baroreflex integrity and cerebral autoregulation [14]. However, the exact mechanism is still unknown.

Not every patient experiences the three typical stages, implying that each patient has distinct major problems with the orthostatic regulatory mechanisms. For example, hypotension and bradycardia do not always occur simultaneously at stage III. Some patients exhibit only a decrease in BP without detectable bradycardia during the HUTT and are considered to have the vasoconstrictive type of VVS; in these patients, a deficiency in peripheral vasoconstriction is thought to be the main problem. In contrast, other patients experience convulsive syncope due to severe bradycardia or sudden asystole without the warning decline in BP (lacking stage II) and are classified as having the cardioinhibitory type of VVS [4]. In addition, in a recent study, VVS patients were divided into two groups according to their baseline supine BP. During the tilt test, low tyrosine hydroxylase levels and reduced norepinephrine (NE) synthesis were found in the low-pressure group, while increased NE transporter levels resulting in enhanced NE reuptake were found in the normal-pressure group [15]. Despite these variations among VVS patients, it is evident that the principles of management should be determined for each patient.

In summary, several potential mechanisms are involved in the pathophysiology of VVS, but the leading cause of symptoms in each patient varies. Any of the mechanisms, such as relatively insufficient central volume leading to an excessive reduction in cardiac preload, inappropriate peripheral vasodilation, abnormal NE metabolism, and a loss of baroreflex integrity, can play the major role and become the therapeutic target in different individuals. Although it is not fully understood why patients with VVS demonstrate the vasoconstrictive type, cardioinhibitory type, or mixed type, and why sometimes one type converts into another, there is a consensus that therapies against these pathophysiological mechanisms may abolish the abnormal orthostatic regulatory process at the first two stages to avoid syncope at stage III. Therefore, in theory, individualized therapy directed against the predominant pathophysiological mechanism can be expected to abort the subsequent symptoms and achieve a more satisfactory therapeutic effect.

### Improvement of Individualized Treatment of VVS in Children and Adolescents

The management of VVS in children includes conventional therapy, pharmacological therapy, and cardiac pacing. According to previous studies, conventional therapy usually involves tilt training, physical counter-pressure maneuvers, and increased intake of salt and water, while pharmacological therapy basically involves fludrocortisone,  $\beta$ -adrenergic receptor blockers,  $\alpha$ -adrenergic receptor agonists, and serotonin transporter inhibitors [3]. These treatment options for VVS in children are based on the theories described above. For example, increased salt and water intake and fludrocortisone are recommended to raise the central volume, while midodrine (an  $\alpha$ 1-adrenergic receptor agonist) is prescribed against probable peripheral vasodilation. For treatment of the cardioinhibitory type of VVS, cardiac pacing should be cautiously considered for patients suffering from recurrent syncope related to reflex vagal asystole [2]. The disappearance of the recurrent syncope during follow-up as well as a negative response in the HUTT at the endpoint of follow-up are usually taken as effective responses. However, there are always non-responders to each therapy. Without individualized therapy, only 20%–29% of children with VVS benefit from conventional therapy, including health education and an increased intake of salt and water [16, 17]. Even with medication, only 43% of pediatric patients with VVS responded to metoprolol and 75% responded to midodrine, in two randomized controlled trials (RCTs) [16, 17]. The major problems in management strategies for VVS may be that the therapeutic options do not specifically target the mechanisms in patients with different primary pathogeneses, and there are no indicators for the various mechanisms to facilitate selection. Therefore, it is necessary to find predictors of the therapeutic effect in VVS patients that indicate the dominant pathophysiological mechanism in each patient, to identify individuals who will respond to the corresponding therapy and consequently improve the quality of life for VVS patients who are affected by recurrent syncope.

#### *Acceleration Index as a Predictor of the Effectiveness of Orthostatic Training in Treating Children with VVS*

Orthostatic training (also known as tilt training) is a protocol to practice standing for gradually prolonged durations. Children with VVS are usually instructed to stand 15 cm away from the foot of a wall with their upper body leaning against the wall for no more than 20 min [4]. This training is considered useful for improving the coordination of the autonomic and cardiovascular systems during orthostatic regulation and, in theory, to adapt the

patient to the upright posture. One RCT in adults showed that well-controlled orthostatic training can significantly enhance baroreflex sensitivity and heart rate variability [18]. However, the symptom improvement rate was not satisfactory in earlier studies, and corresponding data in pediatric patients are limited [19, 20]. The acceleration index is the instantaneous rate of increase of a patient's heart rate when they change from a supine to an upright position and is calculated from the intervals between adjacent R waves (RR intervals) in electrocardiograms during the process. In detail, the acceleration index is calculated as  $[(A - B)/A] \times 100$ , where A is the mean duration (in milliseconds) of the RR intervals during the last 15 s before changing to an upright position and B is the shortest RR interval within the period of 5 to 40 s after standing. This index has been positively correlated with plasma epinephrine levels and represents sympathetic activity [21]. One recent study revealed that VVS children with a lower baseline acceleration index have a better response to orthostatic training, suggesting that this index may predict the effectiveness of orthostatic training in this population. The index has a cutoff value of 26.77 with a sensitivity of 85% in predicting the therapeutic response [22], it is easy to measure, and it may become a useful indicator to improve the therapeutic efficacy of orthostatic training for children with VVS.

#### *Predictors of the Effectiveness of $\beta$ -Adrenergic Receptor Blockers in Treating Children with VVS*

The use of  $\beta$ -adrenergic receptor blockers ( $\beta$ -blockers) as the treatment for patients with VVS has been disputed for years. The supposed therapeutic rationale for these agents is that  $\beta$ -blockers suppress the activation of ventricular mechanoreceptors by attenuating the excessive contractility of the heart, which is deemed to initiate the classic Bezold-Jarisch reflex, leading to vagal excitation in patients with VVS [23, 24]. Nevertheless, as noted above, the role of the Bezold-Jarisch reflex in the pathophysiology of VVS is debatable, and several randomized comparisons of  $\beta$ -blockers and placebo in the treatment of VVS in adults have not confirmed the superiority of the former [25–27]. Studies of VVS in the pediatric population also report conflicting results on the efficacy of  $\beta$ -blockers [16, 28, 29]. It is notable that a number of studies have revealed that  $\beta$ -blockers are beneficial in certain age groups [16, 28, 30]. These different results indicate that  $\beta$ -blockers may be effective for selected patients with VVS and that predictors of the responses to  $\beta$ -blockers are needed to rationalize their use.

#### *Increase in Heart Rate before a Positive Response in the Head-Up Tilt Test* To identify predictors of the

therapeutic efficacy of metoprolol (a  $\beta_1$ -selective blocker) in treating children with VVS, Zhang *et al.* [31] focused on the hemodynamic features during the HUTT. In this process, reflex tachycardia occurs after a patient is tilted from the supine position. The investigators found that, during the period before a positive response in the HUTT, children with a greater increase in heart rate in the tilted position than in the supine position show a better therapeutic response to metoprolol during follow-up. Using a heart rate increase of 30 bpm in the HUTT as the threshold, the sensitivity of prediction of an effective response to metoprolol among children with VVS is 81%, indicating that the change in heart rate during the HUTT can be an ideal predictor.

*Echocardiography-Derived Left Ventricular Ejection Fraction and Fractional Shortening* Previous studies have revealed that the plasma epinephrine levels in the supine position are mildly higher in patients with VVS than in the healthy population, whereas the plasma epinephrine increases significantly after the patient is tilted, and further increases to pre-syncope or syncope during the HUTT [32, 33]. The increased epinephrine is probably associated with excessive ventricular constriction that may evoke reflex hypotension and bradycardia in some patients with VVS, which rationalizes the use of  $\beta$ -blockers. Song *et al.* [34] explored some non-invasive indicators of standing baseline epinephrine to predict the therapeutic response to metoprolol and discovered that the left ventricular ejection fraction (LVEF) and fractional shortening (LVFS) measured by echocardiogram in the supine position can achieve this goal. During the 6-month follow-up, the responders to metoprolol had higher baseline LVEF and LVFS than the non-responders (LVEF:  $72.5\% \pm 3.2\%$  vs  $64.6\% \pm 3.4\%$ ; LVFS:  $40.9\% \pm 2.3\%$  vs  $34.9\% \pm 2.9\%$ ). With a cutoff value of 70.5%, the sensitivity of LVEF to predict a therapeutic response to metoprolol in children with VVS was 81.3% as determined by the receiver operating characteristic (ROC) curve analysis. The predictive sensitivity of LVFS reached 93.8% when using a borderline cutoff of 37.5%. However, the use of LVEF as a predictor for a therapeutic response to metoprolol is limited as the cut-off baseline LVEF value of  $>70.5\%$  may exclude major populations of patients.

*Twenty-Four-Hour Urine NE Level* Recently, Kong *et al.* investigated the 24-h urine NE level, which represents the functional status of the sympathetic nervous system to some extent, in children with VVS [35]. They found that the levels varied within the patient group and were positively correlated with the supine BP, implying that the baseline sympathetic activity differs among children with VVS. This result is consistent with the findings of

Vaddadi *et al.* who reported that patients with VVS can be divided into normal-pressure and low-pressure groups according to their supine BP [15]. As expected, children with a better response to metoprolol had higher 24-h urine NE levels before treatment. With 34.84  $\mu\text{g}/24\text{ h}$  as the cutoff value, the 24-h urine NE level can be used to predict the therapeutic effect of metoprolol therapy in children with VVS with a sensitivity of 70% and a specificity of 100%.

#### *Flow-Mediated Vasodilation (FMD) as a Predictor of the Effectiveness of $\alpha$ 1-Adrenergic Receptor Agonists in Treating Children with VVS*

Excessive vasodilatation is known to be a vital pathophysiological mechanism underlying the reduced cardiac output in a group of patients with VVS [10, 11]. In RCTs, midodrine hydrochloride, an  $\alpha$ 1-adrenergic receptor agonist, has been shown to be effective in treating children with VVS [17, 36]. The effective rate of midodrine therapy is  $\sim 75\%$  in non-selected children with VVS. In a study to search for an indicator of vascular tone to predict the therapeutic effect of vasoconstrictors such as midodrine, Zhang *et al.* measured FMD in pediatric patients with VVS before they received midodrine [37]. The FMD detected by vascular ultrasound represents endothelium-dependent vascular function. During follow-up for 10–18 months, the children with greater baseline FMD had a lower recurrence rate of syncope. The ROC for the predictive value of FMD showed a high sensitivity (90%) for a therapeutic response to midodrine when using an FMD of 8.85% as the cutoff. Thus, they concluded that FMD can be taken as an indicator for the selection of midodrine for the treatment of VVS in children.

#### *Individualized Treatment with Cardiac Pacing in Children with VVS*

Children diagnosed with the cardioinhibitory or mixed type of VVS may experience sudden asystole during episodes of syncope. Nevertheless, it is debatable to treat these children with cardiac pacing against the asystole triggered by the vagal reflex because they often have a benign prognosis. According to recent RCTs and meta-analyses, pacemaker therapy is recommended (Class IIa) by the guidelines from the ACC/AHA and ESC for patients aged  $\geq 40$  years with recurrent syncope and documented asystole  $\geq 3$  s related to syncope or spontaneous asystole  $\geq 6$  s without syncope recorded by an implantable loop recorder [2, 6, 38]. In pediatric patients, there is no strong evidence for the necessity of cardiac pacing in the management of VVS. A retrospective study investigated pacemaker implantation in 11 children 0.8–17 years of age who were diagnosed with

cardioinhibitory VVS or pallid breath-holding spells (a specific type of VVS in infants) and in whom syncope was correlated with a documented asystole  $\geq 10$  s [39]. The results showed that implantation completely prevented the recurrence of syncope in 10 out of the 11 children during follow-up (median, 6.8 years) [39]. The ACC/AHA guideline states that pacemaker therapy might be considered in children with severe reflex syncope secondary to pallid breath-holding spells (Class IIb) [2]. According to the CPCS guidelines, cardiac pacing should be considered in pediatric VVS patients with a symptomatic prolonged asystolic pause  $\geq 4$  s on the advice of experienced pediatric cardiologists [4]. In brief, pacemaker therapy should be cautiously but not regularly considered in the management of VVS children with threatening asystole. The benefits and adverse complications of pacemaker implantation should be weighed before making a decision.

## **Pathophysiology and Individualized Management of Postural Tachycardia Syndrome in Pediatric Patients**

### **Pathophysiology and Theoretical Basis for Individualized Therapy in POTS**

Different from VVS, POTS is a form of chronic OI with heterogeneous etiologies. The identical major sign in patients with POTS is the sustained excessive tachycardia as a compensatory response to orthostatic posture, although their symptoms are diverse and can appear in any posture [40] (Fig. 2). Several mechanisms have been reported for patients with POTS, such as central hypovolemia, peripheral vascular dysfunction, and hyperadrenergic stimulation

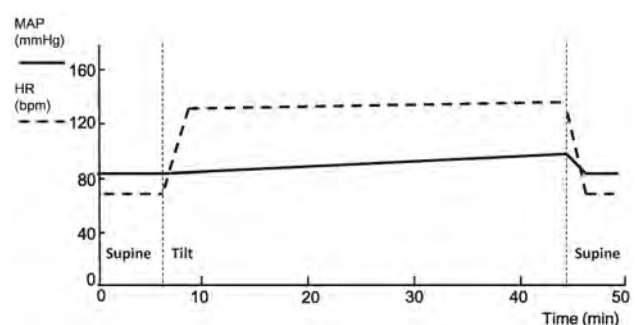


**Fig. 2** Illustration of typical hemodynamic changes in pediatric patients with POTS during the HUTT (solid line, MAP; dashed line, HR; vertical dashed lines, beginning and end of tilting). HR significantly increases while MAP increases slightly and remains relatively stable during the entire course. Both of MAP and HR fall to normal levels soon after the patient returns to the supine position. MAP, mean arterial pressure; HR, heart rate; POTS, postural tachycardia syndrome; HUTT, head-up tilt test; bpm, beats per minute.

[1, 3]. There may be more than one mechanism in an individual patient with POTS; thus, it is necessary to reveal these mechanisms in order to prescribe a sensible therapeutic regimen.

#### *Hypovolemia*

Nearly 70% of patients with POTS have a reduced blood volume [3]. It is apparent that a relatively insufficient blood volume can worsen central hypovolemia when patients are in a long-term upright position, leading to excessive tachycardia as compensation. In some patients, hypovolemia is secondary to specific underlying causes, such as dehydration and anemia. However, in most cases, patients with POTS do not have a definite history of dehydration despite the low blood volume [41, 42]. Raj *et al.* reported that a group of patients with POTS had paradoxically unchanged plasma renin activity and lower aldosterone compared with healthy controls regardless of the significant reduction in total blood volume [43], suggesting that disorders of the renin-aldosterone system contribute to the hypovolemia in some patients with POTS.

#### *Peripheral Vascular Dysfunction*

Dysfunction of the peripheral vascular system can cause a failure of vasoconstriction or excessive vasodilation in certain vascular beds, such as the lower limbs or splanchnic vasculature, resulting in blood volume pooling and distributive central hypovolemia in some patients with POTS, especially when in an upright position [44, 45]. Central hypovolemia inevitably leads to reduced cardiac output and compensatory orthostatic tachycardia.

*Peripheral Autonomic Denervation* Peripheral autonomic denervation is one of the acknowledged causes of vascular dysfunction. Impaired adrenergic vasoconstriction in the lower limbs and splanchnic vascular bed has been found in patients with POTS [13, 46, 47], who were classified as having “neuropathic POTS”. The exact etiology of this autonomic neuropathy is not clear, although studies have indicated that autoimmune processes might contribute to the pathological mechanisms [48–50].

*Imbalance Between Vasoconstrictors and Vasodilators* An imbalance between the vasoconstrictors and vasodilators in the peripheral circulation may be another important factor contributing to vascular dysfunction. Several vasodilators, such as nitric oxide (NO) [51], hydrogen sulfide (H<sub>2</sub>S) [52], and adrenomedullin (ADM) [53], are higher, whereas vasoconstrictors such as endothelin [54] and urotensin II [55] are lower in patients with POTS than in healthy controls. These changes in

vasoactive factors may participate in the abnormal vascular tone in patients with POTS.

*Structural Defects of Peripheral Blood Vessels* Rarely, structural defects of peripheral blood vessels can also predispose individuals to vascular dysfunction. The prevalence of Ehlers-Danlos syndrome, which is a heterogeneous group of heritable connective tissue disorders, is significantly higher in patients with POTS than in the general population [56]. The possible mechanism underlying this syndrome is that the vascular wall of peripheral veins is excessively stretched in response to the increased pressure caused by orthostatic posture, resulting in venous pooling [56]. By a similar mechanism, the symptoms of POTS can be seen in patients with a congenital absence of valves in the deep veins of the legs [57].

#### *Hyperadrenergic Stimulation*

While standing, high levels of circulating NE as well as increased sympathetic nerve activity have been reported in a group of patients with POTS, who are classified as having “hyperadrenergic POTS” [50, 58, 59]. These patients usually have manifestations such as pallor, tremor, palpitations, tachycardia, and hypertension, suggesting sympathetic activation. In some patients, the increased NE level is considered to be associated with autoantibodies to adrenergic receptors [60]. In addition, a mutation of the *SLC6A2* gene encoding the NE transporter has been found in some patients showing significant sympathetic activation because of the decreased reuptake of synaptic NE [61].

#### *Other Mechanisms*

Apart from the classic mechanisms described above, several other functional disorders or diseases are thought to be involved in the pathophysiology of POTS.

*Mechanisms Associated with Autoimmunity* A variety of phenomena support the hypothesis that the autoimmune response participates in the etiology of POTS. Patients with POTS may have experienced a viral infection, vaccination, operation or trauma before the onset of symptoms [62]. Moreover, some autoantibodies, such as those against adrenergic receptors, angiotensin II type I receptors, and ganglionic acetylcholine receptors, have been detected in the plasma of patients with POTS, of whom 20% have a history of autoimmune disease [49, 63–66]. Researchers have studied the roles of these autoantibodies in patients with POTS. Fedorowski *et al.* found that the autoantibodies from some POTS patients can activate  $\alpha$ 1- or  $\beta$ 1/2-adrenergic receptors in transfected cells, and this activation can be suppressed by specific blockers of the corresponding

receptors [64]. Furthermore, the upright heart rate of patients with POTS is correlated with an activated response of adrenergic receptors mediated by autoantibodies. On the basis of studies of plasma autoantibodies to adrenergic receptors, the orthostatic tachycardia in patients with POTS is probably attributable to the direct stimulatory effect of cardiac receptor-activating autoimmune antibodies on sinus rhythm control or to a compensatory response to the excessive vasodilation elicited by vascular receptor autoantibodies [60, 66].

**Prolonged Bed Rest and Deconditioning** Some patients with POTS tend to stay in bed because of the symptoms of OI. However, gravitational deconditioning can appear with prolonged bed rest, leading to decreased blood volume, abnormal redistribution of blood volume, and failure of vasoconstriction as well as dysfunction of the skeletal muscle pump, which can aggravate the symptoms of OI [67, 68]. The prevalence of deconditioning in adult and adolescent patients with POTS is reported to be up to 93% and 68%, respectively [69, 70]. As a result, it is believed that the symptoms of POTS can be alleviated by physical activity rather than bed rest.

### Improvement of Individualized Treatment of POTS in Children and Adolescents

Multiple mechanisms lead to the heterogeneity of POTS and pose a great challenge to management because the patients cannot be treated by a unified method. In addition to common measures such as education for patients and their parents, the advocacy of physical exercise, and psychological support, targeted therapy focusing on the major underlying pathological mechanisms can predictably achieve better therapeutic effects. For example, to attain the best therapeutic outcome, advocating salt and water intake is suitable for patients with hypovolemia; vasoconstrictors tend to be prescribed for patients with vascular dysfunction; and adrenergic receptor antagonists should be used for patients with hyperadrenergic stimulation. Furthermore, the most important thing for successful individualized therapy is to search for appropriate clinical signs or biomarkers that can indicate the major pathological mechanisms to predict the therapeutic effects of different treatments.

#### *Predictors of the Effectiveness of Oral Rehydration Salts in the Treatment of Children with POTS*

Early studies confirmed that increased fluid and salt intake can improve the symptoms of OI by increasing blood volume, although the extent of improvement varies [71, 72]. Oral rehydration salts (ORSs) are the most

commonly used agents in children with POTS. Several markers reflecting hypovolemia have been reported to elevate the pertinence of the use of ORSs.

**Twenty-Four-Hour Urinary Sodium Concentration** The loading of sodium in body fluids is known to be positively correlated with blood volume. Zhang *et al.* [73] aimed to explore the relationship between 24-h urinary sodium and ORS therapy in children with POTS. The ORS therapy resulted in a significant increase in urinary sodium excretion and responders to ORSs, whose OI symptom score was decreased by at least 2 after treatment with ORSs, had a lower baseline 24-h urinary sodium concentration than non-responders. The suggested condition for the prediction of response to ORS therapy is a 24-h urinary sodium concentration <124 mmol/L with a high predictive sensitivity of 93%. These results support the speculation that a low 24-h urinary sodium concentration, which is believed to be associated with decreased sodium loading as well as body fluid volume, can be taken as an indicator for using ORSs as a treatment option.

**Body Mass Index** Another candidate predictor for the effectiveness of ORS therapy is body mass index (BMI), which is calculated from body height and weight. Stewart *et al.* revealed that BMI was correlated with blood flow in a group of young women with POTS [74]. Li *et al.* [75] reported in a pediatric population that children with POTS had a lower BMI than the controls in the same age group. These findings suggest that BMI reflects blood volume to a certain extent. Furthermore, this study found that pediatric POTS patients with a lower BMI respond better to ORS therapy than those with a higher BMI. Using a BMI <18 kg/m<sup>2</sup> as the cutoff, the effectiveness of ORSs in the treatment of children with POTS is well predicted with a sensitivity up to 92% and specificity up to 82.8% [75]. It is easy to measure body height and weight. The results also implied a potential relationship between BMI and blood volume in accordance with previous studies. However, BMI can be influenced by many other factors in addition to blood volume, especially in children.

**Mean Corpuscular Hemoglobin Concentration** The red blood cell (RBC) volume is correlated with blood volume. A previous study showed that RBC volume was significantly reduced in a group of patients with POTS [76]. Lu *et al.* [77] explored the items that reflect RBC volume included in a complete blood count in children with POTS to search for predictors of the therapeutic effect of ORS treatment. According to their findings, responders to ORSs had a lower mean corpuscular volume and a higher mean corpuscular hemoglobin concentration (MCHC) than non-responders, while other items such as hematocrit did not

differ between the two groups. The MCHC also showed a moderate predictive value of a therapeutic effect of ORSs on POTS in children by ROC analysis, and the recommended borderline for predicting responders was an MCHC >347.5 g/L. To illuminate the potential reason that the responders to ORSs have an increased MCHC, the investigators explained that low blood volume may contribute to either insufficient plasma volume or reduced RBC volume or both, and ORSs directly replenish the plasma volume rather than the RBC volume. Therefore, patients with an increased MCHC are likely to have an insufficient plasma volume and benefit from ORS therapy. The complete blood count can be tested in hospitals at different levels, but further evaluation is needed because the sensitivity and specificity of prediction is just about 65%.

**Baroreflex Sensitivity** The baroreflex plays an important role in the autonomic regulation of BP, and baroreflex sensitivity (BRS) reflects the functional status of the autonomic nervous system. Convertino *et al.* reported that decreased blood volume results in an enhanced BRS, implying an association between BRS and blood volume [78]. Li *et al.* [79] designed a study to determine the role of BRS in the prediction of the therapeutic effect of ORS in children with POTS. The BRS was measured supine using a continuous hemodynamic monitoring system. Children in the POTS group showed much greater BRS than the control group, and BRS was positively correlated with the change in heart rate from the supine to the upright posture in the POTS group. In addition, responders to ORS therapy had greater baseline BRS than non-responders. Both high predictive sensitivity (85.7%) and specificity (87.5%) can be achieved when a BRS >17.01 ms/mmHg is taken as a determinant of ORS therapeutic efficacy in pediatric POTS patients. As expected, an increased BRS was found in responders to ORSs who were supposed to have an insufficient blood volume with enhanced BRS. The BRS seems to be an ideal predictor in terms of the high predictive sensitivity and specificity, although the measurement is a little difficult for general use.

#### *Predictors of the Effectiveness of $\beta$ -Adrenergic Receptor Blockers in the Treatment of Children with POTS*

$\beta$ -Blockers are prescribed to relieve symptoms of POTS in children based on the mechanism of hyperadrenergic stimulation and have been shown to be effective in children and adults with POTS [80, 81]. However, one controlled study on children with POTS reported that the effective rate of metoprolol therapy is only 57.9% [82]. Therefore, indicators of hyperadrenergic status that can be

easily detected are needed to improve the therapeutic effect of  $\beta$ -blockers.

**Orthostatic Plasma NE Level** To test the “hyperadrenergic stimulation” hypothesis, Zhang *et al.* [83] examined the orthostatic plasma NE level in children with POTS. The blood samples were collected after the patients remained standing for 5 min. The orthostatic plasma NE levels were positively correlated with the symptom score as well as the increase in heart rate during the HUTT. After treatment with metoprolol for 3 months, the responders who showed significant improvement in symptoms and upright heart rate had higher baseline orthostatic plasma NE levels than the non-responders. Based on the ROC analysis, the authors recommend an orthostatic plasma NE level >3.59 pg/mL as a reference for the selection of metoprolol as therapy for children with POTS. The predictive sensitivity is 77% and the specificity is 92%. As  $\beta$ -blockers can block the effect of increased NE levels, these results may be direct evidence for individualized use of metoprolol; however, it should be noted that the sample size was small.

**Plasma C-Type Natriuretic Peptide** C-type natriuretic peptide (CNP) is a small bioactive peptide that is involved in the pathogenesis of several cardiovascular diseases; it may be an ideal biomarker because it is stable in the circulation and is easily detected [84]. Takekoshi *et al.* reported that CNP increases the synthesis of catecholamines by promoting the expression of tyrosine hydroxylase mRNA *in vitro* [85], while in isolated heart experiments Springer *et al.* reported that CNP increases heart rate by acting on the sinoatrial node through its receptors [86]. Based on these experimental findings, Lin *et al.* [87] assessed the plasma CNP in children diagnosed with POTS and explored its value in the prediction of a therapeutic effect of  $\beta$ -blockers. The plasma CNP levels were markedly higher in children with POTS than in healthy children, indicating a role of CNP in the pathogenesis of POTS. During follow-up, the researchers found that the responders to metoprolol had higher baseline plasma CNP levels than the non-responders. The recommended cutoff value of plasma CNP is 32.55 pg/mL to predict the efficacy of metoprolol in the treatment of children diagnosed with POTS, with high sensitivity (96%) and moderate specificity (70%). Based on this study, the increased plasma CNP levels in responders to metoprolol are in accordance with the results of previous studies showing that CNP promotes the synthesis of catecholamines. Therefore, CNP can be taken as an indicator of “hyperadrenergic POTS”.

**Plasma Copeptin** Copeptin is a glycopeptide derived from the cleavage of the precursor of arginine vasopressin (AVP), which is sensitive to changes in osmotic pressure

and blood volume but is unstable in the circulation [88]. Copeptin is equally released with AVP and is stable for detection as an ideal biomarker of AVP secretion. Franklin *et al.* demonstrated that copeptin is inhibited by high central catecholamine levels [89]. Zhao *et al.* [90] measured plasma copeptin in children with POTS and analyzed its value in the prediction of a therapeutic effect of metoprolol. The responders to metoprolol were found to have lower baseline plasma copeptin levels than the non-responders. A plasma copeptin level  $<10.2$  pmol/L ensures a satisfactory predictive sensitivity reaching 90% and a specificity of 79%. This study revealed that reduced plasma copeptin levels are associated with an improved therapeutic effect of metoprolol, indirectly implying that plasma copeptin may have a negative correlation with catecholamines, although further studies are needed to test this hypothesis.

#### *Predictors of the Effectiveness of $\alpha$ -Adrenergic Receptor Agonists in the Treatment of Children with POTS*

Peripheral vascular tone plays a vital role in the maintenance of hemodynamic stability as well as sufficient cerebral blood flow in an orthostatic posture [1]. As noted above, although several mechanisms can account for the vascular dysfunction in the pathogenesis of POTS, the failure of vasoconstriction or excessive vasodilation, resulting in pooling in the peripheral circulation, is almost uniformly the direct cause of decreased central volume [91]. Based on this rationale, vasoconstrictors such as  $\alpha$ -adrenergic receptor agonists are used to treat patients with POTS. Previous studies have demonstrated the efficacy of midodrine in treating children and adolescents with POTS [80, 82, 92], and a number of indicators of vascular dysfunction have been found to help make the decision to use midodrine [93].

**Erythrocytic Hydrogen Sulfide Production** H<sub>2</sub>S has been confirmed as the third gaseous signaling molecule after NO and CO. H<sub>2</sub>S has significant regulatory effects on the cardiovascular system and is recognized as a strong vasodilator through several different pathways [94, 95]. The role of H<sub>2</sub>S in the prediction of the therapeutic response to midodrine in children with POTS was investigated by Yang and colleagues [52]. They revealed that children in the POTS group had higher erythrocytic H<sub>2</sub>S production than controls. Furthermore, after treatment with midodrine for 3 months, the OI symptom score declined in the POTS group, and the decreasing score was positively correlated with the original erythrocytic H<sub>2</sub>S production. Responders to midodrine had greater baseline erythrocytic H<sub>2</sub>S production than non-responders. The sensitivity and specificity for prediction are 79% and 78%, respectively,

under the condition of an erythrocytic H<sub>2</sub>S production  $>27.1$  nmol/min/10<sup>8</sup> RBCs. They concluded that children with POTS can be treated with midodrine in reference to this cutoff value. It seems that elevated erythrocytic H<sub>2</sub>S production can predict the therapeutic response to midodrine, a vasoconstrictor, basically because of the vasodilatory effect of H<sub>2</sub>S on various peripheral vascular beds. However, the exact mechanisms by which this  $\alpha$ 1-agonist acts on the vasoactive effects mediated by H<sub>2</sub>S still need further investigation.

**Plasma Midregional Pro-adrenomedullin** ADM is a vasoactive peptide involved in several cardiovascular diseases and disorders in other systems [96, 97]. It is known to be a potent vasodilator, but it is difficult to measure its circulatory content [98]. Midregional pro-adrenomedullin (MR-proADM) is a stable fragment of pro-ADM and is produced in equimolar amounts with ADM. Zhang *et al.* [53] reported that children with POTS have significantly higher plasma MR-proADM levels than healthy controls. Children in the POTS group were treated with midodrine and were followed up for at least 3 months, and a symptom score was used to evaluate the therapeutic effect and identify the responders. As expected, the responders had higher plasma MR-proADM levels before treatment than the non-responders. Based on ROC analysis, when the plasma MR-proADM is  $>61.5$  pg/mL, the sensitivity and specificity for the prediction of a therapeutic effect of midodrine are 100% and 72%, respectively. According to this study, the circulatory MR-proADM concentration, which correlates well with ADM production, can be used as an indicator to predict the therapeutic response to midodrine.

**Plasma Copeptin** As noted above, copeptin can be used as a predictor of metoprolol therapy for the treatment of children with POTS. Zhao *et al.* [99] investigated plasma copeptin in another group of children with POTS and monitored the therapeutic effect of midodrine during follow-up. Increased plasma concentrations of copeptin, which in fact represent AVP concentrations, were found in the POTS group compared with the controls. AVP is known to be a strong vasoconstrictor; therefore, the elevated plasma copeptin levels might be explained by a compensatory response to vascular dysfunction in children with POTS. In addition, responders to midodrine in this study showed even higher plasma copeptin levels at the first visit than the non-responders. Applying a plasma copeptin concentration  $>10.5$  pmol/L as the cutoff, the sensitivity and specificity for predicting the efficacy of midodrine in treating children with POTS reaches 86% and 76%, respectively. High levels of copeptin (or AVP) may indicate a state of relative hypovolemia. The authors

explained that midodrine works better in patients with high copeptin levels probably because midodrine can abate the insufficient venous return in these patients by reducing the venous capacity through vasoconstriction.

**Flow-Mediated Vasodilation** Endothelial function has been confirmed to play a critical role in modulating vascular tone. A previous study [51] explored endothelial function in children with POTS by measuring the plasma concentration of NO, the activity of NO synthase, and FMD. Both the plasma NO concentration and NO synthase activity were elevated, while FMD was greater in children diagnosed with POTS than in the control group, indicating that endothelial dysfunction most likely takes part in the pathogenesis of POTS. A subsequent study [100] revealed that baseline FMD is greater in responders to midodrine therapy than in non-responders during the follow-up of children with POTS. An FMD  $>9.85\%$  can be taken as the referral determinant for the use of midodrine with moderate predictive value for treating such children. The sensitivity and specificity of prediction are 74% and 80%, respectively. This study also showed that the FMD of POTS patients decreases after treatment with midodrine, indicating that  $\alpha$ 1-adrenergic receptors may contribute to the regulation of endothelial function. The mechanism by which  $\alpha$ 1-adrenergic receptors interact with endothelium in POTS children is still unknown, although complex interactions have been reported between the endothelium and the autonomic nervous system [101].

**Changes in Blood Pressure during the Standing Test** The orthostatic BP partly reflects the peripheral vascular tone during orthostasis. In a normal orthostatic response, the BP drops immediately after standing because of the gravitational redistribution of blood volume but recovers within 30 s due to the effect of the baroreflex [1]; then, the BP remains stable at a level almost equal to or no more than 10% above the supine BP [102]. It is worth considering focusing on the change in BP to distinguish different types of POTS. Patients with hyperadrenergic POTS may show a stronger increase in orthostatic BP and even orthostatic hypertension [3, 59]. In contrast, a slight decline in BP may appear in POTS patients with vascular dysfunction or hypovolemia [1]. Deng *et al.* [103] studied the difference in BP during the standing test between children diagnosed with POTS who were responsive and non-responsive to midodrine. In the baseline standing test before treatment, there was no significant difference between the two groups in supine BP, while the maximum upright systolic BP (SBP) and diastolic BP (DBP) as well as the increase in the SBP and DBP from the supine to the upright position were lower in responders than in non-responders. Based on further ROC analysis, effectiveness of midodrine in

treating children with POTS can be expected by referring to the increase in SBP combined with an increase in DBP during the baseline standing test. The combined condition was an increase in SBP  $\leq 0$  mmHg (SBP declines) or an increase of DBP  $\leq 6.5$  mmHg. The predictive sensitivity and specificity are 72% and 88%, respectively, with this cutoff value. In other words, a decline in SBP or less of an increase in DBP during standing may indicate insufficient compensatory vasoconstriction or inappropriate vasodilatation and favor treatment with vasoconstrictors. This predictor is favorable because BP measurement during the diagnostic standing test is routine for children with POTS.

#### *Individualized Management of POTS Based on Clinical Symptoms and Signs*

Since POTS is a group of disorders with heterogeneous origins but similar clinical manifestations, researchers have made efforts to construct a proper classification to guide its management.

Early studies attempted to divide patients with POTS into three types according to their calf blood flow measured by venous occlusion strain gauge plethysmography [104, 105]. Low-flow POTS is considered to be related to mild absolute hypovolemia or abnormal regulation of local blood flow [106]. Patients of this type are characterized by cool, pallid extremities and acrocyanosis and are believed to benefit from therapy with volume loading by increased uptake of salt and water or drugs such as fludrocortisone or erythropoietin. Patients with high-flow POTS, manifesting with edema of the lower extremities, have reduced peripheral vascular resistance [46] and relatively enhanced blood volume. Their symptoms can be alleviated by vasoconstrictors such as  $\alpha$ -adrenergic receptor agonists. Patients with normal-flow POTS may have splanchnic regional pooling [13] and can be treated with midodrine or a splanchnic-selective vasoconstrictor such as octreotide. Signs of hypermobility syndrome may occur in this type of patient [107]. These studies mainly involved adolescents and young adults and were aimed at individualized management for patients with POTS based on the characteristic underlying hemodynamic features. However, the optimal therapy for treating each type of POTS is based on theory, and better-designed controlled studies are needed to confirm the efficacy of various therapies in the treatment of the different subgroups.

A more recent study enrolled 708 children and adolescents with POTS and evaluated the effectiveness of available drugs in controlling symptoms including lightheadedness, headache, nausea, gastrointestinal dysmotility, pain, and insomnia [108]. All the drugs were effective in relieving specific symptoms to varying degrees. For

**Table 1** Predictors of effectiveness of different therapies on VVS and POTS in children.

Therapies	Predictors	Cut-off value	Sensitivity (%)	Specificity (%)	Tests or samples required
Research on children with VVS					
Orthostatic training	Acceleration index [22]	< 26.77	85	69.2	HUTT
Metoprolol	$\Delta$ HR in HUTT [31]	> 30 bpm	81	80	HUTT
	LVEF [34]	> 70.5%	80	100	UCG
	LVFS [34]	> 37.5%	90	90	UCG
	24 h urine NE [35]	> 34.84 $\mu$ g/24 h	70	100	24-h urine
Midodrine hydrochloride	FMD [37]	> 8.85%	90	80	Vascular ultrasound
Research on children with POTS					
ORS	24 h urine sodium [73]	< 124 mmol/L	93	77	24-h urine
	BMI [75]	< 18 kg/m <sup>2</sup>	92	82.8	General measurement
	MCHC [77]	> 347.5 g/L	68.8	63.2	Blood routine
	BRS [79]	> 17.01 ms/mmHg	85.7	87.5	CHMS
Metoprolol	Orthostatic plasma NE [83]	> 3.59 pg/mL	77	92	Blood sample
	Plasma CNP [87]	> 32.55 pg/mL	96	70	Blood sample
	Plasma copeptin [90]	< 10.2 pmol/L	90	79	Blood sample
Midodrine hydrochloride	Plasma MR-proADM [53]	> 61.5 pg/mL	100	72	Blood sample
	Ery H <sub>2</sub> S production [52]	> 27.1 nmol/min/10 <sup>8</sup> RBC	79	78	Blood sample
	FMD [100]	> 9.85%	74	80	Vascular ultrasound
	Plasma copeptin [99]	> 10.5 pmol/L	86	76	Blood sample
	$\Delta$ BP in standing test [103]	$\Delta$ SBP $\leq$ 0 mmHg or $\Delta$ DBP $\leq$ 6.5 mmHg	72	88	Standing test

VVS, vasovagal syncope; POTS, posture tachycardia syndrome; HUTT, head-up tilt test;  $\Delta$ HR in HUTT, the increase of heart rate before positive response in head-up tilt test compared with supine heart rate; LVEF, left ventricular ejection fraction; LVFS, left ventricular fractional shortening; UCG, ultrasound cardiogram; 24 h urine NE, 24-hour urine norepinephrine level; FMD, flow-mediated vasodilation; ORS, oral rehydration salt; BMI, body mass index; MCHC, mean corpuscular hemoglobin concentration; BRS, baroreflex sensitivity; NE, norepinephrine; CNP, Ctype natriuretic peptide; MRproADM, midregional proadrenomedullin; Ery H<sub>2</sub>S production 24 h urine sodium twentyfourhour urinary sodium concentration, erythrocytic hydrogen sulfide production;  $\Delta$ BP, changes of blood pressure;  $\Delta$ SBP, the increase of systolic blood pressure from supine to upright position;  $\Delta$ DBP, the increase of diastolic blood pressure from supine to upright position; bpm, beats per minute; CHMS, Continuous hemodynamic monitoring system.

example, fludrocortisone, midodrine, and desmopressin were used to control lightheadedness, and the effective rates were 42.8%, 33.9%, and 38.9%, respectively. For headache, the therapeutic effects of five drugs (cyproheptadine, verapamil, metoprolol, atenolol, and nebivolol) were evaluated, and they ranged from 14.2% for verapamil to 44.8% for metoprolol. For controlling nausea, ondansetron, scopolamine, and meclizine were effective in only 37.9%, 17%, and 8.7% of the patients, respectively. For gastrointestinal dysmotility, the remission rate was 36.7% with pyridostigmine and 32.7% with erythromycin. Duloxetine and pregabalin demonstrated efficacy in 41.2% and 34.3% of the patients suffering from pain symptoms. Finally, four drugs used for insomnia (clonidine, trazodone, zolpidem, and eszopiclone) alleviated the symptoms in 17.9% to 30.7% of patients. These results suggest that

symptoms should be taken as essential references when making the choice of therapy for children with POTS, but treatment simply guided by symptoms does not achieve high effective rates.

### Priorities of Reported Predictors in the Management of VVS and POTS

To date, several predictors of therapeutic effects have been reported to guide the individualized management of VVS and POTS in children. Physicians should cautiously evaluate the clinical manifestations and refer to one or more proper predictors before making the treatment plan for a specific patient. In clinical practice, comprehensive factors should be taken into account in the decision on

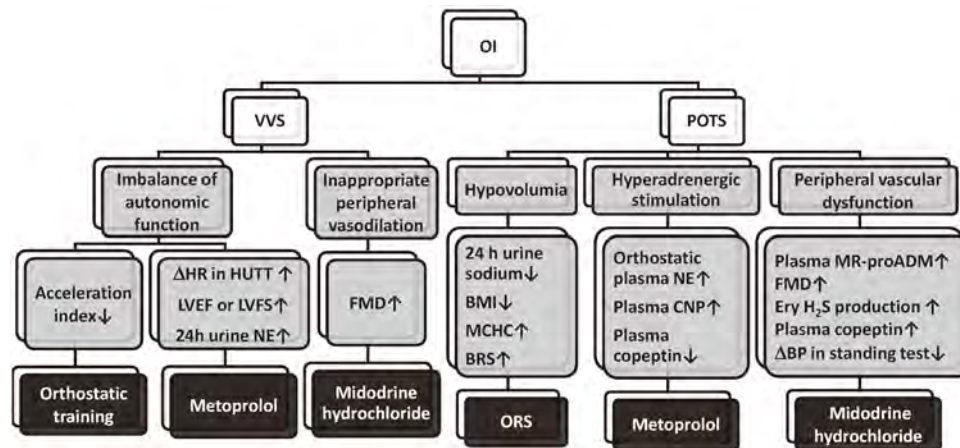


**Fig. 3** Schematic of the pathophysiology, corresponding indicators, and therapeutic options for vasovagal syncope and postural tachycardia syndrome in children. Grey boxes, potential pathophysiological mechanisms and changes in corresponding indicators; black boxes, individual therapeutic options based on the corresponding mechanisms; ↑, increase; ↓, decrease; OI, orthostatic intolerance; VVS, vasovagal syncope; POTS, postural tachycardia syndrome; ΔHR in HUTT, increase of heart rate before positive response in the head-up tilt test compared with supine heart rate; LVEF, left ventricular

ejection fraction; LVFS, left ventricular fractional shortening; 24 h urine NE, twenty-four-hour urine norepinephrine level; FMD, flow-mediated vasodilation; 24 h urine sodium, twenty-four-hour urinary sodium concentration; BMI, body mass index; MCHC, mean corpuscular hemoglobin concentration; BRS, baroreflex sensitivity; ORS, oral rehydration salt; NE, norepinephrine; CNP, C-type natriuretic peptide; MR-proADM, midregional pro-adrenomedullin; Ery H<sub>2</sub>S production, erythrocytic hydrogen sulfide production; ΔBP, changes of blood pressure.

therapeutic modalities. First, more sensitivity and specificity for prediction usually means more certainty of successful treatment. A sensitivity or specificity >90% indicates a high predictive value. Second, methods to determine the value of predictors can also impact the decision. For example, predictors drawn from the HUTT or standing test avoid additional examinations because the test is performed for diagnostic purposes. Predictors detected by ultrasound or 24-h urine collection are easily accepted by children and their parents because of their non-invasiveness. Predictors in items of routine blood tests are more favorable than those detectable only in some large testing institutions. We compare the predictive sensitivity and specificity as well as demands for detection among the reported predictors in Table 1. However, it is difficult to confirm the absolute priorities of these predictors based on the current information. It will be helpful to conduct studies that compare the therapeutic efficacy of individualized therapy based on the different predictors to determine their value in clinical practice and finally provide recommended priorities of the predictors.

### Perspectives for Individualized Management of VVS and POTS in Children and Adolescents

In summary, researchers have made great efforts to achieve individualized management of VVS and POTS in children (Table 1). Treatment strategies based on clinical features and pathogenesis are being established. To a certain extent,

clinical symptoms can indicate the pathogenesis of children with OI. However, the same clinical manifestations can be induced by distinct underlying mechanisms; hence, the subjective symptoms can be taken as important references but not the main evidence for individualized therapeutic approaches. Conversely, objective indexes, such as hemodynamic parameters or biomarkers, can reflect the potential pathogenesis of pediatric VVS or POTS more exactly and are more suitable predictors of the therapeutic effect of different treatment approaches (Fig. 3). It is noteworthy that measures are more preferable if they are uncomplicated and non-invasive or at least minimally invasive for pediatric patients, as noted above. Therefore, a favorable individualized treatment protocol should combine subjective symptoms with objective predictors. We suggest that the relationship between the external symptom spectrum and the intrinsic pathogenesis of VVS or POTS in children should be defined – for example, by establishing a symptom scoring system indicating different mechanisms. In addition, more sensitive predictors of the therapeutic effect of different therapies with favorable detection methods should be identified in multicenter-based clinical studies and large-sample studies to realize the ideal individualized management for children and adolescents with VVS and POTS.

**Acknowledgements** This review was supported by Peking University Clinical Scientist Program (BMU2019LCKXJ001, Beijing) and Fundamental Research Funds for the Central Universities of China.

**Conflict of interest** The authors claim that there are no conflicts of interest.

## References

- Stewart JM, Boris JR, Chelimsky G, Fischer PR, Fortunato JE, Grubb BP, *et al.* Pediatric disorders of orthostatic intolerance. *Pediatrics* 2018, 141. pii: e20171673.
- Shen WK, Sheldon RS, Benditt DG, Cohen MI, Forman DE, Goldberger ZD, *et al.* 2017 ACC/AHA/HRS guideline for the evaluation and management of patients with syncope: A report of the American College of Cardiology/American Heart Association Task Force on Clinical Practice Guidelines and the Heart Rhythm Society. *Heart Rhythm* 2017, 14: e155–e217.
- Sheldon RS, Grubb BP, Olshansky B, Shen WK, Calkins H, Brignole M, *et al.* 2015 Heart Rhythm Society expert consensus statement on the diagnosis and treatment of postural tachycardia syndrome, inappropriate sinus tachycardia, and vasovagal syncope. *Heart Rhythm* 2015, 12: e41–e63.
- Wang C, Li Y, Liao Y, Tian H, Huang M, Dong XY, *et al.* Chinese Pediatric Cardiology Society (CPCS) guideline for diagnosis and treatment of syncope in children and adolescents. *Sci Bull* 2018, 63: 1558–1564.
- Sanatani S, Chau V, Fournier A, Dixon A, Blondin R, Sheldon RS, *et al.* Canadian Cardiovascular Society and Canadian Pediatric Cardiology Association Position Statement on the approach to syncope in the pediatric patient. *Can J Cardiol* 2017, 33: 189–198.
- Brignole M, Moya A, de Lange FJ, Deharo JC, Elliott PM, Fanciulli A, *et al.* 2018 ESC Guidelines for the diagnosis and management of syncope. *Eur Heart J* 2018, 39: 1883–1948.
- Tao C, Tang C, Chen S, Jin H, Du J. Autonomic nervous function in vasovagal syncope of children and adolescents. *Neurosci Bull* 2019, 35: 937–940.
- Aviado DM, Guevara Aviado D. The Bezold-Jarisch reflex. A historical perspective of cardiopulmonary reflexes. *Ann NY Acad Sci* 2001, 940: 48–58.
- Scherrer U, Vissing S, Morgan BJ, Hanson P, Victor RG. Vasovagal syncope after infusion of a vasodilator in a heart-transplant recipient. *N Engl J Med* 1990, 322: 602–604.
- Liu JE, Hahn RT, Stein KM, Markowitz SM, Okin PM, Devereux RB, *et al.* Left ventricular geometry and function preceding neurally mediated syncope. *Circulation* 2000, 101: 777–783.
- Fu Q, Levine BD. Pathophysiology of neurally mediated syncope: Role of cardiac output and total peripheral resistance. *Auton Neurosci* 2014, 184: 24–26.
- Li H, Liao Y, Han Z, Wang Y, Liu P, Zhang C, *et al.* Head-up tilt test provokes dynamic alterations in total peripheral resistance and cardiac output in children with vasovagal syncope. *Acta Paediatr* 2018, 107: 1786–1791.
- Stewart JM, Medow MS, Glover JL, Montgomery LD. Persistent splanchnic hyperemia during upright tilt in postural tachycardia syndrome. *Am J Physiol Heart Circ Physiol* 2006, 290: H665–H673.
- Ocon AJ, Medow MS, Taneja I, Stewart JM. Respiration drives phase synchronization between blood pressure and RR interval following loss of cardiovagal baroreflex during vasovagal syncope. *Am J Physiol Heart Circ Physiol* 2011, 300: H527–H540.
- Vaddadi G, Guo L, Esler M, Socratous F, Schlaich M, Chopra R, *et al.* Recurrent postural vasovagal syncope: sympathetic nervous system phenotypes. *Circ Arrhythm Electrophysiol* 2011, 4: 711–718.
- Zhang Q, Jin H, Wang L, Chen J, Tang C, Du J. Randomized comparison of metoprolol versus conventional treatment in preventing recurrence of vasovagal syncope in children and adolescents. *Med Sci Monit* 2008, 14: CR199–203.
- Qingyou Z, Junbao D, Chaoshu T. The efficacy of midodrine hydrochloride in the treatment of children with vasovagal syncope. *J Pediatr* 2006, 149: 777–780.
- Tan MP, Newton JL, Chadwick TJ, Gray JC, Nath S, Parry SW. Home orthostatic training in vasovagal syncope modifies autonomic tone: results of a randomized, placebo-controlled pilot study. *Europace* 2010, 12: 240–246.
- On YK, Park J, Huh J, Kim JS. Is home orthostatic self-training effective in preventing neurally mediated syncope? *Pacing Clin Electrophysiol* 2007, 30: 638–643.
- Duygu H, Zoghi M, Turk U, Akyuz S, Ozerkan F, Akilli A, *et al.* The role of tilt training in preventing recurrent syncope in patients with vasovagal syncope: a prospective and randomized study. *Pacing Clin Electrophysiol* 2008, 31: 592–596.
- Bergström B, Manhem P, Brammert M, Lilja B, Sundkvist G. Impaired responses of plasma catecholamines to exercise in diabetic patients with abnormal heart rate reactions to tilt. *Clin Physiol* 1989, 9: 259–267.
- Tao C, Li X, Tang C, Jin H, Du J. Acceleration index predicts efficacy of orthostatic training on vasovagal syncope in children. *J Pediatr* 2019, 207: 54–58.
- Chen LY, Shen WK. Neurocardiogenic syncope: latest pharmacological therapies. *Expert Opin Pharmacother* 2006, 7: 1151–1162.
- Sra JS, Murthy VS, Jazayeri MR, Shen YH, Troup PJ, Avitall B, *et al.* Use of intravenous esmolol to predict efficacy of oral beta-adrenergic blocker therapy in patients with neurocardiogenic syncope. *J Am Coll Cardiol* 1992, 19: 402–408.
- Madrid AH, Ortega J, Rebollo JG, Manzano JG, Segovia JG, Sanchez A, *et al.* Lack of efficacy of atenolol for the prevention of neurally mediated syncope in a highly symptomatic population: a prospective, double-blind, randomized and placebo-controlled study. *J Am Coll Cardiol* 2001, 37: 554–559.
- Flevari P, Livanis EG, Theodorakis GN, Zarvalis E, Mesiskli T, Kremastinos DT. Vasovagal syncope: a prospective, randomized, crossover evaluation of the effect of propranolol, nadolol and placebo on syncope recurrence and patients' well-being. *J Am Coll Cardiol* 2002, 40: 499–504.
- Sheldon R, Connolly S, Rose S, Klingenheben T, Krahn A, Morillo C, *et al.* Prevention of Syncope trial (POST): a randomized, placebo-controlled study of metoprolol in the prevention of vasovagal syncope. *Circulation* 2006, 113: 1164–1170.
- Müller G, Deal BJ, Strasburger JF, Benson DW Jr. Usefulness of metoprolol for unexplained syncope and positive response to tilt testing in young persons. *Am J Cardiol* 1993, 71: 592–595.
- Scott WA, Pongiglione G, Bromberg BI, Schaffer MS, Deal BJ, Fish FA, *et al.* Randomized comparison of atenolol and fludrocortisone acetate in the treatment of pediatric neurally mediated syncope. *Am J Cardiol* 1995, 76: 400–402.
- Sheldon RS, Morillo CA, Klingenheben T, Krahn AD, Sheldon A, Rose MS. Age-dependent effect of beta-blockers in preventing vasovagal syncope. *Circ Arrhythm Electrophysiol* 2012, 5: 920–926.
- Zhang QY, Du JB, Zhen JL, Li WZ, Wang YL. Hemodynamic changes during head-up tilt test and predictive value thereof in predicting the efficacy of metoprolol therapy in children with vasovagal syncope. *Zhonghua Yi Xue Za Zhi* 2007, 87: 1260–1262. [Article in Chinese].
- Bondanelli M, Alboni P, Margutti A, Franceschetti P, Dinelli M, Gruppillo P, *et al.* Plasma galanin response to head-up tilt in

- normal subjects and patients with recurrent vasovagal syncope. *Metabolism* 2003, 52: 315–321.
33. Alboni P, Dinelli M, Gruppillo P, Bondanelli M, Bettiol K, Marchi P, *et al.* Haemodynamic changes early in prodromal symptoms of vasovagal syncope. *Europace* 2002, 4: 333–338.
  34. Song J, Li H, Wang Y, Liu P, Li X, Tang C, *et al.* Left ventricular ejection fraction and fractional shortening are useful for the prediction of the therapeutic response to metoprolol in children with vasovagal syncope. *Pediatr Cardiol* 2018, 39: 1366–1372.
  35. Kong Q, Yang X, Cai Z, Pan Y, Wang M, Liu M, *et al.* Twenty-four-hour urine NE level as a predictor of the therapeutic response to metoprolol in children with recurrent vasovagal syncope. *Ir J Med Sci* 2019, 188: 1279–1287.
  36. Strieper MJ, Campbell RM. Efficacy of alpha-adrenergic agonist therapy for prevention of pediatric neurocardiogenic syncope. *J Am Coll Cardiol* 1993, 22: 594–597.
  37. Zhang FW, Liao Y, Li XY, Chen L, Jin HF, Du JB. The predictive value of flow-mediated vasodilation on therapeutic efficacy of midorine hydrochloride for vasovagal syncope in children. *Zhongguo Shi Yong Er Ke Za Zhi* 2012, 27: 102–105. [Article in Chinese].
  38. Brignole M, Deharo JC, Menozzi C, Moya A, Sutton R, Tomaino M, *et al.* The benefit of pacemaker therapy in patients with neurally mediated syncope and documented asystole: a meta-analysis of implantable loop recorder studies. *Europace* 2018, 20: 1362–1366.
  39. Paech C, Wagner F, Mensch S, Antonin Gebauer R. Cardiac pacing in cardioinhibitory syncope in children. *Congenit Heart Dis* 2018, 13: 1064–1068.
  40. Boris JR, Bernadzikowski T. Demographics of a large paediatric Postural Orthostatic Tachycardia Syndrome Program. *Cardiol Young* 2018, 28: 668–674.
  41. Boris JR. Postural orthostatic tachycardia syndrome in children and adolescents. *Auton Neurosci* 2018, 215: 97–101.
  42. Li J, Liao Y, Du J, Zhang Q. Relationship between 24 hour urinary sodium and renin-angiotensin-aldosterone system in children with postural tachycardia syndrome. *Natl Med J China* 2015, 95: 2928–2932. [Article in Chinese].
  43. Raj SR, Biaggioni I, Yamhure PC, Black BK, Paranjape SY, Byrne DW, *et al.* Renin-aldosterone paradox and perturbed blood volume regulation underlying postural tachycardia syndrome. *Circulation* 2005, 111: 1574–1582.
  44. Bai W, Chen SY, Jin HF, Du JB. Vascular dysfunction of postural tachycardia syndrome in children. *World J Pediatr* 2018, 14: 13–17.
  45. Jacob G, Costa F, Shannon JR, Robertson RM, Wathen M, Stein M, *et al.* The neuropathic postural tachycardia syndrome. *N Engl J Med* 2000, 343: 1008–1014.
  46. Stewart JM. Pooling in chronic orthostatic intolerance: arterial vasoconstrictive but not venous compliance defects. *Circulation* 2002, 105: 2274–2281.
  47. Stewart JM, Weldon A. Reflex vascular defects in the orthostatic tachycardia syndrome of adolescents. *J Appl Physiol* 2001, 90: 2025–2032.
  48. Klein CM, Vernino S, Lennon VA, Sandroni P, Fealey RD, Benrud-Larson L, *et al.* The spectrum of autoimmune autonomic neuropathies. *Ann Neurol* 2003, 53: 752–758.
  49. Blitshteyn S. Autoimmune markers and autoimmune disorders in patients with postural tachycardia syndrome (POTS). *Lupus* 2015, 24: 1364–1369.
  50. Fedorowski A. Postural orthostatic tachycardia syndrome: clinical presentation, aetiology and management. *J Intern Med* 2019, 285: 352–366.
  51. Liao Y, Chen S, Liu X, Zhang Q, Ai Y, Wang Y, *et al.* Flowmediated vasodilation and endothelium function in children with postural orthostatic tachycardia syndrome. *Am J Cardiol* 2010, 106: 378–382.
  52. Yang J, Zhao J, Du S, Liu D, Fu C, Li X, *et al.* Postural orthostatic tachycardia syndrome with increased erythrocytic hydrogen sulfide and response to midodrine hydrochloride. *J Pediatr* 2013, 163: 1169–1173.e2.
  53. Zhang F, Li X, Ochs T, Chen L, Liao Y, Tang C, *et al.* Midregional pro-adrenomedullin as a predictor for therapeutic response to midodrine hydrochloride in children with postural orthostatic tachycardia syndrome. *J Am Coll Cardiol* 2012, 60: 315–320.
  54. Grubb BP, Kanjwal Y, Kosinski DJ. The postural tachycardia syndrome: a concise guide to diagnosis and management. *J Cardiovasc Electrophysiol* 2006, 17: 108–112.
  55. Liao Y, Du JB, Tang CS, Jin HF. Change and significance in the levels of plasma urotensin II and catestatin in children with postural orthostatic tachycardia syndrome. *Beijing Da Xue Xue Bao* 2011, 43: 436–439. [Article in Chinese].
  56. Wallman D, Weinberg J, Hohler AD. Ehlers-Danlos Syndrome and postural tachycardia syndrome: a relationship study. *J Neurol Sci* 2014, 340: 99–102.
  57. Bevegard S, Lodin A. Postural circulatory changes at rest and during exercise in five patients with congenital absence of valves in the deep veins of the legs. *Acta Med Scand* 1962, 172: 21–29.
  58. Bonyhay I, Freeman R. Sympathetic nerve activity in response to hypotensive stress in the postural tachycardia syndrome. *Circulation* 2004, 110: 3193–3198.
  59. Grubb BP. Postural tachycardia syndrome. *Circulation* 2008, 117: 2814–2817.
  60. Li H, Yu X, Liles C, Khan M, Vanderlinde-Wood M, Galloway A, *et al.* Autoimmune basis for postural tachycardia syndrome. *J Am Heart Assoc* 2014, 3: e000755.
  61. Shannon JR, Flatter NL, Jordan J, Jacob G, Black BK, Biaggioni I, *et al.* Orthostatic intolerance and tachycardia associated with norepinephrinetransporter deficiency. *N Engl J Med* 2000, 342: 541–549.
  62. Dahan S, Tomljenovic L, Shoenfeld Y. Postural orthostatic tachycardia syndrome (POTS)—A novel member of the autoimmune family. *Lupus* 2016, 25: 339–342.
  63. Watari M, Nakane S, Mukaino A, Nakajima M, Mori Y, Maeda Y, *et al.* Autoimmune postural orthostatic tachycardia syndrome. *Ann Clin Transl Neurol* 2018, 5: 486–492.
  64. Fedorowski A, Li H, Yu X, Koelsch KA, Harris VM, Liles C, *et al.* Antiadrenergic autoimmunity in postural tachycardia syndrome. *Europace* 2017, 19: 1211–1219.
  65. Ruzieh M, Batizy L, Dasa O, Oostra C, Grubb B. The role of autoantibodies in the syndromes of orthostatic intolerance: a systematic review. *Scand Cardiovasc J* 2017, 51: 243–247.
  66. Vernino S, Stiles LE. Autoimmunity in postural orthostatic tachycardia syndrome: Current understanding. *Auton Neurosci* 2018, 215: 78–82.
  67. Meck JV, Dreyer SA, Warren LE. Longduration head-down bed rest: project overview, vital signs, and fluid balance. *Aviat Space Environ Med* 2009, 80: A1–A8.
  68. Arbeille P, Kerbeci P, Mattar L, Shoemaker JK, Hughson R. Insufficient flow reduction during LBNP in both splanchnic and lower limb areas is associated with orthostatic intolerance after bedrest. *Am J Physiol Heart Circ Physiol* 2008, 295: H1846–H1854.
  69. Parsaik A, Allison TG, Singer W, Sletten DM, Joyner MJ, Benarroch EE, *et al.* Deconditioning in patients with orthostatic intolerance. *Neurology* 2012, 79: 1435–1439.
  70. Burkhardt BE, Fischer PR, Brands CK, Sletten DM, Joyner MJ, Benarroch EE, *et al.* Exercise performance in adolescents with autonomic dysfunction. *J Pediatr* 2011, 158: 15–19.

71. El-Sayed H, Hainsworth R. Salt supplement increases plasma volume and orthostatic tolerance in patients with unexplained syncope. *Heart* 1996, 75: 134–140.
72. Hampton JL, Parry SW, Kenny RA, Newton JL. Lower 24 hour urinary sodium concentrations are associated with more severe symptoms in subjects with vasovagal syncope. *Heart* 2004, 90: 687–688.
73. Zhang Q, Liao Y, Tang C, Du J, Jin H. Twenty-four-hour urinary sodium excretion and postural orthostatic tachycardia syndrome. *J Pediatr* 2012, 161: 281–284.
74. Stewart JM, Taneja I, Medow MS. Reduced body mass index is associated with increased angiotensin II in young women with postural tachycardia syndrome. *Clin Sci (Lond)* 2007, 113: 449–457.
75. Li H, Wang Y, Liu P, Chen Y, Feng X, Tang C, *et al.* Body mass index (BMI) is associated with the therapeutic response to oral rehydration solution in children with postural tachycardia syndrome. *Pediatr Cardiol* 2016, 37: 1313–1318.
76. Lin CJ, Chu YK, Chern CM. RBC volume deficiency in patients with excessive orthostatic decrease in cerebral blood flow velocity. *J Chin Med Assoc* 2014, 77: 174–178.
77. Lu W, Yan H, Wu S, Xu W, Jin H, Du J. Hemocytometric measures predict the efficacy of oral rehydration for children with postural tachycardia syndrome. *J Pediatr* 2017, 187: 220–224.
78. Convertino VA, Baumgartner N. Effects of hypovolemia on aortic baroreflex control of heart rate in humans. *Aviat Space Environ Med* 1997, 68: 838.
79. Li H, Liao Y, Wang Y, Liu P, Sun C, Chen Y, *et al.* Baroreflex sensitivity predicts short-term outcome of postural tachycardia syndrome in Children. *PLoS One* 2016, 11: e0167525.
80. Lai CC, Fischer PR, Brands CK, Fisher JL, Porter CB, Driscoll SW, *et al.* Outcomes in adolescents with postural orthostatic tachycardia syndrome treated with midodrine and beta-blockers. *Pacing Clin Electrophysiol* 2009, 32: 234–238.
81. Arnold AC, Okamoto LE, Diedrich A, Paranjape SY, Raj SR, Biaggioni I, *et al.* Low-dose propranolol and exercise capacity in postural tachycardia syndrome: a randomized study. *Neurology* 2013, 80: 1927–1933.
82. Chen L, Wang L, Sun J, Qin J, Tang C, Jin H, *et al.* Midodrine hydrochloride is effective in the treatment of children with postural orthostatic tachycardia syndrome. *Circ J* 2011, 75: 927–931.
83. Zhang Q, Chen X, Li J, Du J. Orthostatic plasma norepinephrine level as a predictor for therapeutic response to metoprolol in children with postural tachycardia syndrome. *J Transl Med* 2014, 12: 249.
84. Moyes AJ, Hobbs AJ. C-type natriuretic peptide: A multifaceted paracrine regulator in the heart and vasculature. *Int J Mol Sci* 2019, 20. pii: E2281.
85. Takekoshi K, Ishii K, Isobe K, Nomura F, Nammoku T, Nakai T. Effects of natriuretic peptides (ANP, BNP, CNP) on catecholamine synthesis and TH mRNA levels in PC12 cells. *Life Sci* 2000, 66: PL303–311.
86. Springer J, Azer J, Hua R, Robbins C, Adamczyk A, McBoyle S, *et al.* The natriuretic peptides BNP and CNP increase heart rate and electrical conduction by stimulating ionic currents in the sinoatrial node and atrial myocardium following activation of guanylyl cyclase-linked natriuretic peptide receptors. *J Mol Cell Cardiol* 2012, 52: 1122–1134.
87. Lin J, Han Z, Li H, Chen SY, Li X, Liu P, *et al.* Plasma C-type natriuretic peptide as a predictor for therapeutic response to metoprolol in children with postural tachycardia syndrome. *PLoS One* 2015, 10: e0121913.
88. Afsar B. Pathophysiology of copeptin in kidney disease and hypertension. *Clin Hypertens* 2017, 23: 13.
89. Franklin L, Bauce L, Pittman QJ. Depletion of central catecholamines reduce pressor responses to arginine vasopressin. *Brain Res* 1988, 438: 295–298.
90. Zhao J, Du S, Yang J, Lin J, Tang C, Du J, *et al.* Usefulness of plasma copeptin as a biomarker to predict the therapeutic effectiveness of metoprolol for postural tachycardia syndrome in children. *Am J Cardiol* 2014, 114: 601–605.
91. Tao C, Liu X, Zhang C, Chen Y, Huang Y. Comments on 2018 CPCS guideline for diagnosis and treatment of syncope in children and adolescents. *Sci Bull* 2019, 64: 291–292.
92. Li J, Zhang Q, Hao H, Jin H, Du J. Clinical features and management of postural tachycardia syndrome in children: a single-center experience. *Chin Med J (Engl)* 2014, 127: 3684–3689.
93. Xu WR, Wang TY. Diagnosis and treatment of syncope in pediatric patients: a new guideline. *Sci Bull* 2019, 64: 357.
94. Li Z, Polhemus DJ, Lefer DJ. Evolution of hydrogen sulfide therapeutics to treat cardiovascular disease. *Circ Res* 2018, 123: 590–600.
95. Zhao W, Zhang J, Lu Y, Wang R. The vasorelaxant effect of H(2)S as a novel endogenous gaseous K(ATP) channel opener. *EMBO J* 2001, 20: 6008–6016.
96. Lyngbakken MN, Myhre PL, Røsjø H, Omland T. Novel biomarkers of cardiovascular disease: Applications in clinical practice. *Crit Rev Clin Lab Sci* 2019, 56: 33–60.
97. Önal U, Valenzuela-Sánchez F, Vandana KE, Rello J. Mid-regional pro-adrenomedullin (MR-proADM) as a biomarker for sepsis and septic shock: narrative review. *Healthcare (Basel)* 2018, 6. pii: E110.
98. Voors AA, Kremer D, Geven C, Ter Maaten JM, Struck J, Bergmann A, *et al.* Adrenomedullin in heart failure: pathophysiology and therapeutic application. *Eur J Heart Fail* 2019, 21: 163–171.
99. Zhao J, Tang C, Jin H, Du J. Plasma copeptin and therapeutic effectiveness of midodrine hydrochloride on postural tachycardia syndrome in children. *J Pediatr* 2014, 165: 290–294.e1.
100. Liao Y, Yang J, Zhang F, Chen S, Liu X, Zhang Q, *et al.* Flow-mediated vasodilation as a predictor of the therapeutic response to midodrine hydrochloride in children with postural orthostatic tachycardia syndrome. *Am J Cardiol* 2013, 112: 816–820.
101. Heaton CM Jr, Kirby BS, Luckasen GJ, Larson DG, Dinunno FA. Endothelium-dependent vasodilatory signalling modulates  $\alpha$ 1-adrenergic vasoconstriction in contracting skeletal muscle of humans. *J Physiol* 2016, 594: 7435–7453.
102. Brignole M, Moya A, de Lange FJ, Deharo JC, Elliott PM, Fanciulli A, *et al.* Practical Instructions for the 2018 ESC Guidelines for the diagnosis and management of syncope. *Eur Heart J* 2018, 39: e43–e80.
103. Deng W, Liu Y, Liu AD, Holmberg L, Ochs T, Li X, *et al.* Difference between supine and upright blood pressure associates to the efficacy of midodrine on postural orthostatic tachycardia syndrome (POTS) in children. *Pediatr Cardiol* 2014, 35: 719–725.
104. Stewart JM, Montgomery LD. Regional blood volume and peripheral blood flow in postural tachycardia syndrome. *Am J Physiol Heart Circ Physiol* 2004, 287: H1319–H1327.
105. Stewart JM. Chronic orthostatic intolerance and the postural tachycardia syndrome (POTS). *J Pediatr* 2004, 145: 725–730.
106. Stewart JM, Medow MS, Montgomery LD. Local vascular responses affecting blood flow in postural tachycardia syndrome. *Am J Physiol Heart Circ Physiol* 2003, 285: H2749–H2756.
107. Gazit Y, Nahir AM, Grahame R, Jacob G. Dysautonomia in the joint hypermobility syndrome. *Am J Med* 2003, 115: 33–40.
108. Boris JR, Bernadzikowski T. Utilisation of medications to reduce symptoms in children with postural orthostatic tachycardia syndrome. *Cardiol Young* 2018, 28: 1386–1392.



CORRECTION

## Correction to: EPAC Negatively Regulates Myelination *via* Controlling Proliferation of Oligodendrocyte Precursor Cells

Zheng-Zheng Gao<sup>1</sup> · Ying-Cong Li<sup>2</sup> · Chong-Yu Shao<sup>2</sup> · Jian Xiao<sup>1</sup> · Ying Shen<sup>2</sup>  · Liang Zhou<sup>2,3</sup>

Published online: 7 May 2020  
© Shanghai Institutes for Biological Sciences, CAS 2020

**Correction to: Neurosci. Bull.**

<https://doi.org/10.1007/s12264-020-00495-6>

The original version of this article unfortunately contained a mistake. The name of first author, Zhen-Zhen Gao, was wrong. It should be Zheng-Zheng Gao.

---

The original article can be found online at <https://doi.org/10.1007/s12264-020-00495-6>.

---

✉ Ying Shen  
yshen@zju.edu.cn

✉ Liang Zhou  
zllzlj@zju.edu.cn

<sup>1</sup> Molecular Pharmacology Research Center, School of Pharmaceutical Sciences, Wenzhou Medical University, Wenzhou 325035, Zhejiang, China

<sup>2</sup> Department of Neurobiology, Zhejiang University School of Medicine, Hangzhou 310058, China

<sup>3</sup> Key Laboratory of Brain Science, Guizhou Institution of Higher Education, Zunyi Medical University, Zunyi 563000, China

## Neuroscience Bulletin Copyright Transfer Statement and Submission Form

We submit this type of article (✓):

- Original Article
- Insight

- Review
- Letter to the Editor

- Research Highlight
- Method

**Title of article:**

Words:                      Figures:                      (Color figures:                      );                      Tables:

### A signature below certifies compliance with the following statements

**Copyright Transfer Statement:** The copyright to this article is transferred to *Neuroscience Bulletin*, Shanghai Institutes for Biological Sciences, CAS and Springer (respective to owner if other than Shanghai Institutes for Biological Sciences, CAS and Springer and for U.S. government employees: to the extent transferable) effective if and when the article is accepted for publication. The author warrants that his/her contribution is original and that he/she has full power to make this grant. The author signs for and accepts responsibility for releasing this material on behalf of any and all co-authors. The copyright transfer covers the exclusive right and license to reproduce, publish, distribute and archive the article in all forms and media of expression now known or developed in the future, including reprints, translations, photographic reproductions, microform, electronic form (offline, online) or any other reproductions of similar nature. An author may self-archive an author-created version of his/her article on his/her own website. He/she may also deposit this version on his/her institution's and funder's (funder designated) repository at the funder's request or as a result of a legal obligation, including his/her final version, provided it is not made publicly available until after 12 months of official publication. He/she may not use the publisher's PDF version which is posted on [www.springerlink.com](http://www.springerlink.com) for the purpose of self-archiving or deposit. Furthermore, the author may only post his/her version provided acknowledgement is given to the original source of publication and a link is inserted to the published article on Springer's website. The link must be accompanied by the following text: "The original publication is available at [www.springerlink.com](http://www.springerlink.com)". The author is requested to use the appropriate DOI for the article. Articles disseminated *via* [www.springerlink.com](http://www.springerlink.com) are indexed, abstracted and referenced by many abstracting and information services, bibliographic networks, subscription agencies, library networks, and consortia.

After submission of this agreement signed by the corresponding author, changes of authorship or in the order of the authors listed will not be accepted by *Neuroscience Bulletin*, Shanghai Institutes for Biological Sciences of Chinese Academy of Sciences and Springer.

### Authorship responsibilities

I/We confirm that:

- (1) The work described has not been published before in any language or in any journal or media; that it is not under consideration for publication elsewhere; that its publication has been approved by all co-authors, if any, as well as (tacitly or explicitly) by the responsible authorities at the institution where the work was carried out.
- (2) We also give an assurance that the material will not be submitted for publication elsewhere until a decision has been made as to its acceptability for *Neuroscience Bulletin* in 2 months, then declare this statement becomes null and void.
- (3) I am/We are responsible for obtaining permission for the use of any material in the manuscript that may be under copyright to my/our employer(s) or other party(ies).
- (4) I have read the complete manuscript and accept responsibility for the content and completeness.
- (5) I have made a significant contribution to this work and am familiar with the contents.

Author (1) signed:                      Date:                      Author (2) signed:                      Date:

Author (3) signed:                      Date:                      Author (4) signed:                      Date:

Author (5) signed:                      Date:                      Author (6) signed:                      Date:

Author (7) signed:                      Date:                      Author (8) signed:                      Date:

Author (9) signed:                      Date:                      Author (10) signed:                      Date:

Corresponding author signed:                      Date:

Corresponding author address:

Tel:                      E-mail:

## Brief Instructions to Authors

*Neuroscience Bulletin* (NB) aims to publish research advances in the field of neuroscience and promote exchange of scientific ideas within the community. The journal publishes original papers of various topics on neuroscience and focuses on potential disease implications on the nervous system. NB welcomes research contributions on molecular, cellular, or developmental neuroscience using multidisciplinary approaches and functional strategies.

### Manuscript Submission

Manuscripts should be submitted through our online submission system, ScholarOne Manuscripts, at <http://mc03.manuscriptcentral.com/nsb> or <http://www.neurosci.cn>.

Manuscript file types that we accept for online submission include Word, WordPerfect, and TXT. For Figure submission, we accept JPEG, TIFF, or AI files. Required items differ for each article type and are specified during the submission process.

The submitted manuscript should be accompanied with a signed “*Neuroscience Bulletin* copyright transfer statement and submission form”.

### Manuscript Preparation

**Original Article:** An original article contains original research materials and presents compelling data on conceptual advances in any area of neuroscience. The total character count of all sections of the main text (including references and figure legends but excluding supplemental data) should not exceed 80,000, including spaces. Up to 8 figures and/or tables are allowed for the entire manuscript. The minimum requirement of a submitted research article is 40,000 characters in total (or 5000 words excluding the references) and at least 6 display items (figures and tables). The submitted manuscript should be a substantial novel research study in all aspects of neuroscience organizing a complete story with complex mechanisms elucidated using multiple techniques or approaches. NB also welcomes clinical research investigating the pathogenesis or diagnostic markers of a disease. Please note that for clinical trials, an Informed Consent should be provided as supplemental material and stated in the main text. NB no longer accepts clinical research that lack insightful mechanistic implications. References are limited to 100.

**Review:** Authoritative reviews contribute greatly to our journal and we are interested in comprehensive articles well-written to describe recent development in any field of neuroscience for a general audience. Authors are expected to cover controversies in the field and propose their own viewpoints in an unbiased and justifiable way. In particular, the scope of the review should not be dominated by the authors’ own work. Review is usually 30,000 to 50,000 characters in length (including an abstract of no more than 150 words, excluding the references and title) and 3-6 schematic illustrations are strongly encouraged. Reviews are often contributed by leaders in the field and solicited by the editors. The authors are encouraged to submit a letter of inquiry before the submission.

**Insight:** For Insight, the article should contain discussion on recent primary research literature similarly as Review. Yet, Insight is shorter in length (no more than 10,000 characters) and focuses on a narrower scope. It is possible that in Insight authors advocate

a position over a controversial issue or a speculative hypothesis. One schematic illustration is allowed to make the Insight more comprehensive. References are limited to 20.

**Method:** NB welcomes Method article on novel experimental techniques in any field of basic neuroscience. The Method can be written in the Research Article format yet the content should follow the criteria described below. The description of the method must be accompanied by its validation, its application to an important biological question, and results illustrating its performance in comparison to available approaches. The manuscript will be judged on its novelty, general interest, through assessments of methodological performance and comprehensive technical descriptions that facilitate immediate application. The detailed step-by-step procedure must be described in the form of flow charts for readers to comprehend easily. Additional annotation for key procedures and special treatments will be encouraged. In addition, please note that NB no longer accepts Method on neurosurgery pathway, surgical techniques, or any other clinical related technical studies.

**Letter to the Editor:** The Letter to the Editor reports a short but exciting finding in a particular field of neuroscience with high quality and of broad interest. The letter should be brief yet concise, and no specific subsections are required. No Materials and Methods section is needed, but any technical information which the authors think is important should be submitted as supplementary materials. The total character count should not exceed 15,000 (exclude references and title) and the display items should be limited to 2. References are limited to 15. No abstract and subsections are needed.

**Research Highlight:** The Research Highlight describes recent research advances by articles published in NB or other journals. It highlights the main results of the research, emphasizes the significance and provides further discussion on the topic. The main text of a Research Highlight is up to 10,000 characters (excluding references and title) with no more than 10 references and one or two figures. Research Highlights are usually by editor invitation, but submitted manuscript with high quality will also be considered. No abstract and subsections are needed.

Submitted manuscripts should be divided into the following sections:

(1) Title Page; (2) Abstract; (3) Introduction; (4) Materials and Methods; (5) Results; (6) Discussion; (7) Acknowledgements; (8) References; (9) Figures, legends, and tables; (10) Supplementary information.

### Manuscript Revision

Upon peer-reviews, the authors may be asked to revise the manuscript. If the authors have substantial reasons to believe that their manuscript was treated unfairly, they may appeal for reconsideration. Revision should be completed within four (minor revision) or eight weeks (major revision). The authors should provide a cover letter and a point-to-point response for addressing the reviewers’ comments. The editor will notify the corresponding author upon the acceptance of the manuscript. Accepted papers will be processed to advanced online publication as soon as possible.

### Proofs

A PDF proof will be sent to the authors for them to correct last minute errors on the manuscript.

### Page Charges

Page charges for the printed form are as follows: 500 CNY (80 USD) for each text page, 800 CNY (120 USD) for each page containing black-and-white figures, 1500 CNY (250 USD) for each page containing color figures. The corresponding author will receive an invoice on all the publication-related charges once the manuscript is accepted for publication and enters the editing process.

### Make checks or money orders payable to:

Beneficiary's Name (帐户名称): Shanghai Institutes of Biological Sciences, Chinese Academy of Sciences  
(中国科学院上海生命科学研究院)

Beneficiary's A/C NO. (帐号): 033924-00801048006

Beneficiary's Bank(开户行): Fenglin Branch of Xuhui District, Agricultural Bank of China (农行徐汇区枫林支行)

Payment can also be mailed by Post Office to the Editorial Office of *Neuroscience Bulletin*.

Editorial Office of *Neuroscience Bulletin*  
(《神经科学通报》编辑部收):

Room 405, Building 31B, 319 YueYang Road, Shanghai 200031, China (200031, 上海市岳阳路 319 号31B 楼 405室).

Tel.: +86-21-54922863; Fax: +86-21-54922833;  
E-mail: nsb@sibs.ac.cn

(Updated March 2019)

## Neuroscience Bulletin

### Editors-in-Chief

**Shumin Duan**, Zhejiang University, Hangzhou, China  
**Ru-Rong Ji**, Duke University, Durham, USA

### Consulting Editors

**Yizhang Chen**, Second Military Medical University, Shanghai, China  
**Muming Poo**, Institute of Neuroscience, CAS, Shanghai, China  
**Larry R. Squire**, University of California, San Diego, USA  
**Charles F. Stevens**, The Salk Institute, San Diego, USA  
**Xiongli Yang**, Fudan University, Shanghai, China

### Executive Associate Editors

**Iain C. Bruce**, Zhejiang University, Hangzhou, China  
**Guangyin Xu**, Institute of Neuroscience, Soochow University, Suzhou, China

### Associate Editors

<b>Zhong Chen</b> , Zhejiang University, Hangzhou, China	<b>You Wan</b> , Peking University, Beijing, China
<b>Tianming Gao</b> , South Medical University, Guangzhou, China	<b>Jian-Zhi Wang</b> , Huazhong University of Science and Technology, Wuhan, China
<b>Shihui Han</b> , Peking University, Beijing, China	<b>Yanjiang Wang</b> , Daping Hospital, Third Military Medical University, Chongqing, China
<b>Cheng He</b> , Second Military Medical University, Shanghai, China	<b>Longjun Wu</b> , Mayo Clinic, Rochester, USA
<b>Tianzi Jiang</b> , Institute of Automation, CAS, Beijing, China	<b>Zhi-Ying Wu</b> , Huashan Hospital, Shanghai Medical College, Fudan University, Shanghai, China
<b>Weidong Le</b> , Dalian Medical University, Dalian, China	<b>Tianle Xu</b> , Shanghai Jiaotong University, Shanghai, China
<b>Tao Li</b> , West China Hospital, Sichuan University, Chengdu, China	<b>Dai Zhang</b> , Peking University, Beijing, China
<b>Mengsheng Qiu</b> , Hangzhou Normal University, Hangzhou, China	<b>Hanting Zhang</b> , West Virginia University Health Sciences Center, Morgantown, USA
<b>Fu-Dong Shi</b> , St. Joseph's Hospital and Medical Center, Phoenix, USA	<b>Chunjiu Zhong</b> , Fudan University, Shanghai, China

### Editorial Board

<b>Philippe Ascher</b> , Pairs Diderot University, Paris, France	<b>Yiru Fang</b> , Shanghai Mental Health Center, Shanghai Jiaotong University School of Medicine, Shanghai, China
<b>George Baillie</b> , Institute of Cardiovascular and Medical Sciences, University of Glasgow, UK	<b>Richard S. Frackowiak</b> , University of Lausanne, Lausanne, Switzerland
<b>Guo-Qiang Bi</b> , University of Science and Technology of China, Hefei, China	<b>Tamás F. Freund</b> , Institute of Experimental Medicine of the Hungarian Academy of Sciences, Budapest, Hungary
<b>Junli Cao</b> , Xuzhou Medical College, Xuzhou, China	<b>Yongjing Gao</b> , Institute of Nautical Medicine, Nantong University, Nantong, China
<b>L. Judson Chandler</b> , Medical University of South Carolina, USA	<b>Charles Gilbert</b> , The Rockefeller University, New York, USA
<b>Jun Chen</b> , The Fourth Military Medical University, Xi'an, China	<b>Xiaosong Gu</b> , Nantong University, Nantong, China
<b>Qing-Hui Chen</b> , Michigan Technological University, Houghton, USA	<b>Junhai Han</b> , Southeast University, Nanjing, China
<b>Isaac M. Chiu</b> , Harvard Medical School, Boston, USA	<b>Philip G. Haydon</b> , Tufts University, Boston, USA
	<b>Joe Herbert</b> , University of Cambridge, Cambridge, UK
	<b>Gregg E. Homanics</b> , University of Pittsburgh, USA

- Zhi-An Hu**, Third Military Medical University, Chongqing, China
- Kazuhide Inoue**, Kyushu University, Fukuoka, Japan
- Yong-Hua Ji**, Shanghai University, Shanghai, China
- Helmut Kettenmann**, Max-Delbrück Center for Molecular Medicine, Berlin, Germany
- O.A. Krishtal**, Bogomoletz Institute of Physiology, Kiev, Ukraine
- Robert H. LaMotte**, Yale University School of Medicine, New Haven, USA
- Pierre Lavenex**, University of Fribourg, Fribourg, Switzerland
- C. Justin Lee**, Korea Institute of Science and Technology, Korea
- Juan Lerma**, Instituto de Neurociencias de Alicante, Alicante, Spain
- Bao-Ming Li**, Nanchang University, Nanchang, China
- Wolfgang Liedtke**, Duke University School of Medicine, Durham, USA
- David J. Linden**, Johns Hopkins University, Baltimore, USA
- Stuart A. Lipton**, Sanford-Burnham Medical Research Institute and University of California at San Diego, San Diego, USA
- Tong Liu**, Institute of Neuroscience, Soochow University, Suzhou, China
- Lin Lu**, Peking University Sixth Hospital, Beijing, China
- Bridget Lumb**, University of Bristol, Bristol, UK
- Benyan Luo**, Zhejiang University School of Medicine, China
- Jian-Hong Luo**, Zhejiang University School of Medicine, China
- Zhen-Ge Luo**, ShanghaiTech University, China
- Lan Ma**, Fudan University, Shanghai, China
- Qiufu Ma**, Dana-Farber Cancer Institute, Boston, USA
- Quanhong Ma**, Institute of Neuroscience, Soochow University, Suzhou, China
- Robert C. Malenka**, Stanford University, Stanford, USA
- Manuel S. Malmierca**, Universidad de Salamanca, Salamanca, Spain
- John H.R. Maunsell**, Harvard Medical School, Houston, USA
- Earl K. Miller**, Massachusetts Institute of Technology, Cambridge, USA
- Enrico Mugnaini**, Northwestern University, Feinberg School of Medicine, Chicago, USA
- Vladimir Parpura**, University of Alabama at Birmingham, Birmingham, USA
- Jos Prickaerts**, School for Mental Health and Neuroscience, Maastricht University, the Netherland
- Bruce R. Ransom**, University of Washington, Seattle, USA
- Tom E. Salt**, University College London, London, UK
- Joshua R. Sanes**, Harvard University, Boston, USA
- Michael N. Shadlen**, Columbia University, New York, USA
- Morgan Sheng**, Genentech, Inc., South San Francisco, USA
- Yousheng Shu**, Beijing Normal University, Beijing, China
- Sangram S. Sisodia**, The University of Chicago, Chicago, USA
- Peter Somogyi**, University of Oxford, Oxford, UK
- Feng-Yan Sun**, Fudan University, Shanghai, China
- Dick F. Swaab**, Netherlands Institute for Neuroscience, Amsterdam, Netherlands
- Keiji Tanaka**, RIKEN Brain Science Institute, Tokyo, Japan
- Xiaoqing Tang**, University of South China, Hengyang, China
- Yong Tang**, Chengdu University of TCM, Chengdu, China
- Makoto Tsuda**, Kyushu University, Fukuoka, Japan
- Alexej Verkhratsky**, The University of Manchester, Manchester, UK
- Steven R. Vincent**, University of British Columbia, Vancouver, Canada
- Guanghui Wang**, Soochow University, Suzhou, China
- Jian-Jun Wang**, Nanjing University, Nanjing, China
- Yun Wang**, Neuroscience Research Institute, Peking University, Beijing, China
- Xu-Chu Weng**, Hangzhou Normal University, Hangzhou, China
- William Wisden**, Imperial College London, London, UK
- Jun-Xia Xie**, Qingdao University, Qingdao, China
- Lin Xu**, Kunming Institute of Zoology, CAS, Kunming, China
- Xiao-Hong Xu**, Institute of Neuroscience, CAS, Shanghai, China
- Ying Xu**, School of Pharmacy & Pharmaceutical Sciences, University at Buffalo, The State University of New York, USA
- Yun Xu**, Nanjing Drum Tower Hospital, Nanjing, China
- Fengwei Yu**, National University of Singapore, Singapore
- Shanping Yu**, Emory University School of Medicine, Atlanta, USA
- Hong Zhang**, The Second Affiliated Hospital of Zhejiang University School of Medicine, Hangzhou, China
- Xiaohui Zhang**, Beijing Normal University, Beijing, China
- Xu Zhang**, Institute of Neuroscience, CAS, Shanghai, China
- Yong Zhang**, Peking University, Beijing, China
- Yu-Qiu Zhang**, Fudan University, Shanghai, China
- Zhi-Jun Zhang**, Zhongda Hospital, Southeast University, Nanjing, China
- Ping Zheng**, Fudan University, Shanghai, China
- Jiang-Ning Zhou**, University of Science and Technology of China, Hefei, China
- Libin Zhou**, Joint Laboratory for Brain Function and Health, Jinan University and The University of Hong Kong, Guangzhou, China
- Richard E. Zigmond**, Case Western Reserve University, Cleveland, USA
- Yimin Zou**, University of California-San Diego, USA

## Neuroscience Bulletin

### Copyright Information

#### *For Authors*

As soon as an article is accepted for publication, authors will be requested to assign copyright of the article (or to grant exclusive publication and dissemination rights) to the publisher (respective the owner if other than Springer Nature). This will ensure the widest possible protection and dissemination of information under copyright laws.

More information about copyright regulations for this journal is available at [www.springer.com/12264](http://www.springer.com/12264)

#### *For Readers*

While the advice and information in this journal is believed to be true and accurate at the date of its publication, neither the authors, the editors, nor the publisher can accept any legal responsibility for any errors or omissions that may have been made. The publisher makes no warranty, express or implied, with respect to the material contained herein.

All articles published in this journal are protected by copyright, which covers the exclusive rights to reproduce and distribute the article (e.g., as offprints), as well as all translation rights. No material published in this journal may be reproduced photographically or stored on microfilm, in electronic data bases, on video disks, etc., without first obtaining written permission from the publisher (respective the copyright owner if other than Springer Nature). The use of general descriptive names, trade names, trademarks, etc., in this publication, even if not specifically identified, does not imply that these names are not protected by the relevant laws and regulations.

Springer Nature has partnered with Copyright Clearance Center's RightsLink service to offer a variety of options for reusing Springer Nature content. For permission to reuse our content please locate the material that you wish to use on [link.springer.com](http://link.springer.com) or on [springerimages.com](http://springerimages.com) and click on the permissions link or go to [copyright.com](http://copyright.com) and enter the title of the publication that you wish to use. For assistance in placing a permission request, Copyright Clearance Center can be contacted directly via phone: +1-855-239-3415, fax: +1-978-646-8600, or e-mail: [info@copyright.com](mailto:info@copyright.com)

© Shanghai Institutes for Biological Sciences, CAS 2020

### Journal Website

[www.springer.com/12264](http://www.springer.com/12264)  
Electronic edition: [link.springer.com/journal/12264](http://link.springer.com/journal/12264)

### Subscription Information

Volume 36 (12 issues) will be published in 2020.

ISSN: 1673-7067 print  
ISSN: 1995-8218 electronic

For information on subscription rates please contact Springer Nature Customer Service Center: [customerservice@springernature.com](mailto:customerservice@springernature.com)

The Americas (North, South, Central America and the Caribbean)  
Springer Nature Journal Fulfillment,  
Harborside Plaza II,  
200 Hudson Street, Jersey City,  
NJ 07302, USA  
Tel. 800-SPRINGER (777-4643);  
212-460-1500 (outside  
North America)

### Outside the Americas

Springer Nature Customer Service  
Center GmbH, Tiergartenstr. 15,  
69121 Heidelberg, Germany  
Tel.: +49-6221-345-4303

### Advertisements

E-mail contact: [advertising@springer.com](mailto:advertising@springer.com) or [anzeigen@springer.com](mailto:anzeigen@springer.com) (Germany)

### Disclaimer

Springer Nature publishes advertisements in this journal in reliance upon the responsibility of the advertiser to comply with all legal requirements relating to the marketing and sale of products or services advertised. Springer Nature and the editors are not responsible for claims made in the advertisements published in the journal. The appearance of advertisements in Springer Nature publications does not constitute endorsement, implied or intended, of the product advertised or the claims made for it by the advertiser.

### Office of Publication

Springer Nature Singapore Pte Ltd.  
152 Beach Road, #21-01/04  
Gateway East, Singapore 189721,  
Singapore



# NEUROSCIENCE BULLETIN

Impact Factor

# 4.246

Q2

2018 Journal Citation Report  
(Clarivate Analytics, 2019)

**NEUROSCIENCE BULLETIN 神经科学通报 (Monthly)**

Vol. 36 No. 6 June 15, 2020

**Sponsored by:** Shanghai Institutes for Biological Sciences, Chinese Academy of Sciences  
Chinese Neuroscience Society  
Second Military Medical University

**Editors-in-Chief:** Shumin Duan, Ru-Rong Ji

**Edited by:** Editorial Board of *Neuroscience Bulletin*

319 Yueyang Road, Building 31 B, Room 405, Shanghai 200031, China

Phone: +86-21-54922863; Fax: +86-21-54922833

E-mail: nsb@sibs.ac.cn; <http://www.neurosci.cn>

**Editors:** Bin Wei, Xu Jiang, Zhi-Rui Liu

**Published by:** Shanghai Institutes for Biological Sciences, Chinese Academy of Sciences (320 Yueyang Road, Shanghai)

**Printed by:** Shanghai Shengtong Times Printing Co., Ltd (A6, No. 2888, Caolang Highway, Jinshan District, Shanghai)

**Overseas Distributed by:** Springer Nature

**Home Distributed by:** Local Post Offices

ISSN 1673-7067

CN 31-1975/R

Post Office Code Number: 4-608

Permit of Ad. Number: 3100420130051

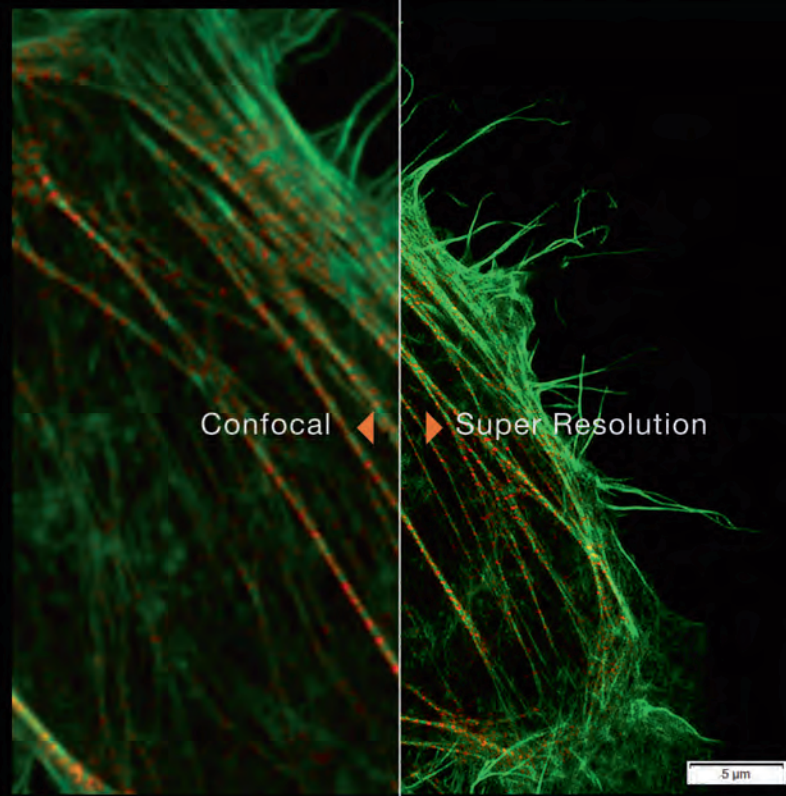
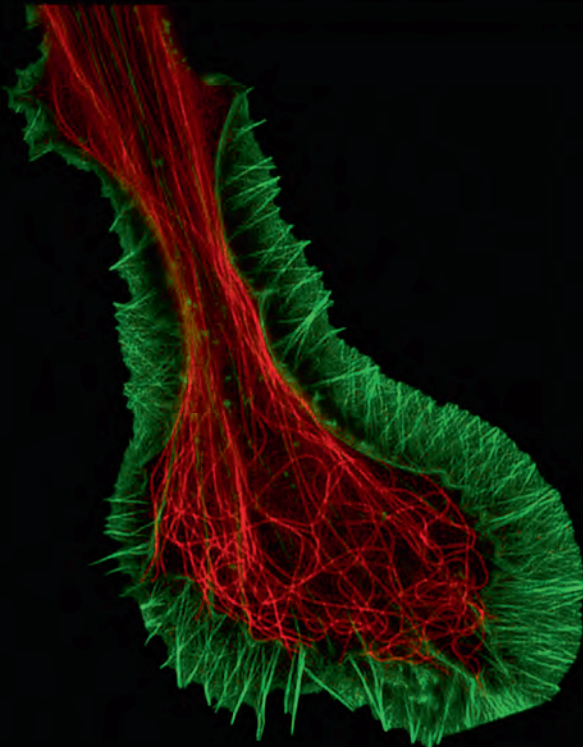
Price: ¥ 100.00

ISSN 1673-7067



兼顾分辨率和速度的

转盘共聚焦活细胞超分辨系统 **SpinSR10**



- 分辨率高达110nm的实时超分辨率成像
- 专有反卷积算法进一步提升图像质量
- 宽视野成像，速度高达 200fps
- 特色硅油物镜可以实现活细胞深层成像
- 宽场、共聚焦、超分辨率模式自由切换
- 功能强大的智能cellSens软件平台



奥林巴斯（北京）销售服务有限公司

北京朝阳区酒仙桥路10号恒通商务园B12C座2F (北京) 010-59756006  
 上海市徐汇区淮海中路1010号嘉华中心11楼 (上海) 021-51582084  
 广州市环市东路403号广州电子大厦16楼 (广州) 020-61227171

陕西省西安市新城区尚德路85号太平洋保险大厦8F

湖北省武汉市江岸区中山大道1628号武汉天地企业中心5号7楼701单元  
 四川省成都市人民南路四段三号来福士广场T1-11楼  
 辽宁省沈阳市沈河区友好街10号新地中心1号楼3501室

(西安) 029-87206108

(武汉) 027-82718838

(成都) 028-86703700

(沈阳) 024-23342084